

University of Windsor

Scholarship at UWindor

Electronic Theses and Dissertations

Theses, Dissertations, and Major Papers

10-1-2021

Efficient Design of Integrated Underbody and Battery Pack for Battery Electric Vehicles

Gabriele Rosso
University of Windsor

Follow this and additional works at: <https://scholar.uwindsor.ca/etd>



Part of the [Automotive Engineering Commons](#)

Recommended Citation

Rosso, Gabriele, "Efficient Design of Integrated Underbody and Battery Pack for Battery Electric Vehicles" (2021). *Electronic Theses and Dissertations*. 8741.

<https://scholar.uwindsor.ca/etd/8741>

This online database contains the full-text of PhD dissertations and Masters' theses of University of Windsor students from 1954 forward. These documents are made available for personal study and research purposes only, in accordance with the Canadian Copyright Act and the Creative Commons license—CC BY-NC-ND (Attribution, Non-Commercial, No Derivative Works). Under this license, works must always be attributed to the copyright holder (original author), cannot be used for any commercial purposes, and may not be altered. Any other use would require the permission of the copyright holder. Students may inquire about withdrawing their dissertation and/or thesis from this database. For additional inquiries, please contact the repository administrator via email (scholarship@uwindsor.ca) or by telephone at 519-253-3000ext. 3208.

Efficient Design of Integrated Underbody and Battery Pack for Battery Electric Vehicles

By

Gabriele Rosso

A Thesis

Submitted to the Faculty of Graduate Studies
through the Department of Mechanical, Automotive & Materials Engineering
in Partial Fulfilment of the Requirements for
the Degree of Master of Applied Science
at the University of Windsor

Windsor, Ontario, Canada

2021

© 2021 Gabriele Rosso

Efficient Design of Integrated Underbody and Battery Pack for Battery Electric Vehicles

By

Gabriele Rosso

APPROVED BY:

N. Zamani

Department of Mechanical, Automotive & Materials Engineering

F. Baki

Department of Mechanical, Automotive & Materials Engineering

J. Urbanic, Co-Advisor

Department of Mechanical, Automotive & Materials Engineering

J. Johrendt, Co-Advisor

Department of Mechanical, Automotive & Materials Engineering

September 16, 2021

Declaration of Originality

I hereby certify that I am the sole author of this thesis and that no part of this thesis has been published for publication.

I certify that, to the best of my knowledge, my thesis does not infringe upon anyone's copyright nor violate any proprietary rights and that any ideas, techniques, quotations, or any other material from the work of other people included in my thesis, published or otherwise, are fully acknowledged in accordance with the standard referencing practices. Furthermore, to the extent that I have included copyrighted material that surpasses the bounds of fair dealing within the meaning of the Canada Copyright Act, I certify that I have obtained a written permission from the copyright owner(s) to include such material(s) in my thesis and have included copies of such copyright clearances to my appendix.

I declare that this is a true copy of my thesis, including any final revisions, as approved by my thesis committee and the Graduate Studies office, and that this thesis has not been submitted for a higher degree to any other University or Institution.

Abstract

Climate change and the consequent more restrictive regulations are pushing the industry towards higher efficiency and lower emissions means of transport. The road transport sector is deeply affected, leading the main Original Equipment Manufacturers (OEMs) to start the transition to alternative powertrains, among which Battery Electric Vehicles (BEVs) are the faster-growing.

The large, heavy, and safety-critical battery pack asks for a specific optimized solution for a lightweight and high-performance vehicle platform.

In this research, a first benchmarking analysis is presented to study the current state-of-the-art for BEV underbody and battery pack designs. Following this investigation, a classification scheme was designed to allow easier comparison between different solutions, pointing out the most relevant characteristics and best design choices.

Starting from the results of the benchmarking analysis, the study followed with a series of Finite Element Analyses (FEAs), on different simplified platform models, organized through a fractional factorial Design of Experiment (DOE). The responses of the experiments were the torsional stiffness and bending stiffness and first resonance mode, evaluated together with the mass of the system.

These investigations revealed that the most influential factors for the analyzed performance outputs were the torque box and rocker rail internal structures, together with the material of the battery pack. Other parameters were less influential, but the study was still able to highlight the more favourable configurations.

Through two additional analyses, the battery pack was found to heavily affect the structure static stiffness, but both the battery pack and floor panels needed appropriate stiffening to avoid low-frequency resonance.

The conducted analysis allowed the development of a linear regression model and the execution of a design optimization which delivered two different optimized solutions, showing good performance and high weight efficiency.

After the discussion of the gathered results, validated design guidelines were created to provide a starting point for the development of future dedicated and integrated BEV underbodies and battery packs.

Dedication

To my mother Pia, my father Giorgio and my girlfriend Noemi, who constantly supported me, and to my dearest friends...

Acknowledgements

Taking part in this project was an incredible opportunity for growth, both from the academic and personal points of view. The program started and developed under many difficulties due to the ongoing pandemic, but despite that, any challenge was a learning opportunity.

I would like to thank Stellantis, the University of Windsor and Politecnico di Torino that gave me this possibility.

Thanks to my academic advisors at University of Windsor, Dr. Jill Urbanic and Dr. Jennifer Johrendt. Their support was crucial to keep me on track during the critical phases of the project, helping me foreseeing possible difficulties and respecting my timetable. Their guidance towards the right research approach as well as the suggestion to develop a classification scheme, heavily enriched the contents of this work. Thanks again to Dr. Jill Urbanic and her research team for the helpful feedback provided during my presentations, as well as the possibility of enlarging my knowledge on the wide range of topics in your research projects.

Thanks to my academic advisor at Politecnico Dr. Alessandro Scattina for his constant feedback and suggestions, from the start to the conclusion of the project. Thanks, as well, to my co-advisor at Politecnico, Dr. Andrea Tonoli, for his detailed suggestions, in particular for the initial set up of the FEA. Thanks to both advisors for your support for the development of the Finite Element Method (FEM) analysis, especially in the trickier initial phases.

Thanks to my Stellantis US advisor Dr. Khaled Shahwan, who, since he joined the project, demonstrated high interest, and provided constant guidance and support in the most critical moments. The constant hints on the FEM analysis, as well as his suggestion to put clear boundaries to the research, heavily contributed to the success of this project.

Thanks to my advisors from CRF and Stellantis EMEA, Eng. Giorgio Luigi Masoero and Eng. Luca Stolcis for their industry insights and suggestions to make the study deliver useful information for the industrial partner.

Special thanks to all the academic supervisors of this project, Dr. Giovanni Belin-

gardi, Dr. Maria Pia Cavatorta, from Politecnico di Torino and again Dr. Jennifer Johrendt from University of Windsor, who assisted us especially in the difficult initial project set-up. Thanks to Stellantis supervisor Eng. Marie Mills for the great support throughout the program with several meetings which gave us the possibility to discuss our project together with the other members of the DIMD program. I would like to acknowledge my committee members, Dr. Nader Zamani and Dr. Fouzia Baki for your precious pieces of advice and contributions while reviewing my work.

Thanks also to Eng. Paolo De Blasi for his kind support and suggestions on the DOE definition.

Thanks to the help of all these collaborators I had the chance to explore new topics and gather a huge amount of knowledge that I will bring with me in my future career.

I then would like to express my infinite gratitude to my parents, Pia and Giorgio for having always supported me and my bizarre ideas inside and outside my academic career. Thanks for having taught me to be humble and patient, to never settle and always strive for the best, being hungry to learn and willing to improve also when crossing difficult moments.

Thanks from my heart to my girlfriend Noemi, who supported me throughout the last six years, despite my continuous complaints under the high study workload. You gave me the strength to continue and reach my goals even when it looked too hard or when you were realizing that I was not the same person under pressure. Thanks for helping me understanding my defects and my strengths. After this long time afar, I can not wait to see you again and give you back the help you gave me.

Thanks also to Roberta and Luca for welcoming me into your family as a son.

Thanks to all my cousins for the special adventures shared together, on holiday, at the *Oratorio* and playing with go karts and pocket bikes.

Thanks to all my aunts and uncles for all the beautiful moments living our family traditions.

Thanks to my friend Lorenzo for always listening to my more or less boring stories and being willing to share his for almost twenty years. I am looking forward to be back and share some new stories from our experiences.

Thanks to all my friends in Italy and abroad for the good times spent together, cutting off from the daily routine and enjoying every simple moment.

A special thanks to all the members of the Fotoclub Chivasso “La Tola”, a wonderful adventure that developed together with my academic career, and allowed me to share a common passion, learn from each other and build a beautiful group of people. I am looking forward to share with you the many pictures I took here in Canada.

Thanks to my travel mates Filippo and Silvio, with which we shared many Canadian

adventures living together in these eight months. It has been a beautiful experience, learning from each other and helping each other.

Thanks to Mike and Ellie for the beautiful moments across Ontario and Canada.

Thanks to the other guys from the DIMD program, Zac, Yhiong and Jiaqi for sharing few but really enjoyable evenings together. Looking forward to see you again in Italy.

Table of Contents

Declaration of Originality	III
Abstract	IV
Dedication	V
Acknowledgements	VI
List of Figures	XIII
List of Tables	XVIII
Acronyms	XX
1 Introduction	1
1.1 Background and Motivation	2
1.1.1 BEVs Historical Background	2
1.1.2 Environmental Concerns and New Regulations	4
1.1.3 BEVs Benefits and Challenges	5
1.1.4 The Need for Dedicated BEV Architectures	9
1.2 Purpose of the Study	11
1.2.1 Importance of the Study	12
1.2.2 Project Scope and Hypothesis	13
2 Literature Review	16
2.1 Underbody Design Principles	17
2.2 Underbody Functions	20
2.2.1 Structural Functions	20
2.2.2 Safety Functions	21
2.3 Battery Technology and Battery Pack	22
2.3.1 BEVs Architecture	27
2.3.2 Relevant Patents	30
2.3.3 New Underbody Concept	32

3	Benchmarking Analysis and Classification Scheme	34
3.1	Methodology	34
3.1.1	Benchmarking Material and Resources	34
3.1.2	Analysis Outline	38
3.2	Review and Highlights of Analysed Solutions	39
3.2.1	BEVs Underbody Distinctive Features	39
3.2.2	BEVs Battery Pack Features	42
3.3	Classification Scheme	43
3.3.1	Methodology	43
3.3.2	Classification Scheme Description	45
	General Vehicle Information	45
	BIW and underbody	47
	Battery pack	52
	Battery Pack and Underbody Integration	56
3.3.3	Validation and Examples	59
3.3.4	Future Uses	60
4	Model Definition	62
4.1	Structural Layout and Dimensioning	62
4.2	CAD Model Development	66
4.3	FEM Model Development	67
4.3.1	Geometry Cleanup and Meshing	67
4.3.2	Material Model	71
4.3.3	Load Cases and Outputs	72
	Torsion Load Case	73
	Bending Load Case	74
	Modal Load Case	75
5	Design of Experiment	77
5.1	Design Space Definition	77
5.1.1	Geometry and Layout Variations	78
	Fixed Parameters	78
	Underbody Geometry	78
	Battery Pack Geometry	82
5.1.2	Material Properties Variations	83

	Underbody Materials	83
	Battery Pack Materials	85
5.1.3	Restricted Design Space	85
	Geometry	86
	Material and Thickness	86
5.2	Experiment Definition	88
5.2.1	Conducted Analyses	91
	Complete Model Analysis	91
	Batteryless Analysis	91
	Panelless Analysis	92
	Optimization and Stiffened Panels Analysis	92
5.3	Methodology for Result Analysis	92
5.3.1	Analysis of Variance (ANOVA)	93
	P-value	93
	Pooling	94
	Percentages of Contribution	94
5.3.2	Linear Regression Model	94
	Analysis of Means	95
	Response Optimization	95
6	Results and Discussion	96
6.1	Complete Model Analysis	96
6.1.1	Mass	96
6.1.2	Torsional Stiffness	99
6.1.3	Bending Stiffness	103
6.1.4	First Modal Frequency	108
6.2	Batteryless Analysis	110
6.3	Panelless Analysis	113
6.3.1	First Modal Frequency - Panelless	113
6.4	Optimization and Stiffened Panels Analysis	117
6.4.1	First Optimization	118
	Stiffened Panels - First Optimization	121
6.4.2	Second Optimization	123
	Stiffened Panels - Second Optimization	126

6.5	Design Guidelines	128
6.5.1	Structure Geometry and Layout	129
	Rocker Internal Structure	129
	Torque Boxes Shape	130
	Lower Battery Pack Enclosure Shape	131
	Number of Battery Pack Cross-Members	132
	Number of Battery Pack Longitudinal Members	133
6.5.2	Material and Thickness	134
	Side Members Material	134
	Torque Boxes Material	135
	Rear Cross-Member Material	135
	Front Cross-Member Thickness	136
	Front Floor Cross-Member Thickness	137
	Battery Pack Material	138
	Panels Embossing	139
6.5.3	Excluded Components	139
7	Conclusions and Future Work	140
7.1	Summary and Conclusions	140
7.2	Future Work	142
	Bibliography	145
	Appendix A Fractional Factorial Plan	154
	Appendix B ANOVA detailed results	156
	B.1 Complete Model Analysis	157
	B.2 Panelless Model	165
	Vita Auctoris	167

List of Figures

1.1	Camille Jenatzy on the “ <i>La Jamais Contente</i> ”, 1899 [7]	2
1.2	GM AUTOonomy concept, 2002 [9]	3
1.3	Tesla Model S and its integrated <i>skateboard platform</i> , 2012 [11, 12] . . .	3
1.4	Global CO ₂ regulations trends for new PLDVs, NEDC equivalent [15] .	4
1.5	Typical electric motor traction characteristics	7
1.6	Energy density comparison, VW id.3 cell and pack [10]	8
1.7	BENTELER Electric Drive System 2.0 [34]	10
1.8	Jaguar I-pace underbody-battery pack integration, underside view [10] .	11
1.9	Main framework for integrated underbody and battery pack design . .	12
1.10	Driving factors towards dedicated BEV platforms, adapted from [13] . .	13
1.11	Jeep [®] Compass 4xe Plug-In Hybrid [35]	14
2.1	Audi A8 spaceframe with main underbody components highlighted, front view. Adapted from [38]	18
2.2	Audi A8 spaceframe with main underbody components highlighted, rear view. Adapted from [38]	19
2.3	Mercedes Benz C-class front and side impact schematic load path [43] .	21
2.4	MQB platform and MEB platform battery packs in comparison, left to right [46, 47]	22
2.5	Trends for Li-ion batteries energy densities	23
2.6	Comparison between different lithium battery cells form factors [24] . .	24
2.7	Stainless steel battery pack concept [49]	25
2.8	Comparison between different cells integration approaches [24]	27
2.9	Advanced Electric Vehicle Architectures (ELVA) project developed con- cepts [57]	28
2.10	Optimized material arrangement configuration [64]	30
2.11	Tesla underbody battery integration and rear torque boxes design . . .	31
2.12	Tesla side impact absorption structure [69]	31

2.13	GM battery pack design [70]	31
2.14	Hyundai BEV platform [71]	31
2.15	VW battery pack structure [72]	32
2.16	Volvo battery pack structure stiffening [73]	32
2.17	Examples of dedicated BEV platforms	33
3.1	Examples of underbody images from Tesla Model Y <i>Autoreverse</i> [44] .	36
3.2	Examples of BIW analysis resources from Tesla Model Y <i>BIW</i> analysis	36
3.3	Battery pack images from Tesla Model Y <i>xEV powertrain</i> [80]	37
3.4	Material from <i>3D Autoreverse</i> and <i>xEV Powertrain</i> , Tesla Model Y [10]	37
3.5	Schematic representation of the benchmarking analysis process	39
3.6	BMW X3 underbody, main ICEV platforms structural features [44] . .	40
3.7	Jaguar I-pace underbody, main BEV platforms structural features [10] .	41
3.8	Audi e-tron battery pack [81]	42
3.9	Classification scheme design process and structure	43
3.10	Cluster 1 classification scheme, <i>General vehicle information</i>	45
3.11	Side mobile barrier and side pole test from Euro NCAP [88]	47
3.12	Cluster 2 classification scheme, <i>BIW and underbody</i>	47
3.13	Examples of different BEV platforms corresponding to different values of the <i>dedicated BEV platform index</i> . Images from [44]	48
3.14	Different <i>rocker rail sizes</i> : small, medium, and large. Images from [79] .	49
3.15	Different <i>rocker rail sizes</i> : small, medium, and large. Images from [79] .	50
3.16	Examples of different <i>torque boxes</i> shapes. Images from [44]	51
3.17	Cluster 3 classification scheme, <i>Battery pack</i>	52
3.18	Examples of different battery pack lower enclosures [80]	56
3.19	Cluster 4 classification scheme, <i>Integration</i>	56
3.20	Different battery packs compared to the vehicle footprint [44, 24] . . .	57
3.21	Examples of different assembly efficiency [80, 24]	57
3.22	Examples of different side-impact absorption structures [24, 80]	58
3.23	Examples of applied classification code. VW id.3 on top and Tesla Model Y on the bottom [44]	59
4.1	3D views of the two BIWs used for the general platform dimensioning .	62
4.2	Simplified underbody layout	63
4.3	Underbody fixed dimensions	64

4.4	Battery pack layout and dimensions	65
4.5	Underbody model, first design	66
4.6	Battery pack model, first design	67
4.7	Split geometry with stitched edges	68
4.8	Convergence of torsional displacement and increase in CPU time in function of the elements size	70
4.9	M10 bolted connection modelling	71
4.10	Torsion loading scheme	73
4.11	Bending loading scheme	75
5.1	Modelled geometries for front and rear torque boxes	79
5.2	Extruded internal rocker structure, CAD, and real implementation	80
5.3	Stamped internal rocker structure, CAD, and real implementation	81
5.4	Modelled lower battery pack enclosures	82
5.5	Modelled variations of internal structure	83
5.6	Relative standard deviation of underbody components thickness	84
5.7	Example of the panelless model used for modal analysis	92
5.8	Example of embossed panels for modal analysis	93
6.1	Distribution of structure masses	96
6.2	Pareto chart of the percentages of contribution for the mass response	97
6.3	Main effect plot for the structure mass, fitted means	98
6.4	Torsional deformation example, amplified by 100x. Z-axis contour plot with displacements in mm	99
6.5	Distribution of torsional stiffness	100
6.6	Pareto chart of the percentages of contribution for the torsional stiffness response	100
6.7	Main effect plot for the torsional stiffness, fitted means	102
6.8	Principal interactions effect plot for the torsional stiffness, fitted means	103
6.9	Bending deformation example, amplified by 300x. Z-axis contour plot with displacements in mm	104
6.10	Distribution of bending stiffness	104
6.11	Pareto chart of the percentages of contribution for the bending stiffness response	105
6.12	Main effect plot for the bending stiffness, fitted means	106

6.13	Principal interactions effect plot for the bending stiffness, fitted means	107
6.14	Example of modal analysis from DOE run No. 7	108
6.15	Example of modal analysis from DOE run No. 16	108
6.16	Distribution of 1 st modal frequencies	109
6.17	Pareto chart of the percentages of contribution for the 1 st modal frequency response	109
6.18	Main effect plot for the 1 st modal frequency, fitted means	110
6.19	Battery enclosure mass distribution	111
6.20	Distribution of underbody stiffness without battery pack structure	111
6.21	Battery pack contribution to system stiffness, in function of battery structure mass	112
6.22	Example of modal analysis from panelless DOE run No. 22	113
6.23	Example of modal analysis from panelless DOE run No. 27	114
6.24	Distribution of 1 st modal frequency - panelless model	114
6.25	Pareto chart of the percentages of contribution for the 1 st modal frequency response - panelless model	115
6.26	Main effect plot for the 1 st modal frequency - panelless model, fitted means	116
6.27	Principal interactions effect plot for the torsional stiffness, fitted means	117
6.28	Comparison between 1 st optimized solution and DOE responses in function of the structure mass	120
6.29	First modal frequencies for the 1 st optimized flat panels model, from complete model to panelless model	121
6.30	Embossed floor and battery pack flat panels - 1 st optimization	121
6.31	First modal frequencies for the 1 st optimized embossed panels model, from complete model to model with no battery pack panels	122
6.32	Comparison between 1 st and 2 nd optimized solutions and DOE responses in function of the structure mass	125
6.33	First modal frequencies for the 2 nd optimized flat panels model, from complete model to panelless model	125
6.34	Embossed floor and battery pack flat panels - 2 nd optimization	126
6.35	First modal frequency = 54.4 Hz for the 2 nd optimized embossed panels model, complete model	127
6.36	Comparison between 1 st and 2 nd optimization normalized values	128

6.37	Rocker internal structure influence and preferred configuration for the analyzed responses	129
6.38	Torque boxes shape influence and preferred configuration for the analyzed responses	130
6.39	Lower battery pack enclosure shape influence and preferred configuration for the analyzed responses	131
6.40	Number of battery pack cross-members influence and preferred configuration for the analyzed responses	132
6.41	Number of battery pack longitudinal members influence and preferred configuration for the analyzed responses	133
6.42	Side members material influence and preferred configuration for the analyzed responses	134
6.43	Torque boxes material influence and preferred configuration for the analyzed responses	135
6.44	Rear cross-member material influence and preferred configuration for the analyzed responses	136
6.45	Front cross-member thickness influence and preferred configuration for the analyzed responses	137
6.46	Front floor cross-member thickness influence and preferred configuration for the analyzed responses	137
6.47	Battery pack material influence and preferred configuration for the analyzed responses	138

List of Tables

1.1	BEVs benefits an challenges compared to traditional vehicles	5
4.1	Mesh convergence analysis	69
4.2	Mesh characteristics and quality indexes	70
4.3	Steel and Aluminum alloy materials properties	72
5.1	Underbody components geometry variability	79
5.2	Battery components geometry variability	82
5.3	Underbody components material and thickness variation	85
5.4	Restricted design space	85
5.5	Steel properties	88
5.6	Aluminum properties	88
5.7	Steel properties	89
5.8	Frame battery pack	89
5.9	Tray battery pack	89
5.10	Example of 4-factors 2-levels fractional factorial plan	90
6.1	Targets for 1 st response optimization	118
6.2	Parameters settings for 1 st optimized solution	119
6.3	Responses prediction and validation for the 1 st optimization analysis . .	120
6.4	Outputs from stiffened panels model analysis for the 1 st optimization . .	122
6.5	Targets for 2 nd response optimization	123
6.6	Parameters settings for 2 nd optimized solution	123
6.7	Responses prediction and validation for the 2 nd optimization analysis . .	124
6.8	Outputs from stiffened panels model analysis for the 2 nd optimization . .	126
A.1	Designed Fractional Factorial plan - factors 1 to 6	154
A.2	Designed Fractional Factorial plan - factors 7 to 11	155

B.1	DOE factors and aliasing structure	156
B.2	ANOVA results for the mass response	157
B.3	ANOVA results for the mass response - after pooling process	158
B.4	ANOVA results for the torsional stiffness response	159
B.5	ANOVA results for the torsional stiffness response - after pooling process	160
B.6	ANOVA results for the bending stiffness response	161
B.7	ANOVA results for the bending stiffness response - after pooling process	162
B.8	ANOVA results for the 1 st modal frequency response	163
B.9	ANOVA results for the 1 st modal frequency response - after pooling process	164
B.10	ANOVA results for the 1 st modal frequency response - panelless model	165
B.11	ANOVA results for the 1 st modal frequency response - panelless model after pooling	166

Acronyms

AHSS Advanced High Strength Steel. 29

ANOM Analysis of Means. 95

ANOVA Analysis of Variance. 88, 93, 96, 113, 156

BEV Battery Electric Vehicle. IV, XIII, XIV, XVIII, 1–14, 16–18, 20–23, 27–34, 38–41, 43, 45–51, 59–62, 65, 81, 83, 138–140, 142–144

BIW Body in White. XIV, 10, 11, 14, 20, 21, 28–30, 32, 35–37, 41, 43, 47–49, 51, 58–60, 62, 72, 135, 143

BMW Bayerische Motoren Werke. XIV, 26, 40

BTMS Battery Thermal Management System. 14, 22, 23

CAD Computer-Aided Design. XV, 14, 61, 63, 66, 78, 80, 81, 96

CCD Central Composite Design. 142

CMA Compact Modular Architecture. 3

CPU Central Processing Unit. XV, 69, 70

CRF Centro Ricerche Fiat. VI

DIMD Dual International Master’s Degree. VII, VIII

DMU Digital Moch-Up. 35

DOE Design of Experiment. IV, VII, XVI, 12, 13, 66, 68, 77, 78, 90, 91, 93, 94, 96, 103, 107, 110, 113, 117, 120, 121, 124, 125, 127, 128, 141, 142, 154

E-GMP Electric-Global Modular Platform. 33

ELVA Advanced Electric Vehicle Architectures. XIII, 28

- EMEA** Europe, Middle East, and Africa. VI
- Euro NCAP** European New Car Assessment Programme. XIV, 35, 46, 47
- FCEV** Fuel Cell Electric Vehicle. 1, 2
- FEA** Finite Element Analysis. IV, VI, 12, 13, 16, 29, 42, 44, 67, 89–91, 95, 96, 110, 118, 120, 122, 124, 126, 141, 142
- FEM** Finite Element Method. VI, 11, 14, 62, 66, 68, 72, 80, 81, 91, 96, 113, 120, 121, 124, 126, 143
- FRP** Fiber Reinforced Polymers. 49, 71
- GE1** Global Electrified 1. 33
- GHG** Greenhouse Gas. 1, 4, 6
- GM** General Motors. XIV, 28, 31
- HEV** Hybrid Electric Vehicle. 1, 2
- ICE** Internal Combustion Engine. 3, 7, 18, 40, 48, 49
- ICEV** Internal Combustion Engine Vehicle. XIV, 2, 5–9, 17, 22, 38–41, 45, 46, 49, 62, 78, 140, 144
- IEA** International Energy Agency. 1
- IIHS** Insurance Institute for Highway Safety. 35
- LFP** Lithium Ferrophosphate. 23
- LMO** Lithium Manganese Oxide. 23
- LNMO** Lithium Nickel Manganese Oxide. 23
- MDO** Multi-Disciplinary Optimization. 29
- MEB** *Modularer E-Antriebs-Baukasten*. XIII, 3, 22, 28, 31, 50
- MQB** *Modularer Querbaukasten*. XIII, 22
- NCA** Lithium Nickel Cobalt Aluminum Oxide. 23, 24
- NEDC** New European Driving Cycle. XIII, 4, 5, 46

- NHTSA** National Highway Traffic Safety Administration. 35
- NMC** Lithium Nickel Cobalt Manganese Oxide. 23, 24
- NVH** Noise, Vibration, and Harshness. 12, 19–21, 24, 42, 81, 83, 141, 144
- OEM** Original Equipment Manufacturer. IV, 1, 3–5, 10, 12, 13, 16, 17, 27–29, 33–35, 38, 53, 57, 65, 140, 144
- PHEV** Plug-in Hybrid Electric Vehicle. 1, 5, 14, 49
- PLDV** Passenger Light-Duty Vehicle. XIII, 1, 4, 12, 13
- RAM** Random Access Memory. 69
- ROI** Return on Investment. 10, 12
- RPM** Revolutions per Minute. 6, 7
- RSD** Relative Standard Deviation. 84, 86
- SUV** Sport Utility Vehicle. 14, 62
- US** United States. VI
- VW** Volkswagen AG. XIV, 22, 28, 32, 50, 59, 62, 80
- WLTP** Worldwide Harmonised Light Vehicle Test Procedure. 46

1 | Introduction

Climate change has pushed governments all over the world to act to reduce Greenhouse Gases (GHGs) emissions. In the next fifty years, the transportation sector will face several challenges to meet the required emissions targets and the industry is asked to provide new and innovative solutions to reach these objectives. In 2018 the transport sector accounted for 21% of the GHG emissions with road transport alone accounting for 15% [1]. Road transport emissions are in turn mainly driven by passenger transport, which accounts for more than half of the GHG emitted by vehicles [1].

This led to more stringent emissions regulations which drove the Original Equipment Manufacturers (OEMs) to start the transition towards alternative propulsion systems. The most diffused solutions range from Hybrid Electric Vehicles (HEVs) and Plug-in Hybrid Electric Vehicles (PHEVs) to fully electric Battery Electric Vehicles (BEVs) as well as hydrogen-powered Fuel Cell Electric Vehicles (FCEVs) [2]. Among these new powertrain technologies, the most diffused are BEVs, accounting for two-thirds of the global electrified vehicle fleet in 2020 [3, 4]. During the last decade, BEVs sales have been constantly increasing, from 51 000 units in 2011 up to 2.25 million in 2020, which represents the 2.9 % of the light vehicles market share [5]. The main market for BEVs in 2020 was Europe, accounting for 43% of the global sales of the global BEVs sales, followed by China at about 41 % [5]. According to the scenarios elaborated by the International Energy Agency (IEA), the full-electric Passenger Light-Duty Vehicles (PLDVs) fleet will grow from the current 6.8 million vehicles up to reach figures between 80 and 140 million vehicles by the end of the decade. By the year 2030, BEV PLDVs are expected to account for almost 4% and reaching up to 7% in the most optimistic forecasts [3].

The current development of electric vehicles has its roots in the first years of the automotive industry. From the 19th century, BEVs have continuously faced advantages towards their adoption and limitations of the electric powertrain technology. The increased BEVs market is pushing OEMs to invest more and more into this technology, developing dedicated solutions to exploit at best the advantages of electric vehicles.

1.1 Background and Motivation

In the following sections, a brief background of the study is presented to better introduce the subject of the work and contextualize its scope in the current regulatory and industrial environment.

1.1.1 BEVs Historical Background

The electric car has its origin in the early 1800s, with the first examples of electric vehicles, such as the electric carriage from Robert Anderson in 1832. During the second half of the 19th century, the electric vehicles continued to develop with several examples of electric carriages such as the one from Thomas Parker and William Morrison up to the 1899 “*Jamais Contente*” electric race car, capable of reaching 100 km/h (figure 1.1) [6, 7].



Figure 1.1: Camille Jenatton on the “*La Jamais Contente*”, 1899 [7]

Development continued through the first years of the 20th century, with electric vehicles accounting for one-third of all road vehicles [6].

With the introduction of the Ford Model T in 1908, gasoline-powered cars became more affordable than BEVs. The advantages of the electric vehicle, which was quieter, easier to drive and less pollutant, came in second place when compared to the higher range and lower cost of Internal Combustion Engine Vehicles (ICEVs) [6].

During the following years, the BEVs development halted just to see a short revamp in the 1970s due to the oil crisis. It was from the 1990s, when the first emission regulations were issued, that the electric vehicle slowly started to gain interest again [6]. In the 2000s, manufacturers began studying new concepts for alternative powertrains and developing the first HEVs and new concepts of BEVs and FCEVs. One example is the 2002 AUTOonomy concept from GM, which introduced the *skate platform* concept, shown in figure 1.2 [8, 9].



Figure 1.2: GM AUTOmomy concept, 2002 [9]

At the start of the new decade, several manufacturers released their first BEV models, like the Mitsubishi i-MiEV, the Nissan Leaf and the Renault Zoe [10]. Among these major OEMs a new startup, Tesla Motors, started developing a new BEV which was based on a dedicated electric platform [6]. In fact, despite never arriving at the production stage, the AUTOmomy launched a vehicle concept that inspired the following 2012 Tesla Model S.

The Model S features an underbody frame designed to house a large battery pack, which exploits almost all the area under the central floor of the vehicle, shown in figure 1.3 [8].

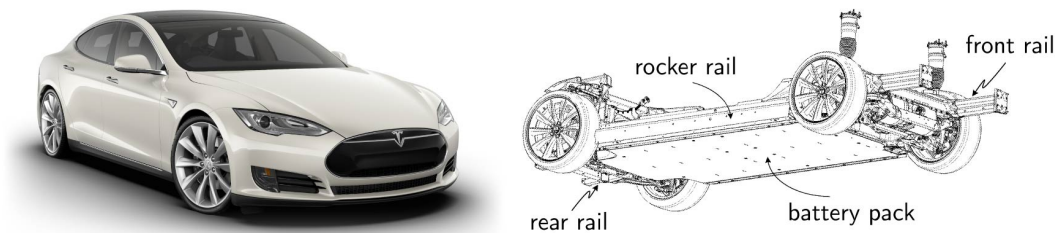


Figure 1.3: Tesla Model S and its integrated *skateboard platform*, 2012 [11, 12]

In the following years, all the major automotive companies started developing their own solution for a BEV platform, often starting from modified and adapted Internal Combustion Engine (ICE) platforms. Currently, two main approaches are present in the industry for what concerns the development of a new BEV architecture: the development of a highly modular dedicated BEV platform, like the Volkswagen MEB, or an optimized multi-powertrain platform, capable of adapting to different powertrain systems such as the Volvo Compact Modular Architecture (CMA) [13].

Despite the high development cost, many OEMs are investing in new dedicated BEV platforms since this approach allows to increase the vehicle driving range and to exploit

the platform for several different vehicles and segments thanks to its modularity. More than 75% of the major global OEMs are expected to have a dedicated BEV platform by 2025 [13].

1.1.2 Environmental Concerns and New Regulations

In the last forty years [14], the anthropogenic air pollutant emissions steadily increased, leading to a global scale “Climate Change”. In particular, the GHGs emissions are generating the “Greenhouse Effect” which is leading to progressive global warming. CO₂ emissions are the most abundant, contributing about 78% of the total GHG [14].

Among all the GHG-emitting human activities, transport accounts for 21% of the global emissions and road transport, accounting for 75% of the whole transport emissions, contributes to 15% of the total released GHG. When considering only passenger road transport, this figure decreases to 45% of the whole transport emissions, still representing almost 10% of the global GHG emissions [1].

To reduce the impact of road transport on the “Climate Change”, during the last three decades, the legislation imposed strong restrictions on automotive exhaust emissions, leading to numerous and more stringent regulations. All the principal countries are imposing fuel economy standards to limit fleet average CO₂ emissions, expressed in g(CO₂)/km, of each automotive corporate. Legislations also impose heavy penalties on the manufacturers not respecting the targets. Figure 1.4 shows the trend of the historical emissions compared with the future targets for passenger cars in several regions of the world.

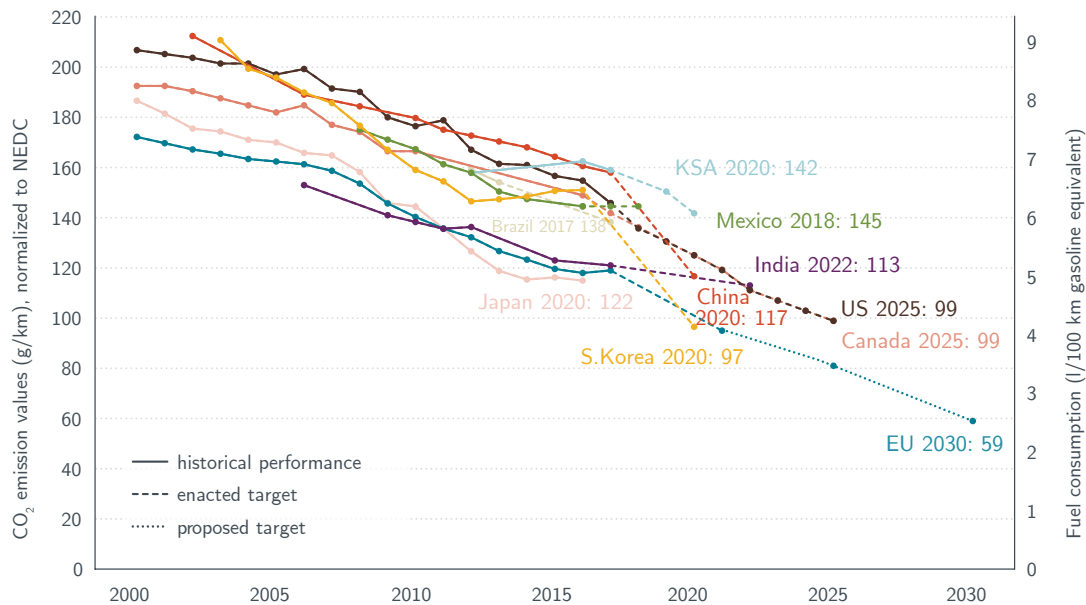


Figure 1.4: Global CO₂ regulations trends for new PLDVs, NEDC equivalent [15]

Specifically, since 2015 the target has been 130 gCO₂/km for the EU fleet average, corresponding to fuel consumption of around 5.6 l/100 km of gasoline and 4.9 l/100 km of diesel [16]. The objective was reached in 2013 and in 2018 the average emission was 120 gCO₂/km. For what concerns the EU regulations, the current standard is 95 gCO₂/km, and the future targets will be 81 gCO₂/km by 2025 and 59 gCO₂/km by 2030 considering emissions expressed in New European Driving Cycle (NEDC) (New European Driving Cycle) terms.

Furthermore, the penalties can be very important, leading to an estimated 14.5 billion euros fine for 2021 considering the top 13 automotive OEMs [17].

Similar objectives are present in North America, with Canada and the US targeting 99 gCO₂/km by 2025 [15].

These strict emission targets are practically impossible to meet with a conventional ICEV, thus these new regulations are pushing all the main OEMs to develop alternative powertrain solutions to reduce their fleet CO₂ emissions. In fact, all the major OEMs are currently investing in PHEVs and BEVs and, specifically, on dedicated EV platforms, in order to reach these goals [13].

1.1.3 BEVs Benefits and Challenges

In the following table 1.1 the benefits and challenges of BEVs with respect to conventional powertrains are listed and will be explained in detail in what follows.

Table 1.1: BEVs benefits and challenges compared to traditional vehicles

E-motor Benefits	Battery Challenges
<p><i>Higher efficiency</i></p> <ul style="list-style-type: none"> • Emissions reduction 	<p><i>Low energy density</i></p> <ul style="list-style-type: none"> • High weight • Complex vehicle packaging
<p><i>Optimal torque-speed characteristic</i></p> <ul style="list-style-type: none"> • High acceleration performances • Smaller and lighter transmission 	<p><i>Long recharging time</i></p>
<p><i>Reversible machine</i></p> <ul style="list-style-type: none"> • Regenerative braking 	<p><i>Lower durability and safety concerns</i></p> <ul style="list-style-type: none"> • Complex management system
<p><i>High durability and lower complexity</i></p> <ul style="list-style-type: none"> • Lower operating cost 	<p><i>High costs</i></p>
<p><i>Lower noise pollution</i></p>	

The main benefits of the electric powertrain come from the almost optimal characteristics of the electric motor, which make it extremely suitable for vehicle traction. One of the most relevant advantages is its higher efficiency when compared to internal combustion engines. This makes BEVs capable of reducing the energy consumption and thus the CO₂ emissions when compared to ICEVs also considering the use of the same fossil fuel as the primary energy source [18]. For a proper evaluation, it is necessary in this case to consider the so-called “Well-to-Wheels” efficiency. Despite being much less efficient in the “Well-to-Plug” energy transfer, with an efficiency of about 45% compared to 80% “Well-to-Tank” efficiency of the ICEVs, BEVs catch up with the higher “Plug-to-Wheels” efficiency, leading to an overall efficiency up to 35% against 25% of the gasoline ICEVs [18]. This results in a driving emissions reduction from 40% to 60% [19, 20].

However, to gather the complete picture it is necessary to look at the total lifecycle emissions of the vehicle, accounting for the emissions from manufacturing, vehicle use and end-of-life. In this case, the GHG emissions during battery manufacturing heavily affect the overall lifecycle emissions of BEVs. Despite that, the overall lifecycle emissions of BEVs are still at least 17% lower than the ones of ICEVs [19, 20]. These evaluations were made considering the current energy sources mix, while if considering wider use of renewable energy, the CO₂ emissions reduction from BEVs could be up to 90% [19]. To further reduce the end-of-life impact of BEVs several solutions have been proposed to recycle or reuse the valuable battery pack and its constituents, which are the discriminant elements between BEVs and conventional vehicles during dismantling and recycling. Battery recycling will play a crucial role in reducing end-of-life emissions as well as minerals extraction and manufacturing emissions. This will allow to reduce the cost of the battery and the whole vehicle [21] while coping with a base element supply (Lithium and Cobalt) which is predicted to be struggling to meet the demand by the year 2035 [22]. In addition, “battery second life” is another possibility to reduce the BEV end-of-life emissions. When the battery loses more than 20% of its capacity it is no more suitable for automotive applications, but still sufficient to be used in less demanding applications like stationary energy-storage services [23, 24].

Apart from the previously mentioned environmental advantages, BEVs customers can benefit from several other advantages of the electric powertrain.

The electric motor presents the optimal torque-speed characteristic for vehicle traction, shown in figure 1.5, starting with a constant torque region with high torque availability at low Revolutions per Minute (RPM), and followed by a constant power region up to the maximum rotational speed. This allows, even with a simplified transmission system with a single or in general few gear ratios, to cover the whole vehicle operating

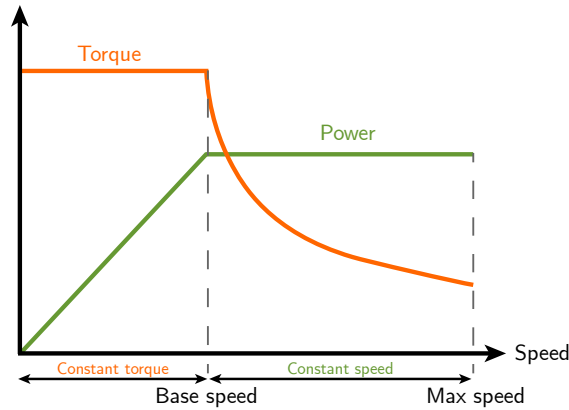


Figure 1.5: Typical electric motor traction characteristics

range from hill start to maximum speed. Furthermore, thanks to the high torque at low RPM, BEVs show higher acceleration performances than their ICE counterpart. The electric powertrain is consequently smaller and lighter both because of the smaller size of the electric motor and the simpler transmission system, usually constituted by a fixed gearing. In addition, the electric motor allows to easily perform active control systems by tuning the output torque with a fast response time.

Another advantage of using an electric motor comes from the reversibility of the electric machine, the regenerative braking. By using regenerative braking, it is possible to recover a large amount of kinetic energy which is usually lost through heat in the braking system, further increasing the energy efficiency of the electric powertrain [2].

A third advantage is the lower operating cost for the customer. Despite the higher initial cost, BEVs are in general more cost-effective to maintain since there are fewer mechanical components and no exhaust aftertreatment system. Moreover, the cost per driven mile can be less than half of the equivalent ICEV thanks to their higher efficiency and the regenerative braking [2, 25].

To conclude, although not as notorious as air pollution, noise pollution represents one of the most impacting social and environmental costs of road transport. BEVs have the potential to reduce noise pollution, especially in urban areas, thanks to the lower noise produced by the electric motor when compared to a ICE [26, 2].

After discussing the main benefits of the battery-electric powertrain, it is fundamental to critically also analyze the challenges that this technology is facing.

The main concerns regarding BEVs are currently associated with their energy storage medium, the battery pack. In the last decades, Li-ion batteries have become the preferred choice for BEVs thanks to their relatively high energy density and good durability [22]. However, the energy density of the battery pack is not comparable with one of the fuels. This leads to a compromise between weight increase and driving range on

a single charge. On average the typical ICEV has a range on a single fuel tank of more than 600 km. The best performing BEVs instead can reach about 500 km on a single charge, with the best-in-class approaching or narrowly exceeding the 600 km range [27]. Furthermore, to reach these ranges, due to the limited battery energy density, BEVs weigh on average 24% more than their ICEV counterpart [28] which harms the dynamics of the vehicle.

The current state-of-the-art technology for automotive batteries is constituted by Li-ion batteries which can reach energy densities close to 270 Wh/kg [10]. In addition to that, the cells need to be integrated into a proper battery pack which needs to guarantee support, safety, and thermal management of the cells [2]. Thus, the actual energy density of the battery pack reduces to values close to 150 Wh/kg and 200 Wh/l for the volumetric energy density, with the best-in-class reaching energy densities of 180 Wh/kg and 250 Wh/l [10].

In figure 1.6 it is possible to see an example of a pouch battery cell and the complete battery pack from the Volkswagen id.3 [10].

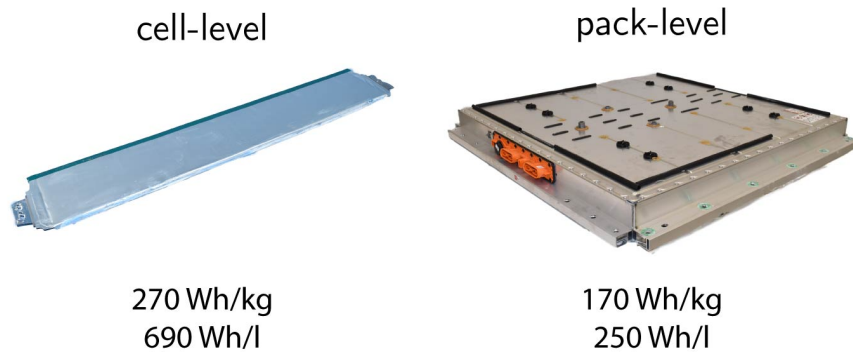


Figure 1.6: Energy density comparison, VW id.3 cell and pack [10]

This implies an increase in the weight of the vehicle as well as packaging issues due to the bulky battery pack, whose positioning needs to be carefully evaluated both for vehicle dynamics and occupants ergonomics.

To have an accurate comparison with conventional liquid fuels it is worth considering the effective energy density ρ_E , obtained by multiplying the gravimetric energy density of the energy source, ρ_g , and the efficiency of the powertrain η_p :

$$\rho_E = \rho_g \times \eta_p \quad (1.1)$$

In this case, despite the higher powertrain efficiency, the effective energy density for BEVs is just about 4% of the effective energy density of common liquid fuels [27]. Due to the battery energy density limitations, it is thus fundamental to save weight in any

other component, to improve both the electric mileage and the vehicle dynamics.

Another concern, directly related to the low battery energy density is the long recharging time. In fact, in addition to the limited range, the slow recharging time adds more issues to the vehicle management. Despite the large improvements in the recharging infrastructure, there are still limits on the maximum energy transmission during recharging. The limits to the recharging are both in the battery cells, which can accept a limited current without damages, but also in the recharging cable and connector which need to be of manageable size but avoid overheating [27]. Currently, the maximum recharging peak powers are around 250 kW, and by 2030 it is expected to reach 350 kW, by the use of water-cooled cables and connectors as well as higher recharging voltages in the order of 1000 V [29]. While with this fast-charging technology it is theoretically possible to recharge 100 km of range in just 3 minutes [30], the real case scenario shows that one of the fastest charging vehicles, the Porsche Taycan, takes 10 minutes for a 100 km recharge [31], compared to less than ten seconds of refuelling on an ICEV [27].

The durability of the battery is another issue as well. The electric battery ages and its actual capacity decreases with ageing. Fast charge and operating conditions far from the ideal range accelerate the ageing process [27]. Thus, it is crucial to optimize the battery chemistry both for fast charge capability and slow ageing, while still reducing the battery cost [22].

As a matter of fact, the battery accounts for more than 30% of the vehicle cost, which leads to a vehicle cost increase of up to 35% more than an equivalent ICEV [32]. To make BEVs competitive with ICEVs it is fundamental to reduce the battery cost through new and more sustainable production processes which can reduce the battery price by up to 20% [32].

The battery pack needs also to integrate proper structures for thermal management to keep the cells in the optimal operating range between 25°C and 35°C, which is just a small portion of the operating temperature range of a vehicle (-30°C - +60°C). This is necessary to guarantee the performance, durability, and safety of the battery [33].

In addition to the thermal management safety concerns, crash safety is another critical aspect since cell damage could lead to fire or explosion. It is thus necessary to devise an appropriate crash absorbing structure to avoid further hazards from the battery pack [2].

1.1.4 The Need for Dedicated BEV Architectures

To overcome limitations and better exploit the advantages of the electric traction illustrated in section 1.1.3 it is fundamental to develop integrated platform solutions for

the new BEVs. The integration of all the main structural and powertrain components is crucial to cope with the limitations of the energy storage medium. An optimal integration allows to improve the weight efficiency of the structure, thus leaving room for battery capacity increase or simply reduction of the vehicle weight, both in favour of a longer range. An integrated platform makes it possible to interconnect and exploit at best the different BEV subsystems, from the underbody and battery pack to the suspension system and electric motor as well as the powertrain thermal management system.

Figure 1.7 shows an example of a dedicated and integrated BEV platform from Benteler, highlighting the main subsystems of the electric vehicle.

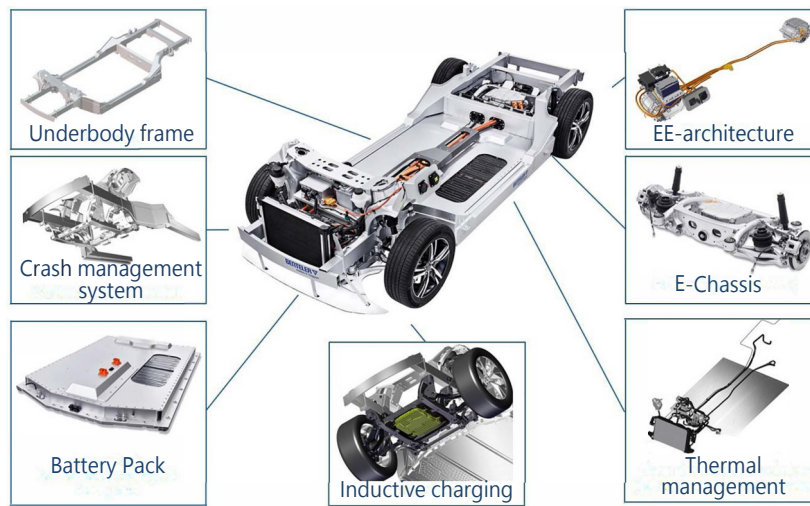


Figure 1.7: BENTELER Electric Drive System 2.0 [34]

In particular, the integration of the underbody structure and the battery pack permits to exploit both structures to reach the desired static, dynamic and safety performances. Optimal integration of these two subsystems is critical for vehicle packaging and passenger ergonomics. Given the high battery weight, its placement will affect the vehicle dynamics while its structure can contribute to enhance the stiffness of the whole Body in White (BIW). This integration is also fundamental to reach the required safety levels, both for occupant and battery cells protection in the event of a crash [2, 34].

In addition to the high integration of the main structural and powertrain components, the majority of the global OEMs are developing highly modular solutions for dedicated BEV platforms. Modularity will play a critical role in the design of the new BEVs since it will allow to cut development costs and time by exploiting the same platform across a wider range of vehicle segments, thus increasing the Return on Investment (ROI) [13].

1.2 Purpose of the Study

The objective of this research project is to provide a novel and relevant academic study as well as improve the know-how of the industrial partner.

Considering the importance that BEVs are gaining in the passenger vehicle market and the need for new dedicated and integrated BEV platforms, this project focuses on the integration between vehicle underbody and battery pack, which have been analyzed from a structural point of view.

The project is subdivided into two main sections, the first concerning the state-of-the-art analysis and the second one dedicated to the Finite Element Method (FEM) modelling of a simplified platform, to investigate the optimal design choices and establish design guidelines for the future platforms.

In first section, a benchmarking analysis is performed, which establishes the main design trends and choices for dedicated BEV platforms, in order to understand the most influential parameters needed to guarantee superior structural performance and optimal integration between the main underbody frame and energy storage medium. In the analysis, several vehicles are compared to highlight key differences and common traits both for what concerns the underbody frame and the battery pack structure.

Figure 1.8 shows an example of the integration of vehicle underbody and battery pack. The vehicle illustrated is the Jaguar I-PACE, which features a BEV-native aluminum BIW and a battery pack exploiting almost all the central floor region, thus reaching a high level of integration among the two structural systems.

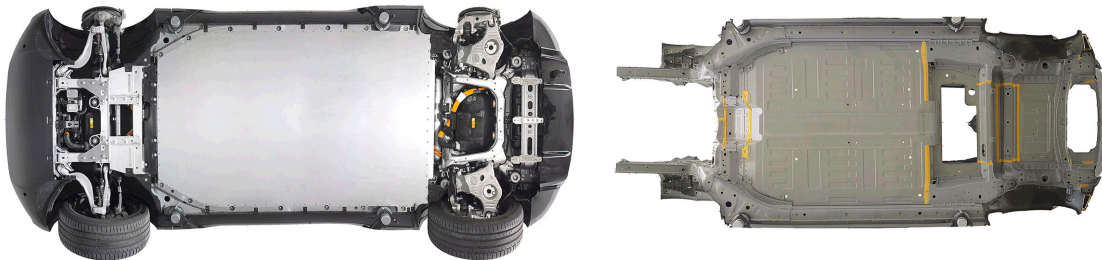


Figure 1.8: Jaguar I-pace underbody-battery pack integration, underside view [10]

After a first analysis, the most relevant parameters were collected to define a classification scheme, able to highlight the key performance factors. This tool was developed to be used as a benchmarking comparison device as well as a preliminary concept selection tool to support the preliminary design phase.

The second part of the project uses the outcomes of the benchmarking analysis and the elaborated classification scheme to develop a simplified underbody and battery pack model and study the most relevant design parameters to search for validated design

principles for these structures.

The analysis was performed using a parametric Finite Element Analysis (FEA), which through a Design of Experiment (DOE) was used to highlight the most influential design parameters. The objective of the analysis is to investigate the static stiffness and Noise, Vibration, and Harshness (NVH) performances of the structures while trying to minimize the weight of the system. Following this analysis, the obtained results were collected and elaborated into validated design guidelines and an optimization was conducted to prove and validate the potential of the derived design principles for dedicated BEV PLDV platforms.

Figure 1.9 illustrates the project framework with all the main components and functions of the two subsystems, underbody and battery pack which are integrated into the underbody-pack system to provide the desired static and dynamic performances while still aiming at optimal lightweighting and acceptable system complexity.

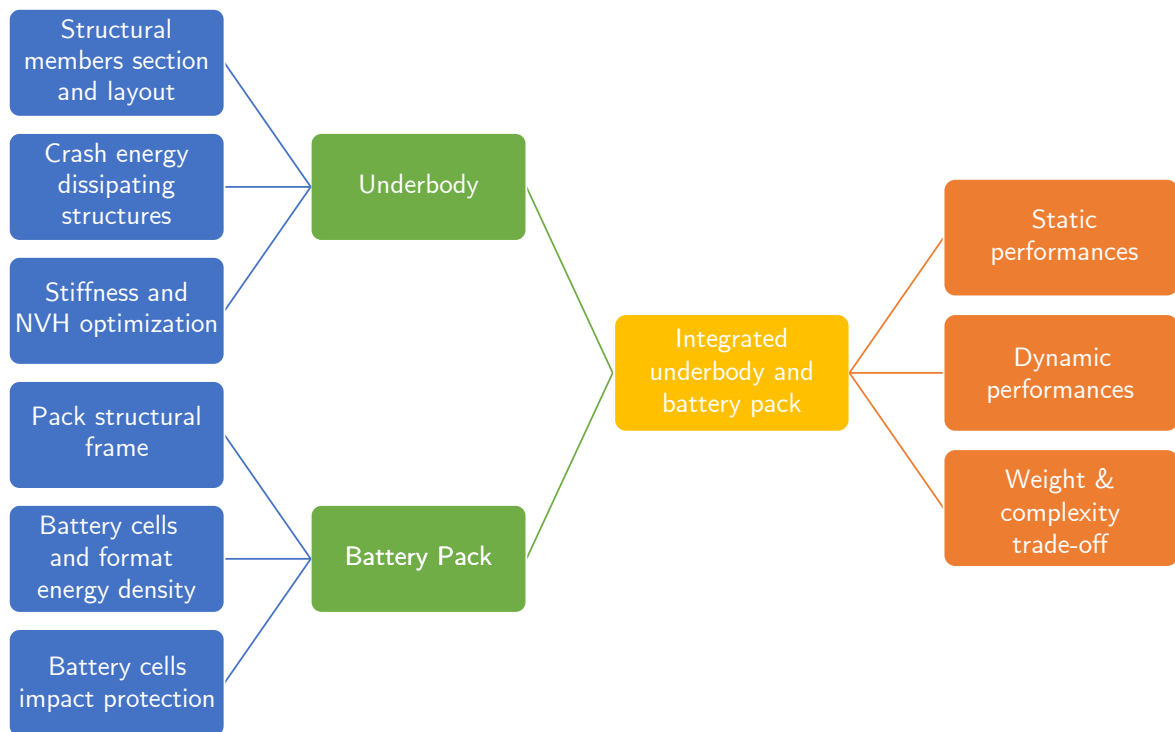


Figure 1.9: Main framework for integrated underbody and battery pack design

1.2.1 Importance of the Study

As already mentioned in section 1.1.4, the growth of the BEVs market pushes the OEMs to develop new dedicated platforms for electric vehicles which, to reach optimal efficiency levels and guarantee an adequate ROI, need to be highly integrated and modular.

The elaborated classification scheme will be a valuable device for current and future BEVs benchmarking analysis. Through the use of the classification scheme, it will be possible to identify the main industry trends for underbody and battery pack design to have a thorough overview of the current state-of-the-art technology. This will lead to understand the most influential parameters as well as the principal design choices, allowing to follow the development and the critical features of this new vehicle architecture concept.

Starting from the benchmarking analysis the project defines validated guidelines for the design of integrated underbody and battery pack platform. Using FEA and a DOE, it was possible to investigate the most critical parameters and the design choices that are more suitable for a new dedicated BEVs platform.

The resulting guidelines will provide a useful starting point for new and more deepened studies on BEV platforms, specifically, for Stellantis, the industry partner of this project.

Figure 1.10 summarizes the main driving factors which are pushing OEMs to develop a dedicated BEV platform and, thus, highlights the importance of this study in the context of the current automotive industry and market developments.

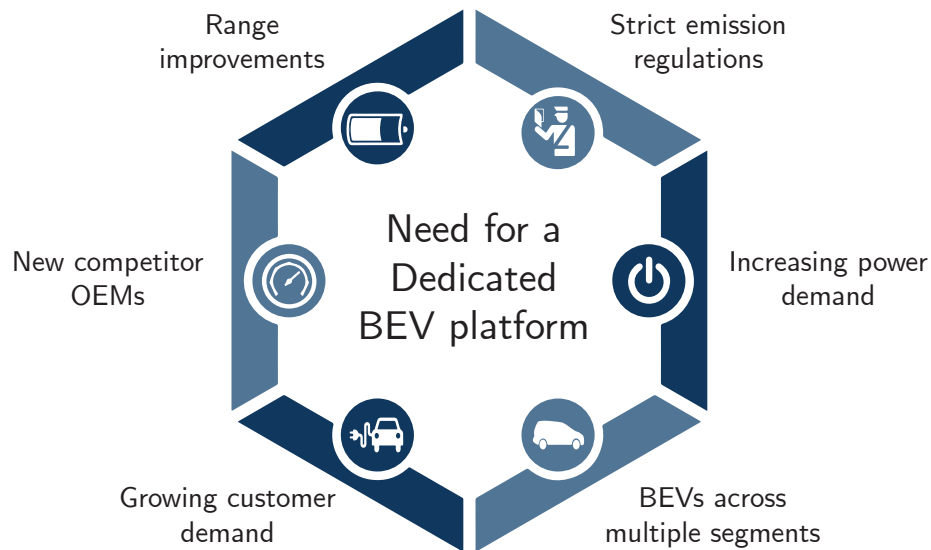


Figure 1.10: Driving factors towards dedicated BEV platforms, adapted from [13]

1.2.2 Project Scope and Hypothesis

The project focuses on the efficient design of an integrated underbody and battery pack for a passenger electric car. Considering PLDV the work was concentrated on the unibody architecture, with no specific investigations on the body-on-frame solutions, which can still benefit from the result of the analysis. A specific vehicle segment was

chosen for this study, considering a trade-off between the current European and North American markets. The choice fell on the C-segment, with particular attention to compact crossovers since, from the current market trends, a large number of compact BEV Sport Utility Vehicles (SUVs) are expected over the next five years [13].

Figure 1.11 shows an example of a PHEV C-segment crossover from Stellantis which was used to define the main dimensions for the development of the simplified BEV platform model.



Figure 1.11: Jeep[®] Compass 4xe Plug-In Hybrid [35]

A parametric Computer-Aided Design (CAD) model was developed according to the state-of-the-art assessed by the benchmarking analysis. The model was adequately simplified to avoid loss of generality and to keep the problem solvable according to the available time and resources.

The project investigates solutions and design best practices for the underbody and battery pack of BEV, considering these two as subsystems of the whole vehicle system. For sake of simplicity, the analysis of the surrounding vehicle subsystems like suspension, electric motors, BIW top hat, etc. was excluded from the study to focus on the integration of the two subsystems under analysis, and complete the project in the available timeframe, obtaining functional and validated results.

The parametric model was developed to analyze the structural aspect of the system, under static and dynamic loading. The modelling of the battery pack was limited to its structural enclosure and components, with the battery modules accounted only as distributed masses, but particularly relevant during dynamic loading. The modelling of the Battery Thermal Management System (BTMS) and the electrical behaviour of the battery pack were not considered for the scope of this project. Different structural configurations were designed and analyzed through a series of FEM analyses to investigate the most influential design parameters and obtain an optimized low-weight solution that can satisfy the performance requirements. The design space was appropriately restricted in order to limit the design variables and the number of FEM models to be constructed and analyzed.

In the end, the more convenient design choices were determined and guidelines for the development of this type of integrated underbody were derived.

Thanks to the parametrical nature of the model, it will be possible in the future to investigate the possibility of having a modular platform, both for what concerns the battery pack and for the whole underbody.

2 | Literature Review

The review of the available literature was the first step of the project. Since from the beginning, it was clear the scarcity of scientific material on the study of the integration between the battery pack and vehicle underbody. In fact, at present, this know-how is highly valuable for OEMs and thus difficult to find in dedicated academic studies. The BEV technology is still relatively new and thus all the strategic knowledge, such as the design of new platforms, is kept under industrial secret.

To exploit at best the available resources, the literature review was subdivided into two main steps:

- Review of the general concepts for underbody design
- Research of material dedicated to BEV platforms

Specifically, the research of dedicated studies on BEVs and BEV platforms were in turn subdivided into three macro-categories:

- Article and Reports: mainly related to battery pack technology and crashworthiness, with useful hints for the FEA and optimization procedures
- Registered technical patents: mainly related to underbody and battery pack and their crashworthiness, with useful hints for the general design layout of the system
- Benchmarking resources: accessed mainly through the portal A2mac1.com, OEMs websites and automotive magazines, used to understand the current state-of-the-art and investigate the most adopted technical solutions. These resources will be analyzed in-depth in chapter 3

In the following, the main outcomes of these different steps are illustrated to describe the background knowledge on which the project was built.

2.1 Underbody Design Principles

The vehicle frame architecture has largely evolved during automotive history, but the underbody has always been the most important component of the car body. Currently, two separate approaches are present depending on the type of vehicle: for commercial and heavy-duty vehicles the body-on-frame is still the predominant solution, while for passenger cars the so-called unibody is the dominant design. This project is focused on the design of an underbody of a passenger vehicle which is then meant to be integrated into the unibody structure with the vehicle upperbody. The study of ladder frame body-on-frame architectures was not considered since out of the scope of this analysis.

Given the great importance of the underbody for the performances of the whole vehicle body, OEMs invest a lot of resources in its development and then exploit the developed platform with several vehicle upperbodies configurations [2, 36].

During the last decades, the underbody has undergone large evolutions, up to the new concepts of BEV *skate underbodies* discussed in section 1.1.1. The underbody design of a BEV is, in general, an evolution of the ICEV know-how adapted to the new necessities of the electric powertrain and, specifically, of the battery pack. Despite the large changes in the design philosophy the main concepts are thus still valid, and it is worth starting to analyze the fundamental principles of an ICEV underbody to better understand the ones dedicated to BEVs.

Figures 2.1 and 2.2 illustrate the main components of the vehicle underbody, which are here analyzed following the descriptions presented by Morello et al. and Khajepour et al. in their books [37, 2].

- *Front side member.* The front side members are usually made out of a closed boxed beam with a rectangular section. They can be made out of stamped steel sheets joined by spot-welding or by hollow aluminum extrusions. Their main function is to absorb the frontal crush energy by a controlled collapse mechanism which is promoted by weakening dents that lead to local instabilities and the axial collapse of the element. In addition to that, the front side members bear part of the load transmitted by the suspensions and by the engine mounts. Their structure is also crucial in determining the bending stiffness of the vehicle body being located at the extremity of the vehicle, far from the centre of gravity.
- *Suspension tower.* The function of this structure is to support the suspension damping and elastic element and, depending on the type of front suspension, may host the upper arm attachment points. The suspension tower also connects the front side members with the upper side rails, exploiting the crash absorption capabilities of this structure.

- *Lower front column.* The lower front column or also lower A-pillar. These structures support the front door and are a critical component in transmitting the load, especially during crashes, to the rear part of the body.
- *Firewall.* The firewall panel connects the two lower front columns and separates the front compartment from the passenger cabin. The firewall structure is usually stiffened by a cross-member which interconnects the front side members and the lower columns. The structure of the firewall is crucially important for the body's torsional stiffness.

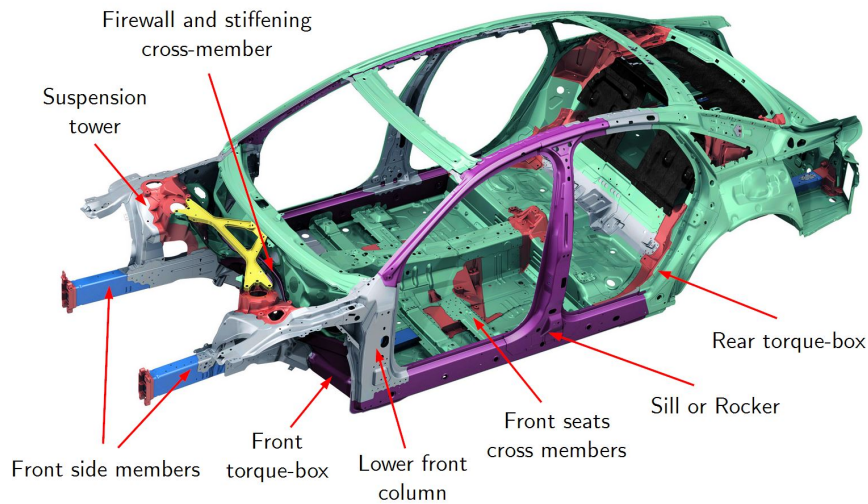


Figure 2.1: Audi A8 spaceframe with main underbody components highlighted, front view. Adapted from [38]

- *Side rocker.* The side rocker or sill is one of the main structural components of the underbody. The sill design is one of the main parameters influencing body stiffness, both in torsion and bending. Furthermore, it plays a crucial role in side impact absorption.
- *Front torque-box.* The front torque box is a stiffening element that connects the side members to the sill allowing to have a stiffer structure and to transfer the load from the front side members to the rocker. Its dimensions are usually limited in the conventional ICE underbody while as it will be explained their function will be crucial in dedicated BEV platforms.
- *Underbody rails.* The underbody rails constitute the backbone of the floor of the vehicle. Originating from the rear end of the front side members, these beams bend

around the front wheel arch and down at the level of the floor. Their main contribution is to the bending and torsional stiffness of the body as well as constituting a crash direct load path from the front rails to the cabin floor.

- *Front seats cross-members.* These structures contribute to stiffening the front floor of the vehicle to allow adequate stiffness and strength for the seat mounts and of the front cabin compartment in case of side impacts.

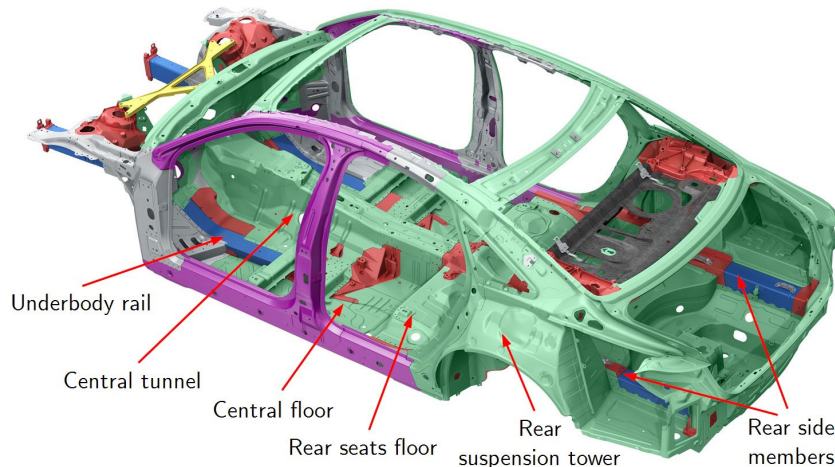


Figure 2.2: Audi A8 spaceframe with main underbody components highlighted, rear view. Adapted from [38]

- *Central tunnel.* This structure is needed to have adequate space for the transmission shaft and exhaust system. It is still present also in front-wheel-drive vehicles since it provides additional bending stiffness which has a positive impact also in the crash load transmission.
- *Cabin floor.* The cabin floor constitutes the set of mainly flat panels connecting the aforementioned rails and members. Their structure presents stiffening ribs and channels to improve the rigidity and the NVH performances. In the rear part of the vehicle, the floor raises to become the support for the rear seats. In this region usually, two cross-members are present at the front and the back of the rear seats. The volume under the rear seats is usually exploited by the fuel tank.
- *Rear torque boxes and side members.* The function and shape of these structures are analogous to the frontal ones. The rear torque box connects the sill to the rear side members allowing to transmit the load of the rear suspensions and the rear impact load, from the rear rails to the rocker rails.

- *Rear suspension tower.* The rear suspension tower houses the connection for the rear suspension damper while usually the arms and elastic element connections are located below the rear side members.

2.2 Underbody Functions

After describing the main underbody components, it is worth mentioning the principal functions and requirements of the whole underbody system. For the scope of this project the most relevant functions are [2, 36]:

- *Structural function:* among which static and dynamic strengths and stiffnesses are of crucial importance for the dynamic and NVH performance of the vehicle
- *Safety function:* the underbody must guarantee appropriate protection for the occupants and, in the case of BEVs, for the battery pack to avoid further fire or explosion hazards to the passengers

These functions are here briefly described to have an idea of the performance requirements of a vehicle body. It is important to note that the following data are relative to the entire body but despite that, they are still relevant since the underbody plays the most critical role in determining these performance figures.

2.2.1 Structural Functions

The vehicle body must be able to resist to use and, occasionally, abuse loading both under static and dynamic conditions. Examples of common static stresses are the ones generated by carried objects and components or the parking condition with one wheel on a road step. Dynamic stresses are instead generated by inertia loads like from limit manoeuvres, hard braking or fast cornering, road unevenness and obstacle overcoming. Excluding the crash loading, the loads derived from obstacle overcoming are in general the most critical, causing accelerations up to $3g$, and forces in the order of 20 kN. Under these loads, the body components must guarantee the structural integrity of the frame [36, 39]. Analysis of dynamic loads is in general complex, thus, to account for the increased severity of these loads additional safety factors are considered [2, 39].

Moreover, when loaded, the body must limit its deflection and vibration transmission not to harm the vehicle dynamics and comfort. The body static stiffness should be the highest possible while keeping the mass as low as possible. In this way, lightweighting and suspension behaviour will be optimal thanks to a light and stiff frame [36].

General reference data for BIW stiffnesses are around 11 kN/mm for the bending stiffness and 1500 kNm/rad for the torsional one. [36, 40]. For the purpose of this

study, it is important to notice that it is difficult to obtain stiffness data for the vehicle underbody, without upperbody, as well as data regarding the stiffness of the underbody and battery pack system. From the available data, it is possible to see how the torsional stiffness of the isolated underbody can reach values as low as 200 kNm/rad, being less than one-quarter of complete BIW torsional stiffness [36].

For what concerns the NVH performances, global or local resonances of the body must be avoided in frequency ranges that may interact with the natural frequencies of other components. It is crucial to avoid body resonance in the frequency range of the suspension's resonance (commonly at 15-20 Hz) as well as avoiding resonances that may lead to cabin noise due to the excitation of the cockpit cavity natural frequency (commonly in the ranges 50-70 Hz and 120-140 Hz). Following these considerations, the ideal first resonance mode both for bending and torsion should be above 40 or better 45 Hz, while avoiding resonances, especially of the floor panels in the range of the cockpit cavity natural frequency range. [36, 41].

2.2.2 Safety Functions

Together with the structural functions, the safety characteristics play a fundamental role in the vehicle body design. The general concept is to ensure the integrity of the passenger compartment, the so-called stiff cage concept and dissipating as much of the kinetic energy through deformation of dedicated crumple zones. The aim is to reduce the deceleration on the occupants to values around 30g as well as reducing injuries to vulnerable road users. For BEVs, the critical aspect of crash absorption is the side impact, given the limited crash absorbing structure that can be implemented and its potential for causing damages to the battery pack and cells [2, 42]. The general concept is thus to dissipate as much energy as possible to local plastic deformation to reduce deceleration levels and possibly keeping them at a constant level. The crash dissipation must be performed limiting intrusions in the passenger compartment and for BEVs in the battery pack.

Figure 2.3 shows an example of the load path during a frontal and side impact, illustrating how the load is absorbed and redistributed across the vehicle frame.



Figure 2.3: Mercedes Benz C-class front and side impact schematic load path [43]

For what concerns crash energy absorption, the rear impact can be considered analogous to the frontal one.

2.3 Battery Technology and Battery Pack

After illustrating the main design principles and functions of the vehicle underbody, a brief introduction to the battery technology and battery pack design is provided to focus on the crucial and distinctive system of BEVs platforms. This review aims at highlighting the most relevant aspects of the energy storage system according to the scope of the project.

The vehicle battery is a crucial and complex system, comprising, among the several components, the energy storage medium i.e.: the battery cells, the structural enclosures, the BTMS and thermal and electrical safety devices. The electric powertrain accounts for at least 50% of the vehicle cost, with the battery constituting up to 35% of the overall vehicle cost, while in conventional ICEV the powertrain accounts for approximately 16% of the vehicle cost. To give an additional view on the relevance of the battery in the vehicle, it is worth noting that the battery weight constitutes more than one-quarter of the vehicle weight, reaching masses close to 700 kg for the complete battery pack [44]. It is thus crucial to focus on the battery technology as well as the battery pack structure to reduce its complexity and cost while improving its performance.

An example of the evolution of the battery pack design is shown in figure 2.4, where the battery pack used by Volkswagen AG (VW) for their MQB platform in 2014 is compared to the newer MEB platform battery pack. The design simplification is clearly visible, and it allowed VW to improve the vehicle performance and range as well as reducing the by 50% the cost of the battery pack [45].

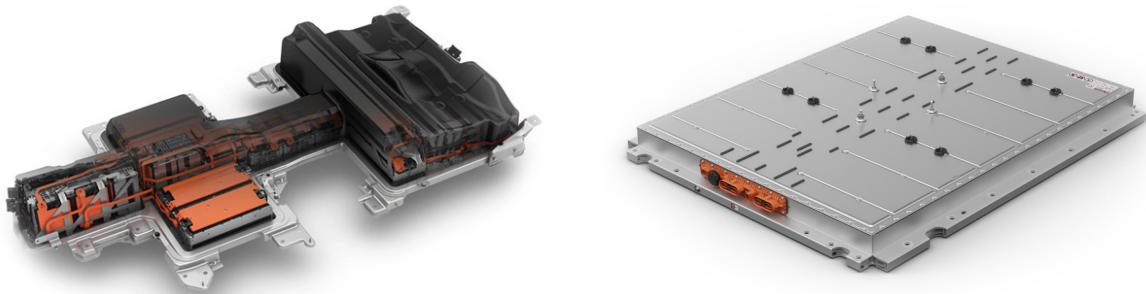
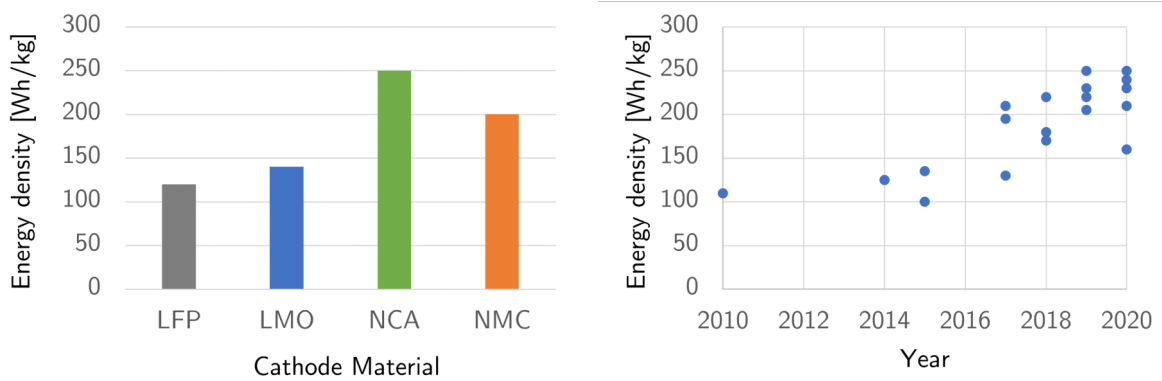


Figure 2.4: MQB platform and MEB platform battery packs in comparison, left to right [46, 47]

In the following, a first introduction to the battery chemistry is presented to better understand the energy density limitations of this energy storage medium and next the attention will move towards the structural aspects of the battery pack from the cell up to the complete system. Since out of the scope of the project, the BTMS and electrical management system will not be analyzed in depth.

Concerning the battery cells chemistry, Ding et al. in [22] provide an overview of the different available technologies for BEVs batteries. The current state-of-the-art technologies result to be: Lithium Ferrophosphate (LFP), Lithium Manganese Oxide (LMO), Lithium Nickel Cobalt Aluminum Oxide (NCA), and Lithium Nickel Cobalt Manganese Oxide (NMC). The most promising chemistries at the moment are the NMC and NCA, topping at around 270 Wh/kg and 250 Wh/kg, respectively. Both technologies are expected to reach 300 Wh/kg by 2025. It is worth noting that to reduce the entry price of BEV, many companies are using cheaper battery chemistries such as LFP, as well as trying to use LMO and Lithium Nickel Manganese Oxide (LNMO) chemistries to reduce the use of cobalt by using LMO, which is expensive and expected to reach critical levels of demand versus supply in the next fifteen years [22, 24]. Figure 2.5a shows a comparison of Li-ion batteries energy density for different cathode chemistries and figure 2.5b shows the trend in prismatic cells energy density improvements.



(a) Energy densities of different Li-ion batteries chemistries [48]

(b) Improvements in prismatic cells energy density [24]

Figure 2.5: Trends for Li-ion batteries energy densities

Another crucial component of the battery is the anode material. At the moment the most used is entirely made by graphite, but in the future silicon is expected to deliver significant improvements thanks to its higher capability to store lithium ions. At the moment its application is still difficult and expensive, but it is starting to be applied as silicon oxides in small percentages [24]. To further increase the performance of lithium

batteries and overcome the NMC and NCA theoretical limit of 350 to 400 Wh/kg, the only solution is to move towards solid-state battery technology [22]. However, several companies are investing in solid-state batteries which are able, apart from increasing the battery energy density to improve battery safety and allow faster recharging. The challenges for mass production are still many, such as high operation temperature, high cost and chemical stability [22, 24]. The first solutions are expected to hit the market in 2023, with more coming after 2025 [24].

From the battery chemistry, the following step in the integration process is to enclose its components in a battery cell. Three main approaches are present: cylindrical cells, prismatic and pouch cells. In cylindrical cells, the anode and the cathode are wound and enclosed in a steel casing. The single cell is usually relatively small reaching a capacity lower than 20 Wh. Prismatic cells use a similar concept to the cylindrical cells, enclosing wound or folded electrodes in an aluminum or steel enclosure with a capacity of around 700 Wh per cell. Lastly, the pouch cells enclose the electrodes in a soft packaging reaching cells capacities up to 300 Wh and usually showing the highest energy densities [24]. The described battery cells from factors are reported in figure 2.6.



Figure 2.6: Comparison between different lithium battery cells form factors [24]

The next stage is the integration of the cell into a battery pack structure. In the following, the main function and critical aspect of the battery pack are reported according to the description presented by Khajepour et al. in [2].

- *Structural stability.* The battery pack must be designed to support and to be properly linked to the underbody to sustain the relevant mass of the battery cells during static and dynamic loading and granting adequate NVH performance
- *Placement.* The battery pack should be placed as low as possible to lower the center of gravity of the vehicle and improve its dynamics performances. The battery placement is also crucial to determine the vehicle packaging and the occupant ergonomics

- *Improvement of underbody stiffness.* Apart from installing it in an adequate location, the battery pack should possibly improve the rigidity of the underbody by stiffening it when mechanically coupled
- *Crash protection.* The battery pack must be placed and protected through adequate crash absorption structures to avoid damages to the cells and possible fire or explosion due to cell breakage.
- *Thermal management:* The battery cells need to be maintained in the optimal operating range between 25°C and 35°C, both by heating and cooling
- *Protection from external environment.* The battery pack must provide adequate protection from road debris and puncture to avoid damages to the cells. Adequate ground clearance and pack shielding are necessary

Figure 2.7 shows a schematic representation of a battery pack design, including its main components.

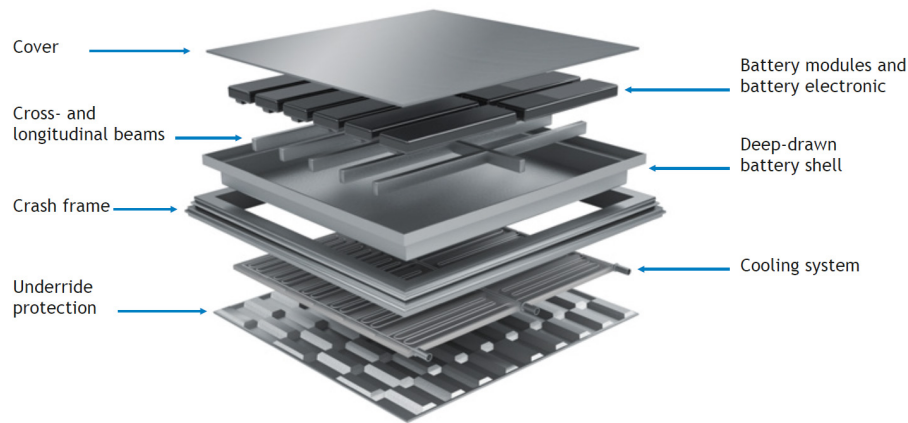


Figure 2.7: Stainless steel battery pack concept [49]

Several studies are specifically dedicated to the design of the battery pack.

Uwai et al. in [50] describe the design choices implemented in the first version of the Nissan Leaf. The dedicated platform was developed to protect the battery pack in the event of a crash, both by limiting the damages and by ensuring no accidental high voltage discharge with automatic shutdown sensors and fuses. The battery pack concept consisted of a stiff battery frame located underfloor in between the underfloor rails. The side sill and underfloor rails act absorbing the impact and limiting the forces on the pack. The floor cross-members are disconnected from the sill to avoid transmission of lateral loads to the battery pack, which during the crash is practically floating in the underfloor and remaining undeformed.

Arora et al. in [51] present a review of several mechanical design features to overcome the safety and reliability concerns of battery packs. Several patents and automotive standards from SAE and FMVSS are analyzed and reported. The key components for a robust battery pack design are illustrated especially for what concerns thermal protection in case of battery fire, vibrational protection, crash protection, and strategic battery placement guidelines.

Shui et al. in [52] performed an optimization analysis on a simplified battery pack structure. The analysis started from a predefined geometry and was optimized through the use of response surfaces. The objective was to decrease the mass and the constraints were maximum deformation under cells weight lower than 1.5 mm and minimum resonance frequency higher than 70 Hz. The design was then validated through an experimental test on a prototype of the battery enclosure. Further studies are needed for crash optimization and integration with the vehicle.

Wech et al. in [53] performed dynamic impact tests on several battery packs from the BMW lineup. The dynamic test was required to improve the testing prescribed by regulations which are limited to static loading. The impact load exceeded the typical crash forces, but the battery packs were able to sustain the load. Two main concepts were studied proving to be both effective: stiff housing limiting the intrusions and compliant internal structure tolerating intrusions. In both cases, the battery should be located in a stiff and protected region of the underbody to limit the load transmitted directly to it.

For what concerns the integration of the cells in the final pack, the current approach is the so-called “cell-to-module-to-pack” to integrate the cells in modules connected in parallel or series and then to locate the modules in the battery pack enclosure (figure 2.8). A crucial aspect is the cell integration efficiency, which is an index of the loss of energy density when passing from the single cell to the final pack. The higher this value the higher the effective density of the battery pack allowing for a lighter and more compact solution for the same capacity. The “cell-to-module-to-pack” is currently limiting the gravimetric energy density of the battery pack to 60%–70% and the volumetric energy density to 30%–40% of the cell energy density. The integration approach in the future is expected to shift towards the “cell-to-pack” integration, which skips the cell grouping into modules. The first solutions using this technology reveal a gravimetric cells integration efficiency of over 80% and volumetric integration efficiency over 60%. This allows to improve the pack energy density or reduce drastically its costs by using a cheaper and less energy-dense chemistry but exploiting it at best with better integration. The last evolution step in cells integration is the “cell-to-vehicle” approach. In this case, the cells are directly inserted into the car underbody effectively becoming

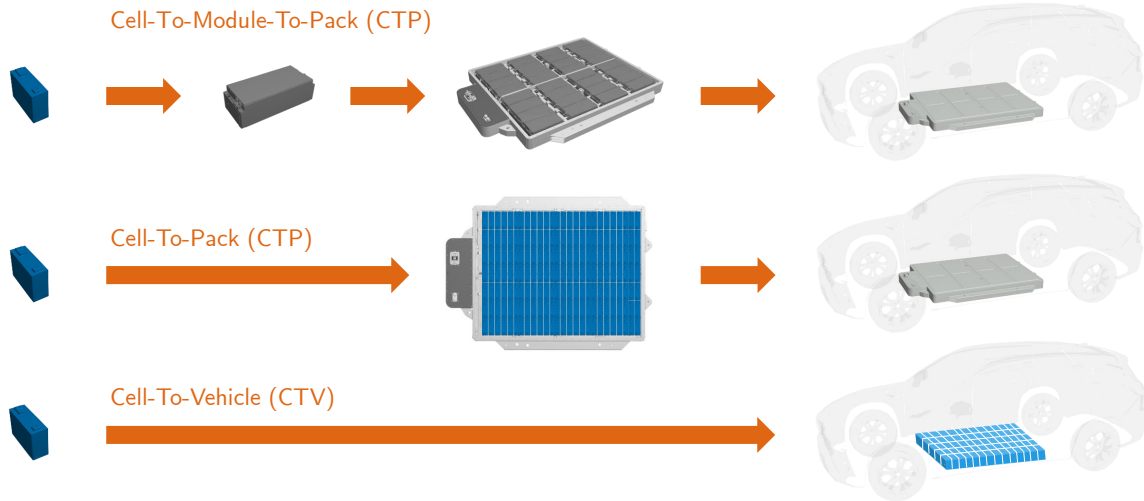


Figure 2.8: Comparison between different cells integration approaches [24]

part of the structure [24]. The structural adhesive is used to bond the cells to the underbody floor panels as a honeycomb structure, giving an integral and structural function to the cells. This application seems to be limited to cells form factors that provide a self-sustaining structure, such as cylindrical and prismatic, leaving out the pouch cells which have a soft enclosure [54, 24]. Several OEMs are planning to bring this new cell integration technology before the end of the decade [24]. These new approaches will allow reducing the cost and complexity of the battery pack while improving its energy density, thus reducing its mass and volume. The described cells integration approaches are graphically represented in figure 2.8.

2.3.1 BEVs Architecture

Following the analysis of the battery pack and its most relevant characteristics, the previously reported information was merged reviewing the available literature on the design of the BEVs platform architecture. The analysis was concentrated on the structural aspects, with a special focus on the underbody design concepts which were developed in past studies. Due to the scarcity of content dedicated to BEV, some of the reported studies are not directly related to electric vehicles but are still a source of valuable information for the development of the project methodology.

A dedicated design for BEV platforms and an appropriate design choice are crucial to exploit the benefit of the electric powertrain and achieve vehicle lightweighting.

Vasiliadis in [55] highlights the necessity for vehicle lightweighting which can potentially decrease the global energy consumption and, especially for BEV, increase the driving range or allow the use of a smaller and cheaper battery. This can be achieved by

integrating a lightweight battery concept with a BEV dedicated BIW presenting high modularity, low weight, and being able to reach economy of scale. The author sets ad a reasonable cost for weight reduction of around 8€/kg through which more than 40% of the weight can be cost-effectively reduced. The suggested approach consists of selectively applying advanced materials such as high-strength steels, aluminum, and magnesium alloys in conjunction with multi-material joining technologies.

Lesemann in the collaborative Advanced Electric Vehicle Architectures (ELVA) project [56], with the contributes of CRF, Renault, Volkswagen and Continental studied in 2010, three possible BEV architectures by forecasting the technology available in 2020. The developed concepts are shown in figure 2.9.

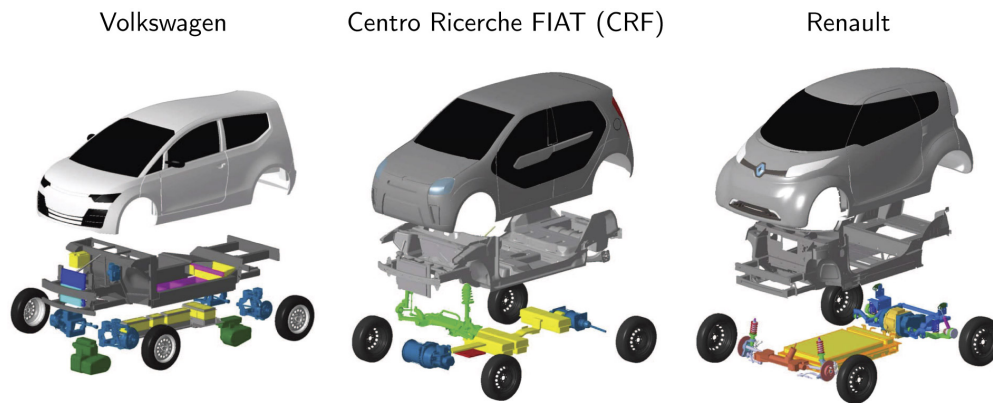


Figure 2.9: Advanced Electric Vehicle Architectures (ELVA) project developed concepts [57]

Despite being quite far from the current BEVs, the project is still valid for the followed approach and especially for the classification scheme used to rank the performance requirements and results of each design.

Currently, OEMs are working to develop dedicated and modular BEV platforms, inspired by the *skateboard* design introduced in section 1.1.1 and showing similarities and differences in design concepts. One example is the VW MEB platform, which is a *skateboard* modular platform, expected to sell 15 million vehicles by the year 2025 with models spacing from compact C-segment cars, up to seven-seater SUVs. The platform is a steel-intensive platform with an aluminum battery pack using pouch cells [58, 59, 44]. The platform is also expected to be used by Ford for the European market. Another OEM investing in electric platforms is General Motors (GM), which unveiled an architecture with pouch cells battery pack. The platform is planned to be shared with Honda. In addition to these manufacturers, several other OEMs and startup companies are investing in BEV platforms and the number of BEV models on the market is expected to increase exponentially over the next five years [58, 60].

Another relevant study was the one by Erriquez et al. on the *Trends in Electric Vehicle Design* [61, 62]. Through a benchmarking analysis, the authors focused the study on the improvements in battery technology and architectural choices that allow OEMs to cut down production costs. Due to the low differentiation possibilities of electric vehicles, manufacturers need to save costs on all the components to guarantee adequate profits. The current focus is on the design-to-cost approach, thus, the trend is towards the use of a validated and cost-effective stamped steel architecture, rather than extensive use of lightweight materials. Furthermore, the battery remains still the most expensive component, so OEMs are trying to optimize the vehicle BIW for optimal cost-effectiveness. Similar considerations are presented in [59] according to which newly developed Advanced High Strength Steel (AHSS) are especially suited for BEVs thanks to their lightweighting capabilities, lower cost for large-scale production and lower manufacturing CO₂ emissions.

The other reviewed studies are related to FEA analysis of BIW structures, particularly relevant to better understand the different approaches in the analysis and optimization of these structures. Despite not being directly focused on underbody design, these studies are useful for the followed methodological approach and will be exploited in the next steps of the project.

Zhang et al. in [63] conducted a Multi-Disciplinary Optimization (MDO) on a BEV BIW in order to minimize the mass while maintaining constraints on the static and dynamic stiffness as well as on the roof crash performances. The study is relevant for the used methodology and FEA techniques. The vehicle floor, roof, rocker panel and side panels are optimized changing their stiffness. However, the researcher did not investigate the influence of the battery pack structure and the resulting static stiffness and resonance frequencies are much lower than the reference industry values, thus suggesting further studies are needed to investigate the battery pack influence and to make the model more resemblant of the actual vehicle.

Park et al. in [64] conducted a material arrangement optimization for an automotive BIW to assess the location in which applying a lightweight aluminum alloy would provide the largest benefits while meeting the performance standards in bending and torsional stiffness. The optimization was made by a first screening of the variables, selecting the most significant components of the BIW for the second optimization phase. The provided indications on which components could be made out of aluminum to save weight without performance losses, reaching a 27% weight reduction when compared to the baseline model. The material arrangement results are shown in figure 2.10. It is worth noting that one limitation of the study is the simple material substitution without changes in components thickness. This leads to a more compliant structure

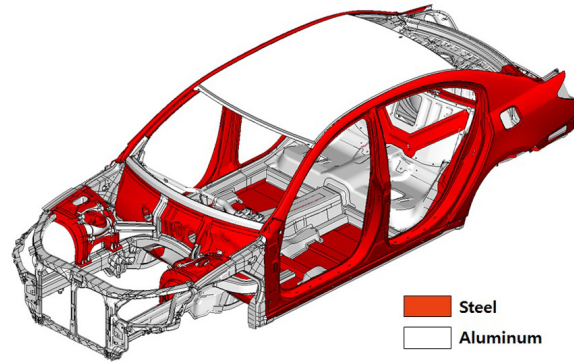


Figure 2.10: Optimized material arrangement configuration [64]

if aluminum is chosen due to its lower young modulus. Further studies are needed to investigate if increasing the stiffness of the aluminum components further weight saving may be possible by applying aluminum to a wider range of BIW components.

Lei et al. in [65] described three different approaches to optimize the design of a B-pillar under lateral impact. The approaches consisted of optimizations based on material substitution with and without cost penalty to reduce the mass while limiting the intrusion below 350 mm and the intrusion velocity below 11 m/s. Particularly relevant is the material substitution technique, which accounts for the lower aluminum Young modulus when replacing a steel-based component.

In this regard the “Design with Aluminium” was reviewed, to understand the advantages and limits of using aluminum for BIW components, as well as its design procedures and applicability. The manual illustrates the techniques to substitute steel-based components with aluminum-based ones while maintaining the desired performance level. These concepts will be further expanded in chapter 4 when discussing the definition of the simplified model.

2.3.2 Relevant Patents

In addition to articles and reports, another source of information came from several filed patents. In what follows the most relevant findings from registered patents regarding BEVs and battery packs are briefly reported. Of great relevance were the patents drawing, of which some examples are here reported.

Tesla Inc. is the assignee of several patents concerning BEVs and especially battery pack and underbody structure. In [67] it is described the integration system for the vehicle battery pack and underbody with special attention to the battery pack structure and connections to the underbody (figure 2.11a). Another relevant patent is [68] which describes the rear vehicle torque boxes, a critical connection structure between rockers and rear side members (figure 2.11b).

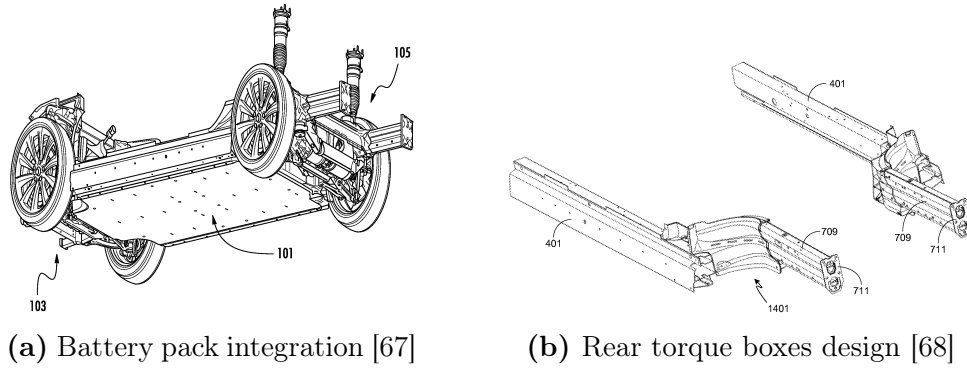


Figure 2.11: Tesla underbody battery integration and rear torque boxes design

The patent [69] outlines the design of a lateral crash absorption structure located inside the door sill, together with the sequence of collapse under a pole impact (figure 2.12).

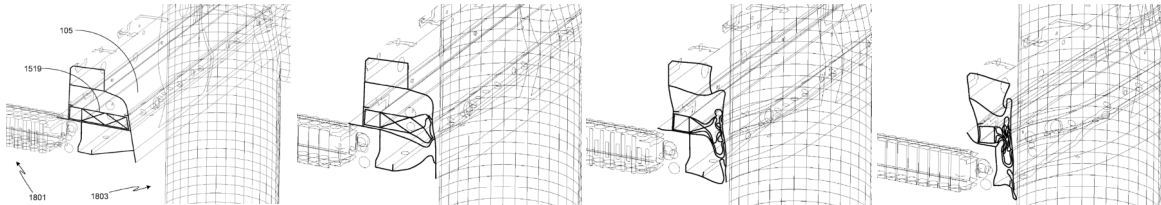


Figure 2.12: Tesla side impact absorption structure [69]

General Motors provides in the patent [70] an accurate description of the battery pack structure which is close to the one implemented in the Chevrolet Bolt. The battery pack presents several stiffening cross and longitudinal members (figure 2.13)

Hyundai Motor Co. presents in the patent [71] a description of a dedicated BEV underbody with particular attention to the torque boxes interconnections (figure 2.14).

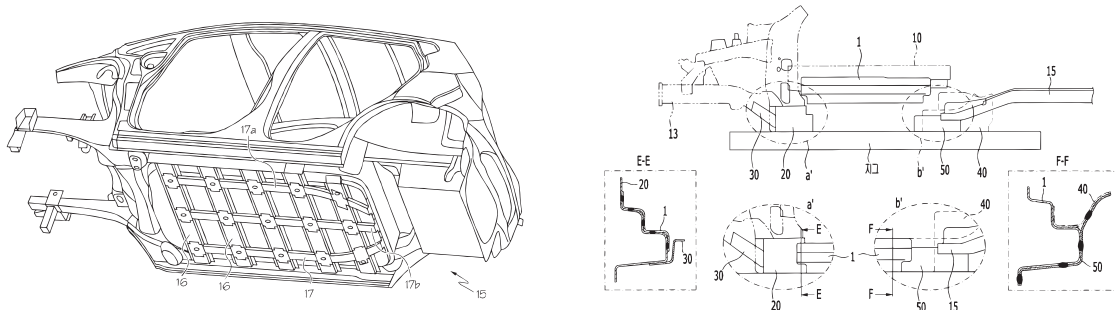


Figure 2.13: GM battery pack design [70] **Figure 2.14:** Hyundai BEV platform [71]

Volkswagen AG describes in [72] the external and internal structure of its modular battery pack, implemented on the MEB platform (figure 2.15).

Volvo Car Corp. registered in [73] a solution for a battery pack surface stiffening by tapered structures, able to redistribute the load under side impact to limit damages to the battery cells (figure 2.16).

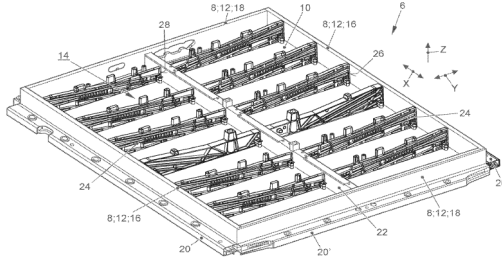


Figure 2.15: VW battery pack structure [72]

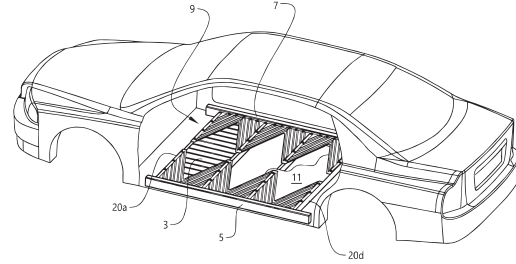


Figure 2.16: Volvo battery pack structure stiffening [73]

Magna Steyr presents in [74] a solution for a battery pack, with top enclosure acting as vehicle floor and bottom detachable enclosure to allow easier maintenance of the battery modules.

2.3.3 New Underbody Concept

To conclude this section, it is clear that the new era of BEV is being built on a new underbody and platform concept. As already discussed previously the new underbody designs are based on a *skateboard* architecture concept.

The archetype of this design was the 2002 AUTOmomy concept from GM, already illustrated in section 1.1.1, figure 1.2. This concept was then evolved and adapted to the BEV architecture.

The basic idea is to have the central portion of the BIW underbody occupied by a large and mostly flat battery pack constituting the ideal *board* [44, 7, 60]. This allows to exploit the underfloor region to house the bulky battery, reducing the impact on the vehicle packaging and keeping a low center of gravity [60, 2]. The other drivetrain components are integrated into the lower part of the BIW by additional subframes and attached to the central portion of the vehicle.

This architecture offers more flexibility to the design of the vehicle, with a simple architecture concept that is dedicated to exploit the advantages of BEV powertrain and coping with its challenges [44, 2, 60].

As already reported the crucial aspect of this design is thus the integration of the underbody structure with the battery pack, which need to work in conjunction to guarantee static, dynamic and safety performances [2]. In figures 2.17a and 2.17b an example of two dedicated BEV *skateboard* architectures from Hyundai and Ford are shown.



(a) Hyundai E-GMP [75]



(b) Ford GE1 [76]

Figure 2.17: Examples of dedicated BEV platforms

The key components and distinctive elements of this new underbody concept will be further described and investigated in chapter 3 when the study will go deeper in the benchmarking analysis, illustrating the different interpretations that the OEMs are using in this new platform design.

3 | Benchmarking Analysis and Classification Scheme

Benchmarking is the process of analyzing and comparing different corporates performances and solutions, understanding the state-of-the-art of a certain technological field. For the scope of this project, the benchmarking analysis was focused on the comparison of different design solutions and implementations for underbody architecture and battery pack structure. The analysis compared vehicles from different OEMs as well as from different generations of BEV, allowing to assess similarities and differences in the design choices, and as evaluate the evolution in design approach with the new developments in the field.

The chapter illustrates the methodology used to conduct the analysis and presents the developed classification scheme, explaining its building blocks and its possible future uses and improvements.

3.1 Methodology

This section illustrates the methodology used to conduct the benchmarking analysis, introducing the used resources, and outlining the analysis procedure.

3.1.1 Benchmarking Material and Resources

The first step in the analysis was the selection of adequate and reliable benchmarking sources. The main source for the analysis was the automotive benchmarking portal *A2mac1* [10]. The portal was used to retrieve data and images about the vehicle of interests, exploiting, in particular, the following sections, which are here reported according to the respective description that *A2mac1* provides [77]:

- *Autoreverse and 3D Autoreverse*. The service provides a database of 800 vehicles that have undergone the teardown process and an average of 1500 parts per vehicle is analyzed providing data including mass, dimensions, fasteners, images, and 3D

scans. The 3D analysis allows to view a reconstruction of the vehicle Digital Mock-Up (DMU), allowing to take measurements, and generate exploded or section views.

- *xEV Powertrain*. The service consists of the complete teardown with pictures and 3D scans of the electric powertrain and high voltage system including the traction battery, the e-motors, the power electronics, and the thermal management system. The analysis include also data on the chemistry and structure of the battery cells and the architecture of the battery management system.
- *BIW*. The service provides a 3D scan of the complete BIW assembly, pictures of internal reinforcements and 360° panoramic views. The BIW is disassembled in the individual panels, generating schematics and assembly tree diagrams. Material thickness, hardness, strength, joining technique and chemical compositions are provided for the different panels. Drawings of the most relevant BIW cross-sections are available as well.

Additionally, to the a2mac1.com portal, data were retrieved mainly through the OEMs websites, dedicated automotive websites and magazines like *QUATTORUOTE* [78]. For what concerns the crash safety data, vehicles ratings were collected from European New Car Assessment Programme (Euro NCAP), Insurance Institute for Highway Safety (IIHS) and National Highway Traffic Safety Administration (NHTSA) reports.

In the following, some examples of the material available from *A2mac1* [10], are reported to better illustrate the analysis methodology. The study exploited the tear-down pictures available on the portal, as well as the 3D scan of the different vehicle components, together with weight, dimension, and material information data. Further data were collected from the above-mentioned dedicated studies performed by *A2mac1*, particularly from the *BIW Analysis* and *xEV-Powertrain*. For what concerns the BIW, and specifically the underbody, data regarding the design of the main structural cross-sections as well the materials, thicknesses, and weight of the various BIW components of interest were gathered. Through the *xEV-Powertrain* studies, data regarding battery pack structure, cells integration and energy densities were collected. In each analysis special attention is given to the connections of the components, especially between the battery pack and underbody.

Figure 3.1 shows some examples of the data used for the underbody analysis, together with some annotations that were added to highlight the structural characteristics. The figure presents two views of the underbody, 3.1a and 3.1b, from which it is possible to investigate the layout of the platform.

From these first pictures, it is possible to note that the floor is almost completely flat. For a deeper analysis of the BIW, the *BIW* analysis service was used [79].

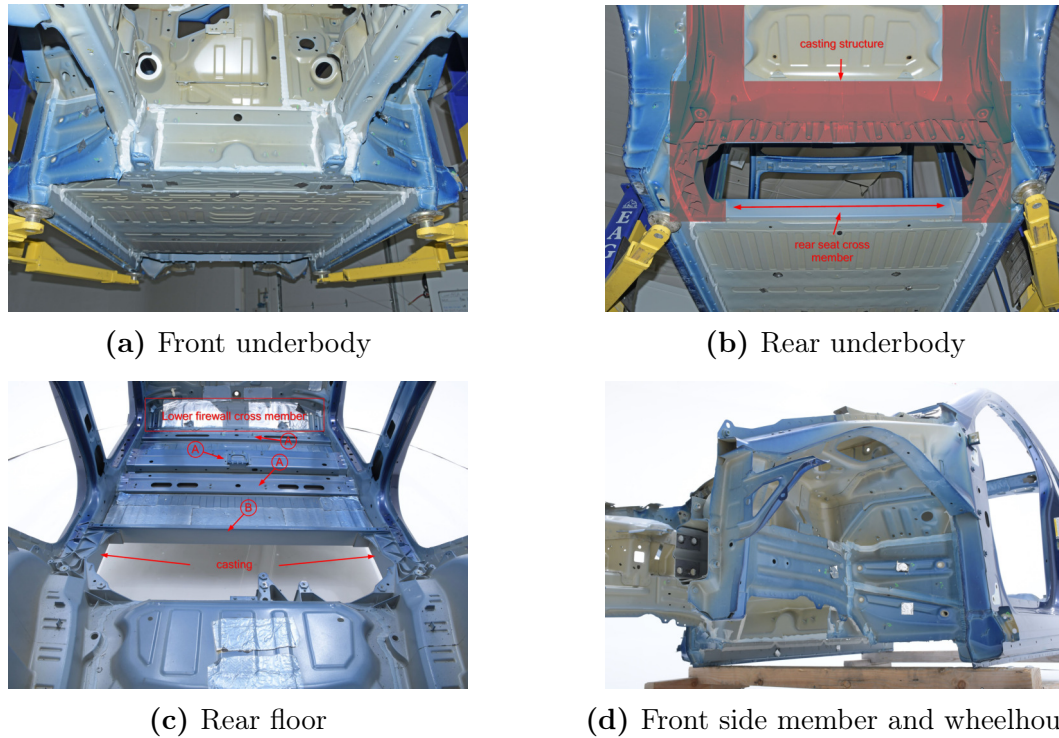
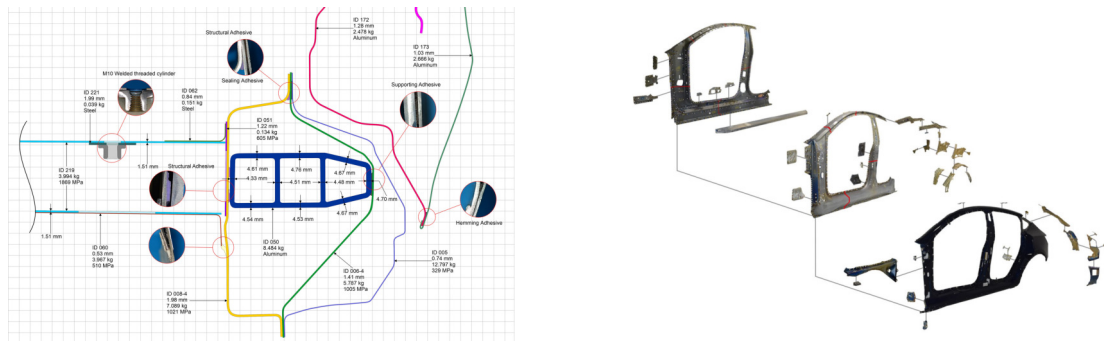


Figure 3.1: Examples of underbody images from Tesla Model Y *Autoreverse* [44]

Particularly useful were the cross-sections drawings, as well as the BIW exploded views, to better understand the panels structure and connections as well as material and thickness of each BIW subcomponent. Figure 3.2a shows an example of the sill cross-section from the Tesla Model Y, providing information on the material used for the different panels and thicknesses. The second figure 3.2b shows instead an example of the exploded view of the Tesla Model Y left body side assembly.



(a) Side sill cross-section, Tesla Model Y [79] **(b)** Left side assembly, Tesla Model Y [79]

Figure 3.2: Examples of BIW analysis resources from Tesla Model Y *BIW* analysis

In figure 3.3 are illustrated some of the visual materials available through the *xEV Powertrain* service [80]. Figure 3.3a shows an exploded view of the battery pack,

with the constitutive components and the assembly sequence highlighted. Figure 3.3b represents a further stadium of the teardown process by which it is possible to better understand the structure of the lower enclosure, which constitutes the most relevant structural component of the battery pack. Lastly, figure 3.3c shows the location of fasteners that are used to interface the battery pack with the underbody.

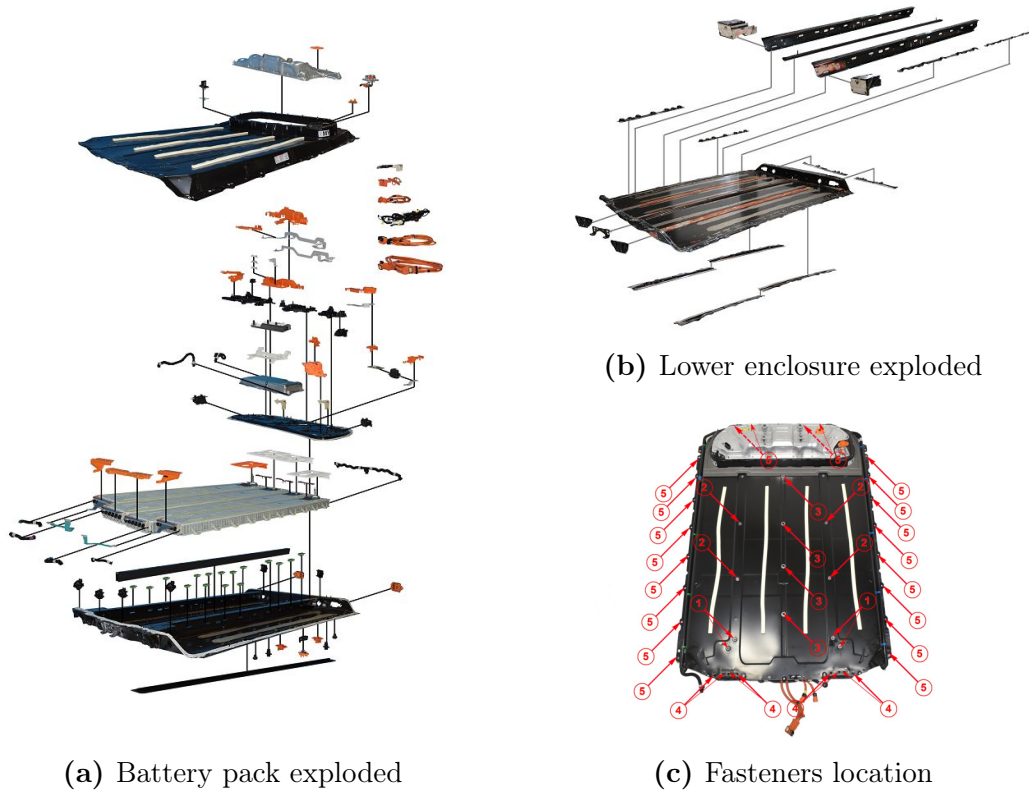


Figure 3.3: Battery pack images from Tesla Model Y *xEV powertrain* [80]

In the end, figure 3.4 shows two examples of the available 3D material retrieved from the *3D Autoreverse* and *xEV Powertrain* services.

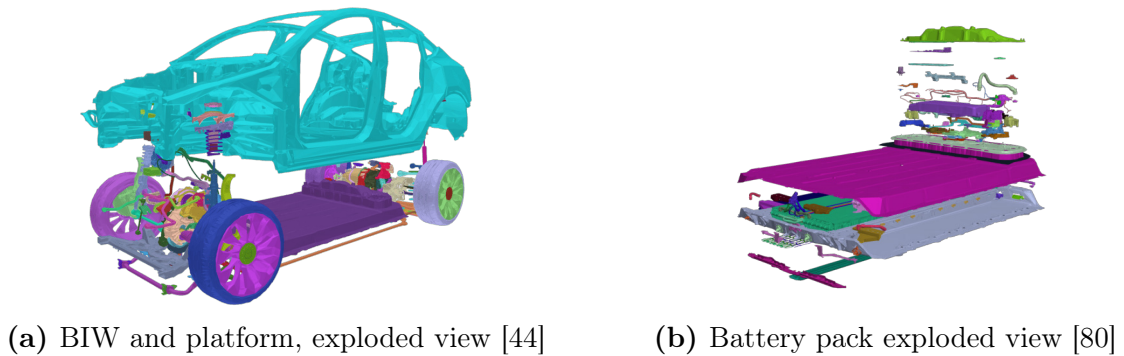


Figure 3.4: Material from *3D Autoreverse* and *xEV Powertrain*, Tesla Model Y [10]

The portal allows to take measurements as well as display sections and exploded views of the parts the user wants to investigate.

3.1.2 Analysis Outline

After illustrating the used resources, an outline of the conducted analysis is presented. The benchmarking analysis focused on 15 BEVs from 12 different OEMs. The vehicles were selected according to the availability of data on the a2mac1.com platform [10], focusing on vehicles with dedicated BEV platforms or highly adapted platforms derived from ICEV and heavily modified. The vehicles were chosen among the ones sold in the European and North American markets.

A total of approximately 45 images and 60 parameters were collected or evaluated per vehicle, concerning:

- *General vehicle information*: weight, global dimensions, safety ratings
- *Underbody and battery pack*: structural topology, shape, dimensions, and materials
- *Battery*: electrical and energy density properties
- *Integration*: underbody and battery pack fasteners, location, and interfacing properties

For each vehicle several numerical data were collected concerning weight, dimensions, battery electrical characteristics and energy density, materials and components shape, and safety ratings. Secondary data are then computed, from the first obtained information, to better evaluate the integration of the underbody-battery pack system and compare the different solutions. A thorough description is presented in section 3.3, in which each of the selected distinctive parameters of the classification scheme is detailed.

The second step was a visual analysis of the underbody and battery pack, through the available images, e.g.: figures 3.4a and 3.4b, on which annotations were added to better understand the platform topology and highlight common and distinctive traits between the different solutions. For a better understanding of sizes, dimensions, and layout, 3D scans (see figure 3.4) were analyzed, taking measurements and sections to gain a more in-depth view of the components shape, volumes, and structure. For completeness, in the end, the suspensions and their attachment points were analyzed. This part of the analysis was not fundamental for the following sections of the project and thus will not be treated in this work. The analysis could still be useful for future studies dedicate to the chassis development for this new type of platforms.

After collecting and analyzing the reported resources, some comments were provided on the design solutions to highlight peculiarities and distinctive characteristics.

Figure 3.5 provides a schematic synthesis of previously illustrated analysis methodology to summarize the used analysis process.

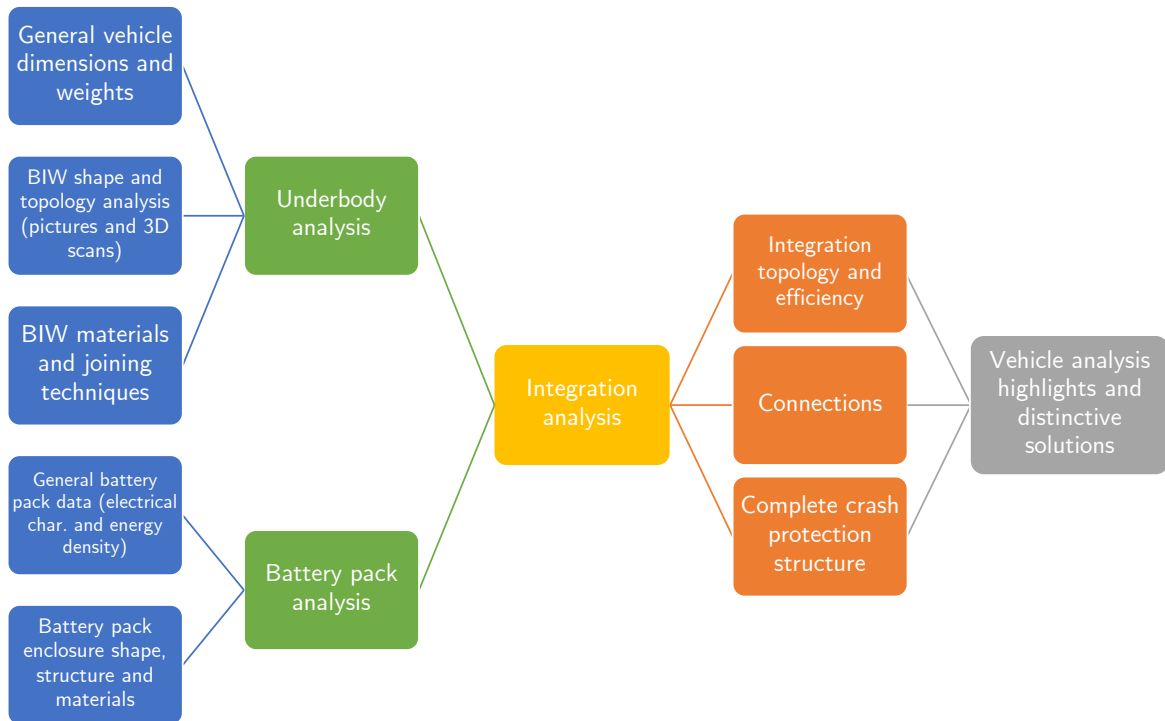


Figure 3.5: Schematic representation of the benchmarking analysis process

3.2 Review and Highlights of Analysed Solutions

After conducting the benchmarking analysis and collecting the previously illustrated data the first step was to highlight the features that are distinctive of a dedicated BEV platform.

3.2.1 BEVs Underbody Distinctive Features

At first, a comparison was made between ICEV and BEV underbodies in order to better understand the major differences between the two design philosophies.

Firstly a conventional ICEV is presented illustrating the main components of this type of platforms. Figure 3.6 shows an example of an ICEV underbody with highlighted its main components.

The figure shows a quite wide separation between the front side members which show also a relatively small section to house the internal combustion engine.

Following towards the back, the torque boxes are connecting the side members to the underfloor rails and rocker rails.

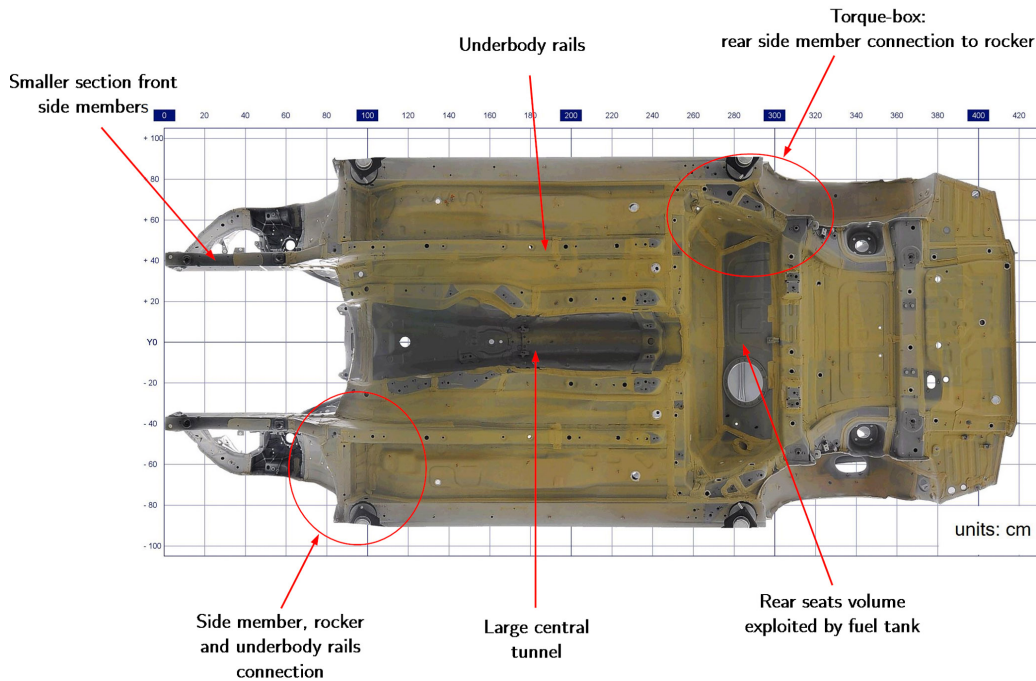


Figure 3.6: BMW X3 underbody, main ICEV platforms structural features [44]

The floor presents two underfloor rails and a large central unevenness due to the presence of a large central tunnel to house the exhaust system and transmission shaft. In the rear part of the floor, under the rear seat bench, the housing for the fuel tank is obtained by a protrusion of the rear floor. In this zone, the rear torque boxes are connecting the side rocker rails to the rear side members.

Following the description of a conventional ICEV underbody, a dedicated BEV underbody is presented in figure 3.7 highlighting the peculiar features of BEVs platforms.

The front side members result to have a wider section, both for the wider space available in absence of the ICE, and to dissipate the higher crash energy due to the increased vehicle weight.

Since no exhaust system is present, it is possible to install a cross-member in the front part of the floor. The cross-beam may be continuous or split and connected subsequently by the battery pack structure.

Two critical structures are the front torque boxes, which in this case, connect the front side members to the door sills. From this first analysis and comparing the different solutions, it was clear that several interpretations are present regarding this complex boxed structure. The torque boxes were thus assumed to be one of the crucial components in determining the underbody design and performance. This hypothesis will then be tested in the following part of the project (chapter 5).

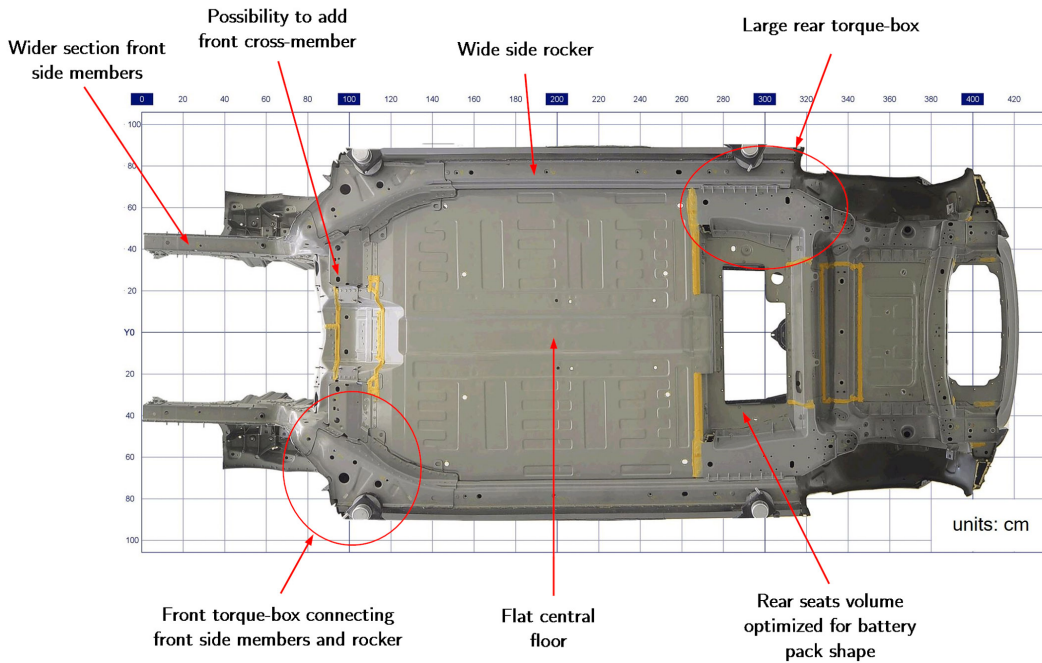


Figure 3.7: Jaguar I-pace underbody, main BEV platforms structural features [10]

The floor is in general flat, with no or low-profile central tunnel. No underfloor rails are present, and their function is transferred to the rocker rails. Being flat it can be exploited at best to house the battery pack. The common trend is to make the battery pack occupy almost the whole central floor region.

The rocker rails are in general wider and stiffer; they may also contain supplemental crash dissipation structures, like extruded aluminum alloy profiles, to protect the battery pack in case of a side impact.

The rear seat volume is more regularly shaped to better fit the shape of the battery pack, which may present a protrusion in that region.

The rear torque boxes have an analogous function to the front ones and may be in general larger than the ones found in ICEVs. In the end, the rear side members are instead analogous to conventional vehicles.

In general, ICEV BIWs are typically steel-intensive structures, while on BEVs, due to the high battery weight, aluminum is more used. In the last years, however, to reach economy of scale, thanks to improvements in the battery technology the manufacturers are going towards a steel-intensive architecture [61, 62].

The BEV architecture is an evolution of the conventional unibody BIW, but still presents crucially distinctive elements which are either needed or allowed to assume a different shape and configuration in a battery-powered electric vehicle.

3.2.2 BEVs Battery Pack Features

After the analysis of the underbody, the common features of battery pack designs are here briefly presented. An example of the typical battery pack structure is shown in figure 3.8.

The pack has, usually, a perimetral frame which may have more or less crash absorption functions depending on the rocker structure. When this frame is not present, the lower enclosure assumes the shape of a tray without any lateral frame but just a perimetral flange to link the pack to the underbody. From the conducted analysis the most commonly used battery pack material is aluminum, extruded, stamped or cast, followed by stamped steel.



Figure 3.8: Audi e-tron battery pack [81]

This perimetral frame is usually connected to the lower tray enclosure which is then stiffened by longitudinal and cross-members.

The structure is completed by the top enclosure which seals the battery pack.

Most of the vehicles tend to exploit the volume under the rear seats with a battery pack protrusion.

All these structures must act to house and protect the battery cells from external agents and impacts, as well as limiting the damages in case of partial fire of some of the cells modules.

Another critical component of the battery pack is the cooling system, which can be constituted by forced air, cooling plate, cooling channels, or phase change materials. These aspects will not be investigated in this study, but their relevance will be further expanded in the conclusions chapter when discussing the future works.

When installed the battery pack should possibly improve the stiffness and NVH performance of the vehicle platform. The extent of these improvements will be investigated through FEA in the next chapters.

3.3 Classification Scheme

Following the benchmarking analysis, a classification scheme was developed to obtain a tool that could be used for concept selection as well as for future benchmarking analysis. By selecting the most relevant parameters and organizing them into appropriate categories, it was possible to describe each solution through a code, allowing easier comparison between different vehicles and highlighting the current state-of-the-art in different aspects of the electric vehicle design.

3.3.1 Methodology

Starting from the 60 parameters collected through the benchmarking analysis, it was necessary to screen the retrieved information to select the most relevant attributes of the different BEVs solutions. To develop an effective classification scheme, the number of characteristics to be considered needs to be carefully restricted to keep into consideration the distinctive traits while not making the scheme too long and complex to read and understand [82].

The final parameters selection resulted in a total of 31 descriptors, each one corresponding to one field of the classification scheme. Four of the 31 fields are defined as “extra” since their information is already partially contained in previous fields. The “extra” fields are still included for a better and easier description of some characteristics and could be used also as validation fields.

In figure 3.9, an outline of the classification scheme design process is provided.

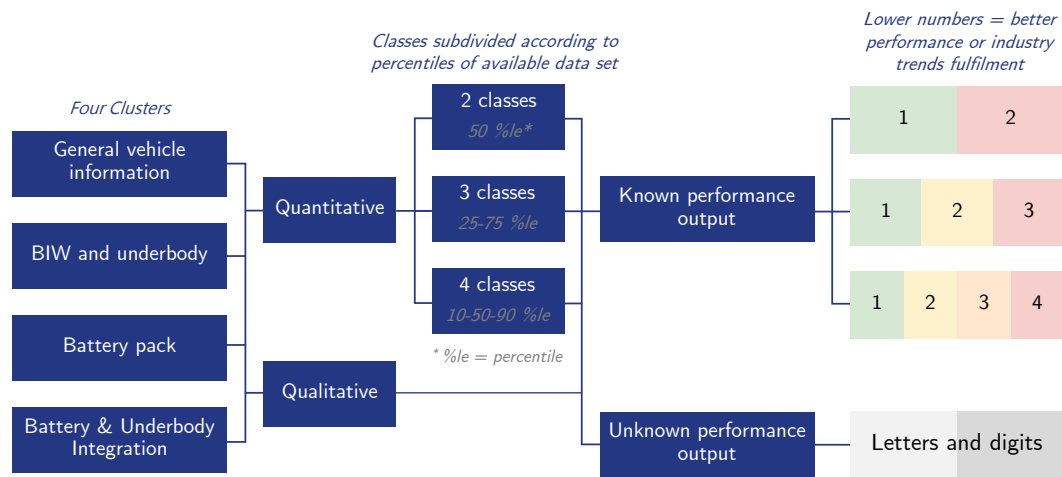


Figure 3.9: Classification scheme design process and structure

At first, the parameters were clustered into four clusters or categories: *General vehicle information*, *BIW and underbody*, *Battery pack* and *Integration*. The categories were a consequence of the scope of the analysis, which for this project was focused

mainly on the parameters influencing the structural design of the electric vehicles platform and battery pack.

Each characteristic can then be subdivided into quantitative or qualitative, with quantitative parameters being directly measurable quantities, and qualitative ones being mainly related to shape and topology characteristics which cannot be easily described numerically.

Concerning the quantitative parameters, to allow the scheme to be used to compare vehicles of different sizes, the variables which are dependent on the vehicle segment were normalized by size or weight.

These factors were then classified into two, three or four classes, according to the variability of the factors among the different analyzed vehicles. A higher range of variation for a certain characteristic implies a higher number of range subdivisions to be properly described. In general, each class subdivision is determined according to some selected percentiles; for two-class factors, the discriminant value was the 50th percentile, for three classes 25th and 75th percentiles and four classes factors were delimited by 10th, 50th and 90th percentiles. The percentiles were based on the available data sample, trying to preview, when possible, the future industry and technological trends, in order to make the scheme future-proof.

The analyzed variables were then classified into factors with *known performance output* and factors with *unknown performance output*.

The parameters for which it was possible to foresee their influence on vehicle performance, were classified with digits as shown in figure 3.9. A lower value of the digit represents a better performance or a better fulfilment of the current industry trend, corresponding in general to a solution closer to the best-in-class. A higher digit instead corresponds usually to outdated technology or in general to a solution that is not close to the best performing vehicles in the selected sample.

For the unknown performance output parameters, the different levels were instead classified with letters and numbers, descriptive of the respective factor, but without any ranking or preferred value, since not possible to judge a priori with the available information without additional FEA or physical tests.

It is worth mentioning that the clustered architecture of the classification scheme, allows it to be modular, thus leaving the user the choice of which module or portion of the code to use, as well as making it easily expandible to other vehicle characteristics, e.g.: adding a classification for suspension systems design. This point will be better expanded in section 3.3.4 dealing with the future uses of the scheme.

Since the classification was based on a limited sample of analyzed vehicles it was needed to validate the tool trying to apply the developed classification to other vehicles.

Furthermore, the vehicles were selected only from the European and North American markets, thus excluding the Asian and Chinese ones. Given the high growth of the Chinese market [5], it was worth including some of these vehicles in the analysis, in particular for the validation of the classification scheme. Thus, six vehicles were selected among the ones available through *A2mac1*, considering most diffused [83] as well as the one showing a dedicated BEV or highly adapted platforms derived from ICEV. For these vehicles, the analysis started with gathering the data needed for the classification scheme and applying the coding to these vehicles. After this process, a deeper review of each design was conducted in order to assess the consistency between the assigned classification and the actual solution. By testing the classification scheme on a new sample on vehicles, not included in the first analysis, it was possible to validate and assess the effectiveness and flexibility of the developed scheme.

3.3.2 Classification Scheme Description

After describing the methodology used to construct the classification scheme, each of its building blocks will be explained by illustrating the factors and classes subdivision of each of the four clusters illustrated in figure 3.9.

General Vehicle Information

This first cluster of the classification scheme, shown in figure 3.10, is meant to include general data of interest to classify these vehicles, mainly for what concerns their size, weight, electric driving range and crash safety.

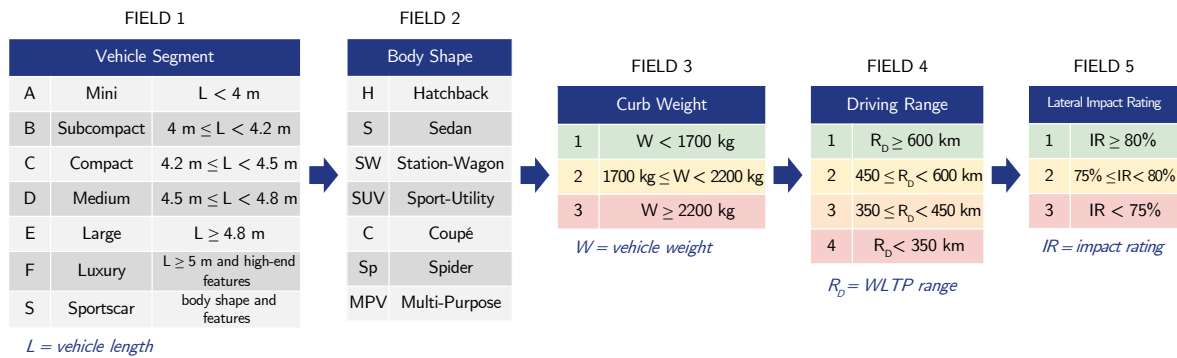


Figure 3.10: Cluster 1 classification scheme, *General vehicle information*

These parameters were selected in order to provide a first general description of the vehicle, but already focusing on the critical characteristics of BEVs.

In figure 3.10 the first cluster is schematically presented with detailed criteria for class subdivision. In the following, the fields listed in the previous figure will be explained and examples will be provided when necessary.

Field 1. *Vehicle Segment.* The first field of the code concerns vehicle segmentation. Vehicles are classified according to their size or characteristics with a letter corresponding to a specific type of vehicle. Since different classifications are available for the vehicle segmentation, the choice was to use the classical letter-based European segmentation [84] and delimiting each class by the vehicle length and/or by the vehicle features and function. For more details on the classes subdivision, see figure 3.10.

Field 2. *Body Shape.* To further classify the type of vehicle, this field categorizes the vehicles according to their body shape, e.g.: hatchback, sedan, station wagon, etc [85]. Each body shape is assigned a letter or a combination of letters representing the specific class.

Field 3. *Curb Weight.* The vehicle curb weight is subdivided from *lightweight*, with a weight $W < 1700$ kg, followed by *average weight* with $1700 \text{ kg} \leq W < 2200$ kg and *high weight* with $W \geq 2200$ kg. This factor was not normalized according to the vehicle size to allow an assessment of the actual mass of the vehicle, which is crucially important to increase the vehicle efficiency [86].

Field 4. *Driving Range.* Crucially important for BEV vehicles [29], the driving range was classified into four categories, from *ICEV equivalent*, corresponding to the best-in-class vehicles able to reach a range on a single charge comparable to the one of conventional ICEV with a range $R_D \geq 600$ km. The second class was then denominated *long range* ($450 \text{ km} \leq R_D < 600 \text{ km}$), followed by *medium range* ($350 \text{ km} \leq R_D < 450 \text{ km}$) and *limited range* with $R_D < 350$ km, the latter representing vehicles using outdated technology or meant primarily for city use. The figures used for this field were corresponding to the combined Worldwide Harmonised Light Vehicle Test Procedure (WLTP) standard. When these values were not available the corresponding range obtained through NEDC was used and converted into WLTP by dividing the NEDC by a conversion factor $f = 1.274$ [87].

Field 5. *Lateral Impact Rating (Euro NCAP).* As introduced in section 2.2.2 for what concerns the crash safety, the frontal impact assessment is generally easier to sustain for BEVs thanks to the absence of the bulky and rigid engine, which is usually in the frontal part of the vehicle. Critical is instead the side impact absorption, which, additionally to the occupant protection, needs to guarantee also proper protection of the battery pack. In fact, not having a large crumpling zone as in the front or rear impact, the battery is more subject to crash loading which may lead to explosion or fires of the cells. For these reasons, the lateral impact was selected to represent the crash safety in the classification scheme. This parameter was classified into *good* with a

rating score $IR \geq 80\%$, *average* ($75\% \leq IR < 80\%$) and *poor* with a score $IR < 75\%$. These values were obtained by using the rating from Euro NCAP and converting the ratings into a percentage. Figure 3.11 provides an example of the lateral impact tests conducted by Euro NCAP.



Figure 3.11: Side mobile barrier and side pole test from Euro NCAP [88]

BIW and underbody

The second cluster, shown in figure 3.12, is dedicated to the classification of the BIW and underbody for what concerns size and weight, materials, and structural topology.

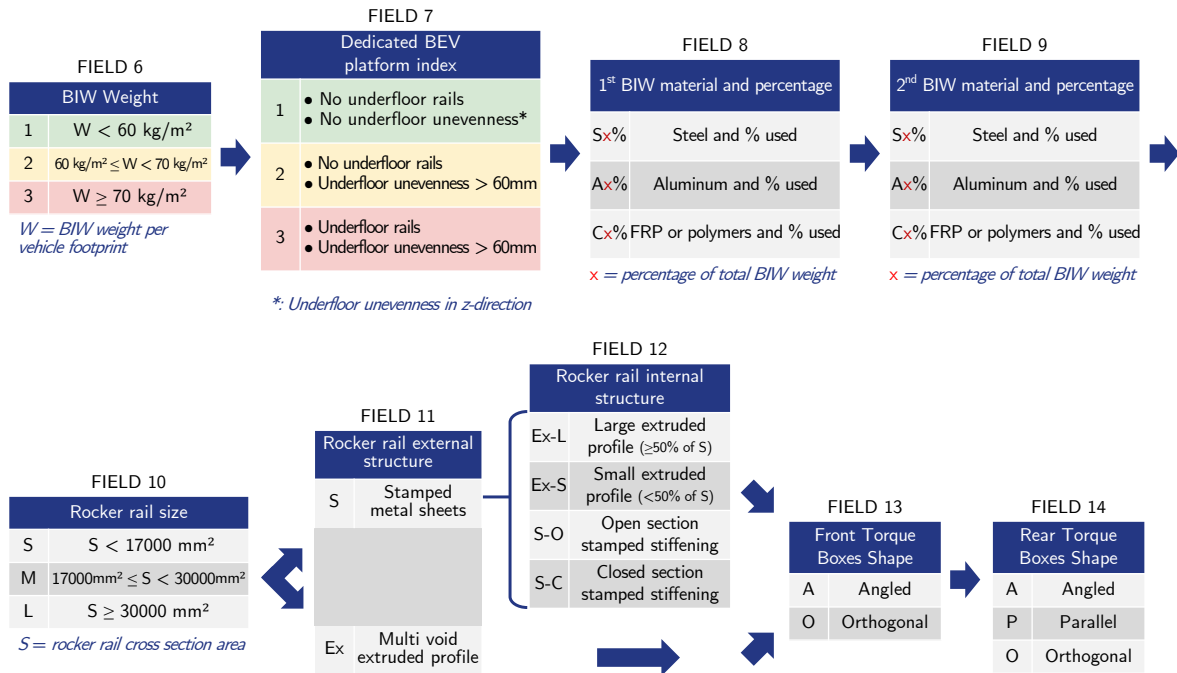


Figure 3.12: Cluster 2 classification scheme, *BIW and underbody*

These parameters were selected to describe the most relevant characteristics concerning BEVs platform architecture.

In figure 3.12 the second cluster is schematically presented with detailed criteria for class subdivision. Subsequently, the fields listed in the previous figure will be explained and examples will be provided when necessary.

Field 6. *BIW weight.* This field classifies the vehicles according to the weight of their BIW in three classes. To make the parameter independent of the vehicle size the BIW weight is normalized according to the vehicle footprint:

$$W = \frac{BIW\ weight}{wheelbase \times width} \quad [\text{kg}/\text{m}^2] \quad (3.1)$$

The footprint is evaluated considering the wheelbase since this corresponds to the size of the bulkier BIW section, while the overhangs are in general more variable and less heavy. By this normalization, it is possible to compare vehicles from different segments and assess their BIW lightweighting technology. The resulting classes are thus *lightweight* with $W < 60 \text{ kg m}^{-2}$, reached by lightweight aluminum-intensive BIW, *average* ($60 \text{ kg m}^{-2} \leq W < 70 \text{ kg m}^{-2}$) and *high weight* with $W \geq 70 \text{ kg m}^{-2}$ including mainly steel-intensive BIW derived from ICE platforms, or modular platforms that are meant to adapt also to larger vehicles.

Field 7. *Dedicated BEV platform index.* This index classifies the vehicles according to the platform design technique. Some examples are shown in figure 3.13.

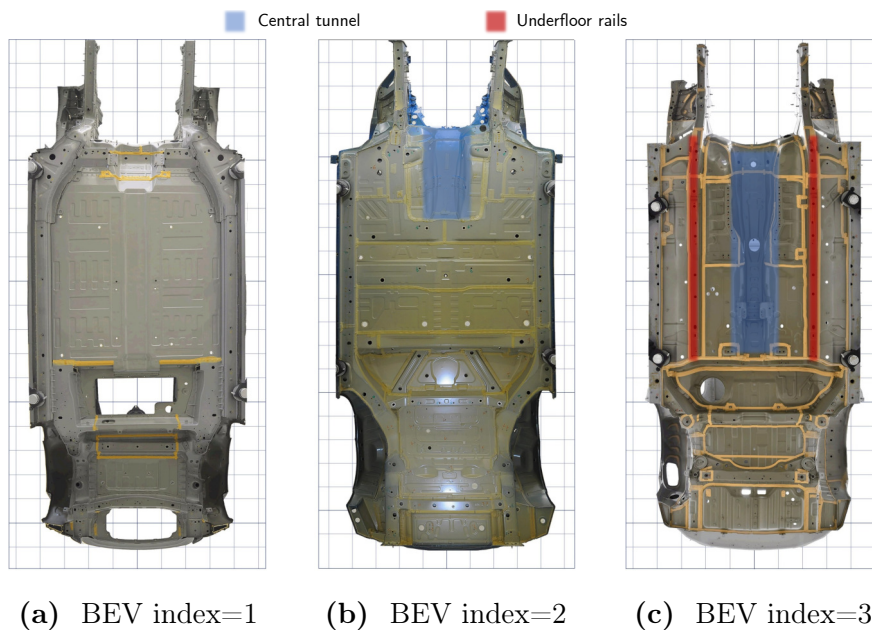


Figure 3.13: Examples of different BEV platforms corresponding to different values of the *dedicated BEV platform index*. Images from [44]

The index starts at ‘ 1 ’, corresponding to an underbody with no underfloor rails and no

considerable underfloor unevenness, excluding the rear seats region. This corresponds in general to a highly specialized BEV platform as the one in figure 3.13a. The value ‘ 2 ’ corresponds to a platform presenting underfloor unevenness greater than 60 mm in depth but with no underfloor rails. This is the case in general for heavily modified ICEV or multi-energy platforms, which may host an ICEV, PHEV or BEV version, and thus must adapt to a compromise. An example is shown in figure 3.13b. The last value ‘ 3 ’ represents platforms that show both the presence of underfloor rails and underfloor unevenness, being in general platforms designed for an ICE powertrain and adapted to the electric traction, like the one shown in figure 3.13c.

Field 8. *1st BIW material and percentage.* This field illustrates the most abundant material in the BIW structure, together with the corresponding percentage of the total BIW mass. The encoding for this parameter is made by a letter indicating the type of material, followed by the mass percentage of the corresponding material. It is worth mentioning that, from the conducted analysis, the most used material was steel, followed by aluminum alloys. At the moment none of the analyzed solutions shows large usage of Fiber Reinforced Polymers (FRP) or polymers but in the future, these solutions may become more common for sports cars.

Field 9. *2nd BIW material and percentage.* Similarly to the previous field, this represents the second most used material in the BIW structure. Given that several solutions presented a multi material BIW, a dedicated field was added for the second most abundant material. The classification follows the same criteria as in Field 8.

Field 10. *Rocker rail size.* A critical element of BEVs underbody is the rocker (figure 3.14).

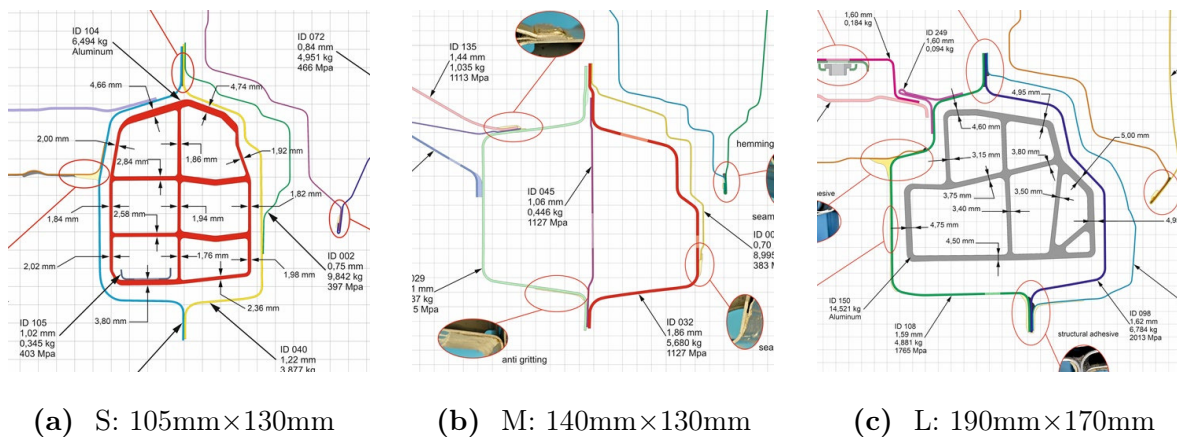


Figure 3.14: Different *rocker rail sizes*: small, medium, and large. Images from [79]

In the absence of underfloor rails, this structure contributes heavily to transfer the

load from the front and rear axles. This element is classified as *small* (figure 3.14a, with cross-sectional area $S < 1700 \text{ mm}^2$, *medium* in figure 3.14b ($1700 \text{ mm}^2 \leq S < 30\,000 \text{ mm}^2$) and *large* with $S \geq 30\,000 \text{ mm}^2$ (figure 3.14c). A larger rocker is usually indicating a platform designed specifically for BEVs and especially a modular platform which, thanks to the large size of the sill, can span up to higher segments like the VW MEB.

Field 11. Rocker rail main structure. The rocker rail was then classified according to its main structure. The external structure can be made out of stamped metal sheets or the complete rocker may be made out of a multi void extruded profile, usually in aluminum. Figure 3.15a shows an example of an extruded rocker, whereas the other ones in figure 3.15 show a stamped metal sheet main structure.

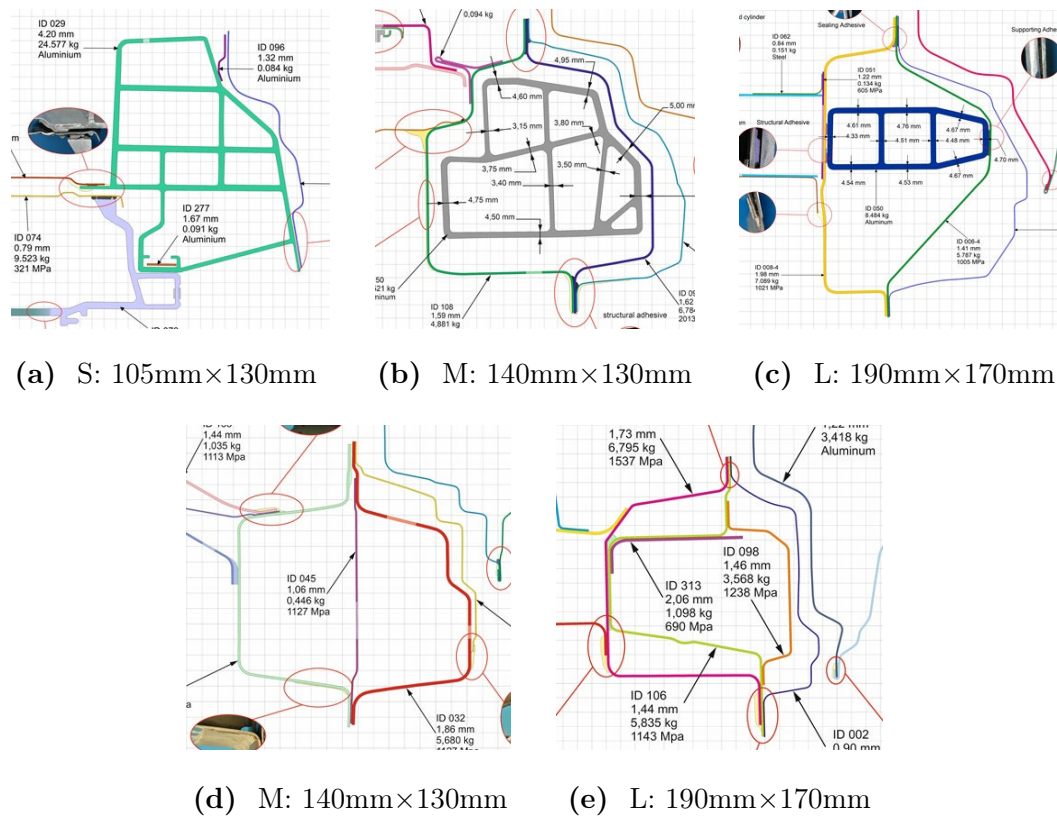


Figure 3.15: Different *rocker rail* sizes: small, medium, and large. Images from [79]

Field 12. Rocker rail internal structure. For what concerns rockers with a stamped main structure, the internal stiffenings were classified into four different classes. The internal structure may be constituted by a large, extruded profile as in figure 3.15b occupying more than 50% of the sill section or a small, extruded profile, figure 3.15c. Other solutions show stamped stiffening panels assembled in an *open-section* stiffening

as in figure 3.15d or *closed-section* stamped stiffening like in figure 3.15e. The rocker structure and its internal structure are critical both for the platform stiffness as well as the side-impact absorption. The most common solution at the moment seems to be a rocker including an *extruded* stiffening, being it *large* or *small*, usually connected to the external rocker panel by structural adhesive.

Field 13. *Front torque boxes shape.* Another crucial and typical element of BEV platforms are the torque boxes. The front torque boxes connect the front side members to the frontal part of the rocker rail, transferring the load from the front axle to the sill and the central part of the BIW. From the conducted analysis the front torque boxes were classified as *angled*, like the one in figure 3.16a or *orthogonal*, shown in figure 3.16b.



(a) Front angled



(b) Front orthogonal



(c) Rear angled



(d) Rear parallel



(e) Rear orthogonal

Figure 3.16: Examples of different *torque boxes* shapes. Images from [44]

The classification was made according to the angle at which the torque box elements join the rail in top view. From the conducted analysis the most common solution is front *angled* torque boxes.

Field 14. *Rear torque boxes shape.* Similarly, to the front torque boxes, the rear ones play a crucial role as well. These elements were classified as *angled*, presented in figure 3.16c, *parallel*, as in figure 3.16d, or *orthogonal*, shown in figure 3.16e. From the

conducted analysis the most common solution was a *parallel* connection followed by the *angled* torque boxes.

It is important to mention that the cross-member architecture was excluded from the classification since, in general, their position was almost constant in the analyzed solutions. One cross-member is usually present in correspondence of the firewall, one in the frontal part of the floor, two for the front seats and two cross-members or stamped structures for the rear seats. In addition, one cross-member connecting the rear side members and if necessary one in the trunk floor. This layout was the most diffused, with minimal variations. Thus, this characteristic was not included in the scheme.

Battery pack

The third cluster, shown in figure 3.17, is dedicated to the classification of the battery pack for what concerns the main electrical properties, cells integration and structural topology.

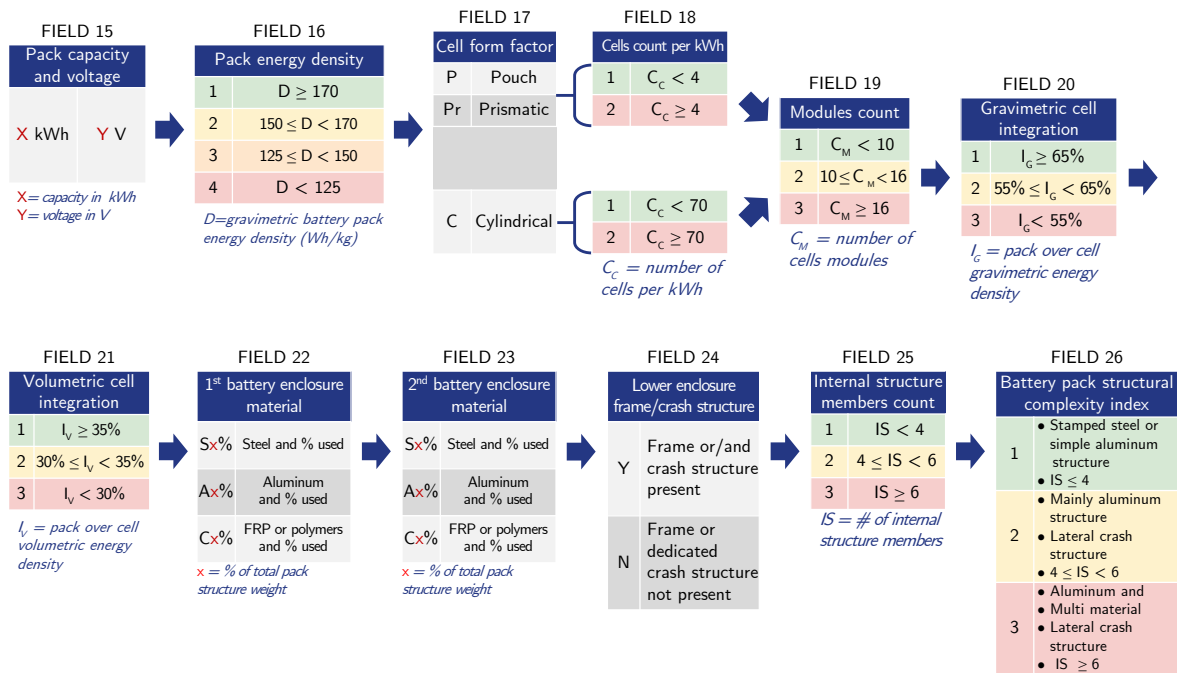


Figure 3.17: Cluster 3 classification scheme, *Battery pack*

These parameters were selected to provide a general description of the battery pack technology followed by a specific focus on its structure.

In figure 3.17 the third cluster is schematically presented with detailed criteria for class subdivision. In the following, the fields listed in the previous figure will be explained and examples will be provided when necessary.

Field 15. *Pack capacity and voltage.* This field is constituted by the battery capacity expressed in kWh and the voltage in V. These parameters were not subdivided into classes since they are listed to give a general introduction regarding the battery pack specifications. For what concerns the capacity it is highly related to the vehicle size and weight, thus, normalizing it according to the vehicle weight, led to low variability in the analyzed sample. For what concerns the battery pack voltage, at the moment, the variability across the solutions is quite limited, with most of the vehicles using 400V battery packs, with 800V and higher voltage packs under development.

Field 16. *Pack energy density.* An important index to understand the achieved technological level is the gravimetric energy density of the battery pack. This indicates the capability of the OEM to build an accumulator that can store a large amount of energy while still being lightweight. Four different classes were selected, from the least advanced, classified as *limited*, corresponding to a density $D < 125$ Wh/kg, followed by *average* ($125 \text{ Wh/kg} \leq D < 150 \text{ Wh/kg}$), *high* ($150 \text{ Wh/kg} \leq D < 170 \text{ Wh/kg}$), and *superior* with $D \geq 170 \text{ Wh/kg}$. This last class represents the best-in-class battery packs and the energy densities that will be reached with future battery chemistry developments. This parameter is crucial also for the structural development, both for what concerns the modal response of the system, as well as the packaging of the vehicle and battery pack. The detailed class subdivision is reported in figure 3.17.

Field 17. *Cell form factor.* Three main cells from factors are currently used in the industry, as already illustrated in section 2.3. Thus, the selected class are *pouch*, *prismatic* and *cylindrical*.

Field 18. *Cells count per kWh.* This characteristic is an index of the complexity of the battery pack, describing how many single cells are used to reach the desired capacity. This is classified in *low* or *high* cells count per kWh. It was necessary to classify separately pouch and prismatic cells from cylindrical cells, because of the much smaller size of the latter. Cylindrical cells battery packs contain up to more than 7000 cells, needing on average 70 cells/kWh. For pouch and prismatic cells, usually, the numbers are much lower, with an average of around 250 cells, corresponding to around 4 cells/kWh.

Field 19. *Modules count.* Another parameter to describe the complexity of the battery pack is the number of modules in which the battery cells are grouped before being integrated into the pack. As reported in section 2.3, the current trend is to reduce the number of modules, influencing the structural design by reducing the room for additional internal structural elements. The module counts were classified in *high*

corresponding to modules count $C_M \geq 16$ followed by *average* ($10 \leq C_M < 16$) and *low*, corresponding to the cells-to-pack integration approach ($C_M < 10$).

Field 20. *Gravimetric cell integration.* This parameter is particularly relevant to assess how the battery pack structure is optimized for lightweighting, allowing to house properly the cells without a large detrimental effect on the gravimetric energy density of the whole pack. This value is computed as $\eta_g = \frac{\rho_{pack}}{\rho_{cell}}$, where ρ_{pack} is the energy density at pack level and ρ_{cell} is the one at the cells level. The best-in-class vehicles can reach more than 65% of gravimetric cell integration efficiency. This was considered the *high* integration efficiency, followed by *average* between 55% and 65% and *low* which corresponds to outdated battery technology with η_g lower than 55%.

Field 21. *Volumetric cell integration.* This field is analogous to the previous but the compared quantities are the volumetric energy densities at pack and cells level. This characteristic is particularly relevant for the packaging of the vehicle. Reaching a higher volumetric integration efficiency leads to a more compact battery pack, allowing a better placement for the battery pack in the underfloor, reducing the increase in the vehicle floor height. The three selected classes were *high* with a volumetric integration efficiency greater than 35%, *average* with integration efficiency between 30% and 35% and *low* corresponding to a less efficient cell packaging reaching values lower than 30%.

Field 22. *1st battery enclosure material and percentage.* This field indicates the most used material for the battery pack structure, followed by its mass percentage compared to the total enclosure mass. The most used materials resulted to be aluminum alloys, followed by steel. At the moment no solutions intensively using composites or polymers were analyzed but these materials may be applied especially in the sports cars sector.

Field 23. *2nd battery enclosure material and percentage.* This field is analogous to the previous but related to the second most used material. Given that several solutions presented a multi material battery pack, a dedicated field was added for the second most abundant material.

Field 24. *Lower enclosure frame or crash structure.* From the analyzed solutions, some battery packs resulted to have a lower enclosure built with a perimetral frame and/or side crash absorption structures, usually obtained with aluminum alloys profiles. Conversely, other solutions present a simpler structure with no perimetral frame or crash absorption structure, thus relying mainly on the crash absorption from the rocker rail (see figure 3.15). Two classes were thus selected, one corresponding to the solutions that present this structure and the other for the battery packs which does not implement this design.

Field 25. *Internal structure members count.* To further describe the structure of the battery pack enclosure, the number of internal structural members is included in the classification. This is an index of both the complexity of the structure and how it is optimized to meet the current trends of lowering the number of cell modules, and thus internal subdivisions. The internal members are mainly cross-members, with, in general, a lower number of longitudinal members. A high number of internal structural members indicate a complex design, which may also result in lower energy density due to the increased weight of the enclosure structure. The classes were subdivided into *low* number of internal members with $IS < 4$, *average* ($4 \leq IS < 6$) and *high*, with $IS \geq 6$ corresponding to a complex internal structure.

extra - Field 26. *Battery pack structural complexity index.* This parameter is labelled as “extra” since it is derived by combining information listed from Field 22 to Field 25. The index was elaborated giving different weights to the previously mentioned characteristics in order to combine them into in a single numerical value.

In particular, the following expression was used:

$$StC = \frac{1}{3} \left(\frac{2}{3}AS + \frac{1}{3}MM \right) + \frac{2}{3} \left(\frac{2}{3}IS + \frac{1}{3}PF \right) \quad (3.2)$$

Where:

- AS is equal to 1 if the most abundant material in the pack enclosure is aluminum, and equal to zero otherwise
- MM is equal to 1 if the second most used material accounts for more than 10% of the enclosure mass, making the enclosure a multi-material structure.
- IS is equal to the number of internal structural members, normalized by 12, which corresponds to the higher number of internal structural members found during the analysis
- PF is equal to 1 if a perimetral frame or crash structure is present, zero otherwise

The weighting factors multiplying the previously illustrated parameters were chosen by giving more importance to the aluminum construction among the material complexity compared to the multi-material construction. More importance was then assigned to the internal structure complexity compared to the perimetral frame structure presence or absence. In turn, the structural complexity was accounted as $\frac{2}{3}$ of the total index, being more weighted than the material complexity.

The designed structural complexity index StC was then tested and validated by as-

sessing the consistency of the index results with the actual complexity of the solutions in the available sample. It was possible to divide the solutions into three classes.

- *Simple.* Solutions with $StC < 0.4$ are characterized by a stamped steel structure or a simple aluminum design, with less than four internal structure members (figure 3.18a)
- *Elaborated.* Solutions with $0.4 \leq StC < 0.75$ with a mainly aluminum structure and $4 \leq IS < 6$ (figure 3.18b)
- *Complex.* Solutions with $StC > 0.75$ showing aluminum or multi-material construction, perimetral frame and/or side crash structure and $IS \geq 6$ (figure 3.18c)

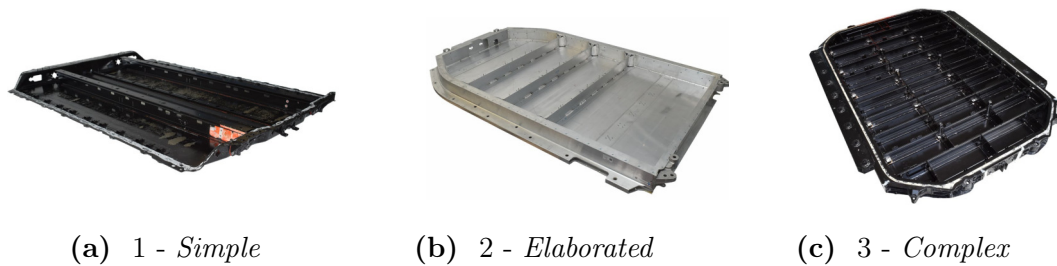


Figure 3.18: Examples of different battery pack lower enclosures [80]

The general trend is to obtain a simpler structure that is still capable of meeting the targeted performance standards, thus the most desirable design is the *simple* one.

Battery Pack and Underbody Integration

This final cluster, shown in figure 3.19, is dedicated to the classification of parameters illustrating the level of integration between battery pack and underbody.

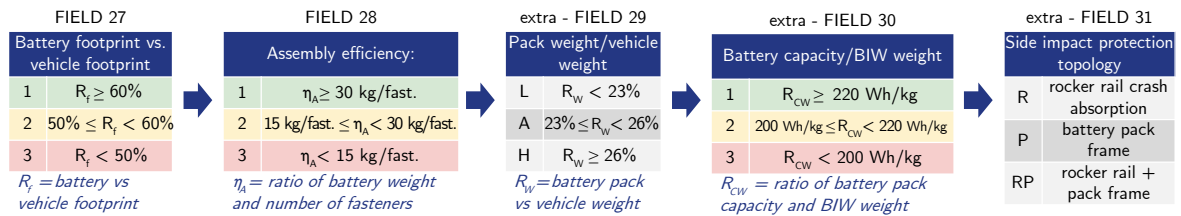


Figure 3.19: Cluster 4 classification scheme, *Integration*

These parameters were selected to provide indexes regarding the size and weight comparison between battery and vehicle, together with assembly efficiency indexes and topology of the integrated lateral side impact structure.

In figure 3.19, the fourth cluster is schematically presented with detailed criteria for class subdivision. In the following, the fields listed in the previous figure will be explained and examples will be provided when necessary.

Field 27. *Battery footprint vs. vehicle footprint.* This parameter is useful to assess the level of exploitation of the central floor by the battery pack. A battery pack with a large footprint will allow to have a lower thickness and thus a center of gravity closer to the ground as well as better vehicle packaging and ergonomics for the occupants. This field is classified into *high* with a ratio between battery footprint and vehicle footprint (evaluated as in Field 6) $R_f \geq 60\%$, *average* ($50\% \leq R_f < 60\%$) and *low* with $R_f < 50\%$, corresponding usually to an underbody which is not optimized for electric traction. Some examples are illustrated in figure 3.20.

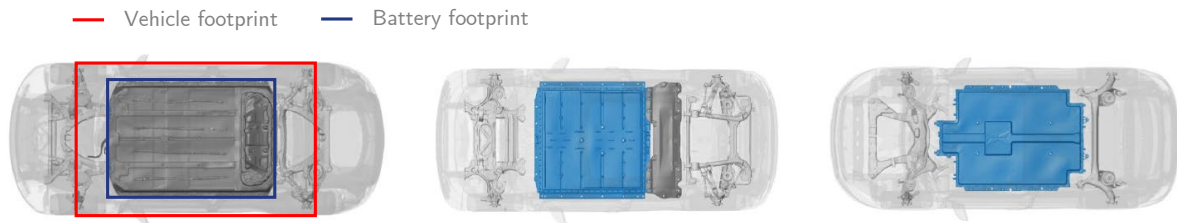


Figure 3.20: Different battery packs compared to the vehicle footprint [44, 24]

Field 28. *Assembly efficiency.* This parameter was evaluated since critical to assess the connection system between battery pack and underbody [24]. This coefficient was computed as the weight supported by each fastener. An efficient connection design implies a high weight per fastener, indicating an easier assembly or maintenance procedure, as well as a more optimized integrated design [24]. Three classes were thus obtained with a *high* assembly efficiency corresponding to more than 30 kg/fastener, shown in figure 3.21a, followed by *average* ($15 \text{ kg/fast.} \leq \eta_A < 30 \text{ kg/fast.}$), reported in figure 3.21b and lastly *low* with less than 15 kg/fast., in figure 3.21c.

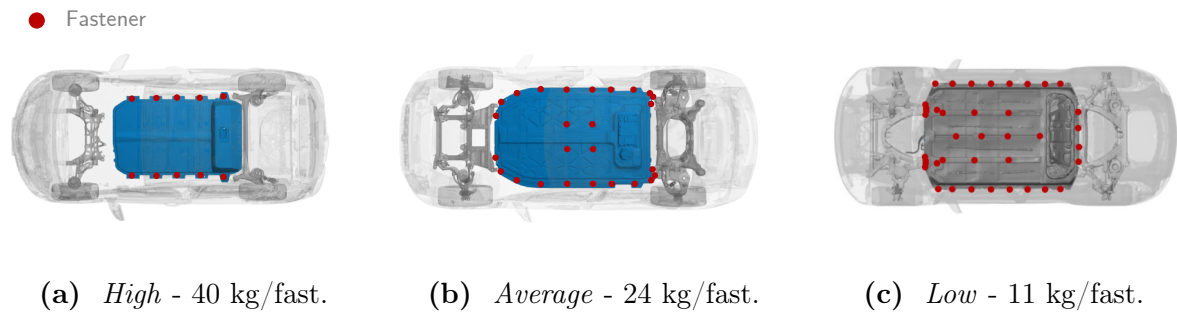


Figure 3.21: Examples of different assembly efficiency [80, 24]

Despite the advantage of higher assembly efficiency, most of the encountered solutions were showing an *average* value of this parameter, indicating that OEMs are favouring a higher number of fasteners, at the cost of a more complex design of the connec-

tions. In general, connections are devised on the perimeter of the pack, as well as in correspondence of the central internal structure and the vehicle floor cross-members.

extra - Field 29. *Pack weight over vehicle weight.* This field compares the battery pack weight to the vehicle curb weight. This information is contained also in previous fields but is still included to give a better insight, as well as to allow separate use of every cluster of the classification scheme. The corresponding classes start from *low*, with the pack accounting for less than 23% of the vehicle weight, *average* from 23% to 26% and *high* reaching more than 26%. Since it is difficult to highlight a clear industry trend or preferred value, this field was classified as *unknown performance output*.

extra - Field 30. *Battery capacity over BIW weight.* This third “extra” field compares the battery capacity in kWh to the weight of the BIW. In general, installing a higher battery capacity on a low-weight battery pack is preferable, since the weight saved on the unibody structure can be exploited increasing the battery capacity and, possibly the vehicle range. Even if the correlation is not direct and it is influenced by other parameters, such as the possible increase of the battery pack weight leading to higher energy consumption, the general industry trend is towards a *high* value of this ratio with $R_{CW} \geq 220 \text{ Wh/kg}$. The second class corresponds to $200 \text{ Wh/kg} < R_{CW} \leq 220 \text{ Wh/kg}$, defined as *average*, and lastly *low* with $R_{CW} < 200 \text{ Wh/kg}$.

extra - Field 31. *Side impact protection topology.* This last “extra” field classifies the integrated side impact protection topology, according to the resulting impact protection structure of the combined battery pack and rocker rail. The first encountered solutions are the *rocker rail* crash absorption structure (figure 3.22a), usually constituted by an aluminum alloy profile, with no particular crash structure on the battery pack. The second solution is constituted by a *battery frame* crash absorption structure, with

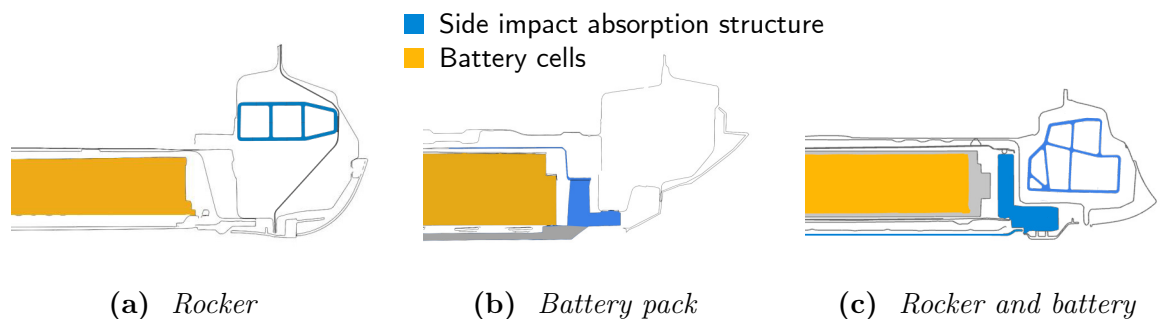


Figure 3.22: Examples of different side-impact absorption structures [24, 80]

a more conventional design of the rocker, shown in figure 3.22b. Lastly, the more complex solution combines the two previous architectures with a side impact absorption

structure both in the battery pack frame and rocker rail, reported in figure 3.22c. From the conducted analysis the most common solutions resulted to be the combined *rocker and battery* crash absorption and the *battery pack* impact absorption structures.

3.3.3 Validation and Examples

After designing the classification scheme, using the first sample of vehicles, it was needed to test its flexibility and adaptability to other vehicles. The scheme was thus applied to six vehicles from the Asian market as anticipated in section 3.3.1. These vehicles presented in some cases a conventional architecture adapted to the electric powertrain, and in other cases a dedicated BEV platform, which showed a high level of technological innovation. The classification scheme was able to adapt and to be efficiently used, delivering results consistent with the actual solution under analysis, also with this new sample of vehicles. The scheme demonstrated to be flexible enough to describe different types of BEVs.

After illustrating the building blocks and the validation procedure of the classification scheme, two examples of the generated code are reported in figure 3.23.

Each field of the classification code has a value with some exceptions. If the field is not applicable a dash “ - ” is inserted, whereas if the information is not available the field presents a “N/A” symbol. Finally, if the field is estimated its value is followed by “ * ”.

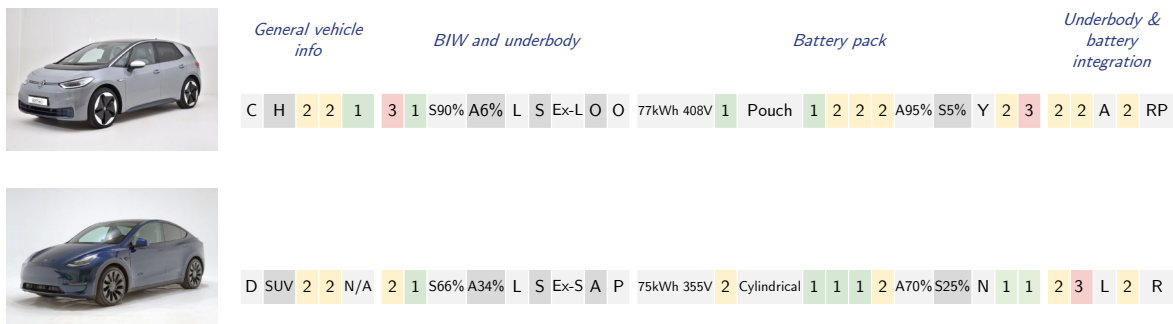


Figure 3.23: Examples of applied classification code. VW id.3 on top and Tesla Model Y on the bottom [44]

From the first part of the code, it is easily visible how the vehicles belong to two different segments and vehicle body shapes. The weight is comparable as well as the driving range and lateral impact safety.

The Model Y shows a lower BIW weight, thanks to the higher use of aluminum. Both are based on a dedicated BEV platform showing large, stamped rocker rails. The Model Y presents a smaller extruded rocker stiffening, while the id.3 shows a wide

extruded internal stiffening. The torque boxes are orthogonal in the case of the id.3 and angled in the front and parallel in the rear for the Model Y.

The battery packs show similar electrical properties but differ in the cells from factor. The Model Y shows a lower number of modules and a better integration efficiency. Both packs are made mainly out of aluminum, but the Model Y shows a multi-material construction since steel accounts for more than 10% of the enclosure mass. The complexity of the id.3 battery pack increases due to the more complex internal structure and the presence of a perimetral crash frame, absent in the Model Y. In the end the id.3 battery pack results having a high structural complexity, while the Model Y shows a low complexity despite the multi-material construction.

For the integration cluster, both show an average battery to vehicle footprint ratio, while the id.3 performs better in the assembly efficiency with a lower number of fasteners. The lightweight construction of the Model Y allows reaching a low pack to vehicle weight and an average battery capacity per BIW weight. Another important difference is the topology of the side impact structure, being a combination of rocker and battery pack for the id.3, with the Model Y relying completely on the rocker absorption.

As previously illustrated the code allows to compare two vehicles, highlighting the key characteristics that differentiate the two solutions, as well as assessing how close the solutions are to the best-in-class in the respective fields.

3.3.4 Future Uses

Concerning the future uses of the scheme, it is important to underline that the class subdivision for the quantitative variables was made based on percentiles. With the advent of new technologies, it will be possible to adapt the classes and tune the subdivisions according to the new benchmarking data.

The modular design of the scheme, based on a first parameters clustering, allows the use of the different blocks together or separately according to the needs of the user. This design allows also to expand the scheme within or across different clusters. For example, the battery pack cluster could be amplified by adding some fields regarding the battery cooling technology or fast charge technology. Additional clusters could be added, describing the electric motor technology and placement as well as the implemented suspension system.

The classification scheme, as currently presented, is focused mainly on the structural aspect and the integration of the two systems under study, underbody, and battery pack. However, the same design methodology can be applied to enlarge the classification to other aspects of the BEV platform as previously illustrated.

The developed tool was used for the next phases of the project as a concept selection

tool, to define the simplified CAD model as well as the parameters on which to focus the analysis and comparisons.

In the future, the classification scheme could also be used as a pure benchmarking and comparison tool, and possibly expanded to investigate the complete design of the BEV platform, from the structural to the powertrain and chassis components.

4 | Model Definition

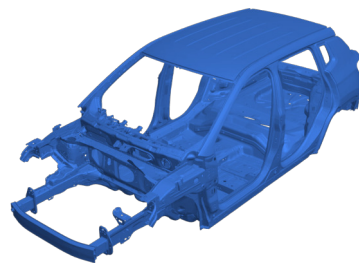
Starting from the results of the benchmarking analysis illustrated in chapter 3, the next step was the definition of the simplified model for FEM analysis.

4.1 Structural Layout and Dimensioning

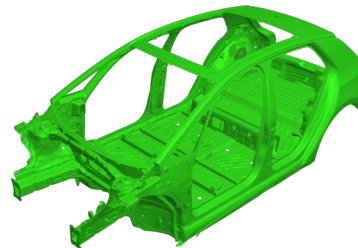
In the following section, the assumptions made to develop the simplified model of the underbody and battery pack are illustrated.

According to the reasoning presented in section 1.2.2 a c-segment SUV was chosen as a guideline to define the global dimensions of the platform model. Since at the moment of the analysis, no benchmarking data were available on compact crossovers, the choice was to dimension the vehicle platform comparing the sizes of a conventional ICEV SUV and a dedicated BEV platform of comparable dimensions. The chosen vehicles were the Jeep[®] Compass and the VW id.3, which showed comparable dimensions and were thus used as a reference.

Furthermore the VW id.3 is based on one of the most recent BEV platforms, and it is considered to be among the best-in-class solutions in this segment [60]. The 3D-scan models of the BIW of the above-mentioned vehicles are shown in figure 4.1.



(a) Jeep[®] Compass BIW [89]



(b) VW id.3 BIW [44]

Figure 4.1: 3D views of the two BIWs used for the general platform dimensioning

The main bounding dimensions are the wheelbase and width of the vehicle, followed by the sizes of the overhang, both in the front and in the rear. These vehicles were

used to also determine the size of the main structural elements of the underbody, e.g.: rocker rails, cross-members, side members and torque boxes. The dimensions of the battery pack are a direct consequence of the space available in the underfloor, thus, fixing the global underbody dimensions set the boundaries for the battery pack size.

After having determined the global dimensions, the first step in the definition of the simplified CAD model was to determine its main structural layout. It was necessary to decide which elements to include and their general topology in order to keep the complexity of the model at a level compatible with the available timeframe.

Figure 4.2 shows an example of the baseline underbody layout with listed the components selected to represent the simplified structure.

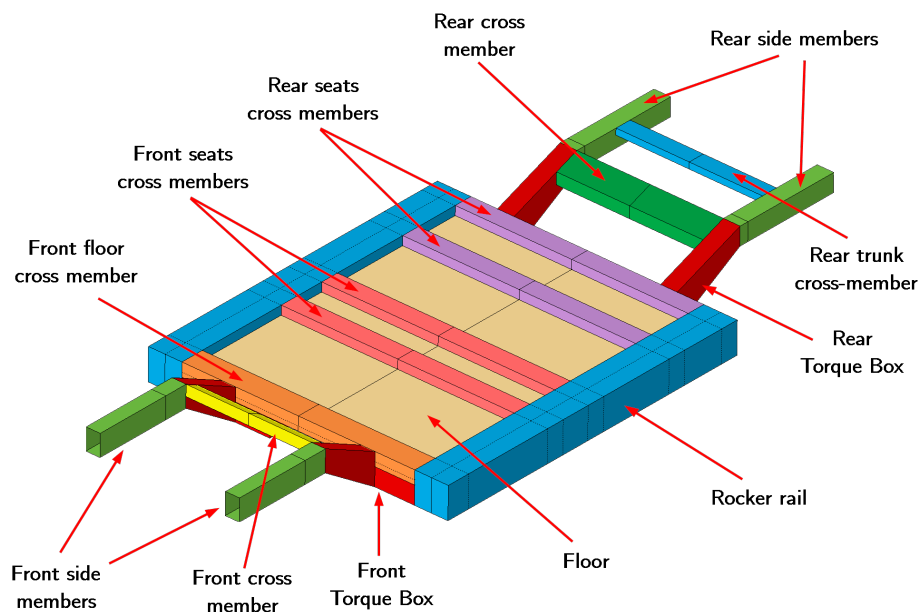


Figure 4.2: Simplified underbody layout

The underbody is structured with the two front side members connected with a front cross-member and linked to the sill through the front torque boxes. The initial design shows orthogonal torque boxes which were easier to model and thus selected for the first modelling and preliminary analysis.

The suspension tower and the firewall are excluded from the model to keep a low complexity and focus on the key components of the underbody.

To link the two sills in the upper part of the floor a front floor cross-member is present. Its shape was modelled as a rectangular profile but could be further optimized for better ergonomics of the driver pedal-box area.

The two rocker rails, constituting a crucial element of the structure, were modelled as a rectangular section beam. Further internal stiffening was designed according to

what was found during the benchmarking analysis. as it will be described in chapter 5.

The central part of the floor was then structured with the front and rear seats cross-members. For what concerns the rear seats structure and cross-members, the design approach is, in general, more various, with different shapes of the cross-members and seats supporting structures. However, this solution was chosen to obtain a flat underfloor that could easily be made modular while keeping a simple design. The floor was then modelled as a flat panel connecting cross-members and rocker rails.

In the following design iterations, an alternate floor was modelled as an embossed panel in order to provide higher stiffness and reduce the low-frequency panels resonance.

Behind the rear seats cross-members, the rear assembly concludes the underbody structure with rear torque boxes, a large rear cross-member, rear side members and a smaller cross-member needed to stiffen the trunk floor and rear region.

The described model is thus restricted to the principal underbody components, without including other panels, pillars and rails which belong to the upperbody.

After defining the general layout, the global dimensions of the underbody and its members were fixed according to the baseline models and the design solutions assessed during the benchmarking analysis. Figure 4.3 shows a drawing of the first design with indicated the characteristic dimensions which were used to size the simplified model.

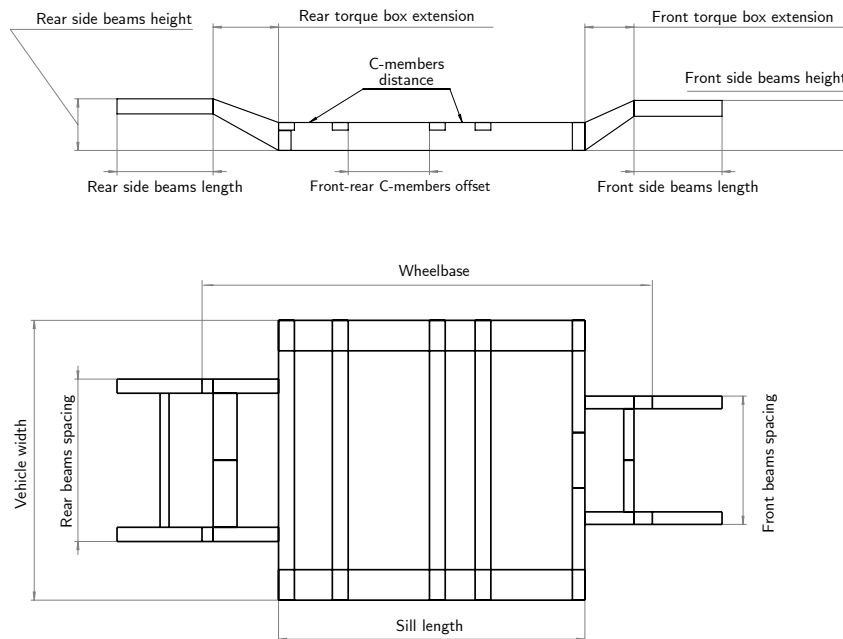


Figure 4.3: Underbody fixed dimensions

Having fixed the dimensions of the wheelbase and vehicle width, the lengths of the different members were determined as well as their positioning in the structure. Being the vehicle width fixed, fixing the sill length determined the space available for the

battery pack in the underfloor. The front and rear cross-members were positioned in correspondence with the connection between torque boxes and side members as found during the comparative analysis. The distance of the side member and the position of the cross-members are determined by crash safety factors and seats positioning [37], thus not distinctive of a BEV platform.

The cross-section of the different members was also fixed and derived from the best-in-class solutions, comparing the different designs and choosing an average dimension that would reflect the current industry trend and possibly the best available solutions.

After determining these dimensions, the space available for the battery pack was bounded. The pack needed to have a clearance of at least 10 mm from the surrounding structures and thus its top view dimensions were constrained by the sills on the sides and the torque boxes longitudinally. It was chosen to model a battery pack capable of housing battery cells for a total capacity C of 81 kWh with a pack gravimetric energy density $\rho_g = 180$ Wh/kg and a volumetric energy density $\rho_v = 245$ Wh/litre. These values represent a best-in-class solution and are not yet reached by many OEMs. However, according to the future short-term technological developments, these energy densities will be more common on the battery packs market [22].

Fixing these figures led to the following battery pack weight and volume:

$$W_p = \frac{C}{\rho_g} = 450 \text{ kg} \quad V_p = \frac{C}{\rho_v} = 0.33 \text{ m}^3 = 330 \text{ l} \quad (4.1)$$

The battery pack thickness is thus the last of the pack dimensions to determine:

$$T_p = \frac{V_p}{w \times l} \quad (4.2)$$

Where the pack width w and length l are constrained by the underbody and the clearance needed between battery pack and underbody structures, as previously explained.

Having determined the global dimensions of the battery pack it was possible to define its general layout and sizes which are reported in figure 4.4.

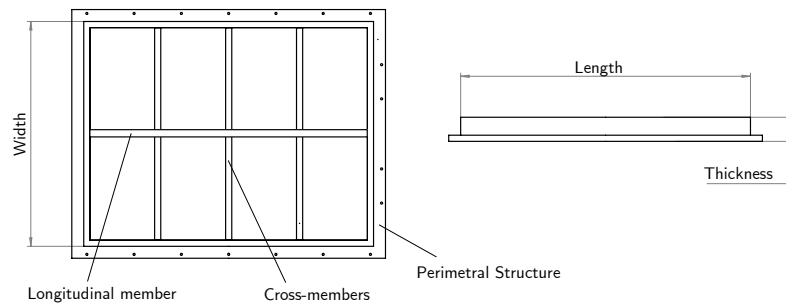


Figure 4.4: Battery pack layout and dimensions

The shape of the pack was kept as simple as possible, being inspired also by some of the analyzed solutions which preferred a simple and modular design to a more complex and optimized one. Since not influential for the scope of the project the exploitation of the volume underneath the rear seats was not considered.

The initial pack design is constituted by a predominantly parallelepipedal shape with a lower perimetral frame and internal structure with cross and longitudinal members. The structure is then completed by the top and lower plates to enclose the battery cells. Further designs variations were then derived and will be illustrated in chapter 5.

4.2 CAD Model Development

After fixing the dimension of the structure the first design was modelled through CAD software SolidWorks[®]. The model dimensions were parametric and driven through an external file, so to make the model easier to edit for future works.

The model of both structures under analysis is based on simple rectangular section profiles. No, complex section shapes were modelled to make the model coherent with the simplified structural layout without loss of generality.

The modelling technique was dictated by the need of having a suitable model to facilitate the following DOE phase. It was planned to run multiple repetitions with the necessity of meshing and setting several FEM models with few available automation procedures.

The model was thus designed as a surface and not solid model, to avoid complex mid-surfaces extraction and geometry cleanup during the meshing phase. Rails and cross-members were modelled as the external surfaces of the components so that changing their thickness would not affect their external dimension.

Figure 4.5 shows a 3D view of the first iteration of the underbody design, characterized by orthogonal torque boxes.

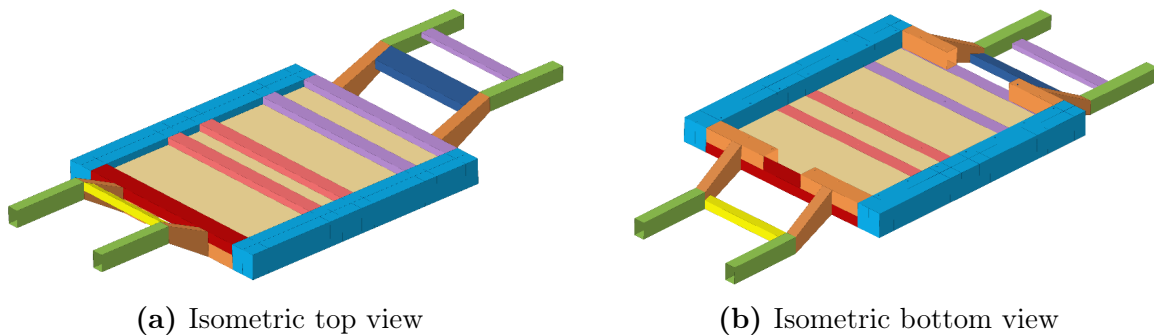


Figure 4.5: Underbody model, first design

In figure 4.6 the battery pack is visualized with a simple flat-box design, characterized by a perimetral frame and a complex internal structure.

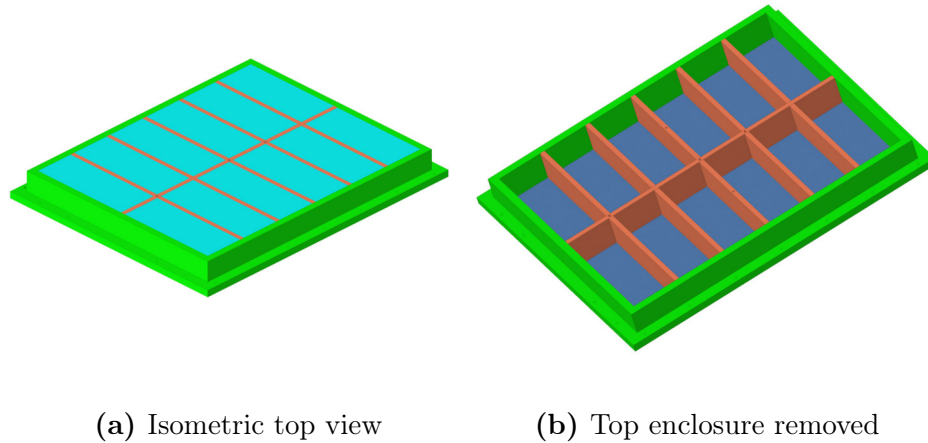


Figure 4.6: Battery pack model, first design

To integrate the two systems under analysis, holes were designed in the battery pack perimetral frame to connect it to the rockers and torque boxes, and, in the internal structure members, to have a connection to the floor cross-members, being these the stiffer regions of the vehicle floor. The connection scheme was designed with 22 fasteners along the perimeter of the pack, four at the front and at the rear, with the remaining 14 along the sides, and additional five internal connections, three in correspondence of the longitudinal member and two on the central cross-member.

The battery pack and the underbody models were then included in an assembly so that, if needed, it was possible to hide one of the two components and import them separately in the FEA software, while still maintaining the same reference frame.

4.3 FEM Model Development

Once having defined the geometry, the FEA workflow was defined. The analysis was conducted through the software Altair[®] HyperWorks[®], which integrates the pre-processor Altair[®] HyperMesh[®], the structural solver Altair[®] OptiStruct[®] and the post-processor Altair[®] HyperView[®].

In what follows the used workflow is described for the baseline model. The same process was then applied to the next design variations.

4.3.1 Geometry Cleanup and Meshing

The designed underbody and battery pack geometry are imported into two separate projects in the Altair[®] HyperMesh[®] environment to proceed with the geometry cleanup.

Since the model is meant to represent a simplified, preliminary design, welds and bonding connections were not modelled but the geometry was made continuous by stitching the surfaces and edges in correspondence of these connections as shown in figure 4.7a. This allowed also to simplify the analysis setup, which was crucial due to the large number of FEM models to be developed in the next DOE.

In this way, the mesh was continuous throughout the different structural components. Despite not representing the real structure connections this solution was used since suitable for the preliminary development phases and especially since the goal is to compare different solutions built using the same technique. This stitching procedure eliminates overlapping surfaces, which again, is not always the case in the real industrial application but was adequate for the scope of the analysis.

To simplify the meshing procedure, and assure to obtain a symmetrical mesh, the geometry was split longitudinally along the mid-plane as illustrated in figure 4.7a. The symmetrically split geometry was then organized according to the different components, to which different material and thickness properties were then assigned. An analogous technique was used for the battery pack geometry. The results of these first two steps are shown in figure 4.7.

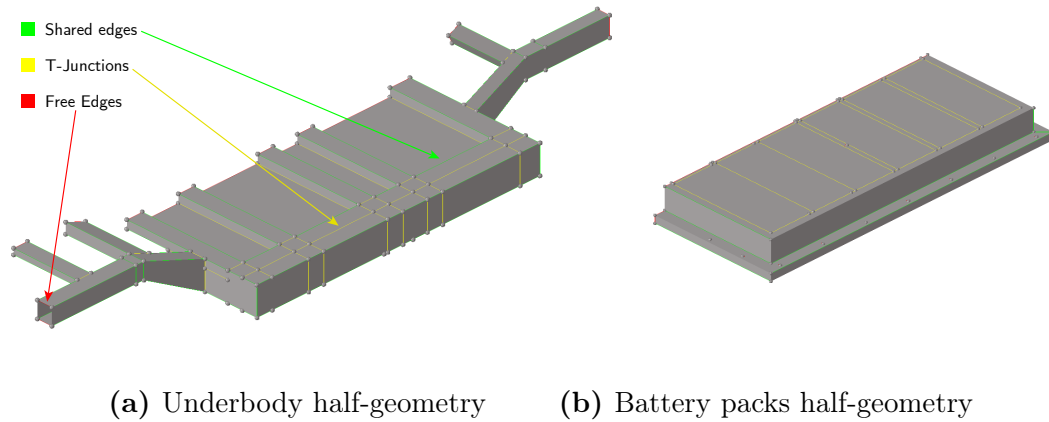


Figure 4.7: Split geometry with stitched edges

The two half-structures were meshed using the BatchMesher function which allowed to discretize the model and perform automatic mesh quality optimization. The software allows also to automatically recognize holes and build concentric elements washers for better meshing of low-radius holes. This led to a good overall mesh quality with homogeneously sized elements, a limited number of triangular elements, and with good aspect ratio. The software was used with the default parameters since these delivered satisfying results.

Given that both structures are constituted by thin stamped metal sheets or thin extruded components, the 2D shell elements were selected. The analysis investigates

deformations and modal resonance, and no stress evaluation was conducted. Thus, it was sufficient to use first-order elements [90]. The mesh was performed using a mixed elements type, meaning that CQUAD4 quadrilateral elements were preferred and CTRIA3 triangular elements were used for mesh transition in complex, variable geometry regions [90]. The percentage of triangular elements was constrained to 15%, but thanks to the simple geometry, the resulting mesh was predominantly quadrilateral with only 0.5% of CTRIA3 elements. Using just half of the geometry allowed to reduce the meshing time by approximately 50%.

Successively a mesh convergence analysis was performed to assess the mesh size as a trade-off between accuracy and computational time. The analysis was conducted using 20 mm, 10 mm, 5 mm, and 3 mm elements. Table 4.1 shows the obtained results for the different configurations and the percentage of discrepancy with respect to the densest 5 mm mesh, considering the torsional load case.

The simulation with a 3 mm mesh is listed as failed since could not run on the available machine; the complexity of the model was too high for the computational capabilities of the used computer.

Table 4.1: Mesh convergence analysis

Element size	No. of elements	CPU time	Percentage discrepancy
20 mm	5.72+E04	87 s	5.4%
10 mm	2.24+E05	455 s	0.6%
5 mm	8.74+E05	2648 s	-
3 mm	2.22+E06	Failed	-

The used machine was a laptop with an Intel[®] quad core processor i7-6700HQ and 16 GB of RAM, no additional software was running together with the finite element solver. Considering the other conducted simulations, it was possible to assess that the 10 mm mesh size was able to deliver good results for what concerns accuracy, using almost one-sixth of the CPU time of the 5 mm one. According to the obtained results, the convergence trend visible in figure 4.8, and the available literature, the choice was to use 10 mm elements [90, 63, 91].

This choice allowed to achieve a good accuracy while still maintaining a reasonable computing time, which, given the multiple iterations to be conducted, needed to be kept under control.

To keep the effective external section of the different members constant when changing the elements thickness, the thickness was assigned inwardly instead of symmetrically across the meshed surface. This led to a slight mass overestimation due to elements

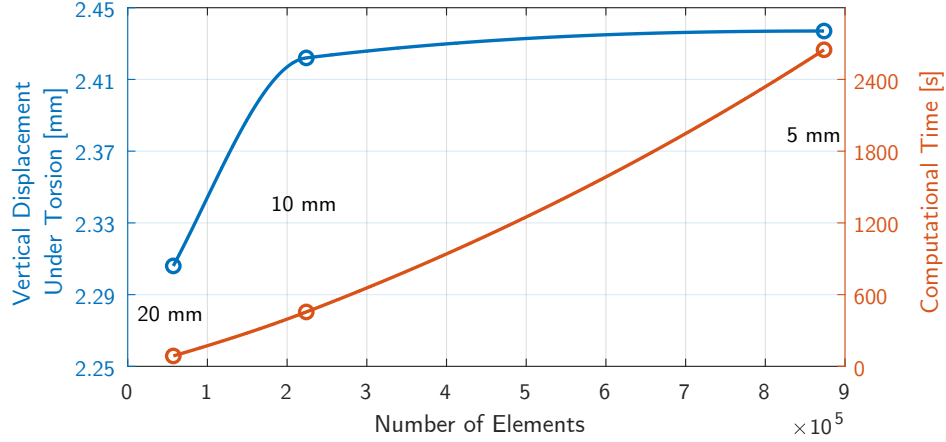


Figure 4.8: Convergence of torsional displacement and increase in CPU time in function of the elements size

overlapping in correspondence of the corners, which however was comparable in the different analyzed solutions, thus acceptable for the comparative analysis.

To conclude, the most relevant mesh characteristics and quality indexes are reported in table 4.2.

Table 4.2: Mesh characteristics and quality indexes

Element family	Element type	Element size	No. of elements	% of trias
2D Linear shell	CQUAD4 & CTRIA3	10 mm	2.24+E05	0.50%

The following step was to model the cells mass. The battery cells were not included in the model, but their mass was modelled as point masses distributed across the lower plate. Supposing an *high* gravimetric integration of around 66.6%, starting from the estimated battery pack mass of 450 kg the equivalent cells mass can be evaluated by:

$$\eta_g = \frac{\rho_{pack}}{\rho_{cell}} = \frac{m_{cells}}{m_{pack}} \quad \text{from which} \quad m_{cells} = \frac{\rho_{pack}}{\rho_{cell}} m_{pack} = \eta_g m_{pack} \quad (4.3)$$

Which results in a total cells mass of 300 kg. This mass was simulated by applying point masses CONM2 corresponding to $\frac{300 \text{ kg}}{\#nodes}$, where $\#nodes$ corresponds to the total number of nodes in the lower plate. The derived point masses were then applied in correspondence of each node of the half mesh of the lower plate.

The final step of the meshing process was to connect the battery pack structure to the underbody. This connection was devised by simulating a bolted connection by M10 bolts, which from the conducted benchmarking analysis resulted to be the most used fasteners. At first RBE3 “rigid elements” were created in correspondence of the holes of the battery pack and underbody, so to generate a new node in the center of each

hole. The RBE3 elements were chosen in order not to introduce excessive stiffness and obtain a more realistic model of the connection [92]. The fastener was then modelled with a circular section beam element with a 10 mm diameter section connected to the respective central “dependent nodes” of the RBE3 elements. An example of the simulated fastener is shown in figure 4.9.

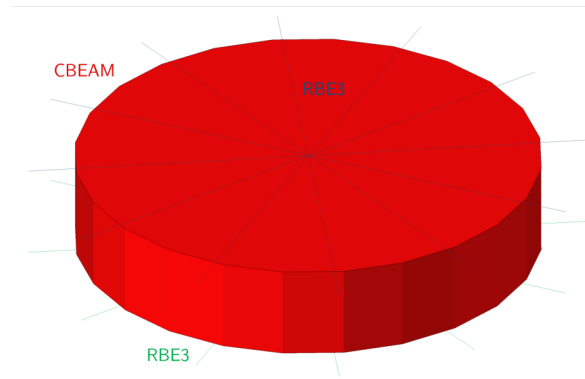


Figure 4.9: M10 bolted connection modelling

The obtained mesh of the two systems was then mirrored in order to obtain the complete, symmetrical mesh of the structure, in order to apply the non-symmetrical loading conditions.

4.3.2 Material Model

The materials were chosen according to the results obtained from the benchmarking analysis, which showed an industry trend to switch towards steel-intensive structures but still using aluminum alloys for some structures. The study of FRP was for the moment excluded from the analysis, but may be relevant for some weight critical components, as well as for crash absorption [86].

For both materials, a linear elastic, isotropic and temperature-independent model was chosen, corresponding to the MAT1 material model. Since the materials are homogeneous and isotropic, to describe the elastic properties it is sufficient to define the Young modulus E and the Poisson’s ratio ν . In addition to these properties, to evaluate the mass of the structure it was necessary to specify the material density. Since the scope of the analysis was to investigate the deformations and resonance frequencies the needed parameters were limited to the above-mentioned elastic properties.

In table 4.3 the selected materials properties are reported.

The choice was to use general steel and aluminum alloys properties, since selecting of a specific type of alloy is out of the scope of the study and the elastic properties are slightly dependent on the alloying elements but mainly on the principal metallic material [93].

Table 4.3: Steel and Aluminum alloy materials properties

Property	Steel	Aluminum alloy
E [GPa]	210	70
Poisson's ratio	0.3	0.33
Density kg/m ³	7850	2700

4.3.3 Load Cases and Outputs

To assess the stiffness and the resonance frequency of the integrated system, the following FEM analyses were conducted:

- *Static analysis.* The linear static analysis was conducted by applying bending and torsional load to assess the resulting displacements and evaluate the corresponding values of bending and torsional stiffness.
- *Dynamic analysis.* The dynamic analysis was performed to assess the first three modal resonance frequencies of the integrated underbody-battery assembly, with particular attention to the 1st.

According to what expressed in section 2.2.1 a range for the desired performance outputs was established:

- *Torsional stiffness.* Being the analysis restricted to the only underbody the torsional stiffness values are expected to be up to one order of magnitude lower than the complete BIW stiffness. The expected stiffness is thus in the order of 200 kNm/rad [36]
- *Bending stiffness.* A similar reasoning is valid for the bending stiffness. However, it was difficult to find in the literature values related to the underbody-only bending stiffness. In this case, the structure under analysis is expected to show performances slightly lower than the complete BIW, in the order of 10 kN/mm.
- *First resonance frequency.* For the dynamic performances it is crucial to avoid the excitation of suspensions resonances, usually in the range 15-20 Hz, and cabin cavity resonances, in the ranges 50-70 Hz and 120-140 Hz. Thus, the first mode resonance frequency should be higher than 40-45 Hz and avoiding resonance of the cabin panels in the previously mentioned critical cabin ranges [36, 41].

In the following, the loading scheme and boundary conditions of the different analyses are explained in detail.

Torsion Load Case

Due to the lack of detailed suspensions attachments points in the simplified model, the constraints were applied on the front and rear side members in correspondence of the wheel hub so that the distance from the front and rear constraints corresponds to the vehicle wheelbase. To apply the constraints, four RBE3 elements were created in the corresponding section of the side members. The load and constraints were applied in the newly generated dependent nodes of the “rigid elements” as shown in figure 4.10a. RBE3 elements were chosen in order not to induce the over stiffening caused by RBE2 elements [92].

To obtain an isostatic constraining scheme while applying the torsional load, the boundary conditions were imposed as described in figure 4.10b.

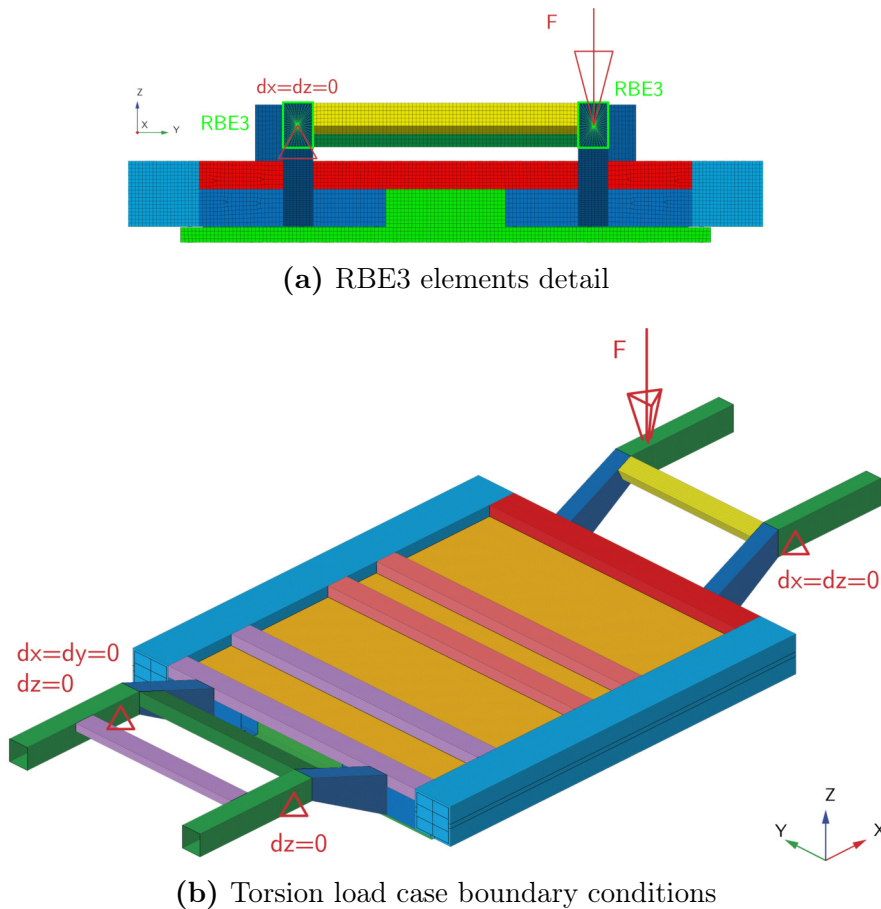


Figure 4.10: Torsion loading scheme

In detail, the rear constraints are limiting all displacements on one side and the vertical displacement on the other side. This allows the rear section of the underbody to rotate around the y axis. In the front, the constrained end is limited in vertical displacements along z-axis and longitudinal displacements along the x-axis. All rota-

tions were left free in order to obtain the isostatic constraining. A load equal to 1 kN was then applied on the remaining free end allowing thus the structure to rotate by deforming around the x-axis [39]. The magnitude was not determinant for the analysis since the desired output was the stiffness, thus comparing the deformation to the applied load without assessing stresses.

It was important to verify that the local deformations in correspondence of the RBE3 elements were negligible when compared to the global deformation. The hypothesis was confirmed meaning that the constraining scheme through the RBE3 elements was effective.

From the analysis, the vertical displacement Δz in correspondence of the load application point was evaluated. To assess the torsional stiffness, it was necessary to evaluate the angular displacement $\Delta\theta$ by knowing Δz and the horizontal distance between the force application point and front constraint, corresponding to the arm of the force l .

$$\Delta\theta = \tan^{-1} \left(\frac{\Delta z}{l} \right) \quad (4.4)$$

With the derived $\Delta\theta$ displacement, it was then possible to evaluate the torsional stiffness K_t as a ratio of the applied torque T and $\Delta\theta$ [94]:

$$K_t = \frac{T}{\Delta\theta} = \frac{Fl}{\tan^{-1}(\Delta z/l)} \quad (4.5)$$

Bending Load Case

For the bending load case, the constraints were applied by using the same RBE3 elements created previously. In this case, four hinge constraints were applied in correspondence of the four extremities of the structure. The hinges constrained all three displacements while allowing the rotations. The constraint, in this case, is hyperstatic but permits to devise a body constraining scheme that allows it to be hinged along two axes in correspondence of the front and rear axles.

A vertical load F of 1 kN was then applied on both sills at the mid-span of the wheelbase. As previously, also in this case, the magnitude of the force was not determinant for the scope of the analysis.

To apply the bending load, it was critical to avoid excessive deformations in correspondence of the force application point and constraining regions. The constraints were applied, as done for the torsion load case, through the modelled RBE3 elements, which were again effective in avoiding too significant local deformations.

However, applying the vertical load through an RBE3 element located in the rocker cross-section, resulted in too large, localized sill deformations, which could negatively

affect the correctness of the stiffness evaluation. It was thus chosen to apply the load through RBE2 “rigid elements” located in the lower part of the sill as shown in figure 4.11a. This method is also similar to the procedure used in real testing in which the sill is stiffened in the loading point, to avoid local deformations. The RBE2 element was constructed in the lower part of the rocker so that the force was spread on a larger surface and applied at the mid-span of the wheelbase, as shown in figure 4.11b.

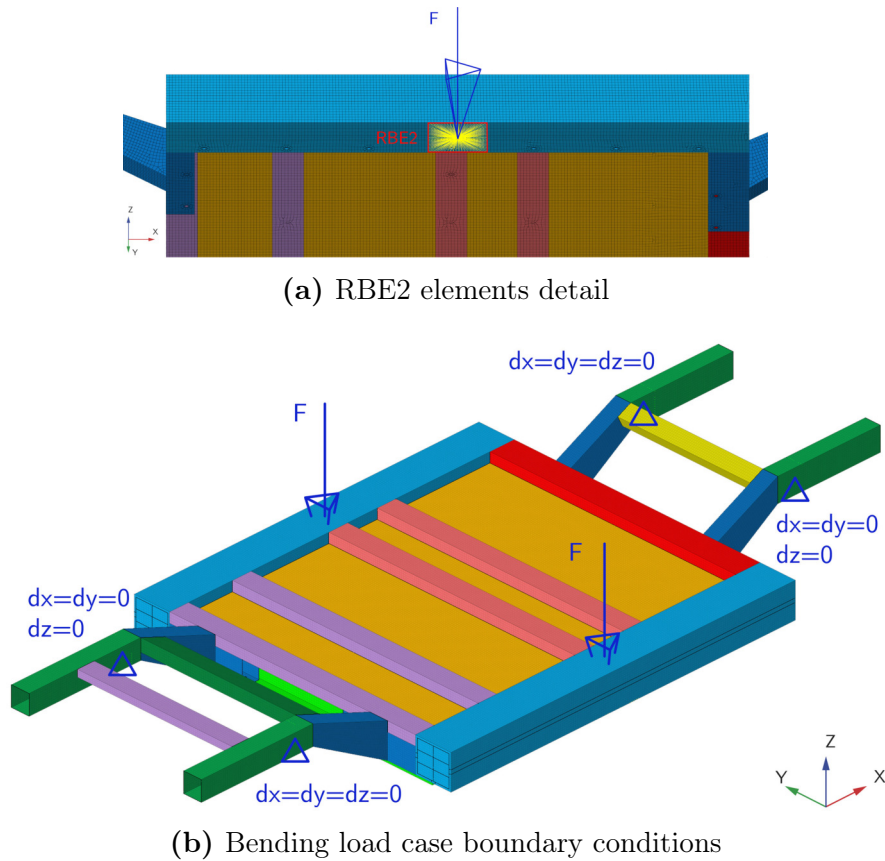


Figure 4.11: Bending loading scheme

From the analysis, the vertical displacement Δz , in correspondence of the force application point, was derived. From this, it was possible to obtain the bending stiffness as:

$$K_b = \frac{2F}{\Delta z} \quad (4.6)$$

Modal Load Case

For what concerns the modal analysis, a so-called “Free-Free analysis” was conducted, meaning with no constraints or loads being applied. This type of analysis was selected to understand the modal behaviour of the unconstrained structure, as in the common

practice of the industrial partner. Since the structure is not constrained the first modes correspond to the six rigid body modes, usually with resonance frequencies close to 0 Hz. Being these modes not meaningful it was necessary to exclude them from the analysis by setting the minimum frequency of the analysis at 1 Hz [95]. Thus, the first three modes above 1 Hz were extracted and evaluated to assess the general behaviour of the structure. However, for the scope of the analysis, the main output of the analysis was the first resonance mode, since the most relevant for the vehicle dynamic performances to avoid coupling with the suspensions resonance [36].

5 | Design of Experiment

In order to assess the influence of the different design choices, it was necessary to systematically compare and analyze various designs. At this aim, a DOE was conducted and the most influential variables were highlighted.

Experimental design is the process of developing a structured experimental approach to identify the effect of one or more factors on a specific output of interest, called response. In other words, for the scope of this study, the DOE aims at collecting the most information regarding the different factors and their influence on the system performance with the least number of experiments possible.

Given the input factors, these need to be considered at different values or levels to assess their influence on the different outputs and understand the values leading to the best results [96].

The goal was to gain a better understanding of the critical parameters in the design of this new type of platform, especially for what concerns the structure static and dynamic stiffness, to establish preliminary design guidelines.

In the following, the design steps that led to the final DOE are explained in detail, starting from the definitions of the design space.

5.1 Design Space Definition

The first step for the experimental design phase was to determine which factors to include and at which levels to consider them, thus determining the design space.

To proceed with the definition of the design space, the results from the benchmarking analysis and classification scheme developed in chapter 3 were used to decide the variables on which to focus the investigation.

The following sections analyze the geometrical variations of the design, the material choices and in the end, the final restricted design space is presented.

5.1.1 Geometry and Layout Variations

Several different designs are implemented in the industry, with largely different interpretations of the shapes of different components and their layout. A key element for an effective investigation is to choose the parameters to investigate following all the available prior knowledge, to limit the number of variables to be studied.

At this aim, the benchmarking analysis was used to highlight the most common solutions and their differences. This allowed to select and reproduce the most relevant design variations, keeping the model simple and limiting the study to a manageable number of model configurations.

Fixed Parameters

To simplify the DOE some geometry parameters were kept fixed. The global vehicle dimensions were chosen and fixed as illustrated in section 4.1. At the same time, the section dimensions of the different rails, beams, and cross-members were fixed according to the results obtained from the previous analysis and the measurements obtained by analyzing the 3D models of the studied vehicles. This step was necessary to restrict the design space and limit the number of experiments to be conducted since limited automation is possible for the conducted analysis.

However, the CAD model was designed to be fully parametric, and, with equation-driven dimensions, it would be possible to easily obtain new models and investigate the effect of different component sizes.

Underbody Geometry

The underbody model illustrated in figure 4.2 from chapter 4 consists of 12 main components. These components were deeply analyzed in the benchmarking analysis in order to select the ones which present the more disparate design interpretation, which is in general an index of a highly influential component. In table 5.1 the underbody components are listed for reference, together with their observed variability across the investigated solutions.

For what concerns the front and rear side members, their main function is to sustain the load from the suspensions attachments points and absorb frontal and rear impact energy. These structures did not show particular geometrical differences when compared to the traditional design for ICEV, thus were excluded from the restricted design space.

The front cross-members showed different designs for its cross-sections, but higher variabilities were found in the used material thickness as reported in the following

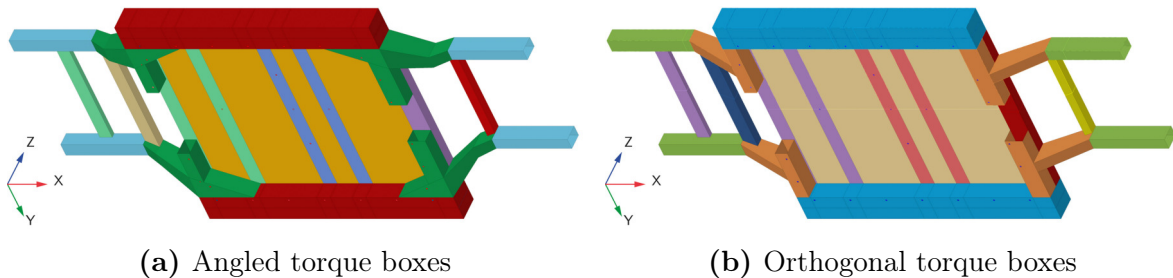
Table 5.1: Underbody components geometry variability

Component	Geometry Variability	Type
Front side members	Low	-
Front cross-member	Medium	Cross-section
Front torque-boxes	High	Shape
Rocker rails	High	Internal stiffening
Front floor cross-member	Medium	Cross-section
Front seats cross-members	Low	-
Floor	Low	-
Rear seats cross-members	Medium	Shape
Rear torque-boxes	High	Shape
Rear cross-member	Medium	Cross-section
Rear side members	Low	-
Rear trunk cross-member	Low	-

section. Thus, the geometry of this structure was kept fixed, and its dimensions were chosen from the reference vehicles.

The front torque boxes were found to have several different interpretations which can be grouped into *angled* and *orthogonal* torque boxes.

The rear torque boxes showed three different solutions, *parallel angled* and *orthogonal*. Since these structures emerged to be highly variable, two different torque boxes designs were implemented, based on the dimensions available from the benchmarking. Front and rear torque boxes were modelled as *angled* and *orthogonal*, shown respectively in figures 5.1a and 5.1b.

**Figure 5.1:** Modelled geometries for front and rear torque boxes

This choice was driven by the similarities between *parallel* and *angled* rear torque boxes and to allow to have the same topology of torque boxes at the front and the rear. The torque boxes integrate also a split cross-member both in the rear and the

front, which is connected by the cross-members in the upper floor and will be further interconnected by the battery pack when installed. Having a split cross-member allows easier installation of cables and pipelines for battery recharging, cooling and power delivery.

The rocker rails showed different cross-sectional shapes, construction, and dimensions (see figures 3.14 and 3.15) with the main structure usually being made of stamped panels. The external section was kept constant, using a *large* cross-section of 190 mm \times 175 mm. This section may be overdimensioned but is in line with the current trend of using large cross-sections to have a modular platform able to adapt also to larger vehicles.

A deeper investigation was conducted instead on the internal stiffening of the sill structure. Two main solutions were found from the comparative analysis: stamped, and extruded stiffening. To limit the number of designs to analyze, the most common solutions were chosen: *large extruded-stiffening* and *open section stamped-stiffening*.

The *large extruded-stiffening* was modelled to occupy most of the internal section of the sill as shown in figure 5.2a, with elements connecting the internal structure to the external one by making it a continuous mesh. Usually, the connection is derived through structural adhesives, but to simplify the model, the geometry was stitched and the mesh was made continuous. The stiffening section is a simplified version of the ones found during the previous analysis, shown in figure 5.2b.

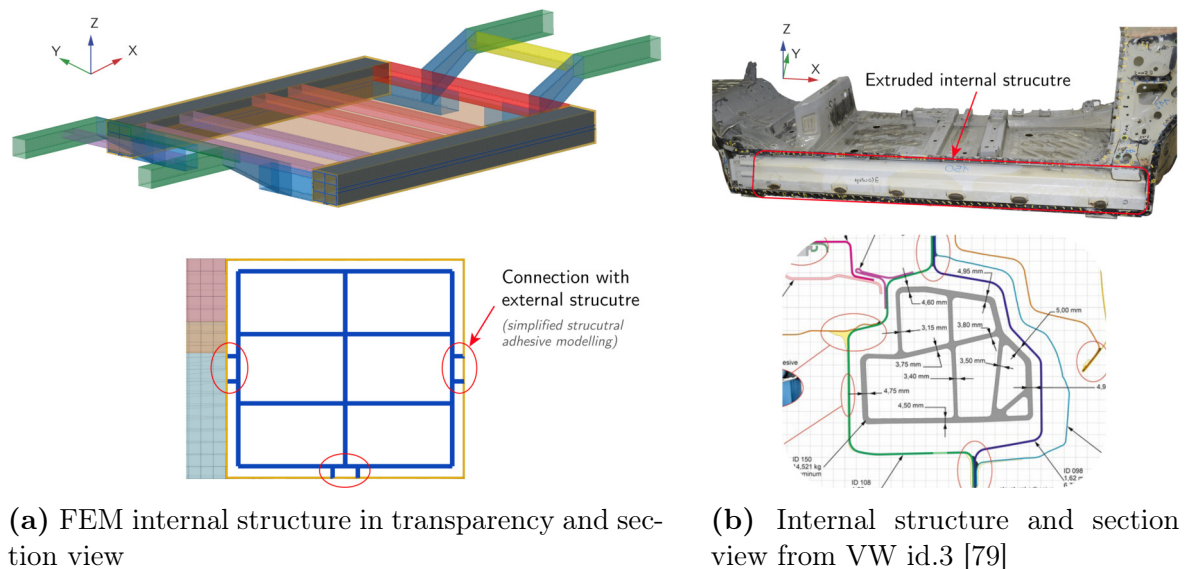


Figure 5.2: Extruded internal rocker structure, CAD, and real implementation

For the stamped stiffening a vertical septum was created in the middle of the section, as shown in figure 5.3a. The sill was also reinforced by adding stiffening sections in

correspondence of the seats and torque box cross-members. This solution was inspired by what was found during the investigation of the Honda e, which has stiffening ribs in correspondence of the cross-members connections (see figure 5.3b).

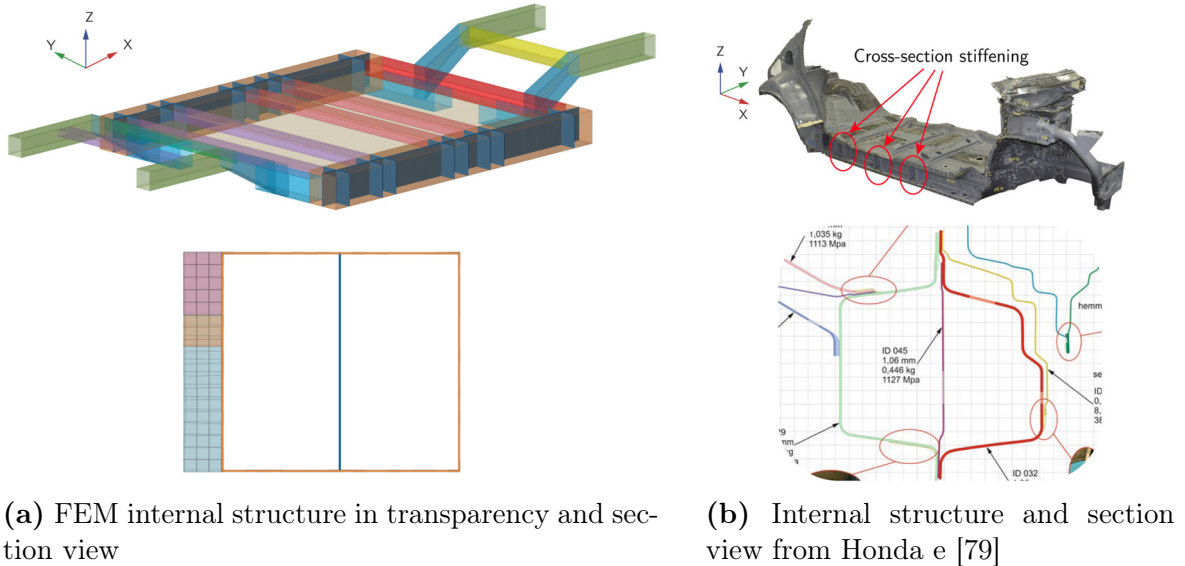


Figure 5.3: Stamped internal rocker structure, CAD, and real implementation

For what concern the front floor cross-member its cross-section was quite variable, but in this case was kept fixed since it needs to be optimized taking into account the driver and passenger ergonomics, which was excluded from the current study.

The front seats cross-members were similar across the various solutions, both for dimension and positioning. This element was thus designed according to the available information and kept fixed.

In a similar way it was done for the rear seats cross-members which showed higher variability in shape. The choice was however to follow a simple design to keep the structure simple and more modular. The support for the rear seats bench is not integrated into the underbody, allowing higher flexibility for the interior design.

The floor showed uniform solutions and was initially modelled as a flat surface. Its design was successively improved by adding embossing to improve the NVH performances. This type of embossing is already quite diffused in the industry but the flatter floor of the new BEVs makes these solutions more important to avoid wide thin-panels resonance.

For the rear cross-member, the reasoning was analogous to the front one, thus its section and shape were kept constant.

To conclude, the rear trunk cross-member was designed according to the reference vehicles since not many changes are needed in this area for the new BEV platforms.

Battery Pack Geometry

The battery pack geometry illustrated in figure 4.4 from chapter 4 consists of four main components. These components were studied in the benchmarking analysis to select the ones on which to focus the attention. Two main different approaches were found in the enclosure design, a lower enclosure with a perimetral frame or a lower tray enclosure, with no perimetral frame. Additionally, the internal structural members were highly variable across the different solutions. In table 5.2 the battery pack components are listed for reference, together with their observed variability across the investigated solutions.

Table 5.2: Battery components geometry variability

Component	Geometry Variability	Type
Lower enclosure	High	Shape
Internal cross-members	Medium	Count and cross-section
Internal longitudinal members	Medium	Count and cross-section
Top enclosure	Low	-

The lower enclosure, as anticipated, showed a high geometry and layout variability, with two opposite solutions showing a perimetral structural and crash absorption frame and the second showing a simpler tray lower enclosure with no lateral crash absorption structure (see figure 3.18 for reference). Two models were thus derived with perimetral frame and with tray structure.

Additionally, due to the different shape of the torque boxes, it was necessary to adapt the battery pack shape to fit in the variable underfloor shape (figure 5.1). Thus, a model with a simpler rectangular top view shape and one with a chamfered shape were designed. Four different lower enclosures were designed as shown in figure 5.4.

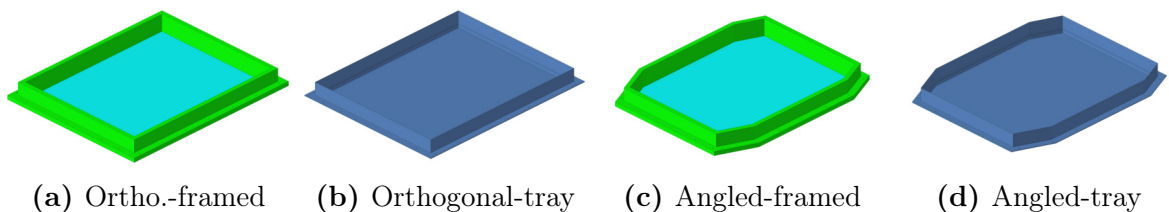


Figure 5.4: Modelled lower battery pack enclosures

For all the different enclosures the focus was on the variation of the main shape, thus the cross-sections of the frame and the tray were kept fixed.

For what concerns the internal structure, the longitudinal and cross-members were variable both in cross-section and in count. Following the previous reasoning, the cross-section variability was not analyzed, and instead, the number of cross-members and longitudinal members was changed to assess the influence of the internal structure on the system performance.

The choice was to insert either one or no longitudinal members and five or no cross-members to assess how these poles apart solutions would perform. In detail, four solutions were derived, showed as an example in figure 5.5 in the orthogonal-framed lower enclosure.

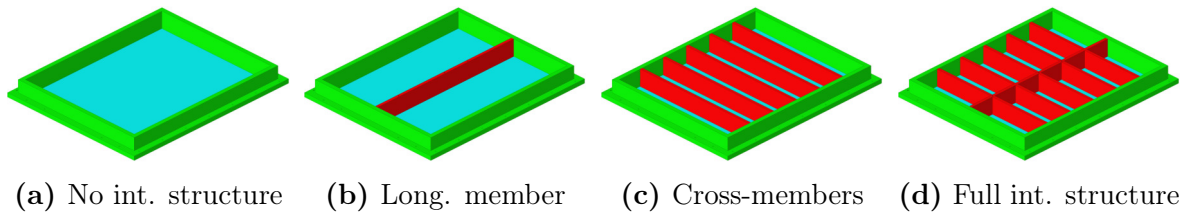


Figure 5.5: Modelled variations of internal structure

The presence or absence of the internal structure members also affected the connection scheme, which with the complete internal structure, had five additional connection in the central part of the floor.

In the end, the top enclosure was modelled as a simple flat panel, since slightly variable across the analyzed battery packs. Its design was successively improved by adding embossing to improve the NVH performances.

5.1.2 Material Properties Variations

For what concerns the material properties, a separate analysis was conducted to assess which materials are used in current BEV for the components under analysis, as well as their thickness.

Underbody Materials

It is important to note that most of the analyzed BEVs showed a steel-intensive underbody, with few being aluminum-intensive and most of them showing the application of aluminum in some elements.

The process of choosing the material for the different components started thus by analyzing which components could be made of aluminum for lightweighting. This choice was driven both by the results of the benchmarking analysis and the outcomes of the study from Park et al. [64] illustrated in section 2.3.1.

The second step was to analyze the thickness variation. Since aluminum was found in few applications, there were not enough data for a meaningful evaluation and thus this analysis was focused on the steel-based components. The thickness of the various elements was sampled from [79], to highlight the components which show the higher variability in thickness and select those for the parametric investigation. To assess the degree of variability the Relative Standard Deviation (RSD) was computed for the thickness of each underbody component j :

$$\text{RSD}_j = \frac{\sqrt{\frac{1}{N-1} \sum_{i=1}^N (t_{i,j} - \bar{t}_j)^2}}{\bar{t}_j} \quad (5.1)$$

This value is obtained for every component j by evaluating the standard deviation of the thickness and dividing it by the average of the thicknesses of the analyzed component j . This allowed to compare the variability of the thickness for the different underbody elements. The results of the analysis are reported in figure 5.6¹.

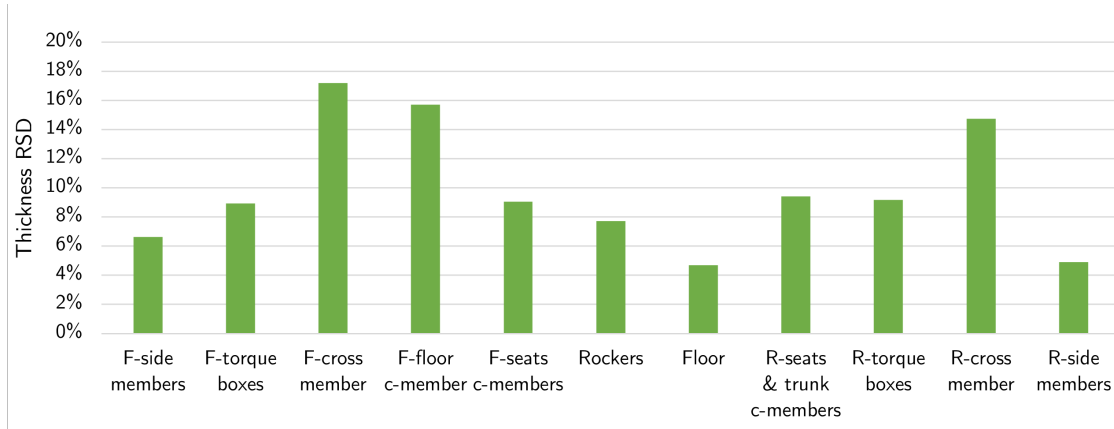


Figure 5.6: Relative standard deviation of underbody components thickness

It is possible to see that the higher variability is present in the front cross-member and front floor cross-member followed by the rear cross-member. To simplify the analysis, it was chosen to focus either on the material variability or on the thickness variability, thus the rear cross-member, which was one of the few components to be made both in steel and aluminum, was not investigated for thickness variation. For the remaining components which showed low variability and a mainly steel construction, both thickness and material were kept fixed in the following analysis.

In table 5.3 the material variations for the different components are summarized, indicating if material, thickness, or no variation was considered.

¹ In the following, these abbreviations are used: F=front, c-member=cross-member and R=rear

Table 5.3: Underbody components material and thickness variation

Component	Variation	Type
F and R-side members	Material	Steel/Aluminum
F and R-torque boxes	Material	Steel/Aluminum
F-cross-member	Thickness	Low/High
F-floor-cross-member	Thickness	Low/High
F-seats cross-members	Fixed	-
Rockers	Fixed	-
Floor	Fixed	-
R-seats & trunk cross-members	Fixed	-
R-cross-member	Material	Steel/Aluminum

Battery Pack Materials

From the conducted analysis, the battery pack resulted to be mainly mono-material and, in particular, with aluminum structure. The choice was thus to consider a mono-material structure, made either entirely out of aluminum alloy or steel.

5.1.3 Restricted Design Space

Following the previous considerations, the final restricted design space was derived, and it is reported in table 5.4. The table expresses the factors under study, and, for each, two values called *levels* are considered, either varying material, thickness, or geometry.

Table 5.4: Restricted design space

Factor Type	Factor	Level 1	Level 2
Geometry	Rocker internal structure	Stamped	Extruded
	Torque boxes	Angled	Orthogonal
	Lower enclosure	Frame	Tray
	No. battery pack cross-members	0	5
	No. battery pack long. members	0	1
Material and thickness	Side members	Steel	Aluminum
	Torque boxes	Steel	Aluminum
	Rear cross-member	Steel	Aluminum
	Front cross-member	Low thickness	High thickness
	Front-floor cross-member	Low thickness	High thickness
	Battery pack	Steel	Aluminum

In the following, the choices made for each factor are explained and justified.

Geometry

- *Rocker internal structure.* The main structure of the rocker showed low variability, being mainly made by stamped steel with low RSD across the selected vehicles. The choice was to analyze the internal structure of this component, which showed much more diverse interpretations. The already mentioned stamped and extruded stiffening configurations were thus chosen (see figures 5.2 and 5.3).
- *Torque boxes.* Front and rear torque boxes, usually showing a homogeneous design, were grouped into a single factor. The torque boxes were found to be highly variable in geometry and shape, thus the two solutions previously illustrated were analyzed, with both front and rear torque boxes being either *angled* or *orthogonal* (see figure 5.1). This factor was directly influencing the shape of the floor, front-floor cross-member and battery pack, whose geometries were changed with this factor to adapt to the torque boxes shape.
- *Lower enclosure.* The battery pack lower enclosure showed the presence of a lateral structural and/or crash frame, or a simpler frame-less tray structure. These two levels were thus chosen for this factor.
- *Battery pack internal structure.* The internal structure was analyzed considering two factors, the *cross-members*, and *longitudinal members*, both assuming two levels corresponding to their respective count. The low level for the *cross-members* was set to 0, while the high to 5. For the *longitudinal members*, 0 or 1 members were considered.

The other components were kept constant in geometry throughout the analysis.

Material and Thickness

- *Side members.* The front and rear side members were grouped in one single factor since, having similar function and construction, can be assumed to share a similar design. Given the low RSD of their thickness, the choice was to study their influence on the design by using steel or aluminum as also indicated in [64].
- *Torque boxes.* The torque boxes are again grouped in one single factor. Since they were found to be slightly variable in thickness. Even if the material for these structures was mainly steel the decision was to analyze this factor on two levels corresponding to aluminum and steel since the element was considered to be a

crucial component of the platform design, and thus, worth to be investigated more in detail.

- *Rear cross-member.* This factor was considered on two levels corresponding to steel or aluminum. It was one of the components which showed an aluminum construction in multi-material underbodies, and hence the material analysis was preferred to the thickness one.
- *Front cross-member.* This element was found to be highly variable in thickness but mainly made of steel. Thus, two levels were set, *low* and *high* thickness steel panels.
- *Front-floor cross-member.* Similarly to the previous factor, *low* and *high* thickness steel panels were considered.
- *Battery pack.* Being the battery pack already analyzed with ample geometric variations, the choice was to study its influence on two materials levels, steel, or aluminum. This choice was driven also by the abundance of mono-material solutions showing either aluminum-intensive or steel-intensive enclosures.

The final restricted design space had 11 factors, each on two levels. It was then necessary to choose the actual thickness for both the variable and constant thickness factors, as well as for the elements excluded from the design space. The following criteria were used:

- *Constant material components.* Their material was fixed as steel or aluminum and their thickness was determined as an average of the analyzed solutions.
- *Variable thickness factors.* The material was fixed as steel and two thicknesses were selected; the lowest and the highest found from the benchmarking analysis.
- *Variable material factors.* The chosen materials were steel and aluminum. The base concept was to start from the steel structure and substitute an aluminum component with equivalent stiffness. Due to the lower aluminum elastic modulus E_{alu} , the thickness was increased according to the benchmarking data, and if not available, the increase was derived from what reported in [36, 66] for equal-stiffness panels under bending:

$$\frac{t_{alu}}{t_{steel}} = \sqrt[3]{\frac{E_{steel}}{E_{alu}}} = \sqrt[3]{\frac{210 \text{ GPa}}{70 \text{ GPa}}} \approx 1.44 \quad (5.2)$$

This equals to approximately a 50% increase in thickness for the aluminum panels, which results still in approximately a 50% lightweighting:

$$\frac{m_{alu}}{m_{steel}} = \frac{t_{alu}}{t_{steel}} \times \frac{\rho_{alu}}{\rho_{steel}} = 1.44 \times \frac{2700 \text{ kg/m}^3}{7850 \text{ kg/m}^3} \approx 0.5 \quad (5.3)$$

However, for a beam under bending or torsion, to reach equal stiffness with constant external dimensions, the aluminum one should be 3 times thicker, thus obtaining no appreciable lightweighting. Despite that, as reported in [66], when dealing with more complex structures, such as an automotive underbody, it is possible to directly substitute aluminum in existing steel structures and obtain comparable stiffness by increasing the aluminum thickness by 50%, while still reducing the weight by 40-45%. Optimizing the cross-section could lead to further lightweighting possibilities, but this investigation is left for future studies.

The next tables 5.5 and 5.6 summarize the chosen material properties.

Table 5.5: Steel properties

Material	Property	Thickness [mm]
Steel	S1	0.75
	S2	1
	S3	1.2
	S4	1.3
	S5	1.4
	S6	1.6
	S7	1.8
	S8	2

Table 5.6: Aluminum properties

Material	Property	Thickness [mm]
Aluminum	A1	1.4
	A2	2.1
	A3	2.5
	A4	2.7
	A5	3
	A6	3.2
	A7	3.6

Tables 5.7, 5.8 and 5.9 show how the above-listed properties were assigned to the different components. The *constant material components* were assigned only one fixed property.

5.2 Experiment Definition

To conduct an efficient and systematic experiment it was needed to proceed choosing a specific and suitable type of experiment plan. To reduce the number of tests and to allow the investigation of possible interactions between different factors it is needed to change simultaneously more than one factor at each iteration of the experiment [96, 97]. The results of the experiment can then be analyzed with proper statistical tools, such as the Analysis of Variance (ANOVA).

Table 5.7: Steel properties

Component	Prop. 1	Prop. 2
F-side members	S7	A4
F-cross-member	S4	S8
F-torque boxes	S7	A4
F-floor-cross-member	S4	S8
F-seats cross-members	S6	-
Rockers	S6	-
Rocker stamped stiff.	S6	-
Rocker extruded stiff.	A7	-
Floor	S1	-
R-seats cross-members	S3	-
R-torque boxes	S7	A4
R-cross-member	S5	A2
R-trunk cross-member	S3	-
R-side members	S7	A4

Table 5.8: Frame battery pack

Component	Prop. 1	Prop. 2
Lower plate	S2	A3
Top plate	S1	A1
Frame	S8	A5
Internal structure	S6	A3

Table 5.9: Tray battery pack

Component	Prop. 1	Prop. 2
Lower enclosure	S8	A6
Top plate	S1	A1
Internal structure	S6	A3

This experimental strategy, consisting of changing multiple factors at the same time is called *factorial experiment* and it allows to define the combinations of input parameters to be tested in the different experimental runs [97].

Different factorial plans are available, the most complete being the *full factorial plan*. This plan consists of evaluating all the possible combinations of every factor at every level, allowing to evaluate the effects on the response of both factors and interactions between factors [97].

The number of experimental runs is thus $N = \prod_{i=1}^n L_i$, where L_i corresponds to the number of levels of the i^{th} factor. For the case under study, this would result in a number of experiments equal to $L^n = 2^{11} = 2048$. Considered the computing time which, for the baseline FEA defined in chapter 4, was in the order of 455 s, this experimental plan was not feasible for the current project.

To reduce the number of the experiments, considered the generally lower influence of higher-order interactions, a *fractional factorial plan* was chosen instead. This plan is derived by extracting specific combinations from the corresponding *full factorial plan*. The extraction process is highly complex for an elevated number of factors and was thus carried out through the Minitab[®] software. This allowed to extract an *orthogonal* plan in which every level of each factor appears with the same frequency [97].

When choosing a fractional factorial design, it is crucial to choose one that ensures a manageable number of runs while still having adequate resolution. The resolution describes which effects are aliased with each other, making it impossible to distinguish

which factor or interaction was causing them. The preferred choice for factorial design is at least a resolution IV plan, in which the main factors are confounded with 3-way interactions.

Therefore, a $1/64$ fractional factorial plan was chosen, consisting of a total of 32 runs, which allows to reach resolution VI. In the chosen design no aliasing is present among the main effects and between main effects and 2-way interactions. However, some 2-way interactions are aliased with each other, and the 3-way interactions are aliased with the main effects as shown in the aliasing structure in table B.1 [98]. No repetition of the runs was necessary since the FEA analysis would have returned the same values. Since the experiments were “virtual” and not conditioned by external noise, there was also no need for randomization of the experiments, which allowed to simplify the matrix of the DOE.

It is important to point out that, in every factorial plan, some factors change level just few times across the different runs, while others are changed possibly at every run. Table 5.10 shows an example of a $1/2$ factorial plan with 4 factors on two levels, indicated as -1 and 1.

Table 5.10: Example of 4-factors 2-levels fractional factorial plan

A	B	C	D
-1	-1	-1	-1
1	-1	-1	1
-1	1	-1	1
1	1	-1	-1
-1	-1	1	1
1	-1	1	-1
-1	1	1	-1
1	1	1	1

From the generated fractional factorial plan it is possible to see that factor C is changed just once throughout the runs, whereas the others are changed more frequently up to factor A which changes at every run.

For the current study, some parameters were easy and fast to change in the FEA model. Changing the material property was done simply by assigning the shell elements of the component of interest with the new property. This process was estimated to take approximately 5 minutes per run. On the other side, geometry changes needed a complete re-meshing and creation of the RBE2 and RBE3 elements and bolted connections. This procedure took up to 1.5h for the more complex geometrical changes.

It was thus necessary to place the most critical factors in the columns which showed fewer changes across the runs so to optimize the experiment execution time. The

obtained fractional factorial plan is reported for reference in chapter A.

5.2.1 Conducted Analyses

After defining the experimental plan, different types of analysis were conducted. Starting from the complete fractional factorial DOE, three runs of the complete experiment were performed by using the full model or removing some components to gather different types of information. In the following, the above-mentioned experiments are briefly illustrated.

Complete Model Analysis

In this experiment, the complete model was studied, and the needed FEM models were created according to the combination of factors defined from the DOE. It consisted of 32 FEA runs which gathered the following responses:

- Structure mass
- Torsional stiffness in kNm/rad
- Bending stiffness in kN/mm
- 1st, 2nd, and 3rd modal frequencies, with the 1st as the most important response

The analysis showed good results and realistic behaviour for the torsional and bending load cases, but the modal analysis showed low-frequency resonances caused by the flat floor and battery pack panels.

Batteryless Analysis

After conducting the complete model experiment, an additional analysis was conducted, without considering the battery pack but only the underbody structure. The scope of this analysis was to assess the extent of the contribution of the battery pack to the complete system stiffness. At this scope the experiment provided the following responses:

- Structure mass
- Torsional stiffness in kNm/rad
- Bending stiffness in kN/mm

In this case, the resonance frequency was not relevant since the system was not complete. However, the conducted modal analysis showed low-frequency resonance of the floor panels also in this case. Another experiment was thus necessary to assess the resonance of the main frame structure, without flat panels.

Panelless Analysis

The model was modified by removing the floor and battery pack flat panels. In this phase, only the modal analysis was conducted, and the first three resonance modes were analyzed to understand the resonance behaviour of the structure. For the scope of the study, only the 1st resonance mode was considered in the following statistical analysis. In figure 5.7 an example of one of the panelless model is shown.

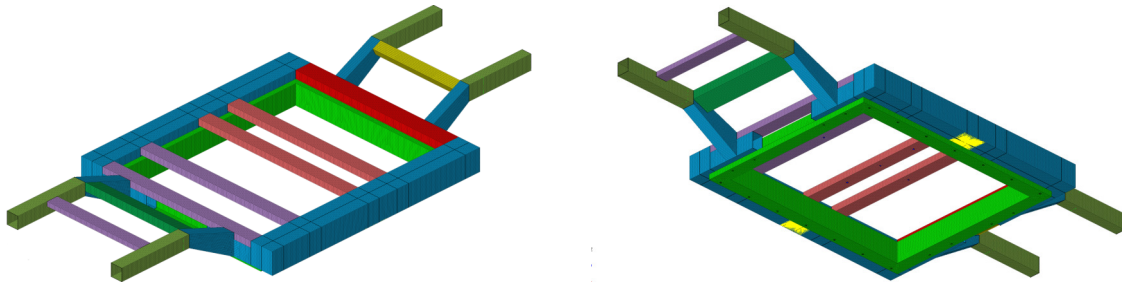


Figure 5.7: Example of the panelless model used for modal analysis

Optimization and Stiffened Panels Analysis

For the final analysis, an optimized model was derived and tested as it will be explained in section 5.3.2. The obtained optimized models were tested substituting the flat panels with embossed panels to assess the capability of this solution to solve the low-frequency resonance issues found in the analysis of the complete model. Since the design of the floor embossed panels is already well established in the industry the analysis was mainly performed for hypotheses validation. As already anticipated, the study of this model was limited to the two solutions obtained in the final optimization phase. Figure 5.8 shows the embossed panels both for the floor and the battery pack.

5.3 Methodology for Result Analysis

After conducting the experiment, it was necessary to analyze the obtained results with proper statistical tools. The goal was to detect which factors or interactions were more determinant for the performance of the system, for every of the defined responses. In the following, the different methods used are illustrated.

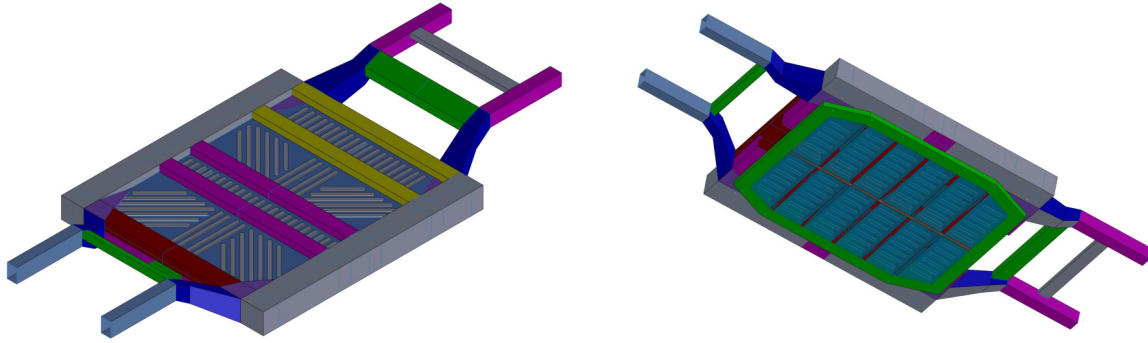


Figure 5.8: Example of embossed panels for modal analysis

5.3.1 Analysis of Variance (ANOVA)

For the current DOE, a factorial ANOVA was used and conducted through Minitab[®] DOE analysis tool. In fact, in this study, 11 independent factors were analyzed, and a total of five dependent variables or response was gathered. The factorial ANOVA was conducted for each of the gathered responses to assess the influence of the various factors and interactions on the respective output.

ANOVA assesses the relevance of each factor by comparing the obtained responses at different factor levels [99]. The approach tests the null hypothesis that all the responses from the different factor levels are equal. This is done by using the variances between different levels to determine if the means are different [97].

In the following, the used outputs from the ANOVA are listed.

P-value

The P-value calculated by the software indicates the significance level of each analyzed factor or interaction. The null hypothesis tested is that the means of the different factor levels are equal, meaning that the correspondent factor is not significant. Through the P-value, it is possible to test this hypothesis and determine which factors are relevant in influencing the response and which are likely not relevant [97].

The common practice is to use a confidence level α of 0.05, indicating that there is a 5% risk of considering a factor as significant when instead it is non-significant, also called Type I error [99]. Using the P-value and the confidence level $\alpha = 0.05$ the factors or interactions can be subdivided into [99, 97]:

- P-value $\leq \alpha$: the factor or interaction is statistically significant.
- P-value $> \alpha$: the risk Type I error is considered too high, so the null hypothesis cannot be rejected and, in general, the factor/interaction is considered not significant.

Pooling

The process called *pooling* or *model reduction* consists in removing from the analysis the factors or interactions that could not be identified as significant, to simplify the linear regression model that will be developed and increase the precision of the model predictions [100]. The process is conducted by removing from the model one by one the “least” significant factors or interactions starting from the ones with higher P-value. It is then repeated, and the analysis is conducted again with the excluded factor contribution being added to the error. This may cause the P-value of other factors to change, thus there is the need of proceeding one factor/interaction at a time. Due to the resolution IV of the fractional factorial DOE, the 3-way and several 2-way interactions are aliased, thus they are removed all at once if one is considered not significant [97].

It is important to highlight that to maintain the model hierarchical it is necessary to include each main factor that contributes to a significant interaction, even if its main effect is not relevant [97].

Percentages of Contribution

After conducting the *pooling* of the non-significant factors and interactions, it was possible to analyze which factors among the remaining influential ones had the biggest impact on the studied responses. This was carried out by plotting the Pareto chart of the “percentages of contribution”. To do so, the adjusted sum of squares calculated by Minitab[®] were used. The adjusted sum of squares indicates the amount of the total variation associated with one term or interaction, considering all the other terms in the model [101]. The sum of squares is called adjusted because independent of the order the terms are entered in the model but evaluating the influence of each considering at the same time the cumulative influence of the others.

The obtained values were plotted in a Pareto chart to easily highlight the percentage of contribution of each factor to the variability of the response as well as underline the most relevant parameters.

5.3.2 Linear Regression Model

After the *pooling* procedure, the Minitab[®] DOE analysis tool could be used to develop a linear regression model, through which it is possible to predict the value of the outputs for non-tested input as well as run a preliminary design optimization.

Analysis of Means

With the developed model, the Analysis of Means (ANOM) was used to build the factorial plots which show the obtained relationships between outputs and factors or interactions. The main effects plot was used to study the relationship between main factors and responses, while the interaction plots were used to investigate the effect of the 2-way interactions on the model fitted output [97].

Response Optimization

By using the developed model, it was possible to run the Minitab[®] response optimizer to gain initial design suggestions to optimize the system. The response optimizer uses the linear regression model to give the suggested values of the input factors to reach the desired optimized configuration. Two different optimizations were conducted; *complete optimization* where the mass was minimized, and all the other responses were maximized and a *target optimization* in which the mass was minimized while meeting the desired constraints for torsional and bending stiffness and 1st resonance mode [102].

After obtaining the desired optimized values, the model was developed and a validation FEA run was conducted. For better clarity, this procedure will be thoroughly illustrated in the following chapter 6, after having discussed the results obtained in the previous steps.

6 | Results and Discussion

After describing the methodology used to develop the CAD and FEM models, and the procedure for the DOE, the obtained results are here analyzed. From the results of the analysis, the derived design guidelines are then presented.

6.1 Complete Model Analysis

As described in chapter 5, at first the complete experiment was conducted, involving the total model with factors evaluated according to the defined DOE (see chapter A). The analysis gathered 32 different values for each response, through the 32 conducted FEAs. The results obtained from the selected responses are here reported and discussed.

For more details on the conducted ANOVA see the section B.1.

6.1.1 Mass

The first output of the analysis was the total mass of the structure. The mass was evaluated as structure mass, excluding the 300 kg of the simulated battery cells. The resulting mass was ranging between 151 kg and 252 kg with an average around 200 kg and a standard deviation of 26.55 kg. The obtained results are reported in the histogram in figure 6.1.

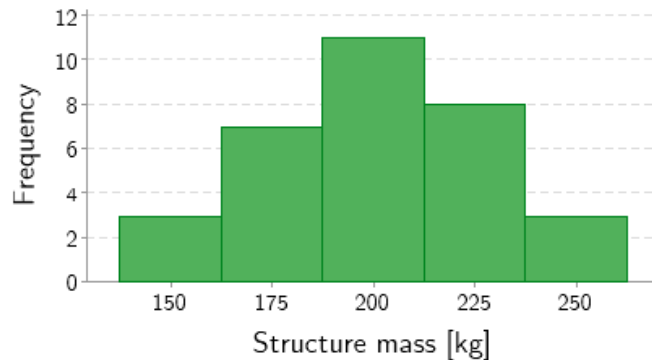


Figure 6.1: Distribution of structure masses

As expected all main factors were significant since a variation in one of them would automatically cause a variation in the mass. Only some 2-way interactions could be excluded from the analysis by the pooling process. Nevertheless, it was possible to highlight which factors are contributing the most to the variation.

The most relevant was the battery pack material, accounting for 48.5% of the variability, followed by the rocker rail internal structure, the number of battery pack cross-members and the torque boxes material. These factors combined contributed to 95.7% of the total variability, with the remaining main factors and interactions accounting for 4.3%. Figure 6.2 represents the Pareto chart of the percentage of contribution of the different factors to the variability.

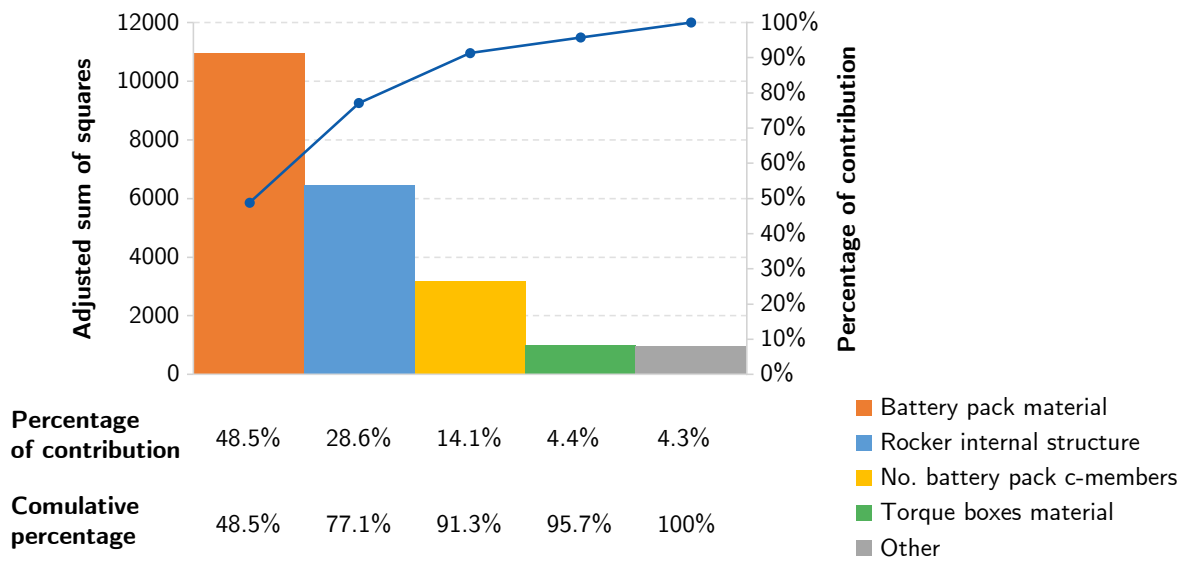


Figure 6.2: Pareto chart of the percentages of contribution for the mass response

In the next paragraphs, the factorial plots were analyzed to investigate how the different factors influenced the mass response. The plots obtained from the derived linear model are reported in figure 6.3. For sake of simplicity in the following, steel and aluminum alloy are abbreviated as “S” and “A”.

From the analysis of the mass response, it is possible to highlight the elements with the higher lightweighting possibilities. In particular, if the factors that can highly influence the mass response are not influential for the static and dynamic stiffness, they have high lightweighting potential. Those factors should then be set to the level which delivers the lowest weight.

It is possible to see how the battery pack material had a large influence on the total structure weight. Switching to an aluminum structure may allow to save up to 40 kg for the considered designs.

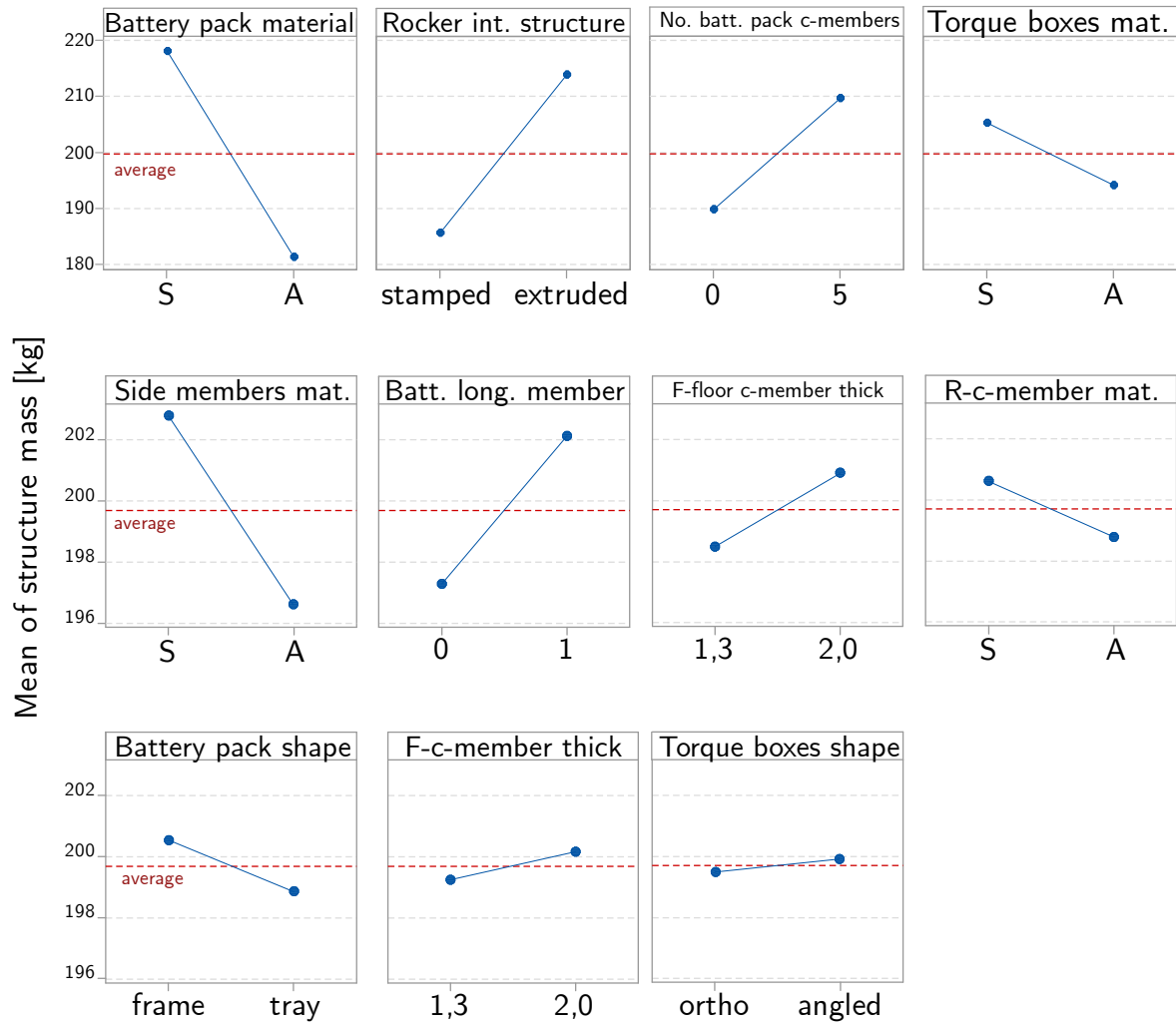


Figure 6.3: Main effect plot for the structure mass, fitted means

The rocker internal structure, being a large size component was highly influential as well. The stamped internal structure results to be the most lightweight, with the extruded one adding a considerable amount of mass. This solution may still be advantageous for the stiffness and may be crucial for the side impact.

The number of battery pack cross-members, changing from zero to five, largely influenced the mass of the structure. Their effect must be compared with the other performance outputs to assess the best solution, which may fall in between these two extremes.

The torque boxes material contributed to 4.4% of the variability, with the aluminum solution being the lighter one. This needs still to be carefully compared with the stiffness performances, because a weight saving of 10kg may not be justified if the stiffness is dramatically reduced.

The next most relevant parameter was the side members material, accounting for

1.4% of the variability, with a weight change of around 5 kg. This indicates a low but still relevant lightweighting if the side members are made of aluminum.

For what concerns the remaining factors, the number of longitudinal members, accounted for 0.7%, while the other factors were less influential but are still reported in figure 6.3 for reference. Interestingly, the torque boxes shape was not highly influential and could consequently be exploited to increase the static and dynamic stiffness performances. This and the other less influential factors could be tuned for best performance and their level is thus strictly dependent on the static and dynamic stiffness rather than their effect on the mass.

6.1.2 Torsional Stiffness

The second response to be analyzed was the torsional stiffness. In figure 6.4 an example of the deformed structure under torsion is shown. The resulting stiffness was ranging

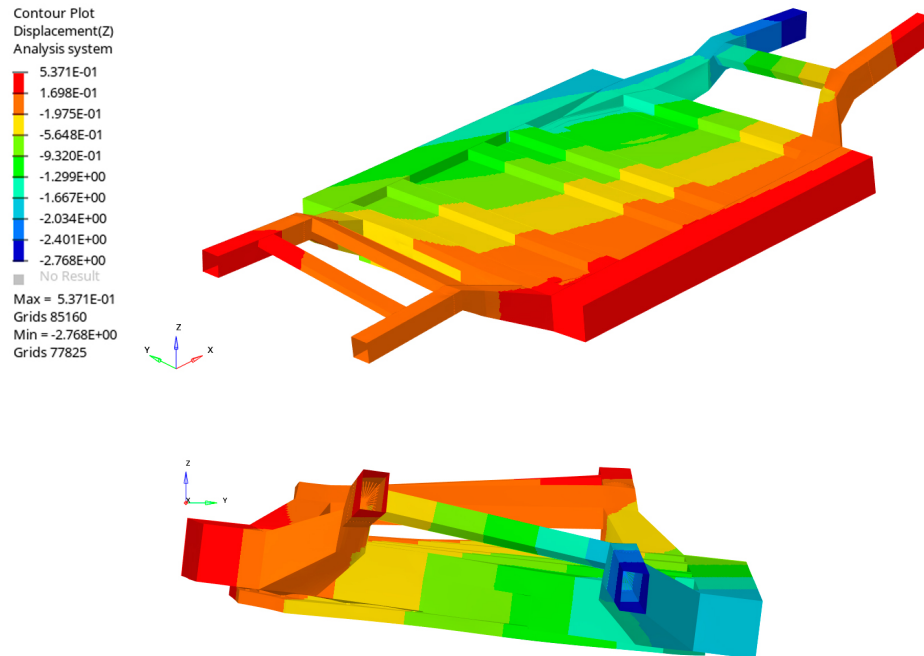


Figure 6.4: Torsional deformation example, amplified by 100x. Z-axis contour plot with displacements in mm

between 214 kNm/rad and 350 kNm/rad with an average of around 272 kNm/rad and a standard deviation of 35.75 kNm/rad. The obtained results are reported in the histogram in figure 6.5. The deformation was in the order of 3 mm, and it was thus necessary to amplify it by 100 times to make it more appreciable.

In this case, the pooling excluded several interactions which were considered not influential, with a p-value > 0.05. There were also some main factors with a p-value > 0.05

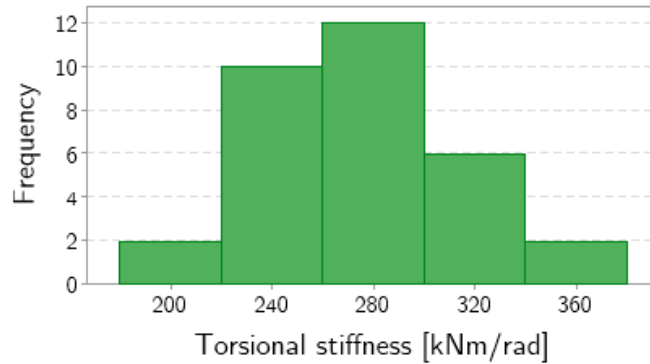


Figure 6.5: Distribution of torsional stiffness

such as the battery longitudinal member that showed a p-value of 0.646 after the pooling, hence indicating a low influence on the torsional stiffness. The battery cross-members count was also at p-value=0.057, so slightly over the limit to be considered influential. Both these factors could not be excluded from the model to keep it hierarchical, because their interactions were significant. Furthermore, due to the aliasing of the 2-way interactions, it was not possible to distinguish if it was the interaction of these two factors to determine the significant effect. In any case, it was possible to highlight that their contribution to the total response was minimal, at less than 0.015% of the total contribution.

Figure 6.6 represents the Pareto chart of the percentage of contribution of the different factors to the variability of the torsional stiffness response.

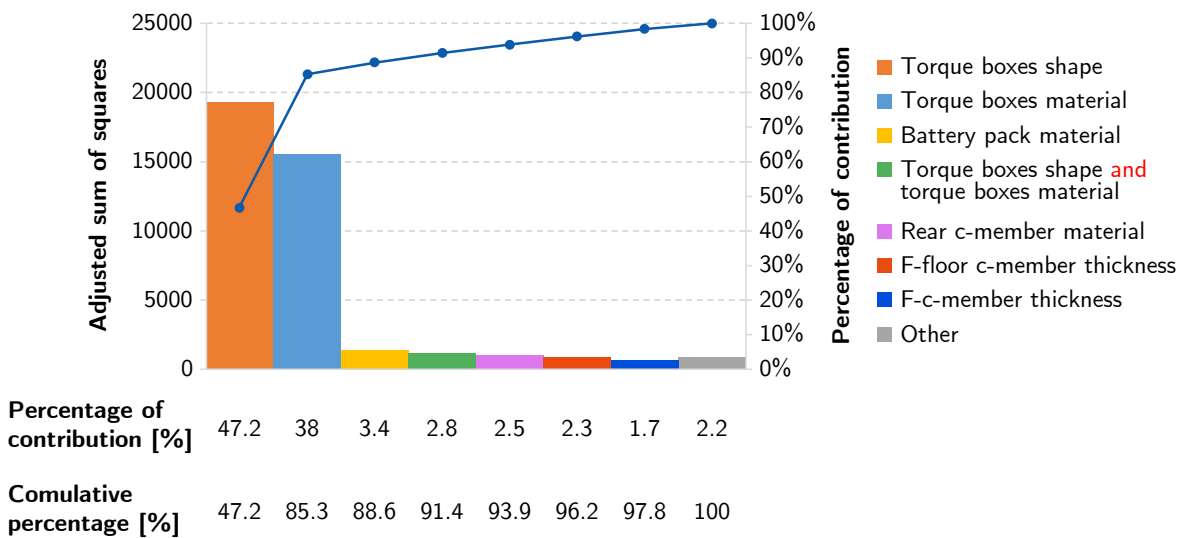


Figure 6.6: Pareto chart of the percentages of contribution for the torsional stiffness response

The most influential factor was the torque boxes shape accounting for 47.2% of the variability. This factor was not considerably influential on the mass of the structure, so it has the potential to increase the stiffness without significantly affecting the mass.

The second percentage of contribution was from the torque boxes material, accounting for 38% of the effect. In this case, the factor influence on the mass was not negligible, so the material choices for the torque boxes need to be evaluated also considering the other responses.

From the third most influential factor, there was a big drop in the influence on the torsional stiffness response. The battery material accounted for only 3.4%, and being highly influential on the mass, could be preferred as aluminum, to have a large lightweight with a low decrease in torsional stiffness. Following this factor, the interaction between torque boxes shape and torque boxes material accounted for 2.8%. It must be said that this 2-way interaction was aliased with other interactions:

- *Side members material* and *rocker internal structure*
- *No. battery pack longitudinal members* and *Rear cross-member material*
- *Front floor cross-member thickness* and *battery material*

Therefore, it was not possible to undoubtedly attribute this effect to the torque boxes shape and torque boxes material interaction. However, being it the combination of the two most influential factors, and the lack of direct correlation between the other interacting parameters, this was the most likely to be influential.

Following this interaction, other main factors were slightly influential with the rear cross-member material accounting for 2.5%, the front floor cross-member thickness at 2.3% and the front cross-member thickness at 1.7%. These factors and interactions combined contributed to 97.8% of the total variability, with the remaining main factors and interactions accounting for 2.2%.

Next, the factorial plots were analyzed to investigate the model factors and understand their effect on the response. The plots obtained from the linear regression model are reported, in order of factor influence, in figure 6.7¹.

From these plots, it is possible to confirm the previous analysis. The torque boxes shape was highly influential, with a possible change in the stiffness of approximately 50 kNm/rad. The angled torque boxes delivered the best torsional stiffness performance.

¹ In this and the next figures, in addition to the previous abbreviations, the following are also used: ortho=orthogonal, mat.=material, F=front, R=rear, c-member=cross-member, thick.=thickness int.=internal, struct.=structure, long.=longitudinal

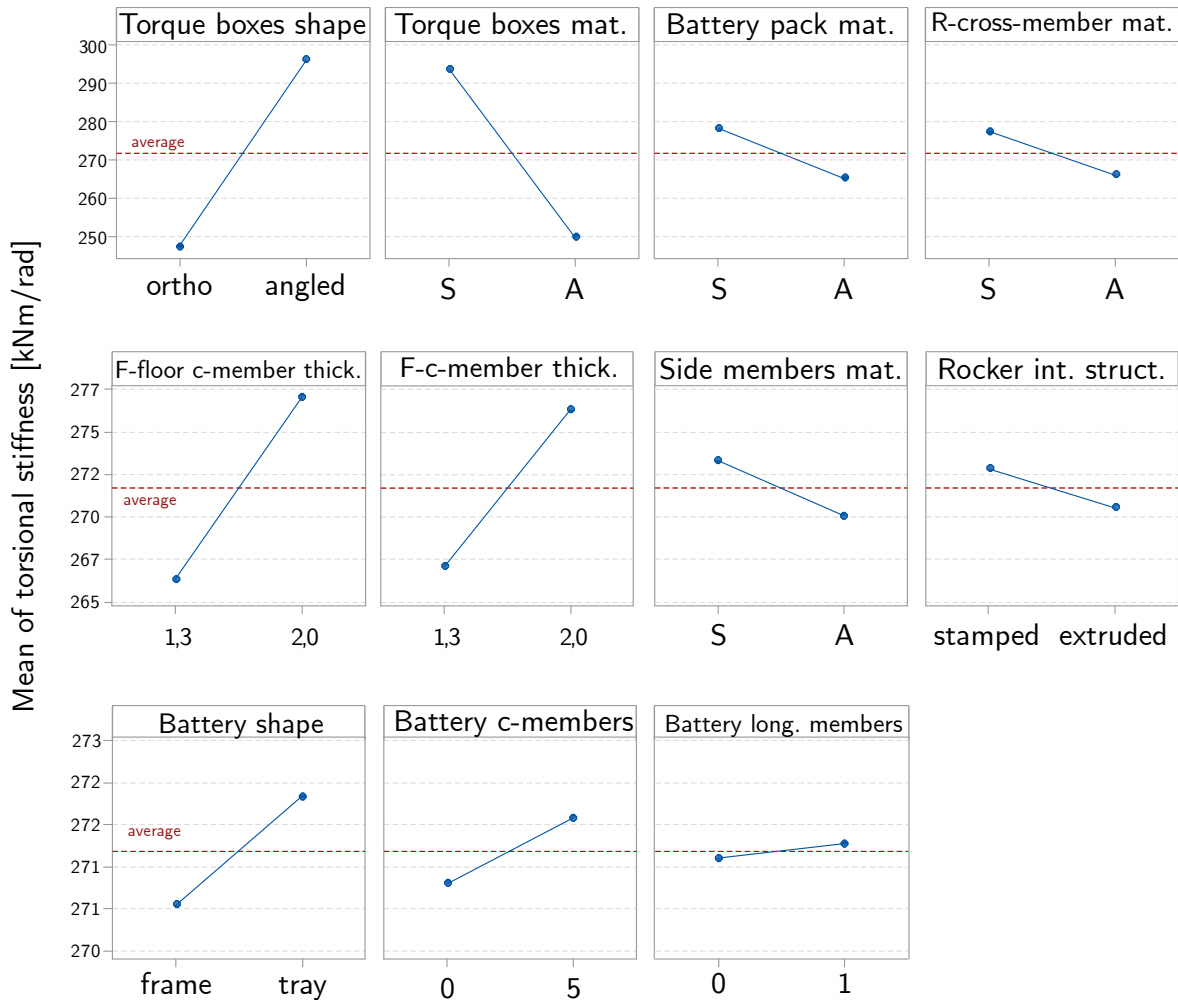


Figure 6.7: Main effect plot for the torsional stiffness, fitted means

The torque boxes material largely affects the stiffness as well. In this case, the preferred material is steel.

The following factor was the battery pack material, which was preferred as steel. Although, the stiffness advantage of choosing steel may not be justified due to the high increase in the structure mass.

A rear cross-member made of steel delivered a higher stiffness which may be exploited given its minimal effect on the structure mass.

The front cross-member and the front floor cross-member, as expected delivered a higher stiffness when the thickness was increased at 2 mm. The stiffness variation is however not as significant as for the previous factors, and thus a possible weight saving may be considered.

The side members were preferred as steel, but the weight saving from using aluminum may be worth the stiffness loss.

The rocker internal structure was instead just slightly influential, with the heavier extruded stiffening performing worse than the stamped one.

To conclude, the battery shape was preferable as a tray and a higher number of internal structural members lead to higher stiffness, even if the increase was minimal. Consequently, there were lightweighting possibilities by reducing the complexity of the internal structure.

For what concerns the most relevant interactions, figure 6.8, reports the factorial interaction plots for the torsional stiffness.

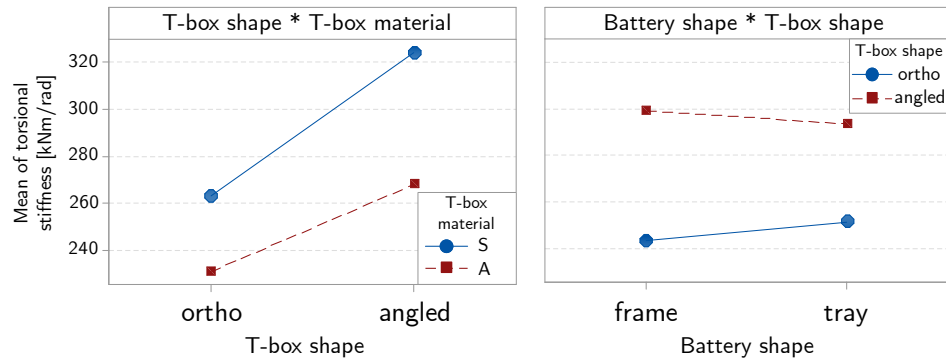


Figure 6.8: Principal interactions effect plot for the torsional stiffness, fitted means

The interaction between torque boxes shape and material, led to better performances for angled and steel torque boxes, with the aluminum orthogonal ones performing at the worst. In any case the interaction has little effect since the two lines are almost parallel.

Even if excluded from the significant interactions, the one between battery shape and torque boxes shapes showed one of the strongest interactions and it was thus reported in figure 6.8. In this case a slightly negative interaction is present, with the angled torque boxes performing worse with a tray battery pack and the orthogonal ones delivering better performance with the tray battery pack. In any case, the angled torque boxes outperformed the orthogonal ones. However, due to the aliasing from the fractional factorial DOE, it was not possible to draw unequivocal conclusions.

6.1.3 Bending Stiffness

The third response to be analyzed was the bending stiffness. In figure 6.9, an example of the deformed structure under bending is shown. The deformation was in the order of 0.2 mm, and it was thus necessary to amplify it by 300 times to make it more appreciable.

The resulting stiffness was ranging between 9.7 Nm/mm and 14.1 Nm/mm with an average of around 11.8 Nm/mm and a standard deviation of 1.25 Nm/mm.

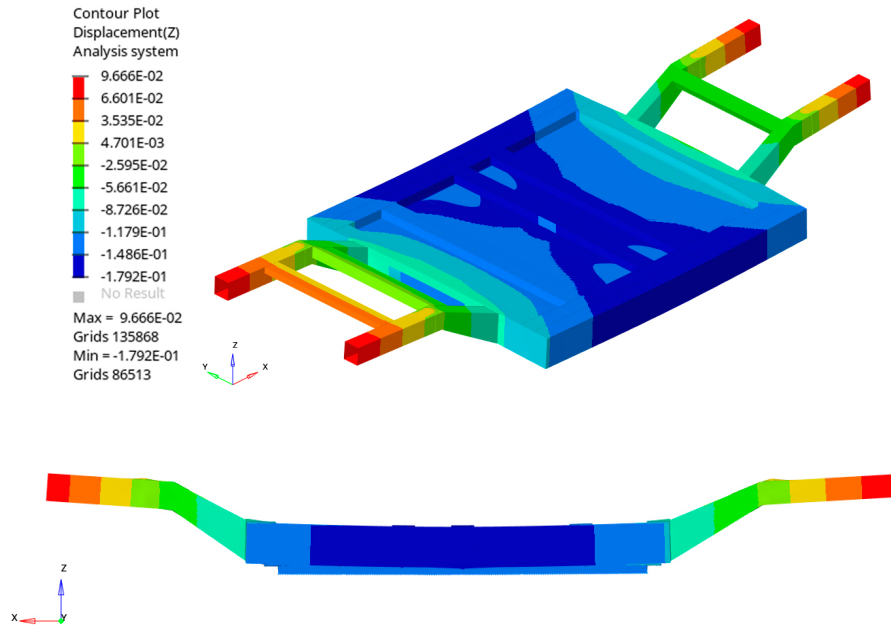


Figure 6.9: Bending deformation example, amplified by 300x. Z-axis contour plot with displacements in mm

The obtained results are reported in the histogram in figure 6.10. In this case, the pooling excluded several interactions which were considered not influential, with a $p\text{-value} > 0.05$.

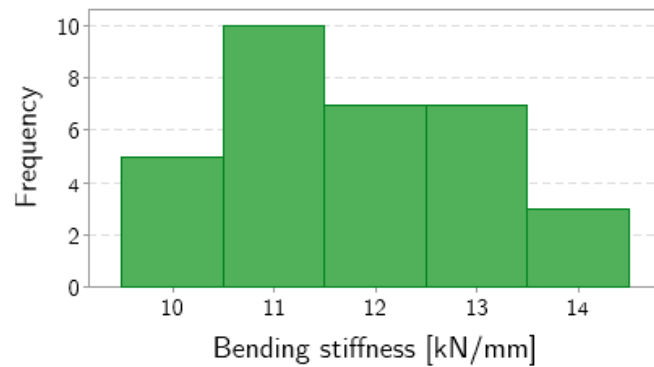


Figure 6.10: Distribution of bending stiffness

Again, there were also some main factors with a $p\text{-value} > 0.05$ which could not be pooled out since their interactions were considered significant. For example, the battery shape showed a $p\text{-value}$ of 0.820 after the pooling, hence indicating a low influence on the bending stiffness, as already found for the mass and torsional stiffness. The front and rear cross-members thickness and material were both showing low influence with $p\text{-values}$ in the order of 0.4. This behaviour was already encountered in the torsional

stiffness, thus leading to the possibility of choosing the lowest weight solution with few detrimental effects on both stiffnesses. In the end, also the torque boxes shape was not influential for the bending stiffness response, differently from the torsional loading in which it was the most influential. The contribution of these factors to the bending stiffness was practically null.

Figure 6.11 represents the Pareto chart of the percentage of contribution of the different factors to the variability of the bending stiffness response.

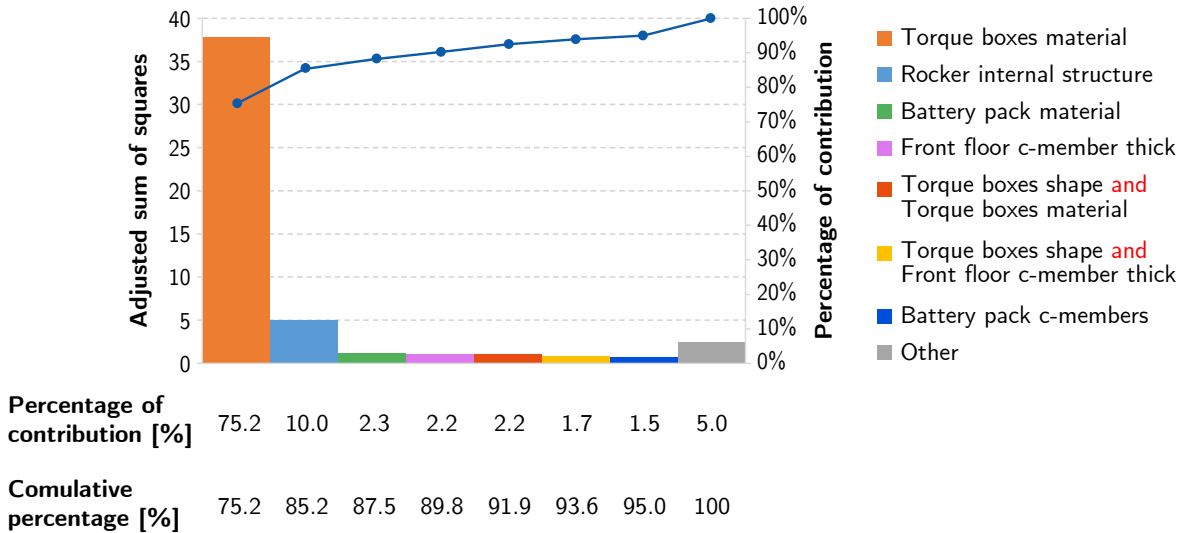


Figure 6.11: Pareto chart of the percentages of contribution for the bending stiffness response

In this case, the most influential factor was undoubtedly the torque boxes material, accounting for 75.2% of the variability. This factor was quite relevant to the mass of the structure, thus must be carefully evaluated for a compromise between stiffness and weight efficiency.

The second percentage of contribution was from the rocker internal structure, accounting for 10.0%. This effect was predictable since these are the directly loaded structures by the bending forces.

The following relevant factors were just slightly influential, with contributions in the order of 2.3%. In particular, the battery pack material, which was highly influential for the mass response, confirmed its lightweighting potential already found in the analysis of the torsional response.

The next influential factor was the front floor cross-member thickness at 2.2%, following a similar trend as with the torsional response.

The interaction between torque boxes shape and torque boxes material accounted for 2.2%, followed by the interaction between torque boxes shape and front floor cross-

member thickness which contributed to 1.7%. Also in this case, it was not possible to undoubtedly attribute their effect to the specific interaction due to confounding. In the end, the battery pack cross-members represented 1.5% of contribution to the response.

The remaining interactions and main factors were less influential, being each under 1% of contribution, with the ones showing high p-values being practically negligible.

Subsequently, the factorial plots were analyzed to investigate the above-mentioned factors and understand their effect on the bending stiffness. The plots obtained from the linear regression model are reported, in order of factor influence, in figure 6.12.

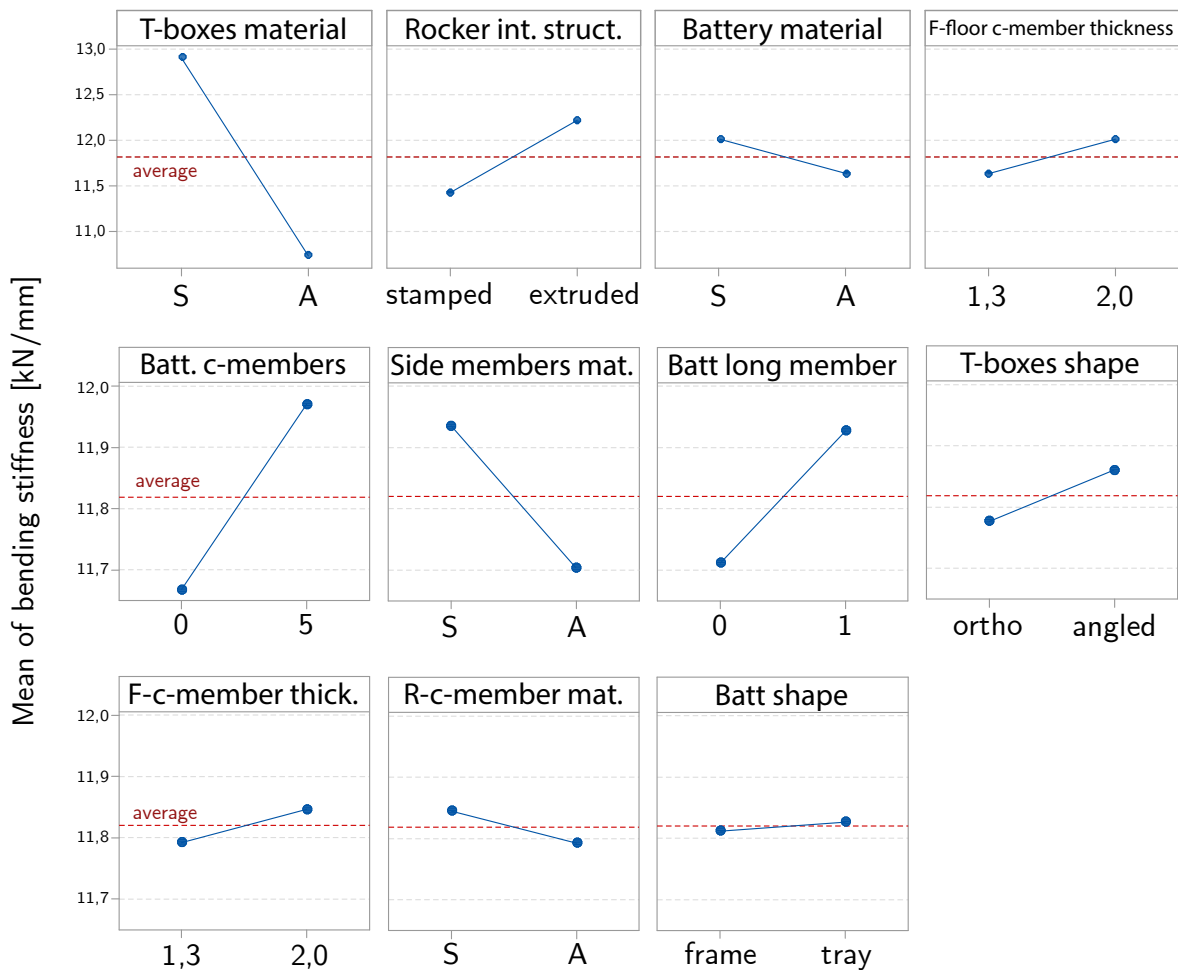


Figure 6.12: Main effect plot for the bending stiffness, fitted means

From these plots, it is possible to confirm the previous reasoning. The torque boxes material was highly influential, with a possible change in the stiffness of more than 3 kN/mm. The steel torque boxes delivered the best bending stiffness performance.

The rocker internal structure followed, with the best stiffness encountered with extruded torque boxes. The steel battery pack was slightly better, but in this case, the improvements in the bending stiffness were less than 0.5 kN/mm. However, the

stiffness advantage of choosing steel may not be justified due to the high increase in the structure mass.

Predictably the thicker front floor cross-member delivered a higher bending stiffness. This indicates that also this region should be considered for the flexural underbody stiffness. The following factors were less influential, accounting for at most a difference of 0.3 kN/mm. In general, steel and high thickness components, together with a more complex battery internal structure, delivered higher stiffness, but the rigidity improvements may not be worth the increase in the structure mass. This also applies to the angled torque boxes, which showed better performance, even if the improvement was far less relevant than in the torsional response.

For what concerns the most relevant interactions, figure 6.13, reports the factorial interaction plots for the bending stiffness.

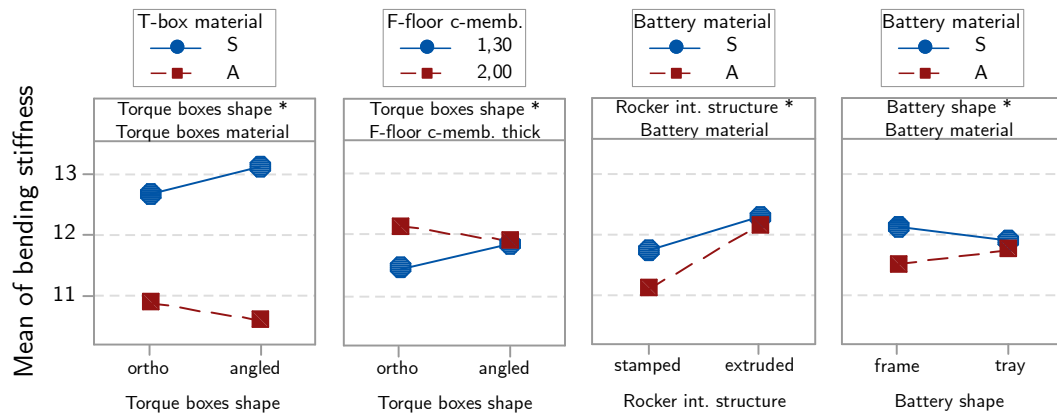


Figure 6.13: Principal interactions effect plot for the bending stiffness, fitted means

As previously the analysis was conducted considering the interactions which were most likely effective among the aliased ones. Nevertheless, due to the confounding from the fractional factorial DOE, also in this case, it was not possible to draw unequivocal conclusions.

The interaction between torque boxes shape and material led to better performances for angled and steel torque boxes while the aluminum angled ones delivered the worst results.

The interaction between torque boxes shape and front floor cross-member thickness showed the best performance for thick cross-member and orthogonal torque boxes.

To conclude, the other two interactions between rocker internal structure and battery material, followed by battery shape and battery material, were less influential and not too strong. Interestingly a steel-tray battery pack performed similarly to the equivalent aluminum version, while it slightly outperformed the light-alloy one in the frame version.

6.1.4 First Modal Frequency

The last response to be analyzed in the complete model analysis was the 1st resonance mode. The first three modes were calculated starting from frequencies higher than 1 Hz to exclude the rigid body modes. The deformations of these modes were analyzed to detect the structure local and global resonances as well as possible problems in the model. In figures 6.14 and 6.15 are reported two examples of the amplified deformations for the first three modes.

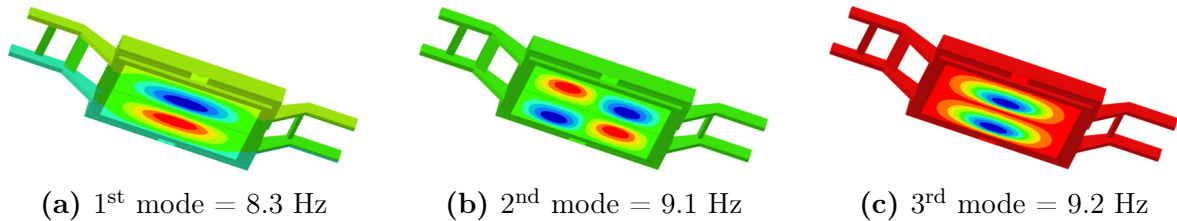


Figure 6.14: Example of modal analysis from DOE run No. 7

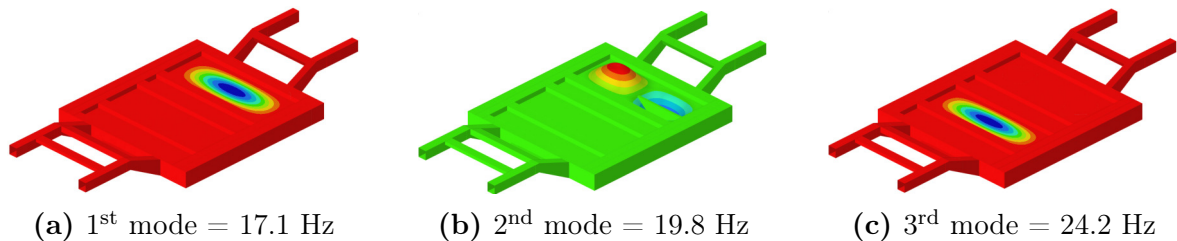


Figure 6.15: Example of modal analysis from DOE run No. 16

The 1st mode was then selected as response since the most significant [36]. From this first assessment, it was clear that the resonance was caused by the large flat panels. If the battery pack had a simple internal structure, like with a single longitudinal member as in figure 6.14, the resonance occurred in the battery enclosure panels. Instead, with a more complex internal structure, with both longitudinal and cross-members, the resonance occurred in the vehicle floor, as shown in figure 6.15. In both cases, it was not possible to assess the resonance of the frame structure because the flat panels resonance was dominant.

This resulted in a not even distribution of the resonance frequencies, which ranged from 1.9 Hz to 17.21 Hz with an average around 11.3 Hz and a standard deviation of 6.3 Hz. The obtained results are reported in the histogram in figure 6.16. These values are much lower than the desired value which is around 40-45 Hz [36]. In this case, the response was mainly influenced by the internal structure of the battery pack, which, reducing or increasing the sizes of the enclosures flat panels, determined an increase or a decrease of the 1st resonance mode.

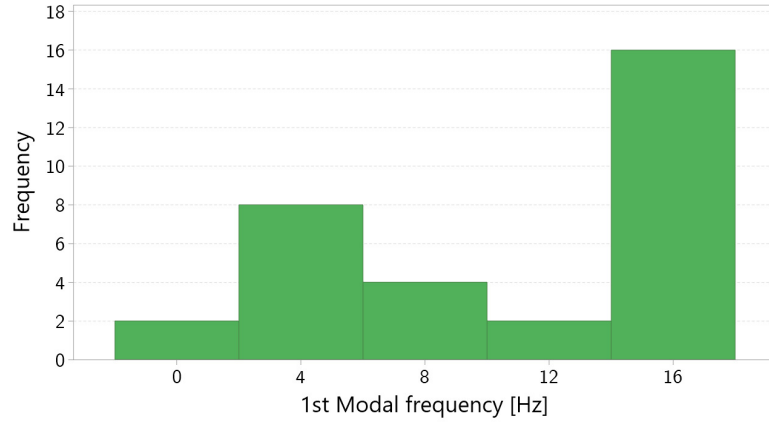


Figure 6.16: Distribution of 1st modal frequencies

The pooling excluded several interactions which were considered not influential, but it was not possible to exclude any principal factor because of the significance of their interaction. From the obtained Pareto chart shown in figure 6.17, it is possible to notice how the battery cross-members are clearly the dominant factor at 68.8% of the effect, followed by the battery longitudinal members and the interaction between these two variables both at around 8.3%.

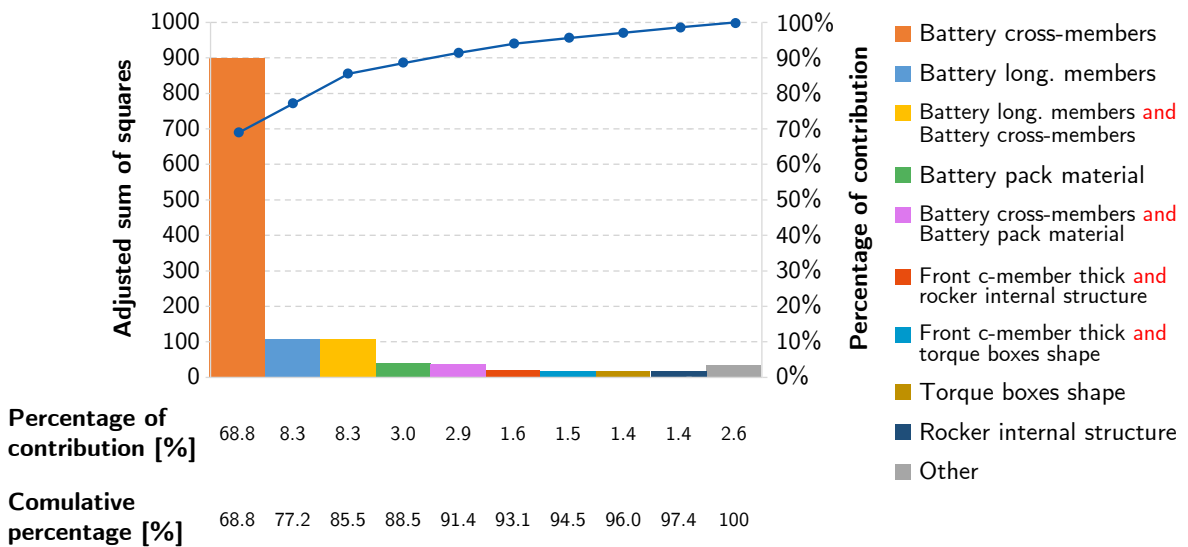


Figure 6.17: Pareto chart of the percentages of contribution for the 1st modal frequency response

The battery pack material and its interaction with the cross-members was the following most influential since directly affecting the stiffness of the battery pack flat panels.

In general, the response was highly influenced by parameters that were kept fixed

during the DOE, thus making the analysis less relevant. These encountered issues impeded to assess the influence of the other design variables on the resonance frequency. However, some interesting outcomes were found through the factorial plots reported in figure 6.18.

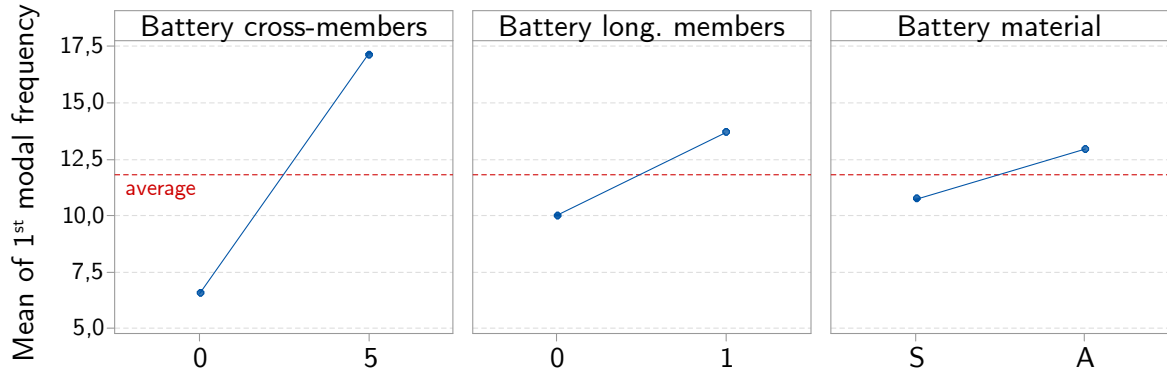


Figure 6.18: Main effect plot for the 1st modal frequency, fitted means

It was, in fact, possible to understand that the resonance frequency increased with the increase of the flat panels stiffness obtained by adding the cross-members or longitudinal members, thus decreasing the panels size. From these findings, a model with embossed and stiffened panels was derived and tested in the final optimization analysis in section 6.4. Interestingly the aluminum battery pack performed better, most likely thanks to the higher thickness of the aluminum panels, which led to a higher resonance frequency.

The outcomes of this analysis were not particularly relevant for the study but were useful to understand some issues in the model and develop the following analyses.

6.2 Batteryless Analysis

After conducting the first complete analysis, it was relevant to assess the contribution of the battery pack to the total stiffness of the structure. The analysis was conducted on the same models developed for the complete DOE, where the battery pack was removed. The resulting DOE analysis is not reported since it is non-meaningful because the original DOE also included the battery factors which were excluded in this FEA analysis. Furthermore, for the underbody components, the results were similar to the previous findings from the complete model. Still, it was interesting to assess the contribution of the battery pack in different conditions, as will be explained in the next paragraphs.

Before presenting these results, it should be pointed out that the modal analysis was conducted also for this model configuration. The outcomes were non-conclusive

since the resonance was driven almost solely by the floor panels, thus leading to almost constant results since the floor properties were kept fixed. This analysis will thus be excluded from the next discussion.

On the other side, more interesting were the outcomes from the torsional and bending stiffness analysis, which were able to highlight the high contribution of the battery pack to the integrated underbody stiffness. Data were gathered regarding the battery-less structure mass and stiffness performance.

For what concerns the mass, its contribution to the total structure mass ranged between 21% to 49%, with an average weight of 69 kg. The distribution of the battery pack masses is shown in the histogram in figure 6.19.

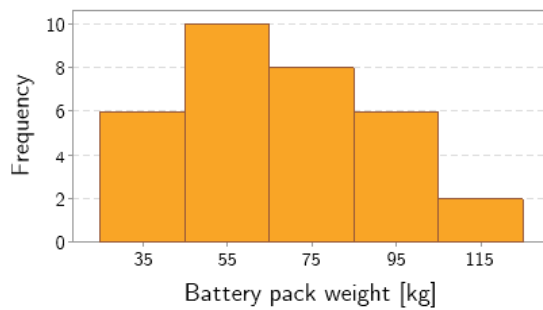
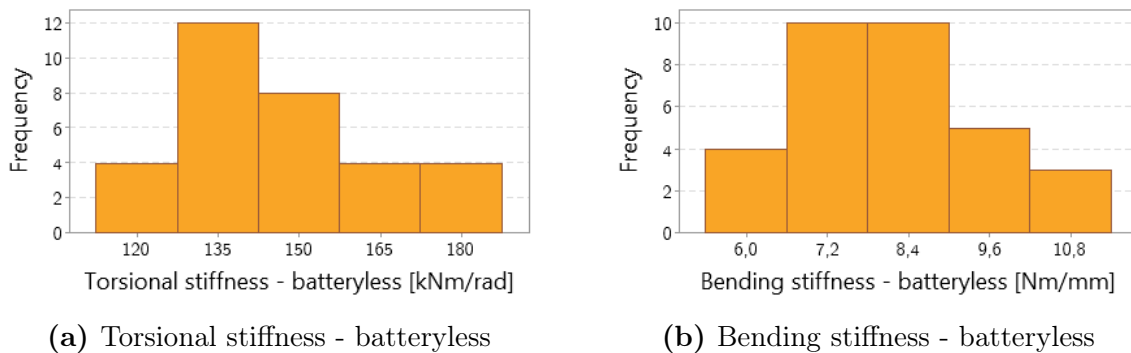


Figure 6.19: Battery enclosure mass distribution

By knowing the stiffnesses for the complete system and the batteryless one it was possible to calculate the battery pack contribution to the assembly rigidity. The resulting torsional and bending stiffness were considerably lower, their distribution is shown in figure 6.20.



(a) Torsional stiffness - batteryless

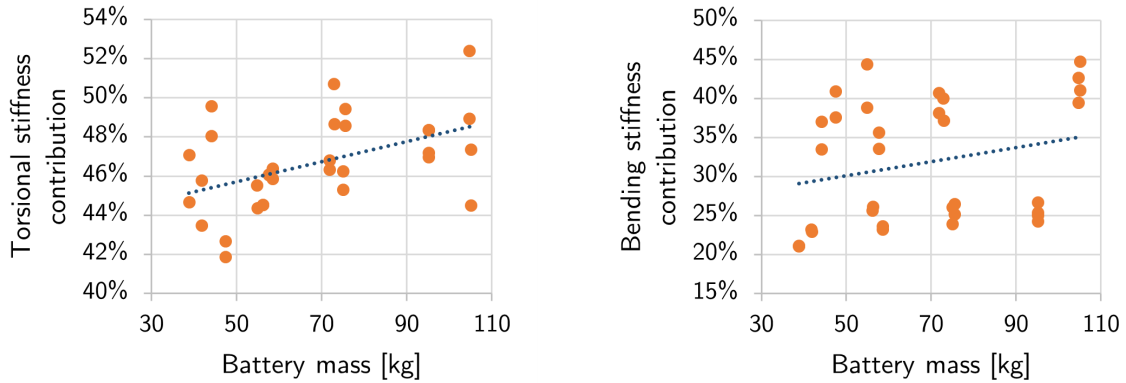
(b) Bending stiffness - batteryless

Figure 6.20: Distribution of underbody stiffness without battery pack structure

For the torsional stiffness, the battery pack contribution ranged from 42% up to 52%, contributing on average to 47% of the stiffness. This contribution is reported in function of the battery mass in figure 6.21a. From the figure, it is possible to see that

the contribution is visibly relevant, with some battery pack solutions able to deliver a very high stiffness at a low weight. These were mainly structures without internal cross-members, showing a simpler and lighter internal structure, while still being able to provide a good improvement to the stiffness.

A similar behaviour was observed for the bending stiffness, for which the battery pack contributed between 21% and 45%, with an average contribution of 32%. The battery pack contribution to the bending stiffness, compared to the battery weight is reported in figure 6.21b.



(a) Torsional stiffness contribution

(b) Bending stiffness contribution

Figure 6.21: Battery pack contribution to system stiffness, in function of battery structure mass

For what concerns the bending stiffness it was possible to highlight the presence of two clusters of solutions, accumulating above and below the trendline in figure 6.21b. The configurations on the top cluster were all characterized by orthogonal torque boxes while the ones in the lower cluster have angled torque boxes. The battery pack mass of the orthogonal torque boxes solutions was slightly higher due to the lack of the top-view chamfering needed to adapt to the angled torque boxes, which effectively reduce the mass of the battery pack structure.

For a comparable weight of the battery pack, this component was more influential on the platform bending stiffness in the configurations with orthogonal torque boxes. This can be explained by the lower performance in bending of the orthogonal torque boxes (see figure 6.12) combined with a low influence of the torque boxes shape on the mass. This led to a greater contribution of the battery pack structure to the platform stiffness when the less stiff orthogonal torque boxes were used.

From this analysis, it was possible to conclude that the battery pack can have structural functions and widely improve the underbody stiffness once installed. Being the

battery pack enclosure necessary, either as a separate structure or directly integrated in the underbody, it can provide large performances improvements to the vehicle dynamics.

Further investigations are necessary to understand which solution is the best compromise between high stiffness and lightweighting. This will be explained more in detail in section 6.4 dedicated to the optimization analysis.

6.3 Panelless Analysis

This analysis was conducted following what was observed in section 6.1.4, in which, the first model resulted to show low-frequency resonance from the large flat panels. In this analysis, the panels were excluded from the model, together with the battery cells mass which was applied on the lower battery pack panel. This allowed to better investigate the general modal deformations for the underbody and battery pack frame structure, without having low frequencies modes from the flat panels altering the result.

For more details on the conducted ANOVA see the section B.2.

6.3.1 First Modal Frequency - Panelless

The modal analysis reported in this section was conducted following the same DOE used for the complete model analysis (reported in chapter A). Nevertheless, the FEM models were modified removing the elements constituting the flat panels. The DOE was still meaningful since the excluded components were not included as input variables; thus, the effects of the variable factors could be accurately described. As previously the first three modes were calculated starting from frequencies higher than 1 Hz to exclude the rigid body modes. The deformations of these modes were analyzed to assess the structure global deformation. In figures 6.22 and 6.23 are reported two examples of the amplified deformations for the first three modes.

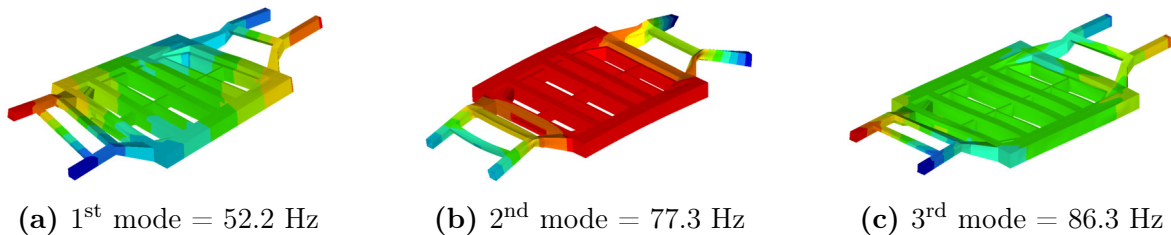


Figure 6.22: Example of modal analysis from panelless DOE run No. 22

Removing the panels the structure showed a global deformation under resonance, with no localized resonances. In particular, all the analyzed model variations showed a

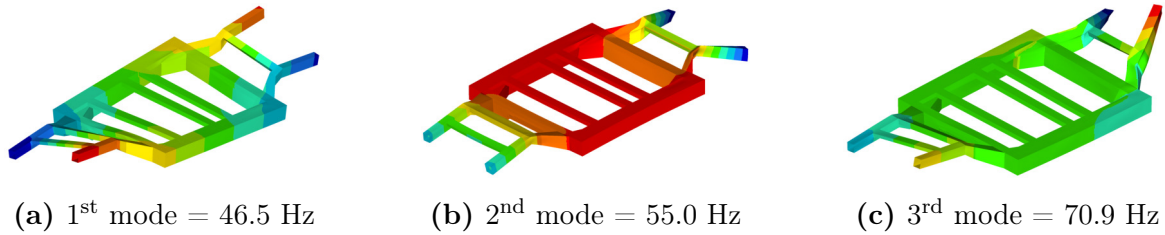


Figure 6.23: Example of modal analysis from panelless DOE run No. 27

torsional deformation for the 1st mode. The 1st resonance frequency was then selected as response since the most significant for the scope of the study [36].

The distribution of the obtained 1st mode response is reported in figure 6.24.

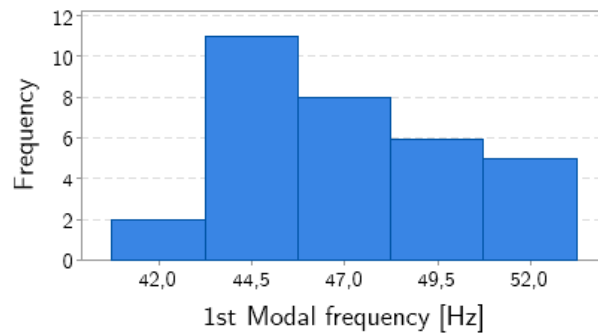


Figure 6.24: Distribution of 1st modal frequency - panelless model

The 1st mode was, in this case, ranging between 42 Hz and 52 Hz with an average around 47 Hz and a standard deviation of 2.9 Hz.

As previously, the pooling excluded several interactions which were considered not influential, with a p-value > 0.05. In this case, all main factors were significant.

Figure 6.25 represents the Pareto chart of the percentage of contribution of the different factors to the variability of the 1st modal frequency response. The most influential factor was the side members material accounting for 69.8% of the variability. This factor was also slightly effective on the torsional and bending stiffness, thus it could be optimized for the dynamic stiffness performances.

The second percentage of contribution was from the rocker internal structure, contributing to 16.1% of the effect. In this case, the factor influence on the mass was quite relevant, so the choice of the sill internal stiffening structure must be carefully evaluated after investigating the factorial plots reported in figure 6.26.

From the third most influential factor, there was a big drop in the influence on the torsional stiffness response. The torque boxes shape, already influential for the torsional stiffness, accounted for only 3.0%. Being this factor just slightly influential

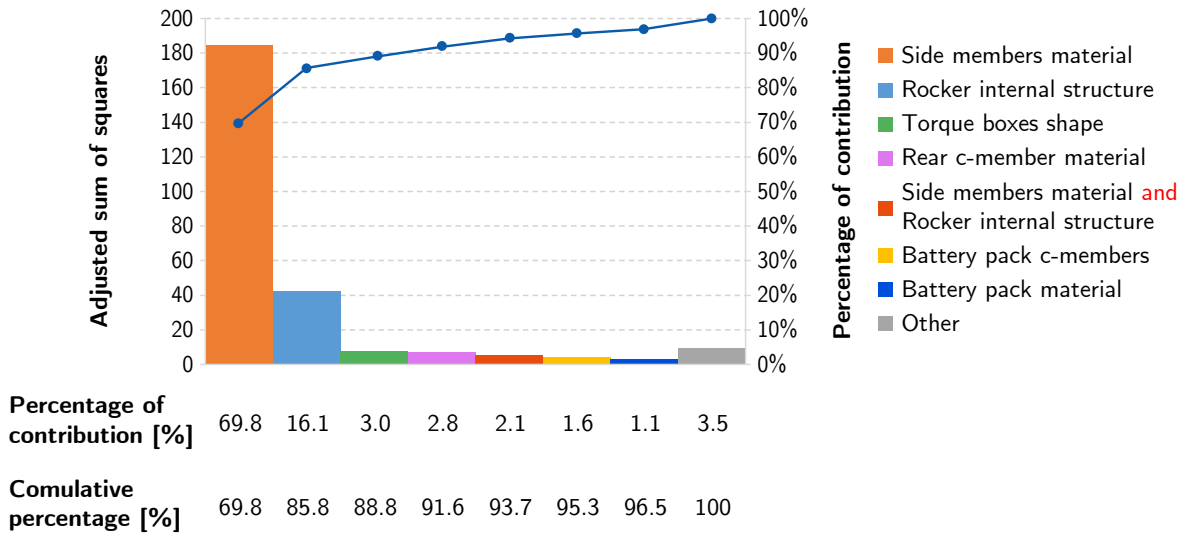


Figure 6.25: Pareto chart of the percentages of contribution for the 1st modal frequency response - panelless model

on the structure mass, it could consequently provide improvements both to the torsional and resonance frequency performance.

Following this factor, the rear cross-member material accounted for 2.8%. This factor was similarly influential for the torsional stiffness but had a low impact on the mass and bending stiffness.

The next was the interaction between the side members material and the rocker internal structure, the two most influential factors. This interaction, or the others with which it is confounded, contributed to 2.1%.

In the end, the battery pack design was less influential in the panelless configuration, with the battery pack cross-members accounting for 1.6% and the battery pack material accounting for 1.1%. These were highly influential for the mass and slightly influential for both the torsional and bending stiffness.

The previously listed factors and interactions combined contributed to 96.5% of the total variability, with the remaining main factors and interactions accounting for 3.5%.

In what follows, the factorial plots were analyzed to investigate the model factors and understand their effect on the response. The plots obtained from the linear regression model are reported, in order of factor influence, in figure 6.26. From these plots, it is possible to confirm the previous analysis.

The side members material was highly influential, with a possible 1st modal frequency improvement in the order of 5 Hz. The aluminum side members delivered the best performance and allowed to reduce the mass of the structure. Being them slightly influential for the static stiffness, an aluminum construction could deliver a

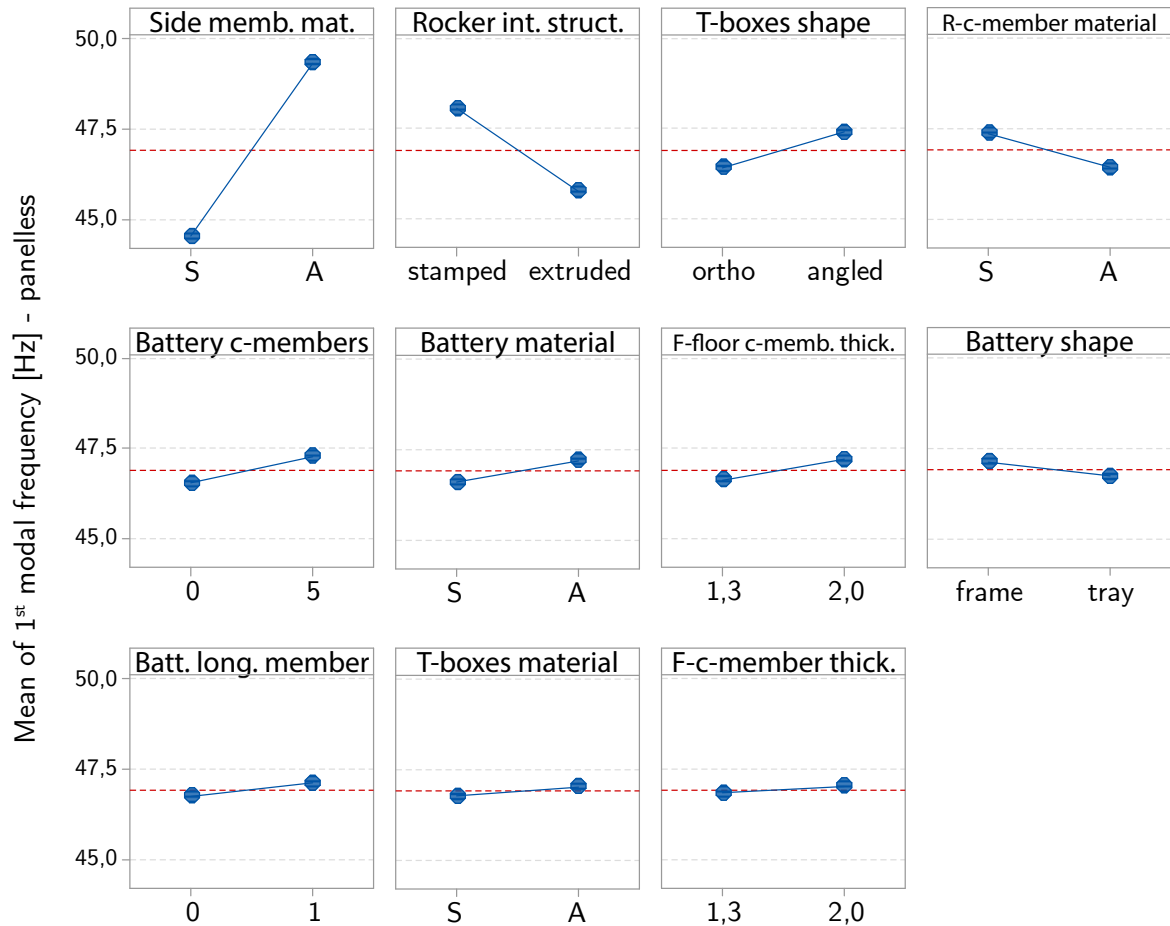


Figure 6.26: Main effect plot for the 1st modal frequency - panelless model, fitted means

good lightweighting and improve the dynamic stiffness with limited effect on torsional and bending stiffness.

The rocker internal structure was found to be better in the stamped variation, which was the best performing one also for the other responses.

The best performing torque boxes shape was the angled one, as already encountered with the previously analyzed outputs. This shape caused a slight increase in the mass but being it almost negligible, the consequent performance improvements, more than compensated for the higher weight.

A rear cross-member made of steel delivered a slight increase in the resonance frequency, but its effect may not be worth the increase in the structure mass.

An high number of battery pack cross-members provided and higher resonance frequency, even if in this case the influence of this factor was much less relevant than for the resonance of the complete model.

Interestingly the aluminum battery pack performed better than the steel one, differ-

ently from the static stiffness responses. This need thus to be chosen as a compromise between lightweighting and static stiffness performance deficit.

A thicker front floor cross-member provided a higher 1st resonance mode, as well as better torsional and bending stiffness. Its influence on the mass was limited, thus the thicker structure could be preferred. The following factors were less influential, but their effect can still be observed in figure 6.26

For what concerns the most relevant interactions, figure 6.27, reports the factorial interaction plots for 1st modal frequency for the panelless model.

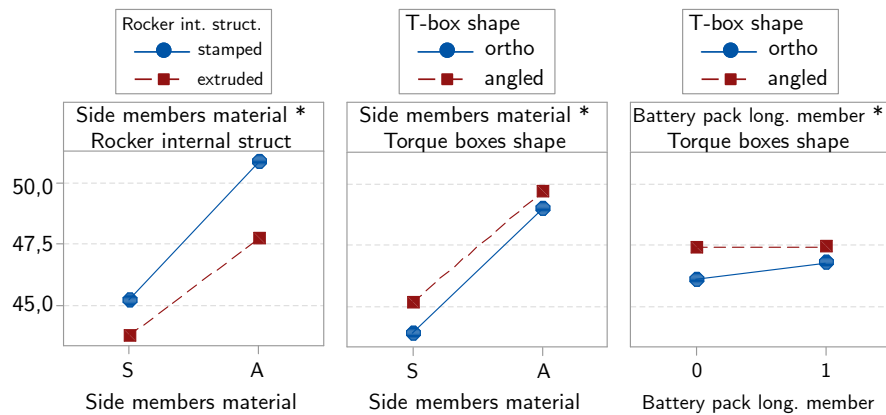


Figure 6.27: Principal interactions effect plot for the torsional stiffness, fitted means

The interaction between the side members material and rocker internal structure followed a predictable trend with the aluminum side-members and stamped stiffening performing at best. Nevertheless this and the other two reported interactions were not strong, as can be observed by the almost parallel interaction lines.

In any case, due to the aliasing from the fractional factorial DOE, it was not possible to draw unequivocal conclusions.

6.4 Optimization and Stiffened Panels Analysis

The final analysis was conducted to obtain two different optimized solutions through the Minitab[®] response optimizer. The software used the derived linear model to predict the best level for each parameter to reach the desired targets. For the 1st modal frequency, given the more meaningful results, the optimization was conducted with the model derived from the panelless analysis.

In particular, the following optimizations were conducted:

- *1st optimization.* The mass was minimized, and all the other responses were maximized

- *2nd optimization.* The mass was minimized, the bending and torsional stiffness were set to be at least higher than the 75th percentile of the obtained results, and the 1st modal frequency of at least 45 Hz as suggested in [36]

After obtaining the suggested values for the different factors, the software also predicted the values for the responses. These needed to be validated through FEA especially since the linear model could lead to some estimation errors.

After validating the solution, a final improvement was implemented by applying a stiffening to the floor and battery pack flat panels by embossing. This final analysis was meant as a complement of the previous to assess the possible improvements in the resonance performance from the panels design.

In the following, the results obtained for the two optimizations analysis are reported.

6.4.1 First Optimization

The 1st optimization aimed at minimizing the mass, while maximizing the other responses. The optimization targets are shown in table 6.1.

Table 6.1: Targets for 1st response optimization

Response	Target
Mass	Minimize
Torsional Stiffness	Maximize
Bending Stiffness	Maximize
1 st Modal frequency	Maximize

The software conducted the optimization through the previously derived linear model and delivered the following suggested parameters, reported in table 6.2.

The selected rocker internal structure was the stamped one, which was much lighter than the extruded stiffening and was outperforming the aluminum internal structure in every response apart from the bending stiffness.

The torque boxes were selected as angled since this parameter had minimal influence on the mass and delivered better performances in all the other responses.

The lower battery enclosure was suggested as a frame structure. This solution was actually heavier than the tray one but performed slightly better in the modal resonance. On the contrary, the tray performed better both in torsional and bending stiffness. Despite that, the optimizer selected a simple internal structure, with just one longitudinal member, thus possibly leading to the need for an external frame structure.

No cross-members were inserted in the battery pack. These were highly influential on the mass, while less influential on the other responses.

Table 6.2: Parameters settings for 1st optimized solution

Factor Type	Factor	Selected Level
Geometry	Rocker internal structure	Stamped
	Torque boxes	Angled
	Lower enclosure	Frame
	No. battery pack cross-members	0
	No. battery pack long. members	1
Material and thickness	Side members	Aluminum
	Torque boxes	Steel
	Rear cross-member	Steel
	Front cross-member	High thickness
	Front-floor cross-member	High thickness
	Battery pack	Aluminum

One longitudinal member was inserted, being slightly influential on the mass it could provide slight static and dynamic stiffness improvements at a low weight penalty.

For what concerns the material and thickness parameters, the side members were selected as aluminum. This factor was slightly influential on the torsional and bending stiffness, with the steel side members performing better. However, it was the most influential in the resonance mode analysis with the aluminum members performing better and allowing also considerable lightweighting.

The torque boxes material was chosen as steel. This parameter was not influential on the mass, but the steel made configurations obtained better performances for the torsional stiffness and the bending stiffness, for which it was the most influential parameter. The aluminum torque boxes performed slightly better in the modal frequency response, but the improvement was just marginal.

The rear cross-member material was selected as steel. This choice caused a minimal weight increase while improving all the other performances. The same reasoning is valid for the front and front floor cross-members, which were selected as the higher stiffness steel material, slightly affecting the mass, but considerably improving the torsional and bending stiffness.

In the end, the battery pack was selected as aluminum material. This factor was the most influential on the mass and the aluminum material provided better performances for the dynamic stiffness. The torsional and bending stiffness were slightly penalized but the weight saving from the aluminum construction was much more relevant than the static stiffness improvements from steel construction.

The optimized configuration was implemented in the FEM model and tested to validate the solutions obtained from the linear regression model.

The obtained results are reported and compared to the optimization prediction in table 6.3.

Table 6.3: Responses prediction and validation for the 1st optimization analysis

Response	Minitab [®] prediction	FEA response	Prediction error
Mass [kg]	162.8	169.5	-4.0%
Torsional Stiffness [kNm/rad]	335.5	331.1	1.3%
Bending Stiffness [kN/mm]	12.6	12.4	1.7%
1 st Modal frequency ² [Hz]	52.2	52.5	-0.6%

These results confirmed that the model, despite being a simplified linear regression it is able, in this case, to predict quite accurately the results.

The obtained configuration was then compared with the other available results to assess the obtained improvements. Figure 6.28 shows the comparison of the optimized solution with to the ones obtained through the DOE for what concerns torsional and bending stiffness and 1st modal frequency.

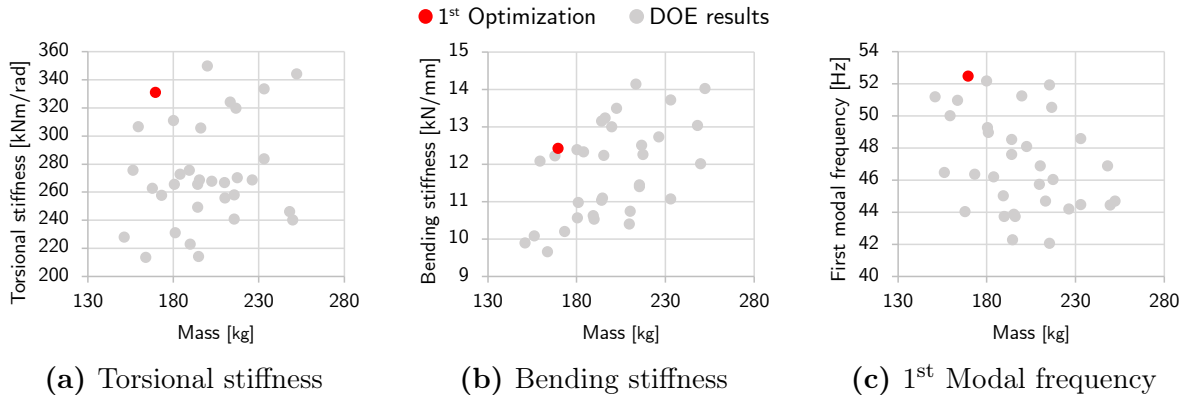


Figure 6.28: Comparison between 1st optimized solution and DOE responses in function of the structure mass

For the torsional stiffness, the achieved performance was among the best obtained, with a considerable weight reduction. The mass was in fact lower than the 15th percentile, while the torsional stiffness was above the 90th percentile.

Likewise, for the bending stiffness, which was at around the 70th percentile, but still with a higher performance than the other mass equivalent solutions.

² From panelless analysis

For the modal frequency, the achieved result was better than any other obtained through the DOE configurations, still with considerable lightweighting.

For what concerns the low-frequency panels resonance, this phenomenon was still present in the optimized solution, with a complete model resonance of 8.5 Hz. This resonance arose in the lower battery pack panel as shown in figure 6.29a. Removing the

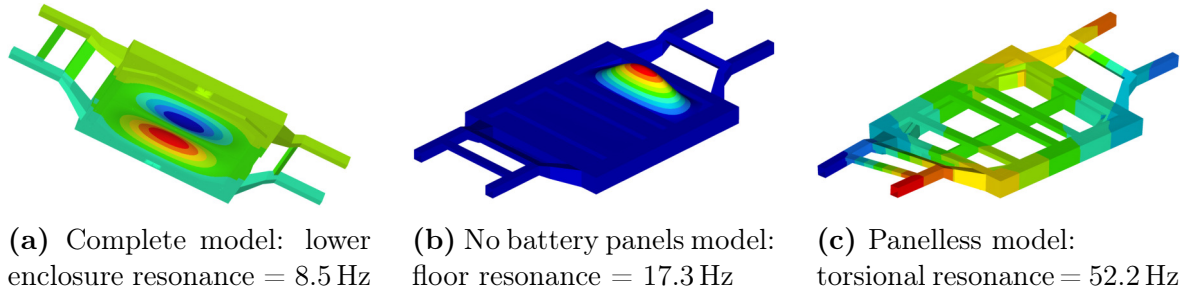


Figure 6.29: First modal frequencies for the 1st optimized flat panels model, from complete model to panelless model

battery pack panels or the cell masses, the first resonant frequency increased to 17.3 Hz, with the resonance caused in this case by the floor panel, as shown in figure 6.29b. In contrast, removing the panels led to the previously reported resonance of 52.2 Hz, which showed a torsional deformation mode (see figure 6.29c).

Stiffened Panels - First Optimization

A stiffened panels design was then implemented with embossed panels both for the floor and the battery pack, as reported in figure 6.30.

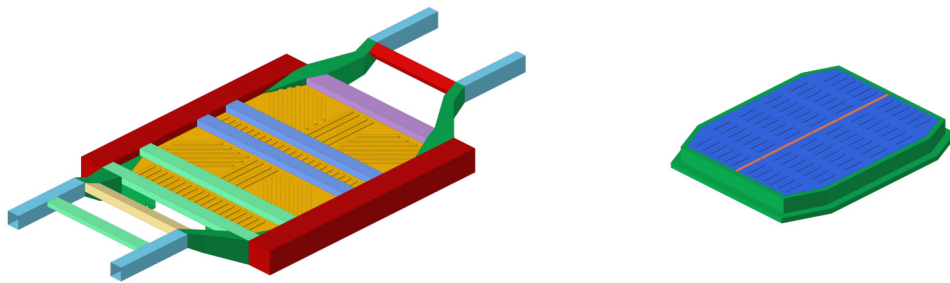


Figure 6.30: Embossed floor and battery pack flat panels - 1st optimization

The FEM analyses were repeated on this new model, delivering the results listed in table 6.4.

The mass was slightly higher than the flat panels model, by about 2.5%. An unexpected outcome was found for the torsional stiffness which resulted to be 8% lower than the original model.

Table 6.4: Outputs from stiffened panels model analysis for the 1st optimization

Output	FEA response
Mass [kg]	173.7
Torsional Stiffness [kNm/rad]	304.4
Bending Stiffness [kN/mm]	12.4
1 st Modal frequency ³ [Hz]	53.2

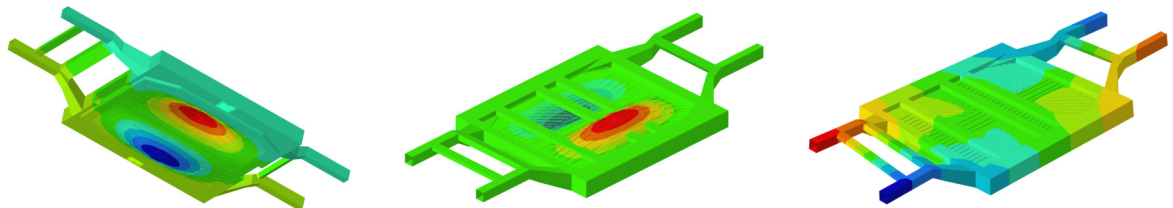
This aspect will need further investigations in the future to assess the root causes of this unexpected performance deficit. The bending stiffness was instead comparable.

For what concerns the 1st modal frequency, in this case, the frequency reported in table 6.4 was evaluated for the structure with the battery pack panels removed.

In fact, the improvements for the complete embossed panels model were marginal at 8.9 Hz. The lower battery pack panel was still causing the resonance despite the stiffening structures (see figure 6.31a).

Removing the simulated battery cells led to a resonance frequency of 24.9 Hz, which was higher than the one obtained with flat panels, but still caused by the resonance of the top battery pack panel as shown in figure 6.31b.

By completely removing the battery pack stiffened panels, the resulting 1st resonance frequency was 53.2 Hz, higher than the one from the panelless model but with the floor panel installed. In this case, the resonance deformation was of the torsional type (see figure 6.31c).



(a) Complete model: lower enclosure resonance = 8.9 Hz (b) No battery cells model: floor resonance = 24.9 Hz (c) No battery panels model: torsional resonance = 53.2 Hz

Figure 6.31: First modal frequencies for the 1st optimized embossed panels model, from complete model to model with no battery pack panels

This confirmed the positive effect of panel embossing in increasing the dynamic stiffness. The embossing was still not sufficient to guarantee adequate battery pack stability due to the relatively simple internal structure with only one longitudinal member. Further stiffening, of the panels or in the internal structure is needed to avoid low-frequency resonance of the battery pack panels.

³ Analysis with battery pack panels removed

6.4.2 Second Optimization

The 2nd optimization aimed at minimizing the mass, while reaching a minimum target for the other responses. The optimization targets are shown in table 6.5.

Table 6.5: Targets for 2nd response optimization

Response	Target
Mass	Minimize
Torsional Stiffness	>290 kNm/rad
Bending Stiffness	>12.8 kN/mm
1 st Modal frequency	>45 Hz

The software conducted the optimization through the previously derived linear model and delivered the following suggested parameters, reported in table 6.6.

Table 6.6: Parameters settings for 2nd optimized solution

Factor Type	Factor	Selected Level
Geometry	Rocker internal structure	Stamped
	Torque boxes	Angled
	Lower enclosure	Tray
	No. battery pack cross-members	5
	No. battery pack long. members	1
Material and thickness	Side members	Steel
	Torque boxes	Steel
	Rear cross-member	Aluminum
	Front cross-member	High thickness
	Front-floor cross-member	Low thickness
	Battery pack	Aluminum

The selected rocker internal structure was again the stamped one, with the previously listed advantages.

Likewise the torque boxes were again selected as angled.

The lower battery enclosure was suggested as a tray structure. This solution was on average lighter than the framed battery packs but performed slightly worse in the modal resonance. On the other hand, it delivered higher torsional and bending stiffness.

The internal structure was in this case more complex, with five cross-members and one longitudinal member. The response optimizer suggested 4.5 cross-members, which needed to be rounded up to the following integer. This highly complex internal

structure has a high influence on the mass but could provide improvements to the bending stiffness.

For what concerns the material and thickness parameters, the side members were selected as steel. This, even if slightly increasing the mass of the structure could be beneficial for a higher torsional and bending stiffness. Nevertheless, the steel side members could perform slightly worse in the dynamic stiffness analysis.

The torque boxes material was chosen as steel, as in the previous optimization.

The rear cross-member material was selected as aluminum. This decreased the static and dynamic stiffness performances in favour of a slightly lower weight.

The front cross-member was selected as high thickness steel, slightly affecting the mass, but considerably improving the torsional and bending stiffness.

The front floor cross-member was instead selected as low thickness offering higher lightweighting possibilities than the front cross member and being just slightly influential on the stiffness.

In the end, the battery pack material was selected as aluminum, allowing high weight saving with a low performance penalty. The optimized configuration was implemented in the FEM model and tested to validate the solutions obtained from the linear regression model.

The obtained results are reported and compared to the optimization prediction in table 6.7.

Table 6.7: Responses prediction and validation for the 2nd optimization analysis

Response	Minitab [®] prediction	FEA response	Prediction error
Mass [kg]	180.5	183.0	-1.4%
Torsional Stiffness [kNm/rad]	308.6	311.0	-0.8%
Bending Stiffness [kN/mm]	12.8	13.0	-1.2%
1 st Modal frequency ⁴ [Hz]	45.5	45.5	0.0%

These results confirmed again the capability of the model to accurately predict the FEA results.

The obtained configuration was then compared with the other available results to assess the obtained improvements. Figure 6.32 shows the comparison of the 2nd optimized solution against the ones obtained from the DOE and from the 1st optimization for what concerns the studied static and dynamic stiffness responses.

For the torsional stiffness, the achieved performance was lower than the one from the 1st optimization but still higher than the 80th percentile. However, also the mass was higher than the one in the 1st optimization, reaching the 25th percentile of the

⁴ From panelless analysis

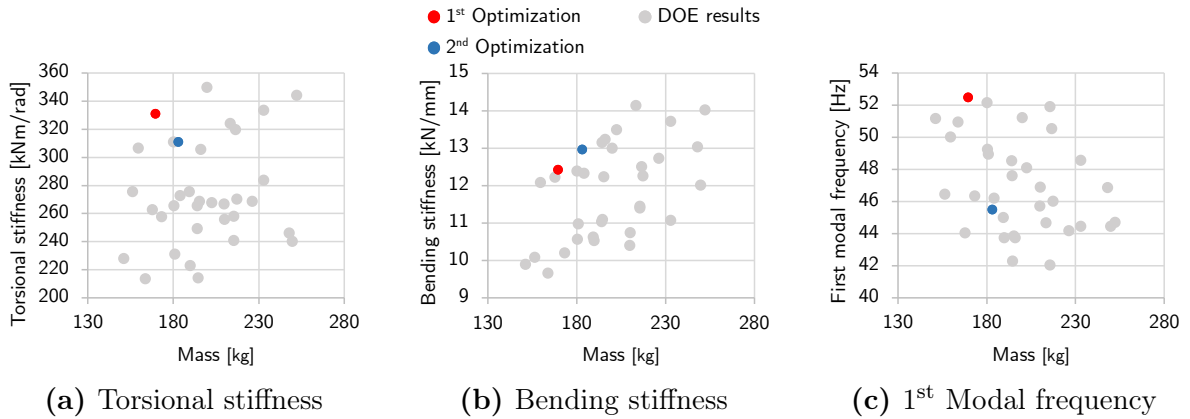


Figure 6.32: Comparison between 1st and 2nd optimized solutions and DOE responses in function of the structure mass

results from the DOE. On the other hand, the bending stiffness was higher than the first optimization, reaching the 80th percentile.

To conclude, the 1st resonance frequency was considerably lower when compared to the one obtained in the first optimization, but still satisfying the target of 45 Hz. However, further observations are needed for what concerns the dynamic stiffness analysis.

For the complete model, low-frequency resonant modes were present again due to the floor resonance. Thanks to the complex battery pack internal structure, the battery pack panels were not resonating, thus in this case the low-frequency resonance of 17.2 Hz was due to the underbody floor panels, as shown in figure 6.33a.

This was confirmed by the subsequent analyses which were conducted removing first the battery cells mass and next by removing completely the battery pack panels. This led to basically no improvements in the 1st resonant frequency that was mainly driven by the vehicle floor panels (see figure 6.33b).

The panelless structure showed instead a 1st mode of 45.5 Hz, with a torsional resonance deformation, shown in figure 6.33c

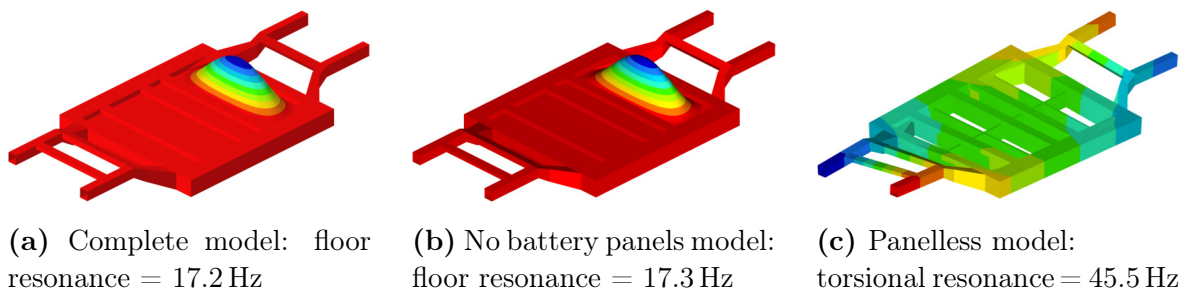


Figure 6.33: First modal frequencies for the 2nd optimized flat panels model, from complete model to panelless model

Stiffened Panels - Second Optimization

A stiffened panels design, shown in figure 6.34 was thus implemented for the second optimized model, as already done for the 1st optimization.

The FEM analyses were repeated on the new model, delivering the results in table 6.8. The mass was slightly higher than the flat panels model, by about 2%. Again, the torsional stiffness was 7% lower than the original model, a result that needs more investigations in the future. Concerning the bending stiffness, the stiffened panels model delivered comparable results to the flat panels one.

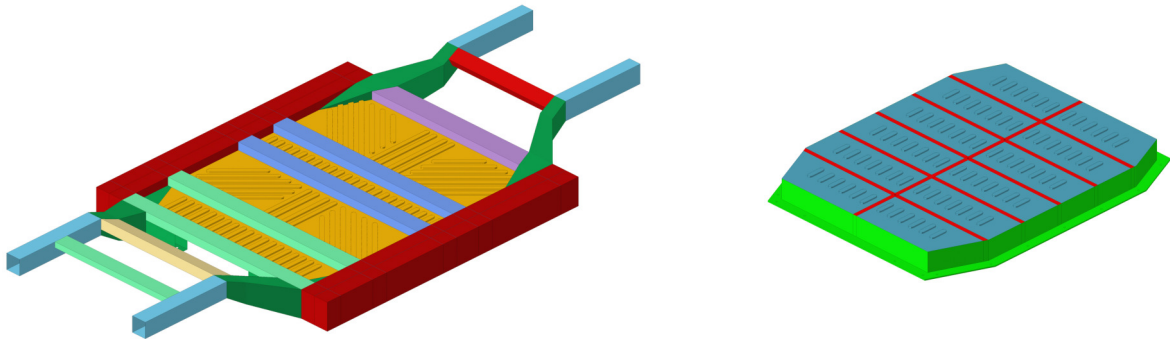


Figure 6.34: Embossed floor and battery pack flat panels - 2nd optimization

The 1st modal frequency listed in table 6.8 of 54.4 Hz, in this case, is the resonance frequency of the complete model. The model included all the stiffened floor and battery

Table 6.8: Outputs from stiffened panels model analysis for the 2nd optimization

Output	FEA response
Mass [kg]	186.7
Torsional Stiffness [kNm/rad]	289.2
Bending Stiffness [kN/mm]	13.0
1 st Modal frequency ⁵ [Hz]	54.4

pack panels and was still able to deliver a high 1st resonant mode, with low localized panels resonance.

In fact, the complete model showed a torsional resonance deformation, with minimal resonance of the lower battery plate as shown in figure 6.35.

This confirmed the need for an improved design of the battery pack to avoid resonance of the battery pack panels. It must be reminded that the used model was extremely simplified and not representative of the real internal structure of the pack.

⁵ Analysis with battery pack panels removed

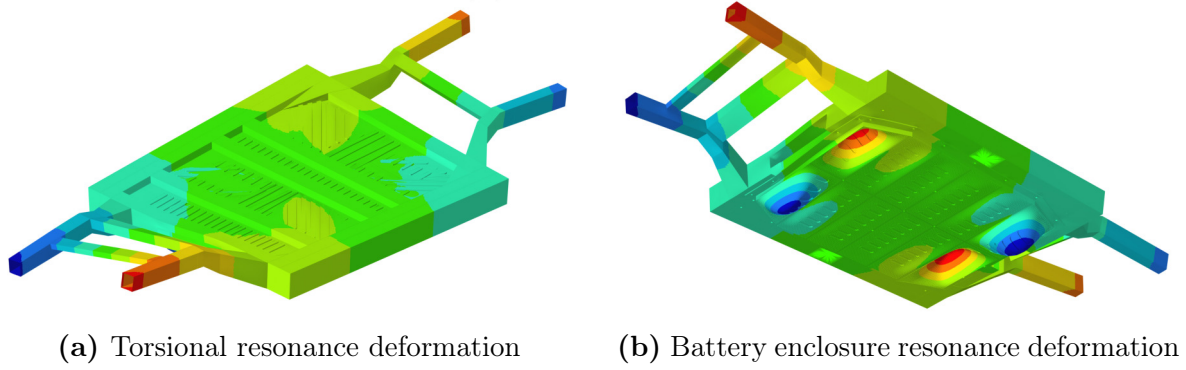


Figure 6.35: First modal frequency = 54.4 Hz for the 2nd optimized embossed panels model, complete model

Despite that, the study was able to put in evidence the importance of internal battery pack stiffening for the dynamic stiffness performances of the system. Given the low influence of the internal structure on the static stiffness, and its heavy weight, different stiffening structures could be implemented in future developments, to add localized stiffness on the panels, without considerably increasing the mass.

In general, the analysis confirmed the positive effect of the embossed panels but highlighted the need for further stiffening for larger span panels. In fact, in this case, the battery pack structure with five cross-members and one longitudinal member contributed to increase the battery pack panels dynamic stiffness by reducing their span.

To conclude the two previously obtained optimizations were compared. The data are normalized with a rescaling or min-max normalization as in equation (6.1), accounting for the responses from the DOE and the two optimizations:

$$\bar{x} = \frac{x - \min(x)}{\max(x) - \min(x)} \quad (6.1)$$

From figure 6.36 it is possible to see how both solutions provided good lightweighting and static stiffness, with the 1st edging in torsional stiffness and the 2nd performing better in bending stiffness. The 1st optimized solution showed however a considerably higher 1st resonance frequency as well as a lower structure mass.

For the scope of the study, the 1st solution is thus preferable, considered that the reached bending stiffness is already at a reasonable level, without the need of reaching the higher performance of the 2nd solution.

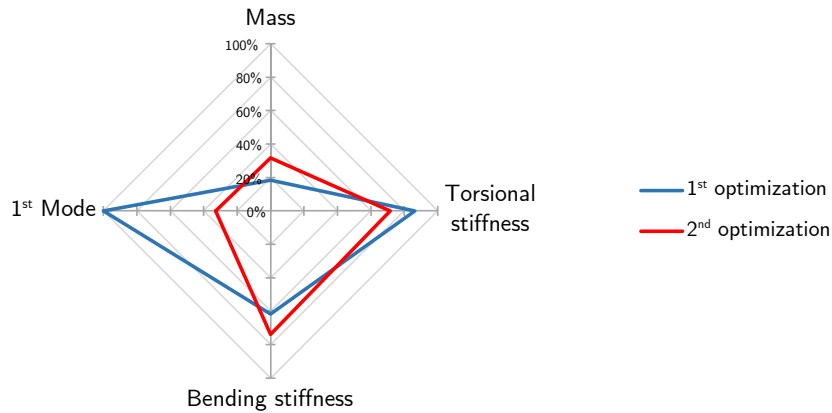


Figure 6.36: Comparison between 1st and 2nd optimization normalized values

6.5 Design Guidelines

After presenting the obtained results, the collected information is summarized in what follows to provide some preliminary design guidelines, to achieve structural lightweighting, while maintaining good static and dynamic stiffness performance. Each of the studied parameters is presented analyzing its influence on the different responses and adding additional considerations regarding possible critical aspects which need to be investigated more in detail.

The parameters are compared according to their influence on five of the gathered response:

- *Mass*
- *Torsional stiffness*
- *Bending stiffness*
- *1st Modal frequency - complete model*
- *1st Modal frequency - panelless model*

Even if influenced mainly by non-variable factors, which were excluded from the DOE, the 1st modal frequency for the complete model was still included for completeness and to evidence the need for flat panels stiffening.

In this section only the influence of the main factors is analyzed since, as already explained, due to the confounding from the fractional factorial DOE, it was not possible to unequivocally attribute one effect to a specific interaction.

In general, the guidelines presented in what follows coincided with the configuration of the 1st optimization.

6.5.1 Structure Geometry and Layout

In this section, the guidelines for the geometrical layout of the underbody and battery pack are outlined according to the results previously analyzed.

Rocker Internal Structure

The rocker internal structure was highly influential on the mass of the system and the global structure resonance for the panelless mode. Figure 6.37 shows the percentage contribution of the five responses under analysis and highlights the preferred level of this factor for each response, stamped internal structure in red and extruded in blue. Despite the better performance of the extruded stiffening in bending, the stamped

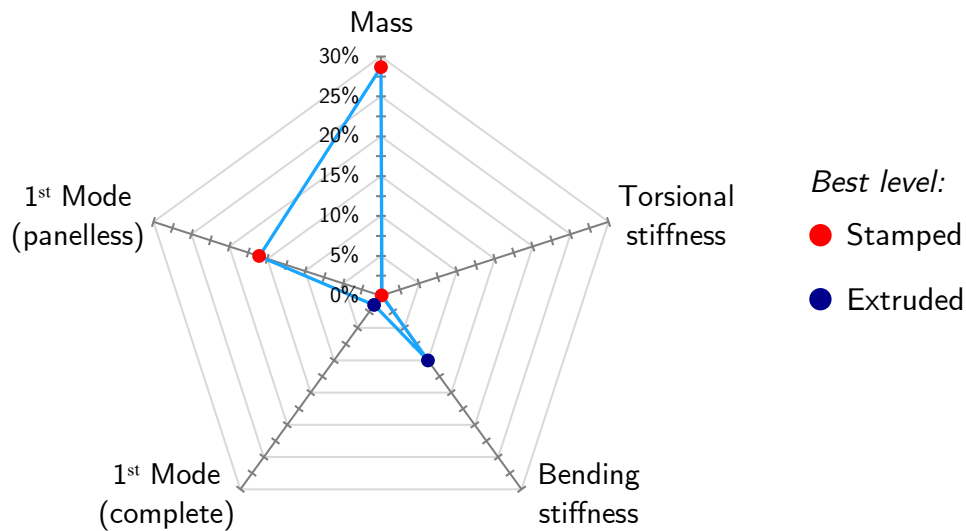


Figure 6.37: Rocker internal structure influence and preferred configuration for the analyzed responses

structure prevailed in the panelless modal analysis as well as in the torsional stiffness. Furthermore, it allowed considerable lightweighting with the only drawbacks being a slight decrease in the bending stiffness performances. The extruded stiffening performed slightly better in the complete model resonance, but its influence was minimal, and the resonance was driven mainly by the flat panels.

The stamped structure also offers a simpler construction than the extruded stiffening beam, as well as a simpler assembly. The main rocker structure can be combined with the stiffening by spot welds without the need for structural adhesive [36, 79].

It must be noted that the extruded stiffening could be crucial for side-impact absorption, thanks to the almost three times higher crash energy absorption from aluminum [103] and the extruded structure which could be optimized for progressive crushing and

energy redistribution [69]. Several solutions from the benchmarking analysis showed an extruded internal structure, thus additional analyses are necessary to assess its importance for lateral impact protection, both for the occupants and battery pack.

A compromise solution may be a combination of a smaller and lighter aluminum extrusion with a stamped steel stiffening, for a lightweight solution with increased crash absorption capabilities.

Further improvements could then be reached, for both the stamped stiffened and extruded stiffened rockers, by optimizing the rocker cross-section for a more elaborated and weight-efficient design.

Torque Boxes Shape

The torque boxes shape was slightly influential on the mass response as well as for the bending stiffness and complete model resonance, being more influential for the panelless resonance. On the other hand, this parameter was crucial for the torsional stiffness, being the most influential at around 50% of the contribution to this response. Figure 6.38 compares the influence of the torque boxes shape on the mentioned responses. In most cases, the preferred configuration was the angled torque boxes, guaranteeing

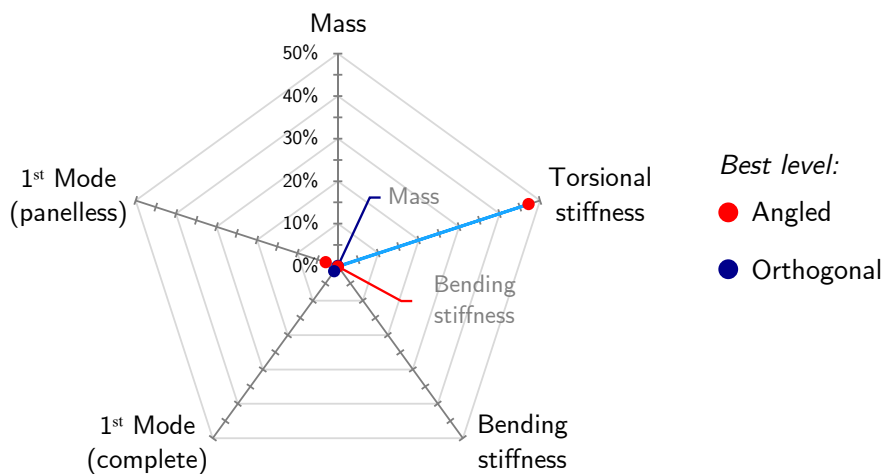


Figure 6.38: Torque boxes shape influence and preferred configuration for the analyzed responses

better performances, falling behind the orthogonal one, just in the complete model dynamic stiffness. Again, this last result was less relevant since the resonance was mainly derived by non-variable parameters. The angled torque boxes seemed thus to be preferable, despite their slightly higher mass.

It must be noted that choosing this type of torque boxes implies a more complex battery pack design, which needs chamfering to fit in the non-rectangular underfloor.

This may also decrease the volumetric cell integration if the battery cells are larger and cannot be modelled to adapt to the more complex battery pack shape.

Moreover the implemented designs for orthogonal and angled torque boxes were considerably different, with the angled one offering a stiffer structure. In spite of that, these results contributed to highlight the critical influence of the design of this component for the platform performances.

Further investigations are necessary to optimize the design of this structure, which revealed to be crucial in determining the torsional stiffness performances of the underbody.

Lower Battery Pack Enclosure Shape

The shape of the lower battery pack enclosure was only minimally influential on the analyzed responses, with the maximum contribution at around 0.5% on the panelless 1st mode. The influence was lower to negligible on the other responses. Figure 6.39 shows the influence of the lower battery pack enclosure shape on the studied responses. At first, the most advantageous solution seemed to be tray lower enclosure, which also

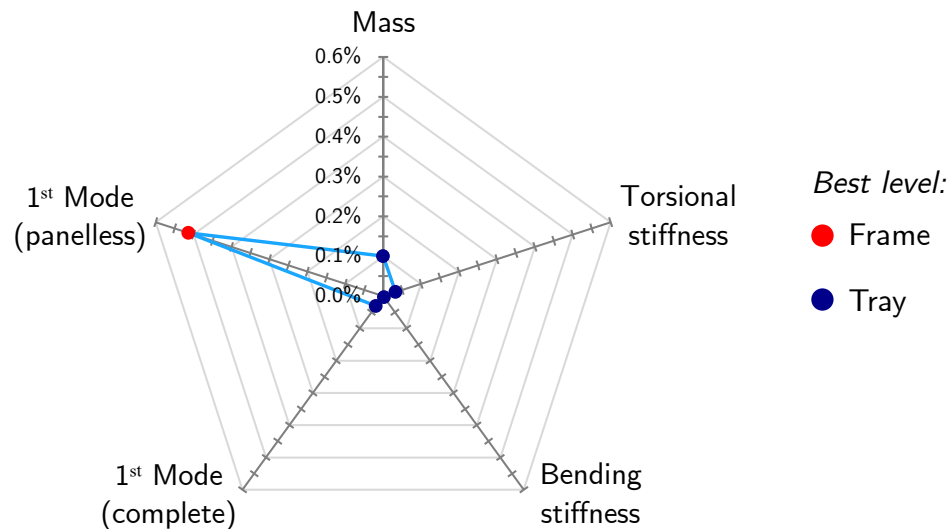


Figure 6.39: Lower battery pack enclosure shape influence and preferred configuration for the analyzed responses

delivered a lower structure mass. However, the highest influence was, as already said, on the 1st resonance mode in the panelless configuration. In this case, the best solution was the frame structure.

The frame structure could thus be preferred despite the slight penalty in mass and torsional stiffness. Moreover, the influence on all responses is limited, thus different designs interpretations are possible in this case.

It must be underlined that the battery pack needs proper side impact absorption structure to avoid damages to the battery cells [2]. The tray structure is, in general, not capable of providing sufficient protection and thus usually needs some crash absorption structures in the rocker rail, like an extruded internal structure [24]. At the same time, the stamped internal structure for the rocker may not be sufficient to dissipate the side impact and additional absorption structures may be necessary on the battery pack. In this case, the frame solution offers a more effective crash absorption structure. [24, 80].

Number of Battery Pack Cross-Members

The number of battery pack cross-members was the most influential on the complete model resonance, as well as being quite impacting on the structure mass. Figure 6.40 shows the influence of this parameter on the studied responses. The parameter was

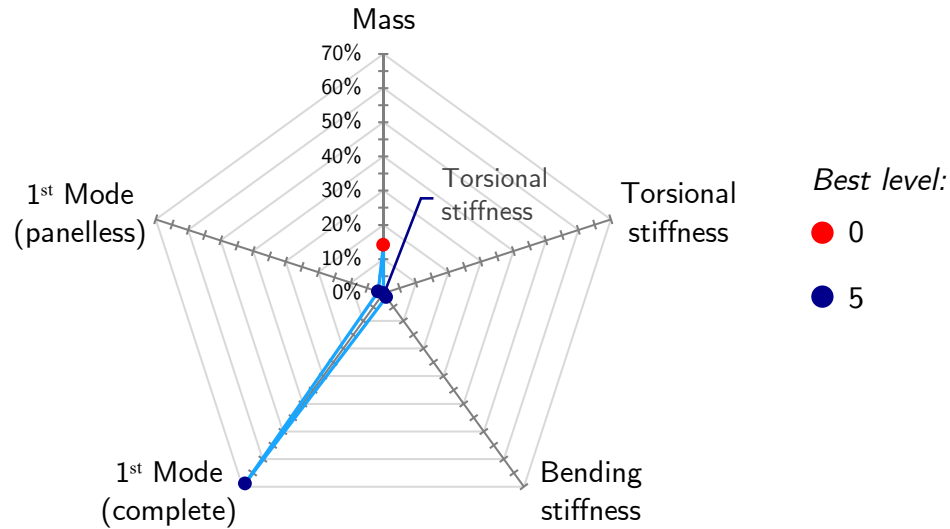


Figure 6.40: Number of battery pack cross-members influence and preferred configuration for the analyzed responses

marginally influential on the static stiffness and the dynamic stiffness of the panelless structure, with the more complex internal structure with five cross-members performing better. The highest influence was on the complete model 1st resonance frequency, thanks to the stiffening provided by the cross members to the battery pack flat panels.

Despite that, this solution is not the most weight-efficient to stiffen the panels, adding considerable weight to the structure. Furthermore, the future trends of the cells-to-pack integration ask for simpler battery pack internal structures, with fewer subdivisions [24]. This leads to the preferred choice being the battery pack with no cross members. Further solutions need to be studied to improve the stiffness of the

battery pack panels, as well as assess the possible need of internal cross members to redistribute the load from a side impact.

Moreover, removing the cross members decreases the possibilities of connecting the battery pack to the underbody in the central part of the floor. The fastened connection needs, usually, a stiff structure to offer adequate stability, which is not provided by the battery pack flat panels.

Number of Battery Pack Longitudinal Members

This parameter was tested considering one or no longitudinal member. Figure 6.41 shows the influence of this parameter on the responses under analysis. This factor was

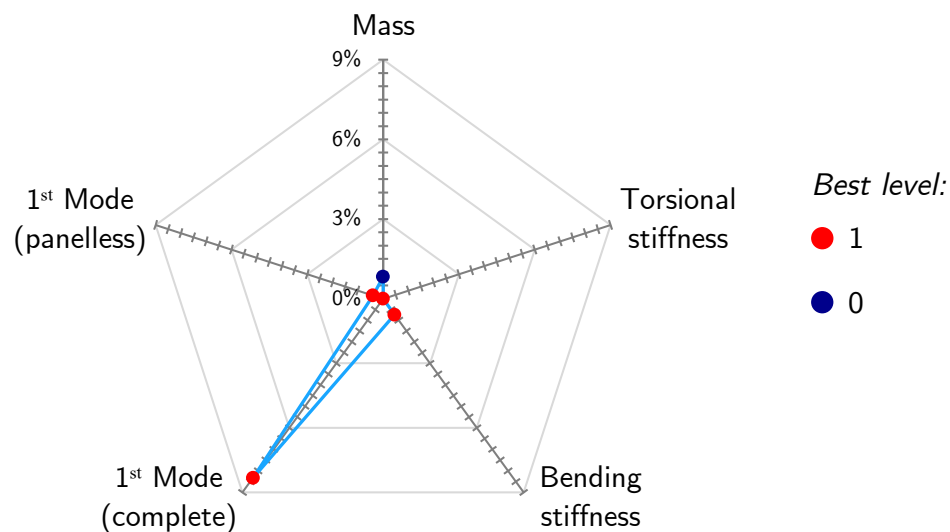


Figure 6.41: Number of battery pack longitudinal members influence and preferred configuration for the analyzed responses

slightly influential on the mass and in general on all the responses, except the 1st mode of the complete model. This was again determined by the stiffening action provided by the internal structure to the battery pack flat panels. In addition, its influence was marginal, but considerable on the bending stiffness, for which better performance was achieved by the packs with one longitudinal member.

Also in this case, more weight-efficient solutions to stiffen the flat panels are needed. Anyway, since the longitudinal member contributed just slightly to the mass it could be included into the structure, allowing an improvement in the bending stiffness as well as providing room for bolted connections to the central underbody floor. The complexity of the integral structure would not increase significantly in this case, allowing an almost perfect and efficient cell-to-pack integration [24].

6.5.2 Material and Thickness

In this section, the guidelines for the material choice and material thickness of the underbody and battery pack are outlined according to the results previously analyzed. To recall what was explained in section 5.1.3, some parameters were made variable between steel or aluminum, while for other the material was fixed as steel and the thickness was made variable.

As it will be noted in the following, it is important to highlight also the more complex joining techniques between dissimilar materials, due to the impossibility of direct welding and the possible galvanic joint effect.

Side Members Material

The side member material was the most influential factor on the panelless 1st modal frequency, with a lower influence on the other responses. In figure 6.42 are reported the influence of this factor on the analyzed outputs. The aluminum side members

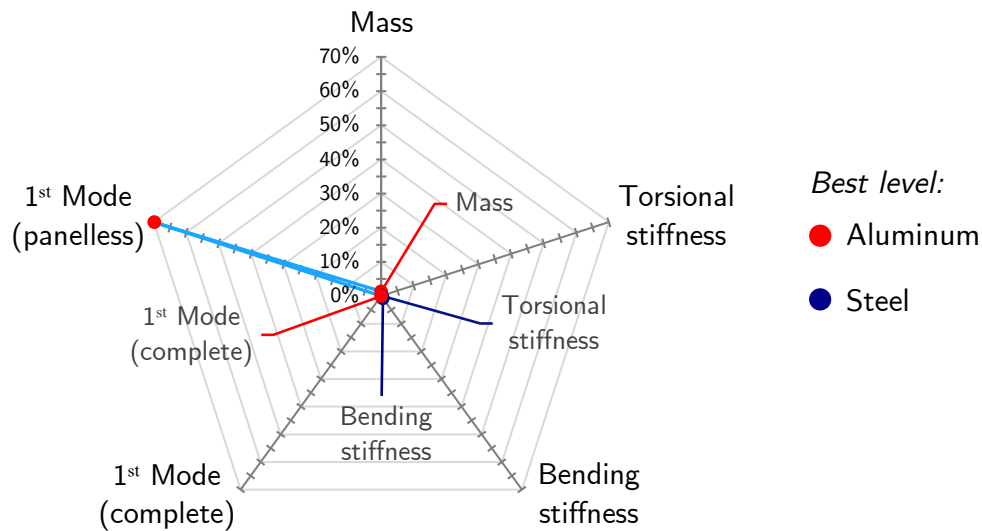


Figure 6.42: Side members material influence and preferred configuration for the analyzed responses

allowed a low but considerable lightweighting while performing better in both modal tests. The steel side members delivered slightly better performances in torsional and bending stiffness.

However, the aluminum members section can be further optimized to reach comparable stiffness, while still providing lightweighting to the structure.

Furthermore, the design of these components is driven also by the need to efficiently absorb frontal and rear impacts. In this case, the good crash absorption properties of aluminum [103] could be another advantage for choosing this solution.

Torque Boxes Material

The torque boxes material was the most influential on the bending stiffness, and at the same time was highly impacting on the torsional stiffness. The percentage of contribution of this factor on the different responses is presented in figure 6.43.

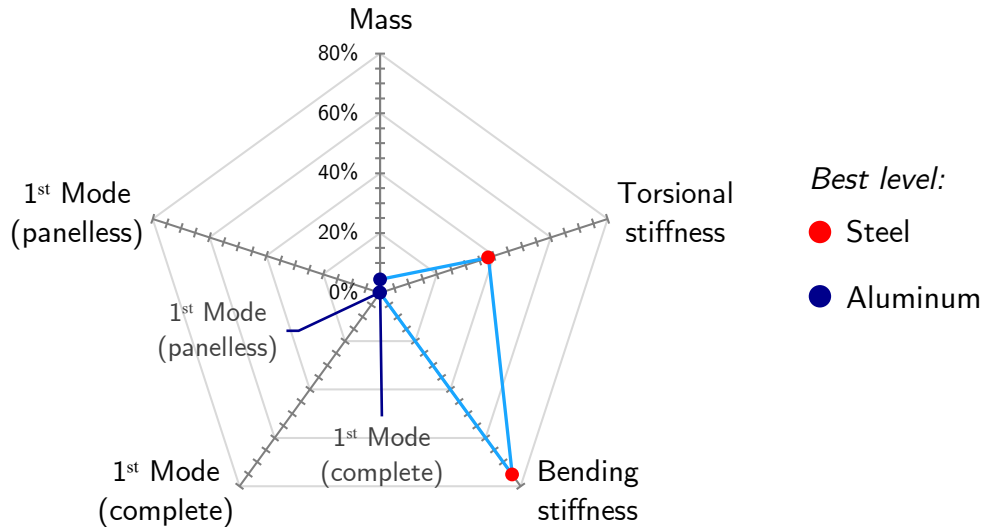


Figure 6.43: Torque boxes material influence and preferred configuration for the analyzed responses

The preferred material resulted to be steel in this case. In fact, the torque boxes material was slightly influential on the mass, and despite the higher mass of the steel component, the higher static stiffness was more relevant than the possible lightweighting. Additionally, given the current trend towards steel-intensive structures, applying aluminum in this component could be complex, given the multiple connections with several other BIW elements, from the firewall to the lower A-pillar column and the rocker panel.

This critical component should thus be made of steel, with an additional optimization needed for the structure design, which may be stiffened by additional panels and reach a high level of complexity.

It is worth highlighting that some of the analyzed vehicles present large aluminum casting torque boxes, with a highly optimized structure [79, 44]. Nonetheless, these solutions must be carefully evaluated for what concerns the applicability on high volumes production.

Rear Cross-Member Material

The material of the rear cross member was slightly influential on the analyzed response, with the biggest influence on the torsional stiffness and 1st modal frequency for the

panelless model. Its percentage of contribution for the different responses is presented in figure 6.44. The most suitable solutions were found to be with a steel rear cross-

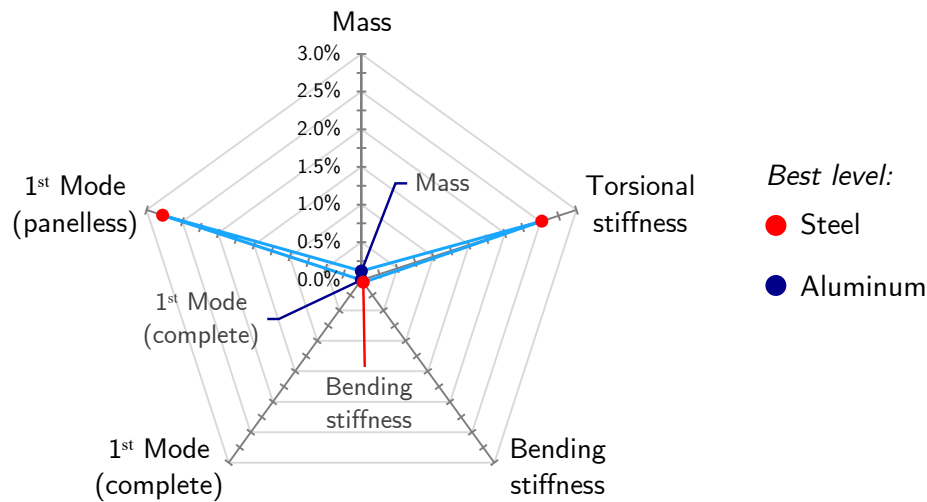


Figure 6.44: Rear cross-member material influence and preferred configuration for the analyzed responses

member, guaranteeing higher torsional stiffness and a higher 1st resonance mode. Slight improvements were present also in the bending stiffness, while the weight saving of the aluminum solution was not sufficient to justify the loss in stiffness.

Several industry applications use an aluminum rear cross member, thus with further optimization of the component section and shape, adequate stiffness and lightweighting could be achieved at the same time.

In general, from the conducted analysis this component was not highly determinant for the structure performances.

Front Cross-Member Thickness

The front cross-member was made variable in thickness between 1.3 mm and 2 mm. In this case, the influence of this factor was minimal, with a considerable influence found only on the torsional stiffness, derived from the direct connection between this element and the front side members. The influence of this parameter on the analysis outputs is reported in figure 6.45.

Given the higher performances in torsional stiffness and the slight improvements in the other responses, the material could be chosen as high thickness, with only a slight weight increase. It is noteworthy that this component could be additionally optimized in the cross-section leading to higher stiffness and allowing a lower steel gauge to be used. In general, this parameter was slightly influential in the conducted analysis.

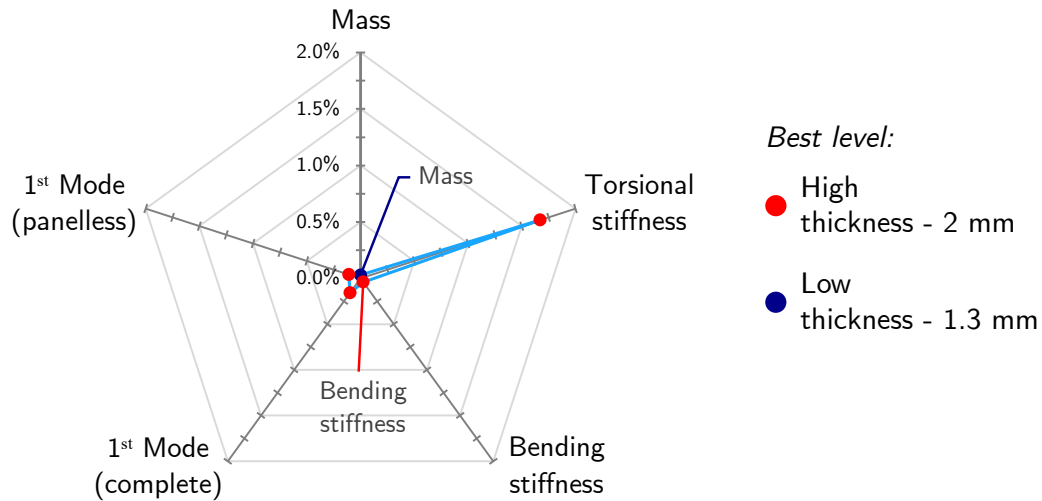


Figure 6.45: Front cross-member thickness influence and preferred configuration for the analyzed responses

Front Floor Cross-Member Thickness

As for the front cross-member, the front floor cross member was made variable in thickness between 1.3 mm and 2 mm. Similarly, the influence of this factor was minimal, with the most influenced responses being the torsional and bending stiffness and the panelless resonance mode. The contribution of this factor to the different responses is shown in figure 6.46. Given the low influence on the structure mass, the more favourable

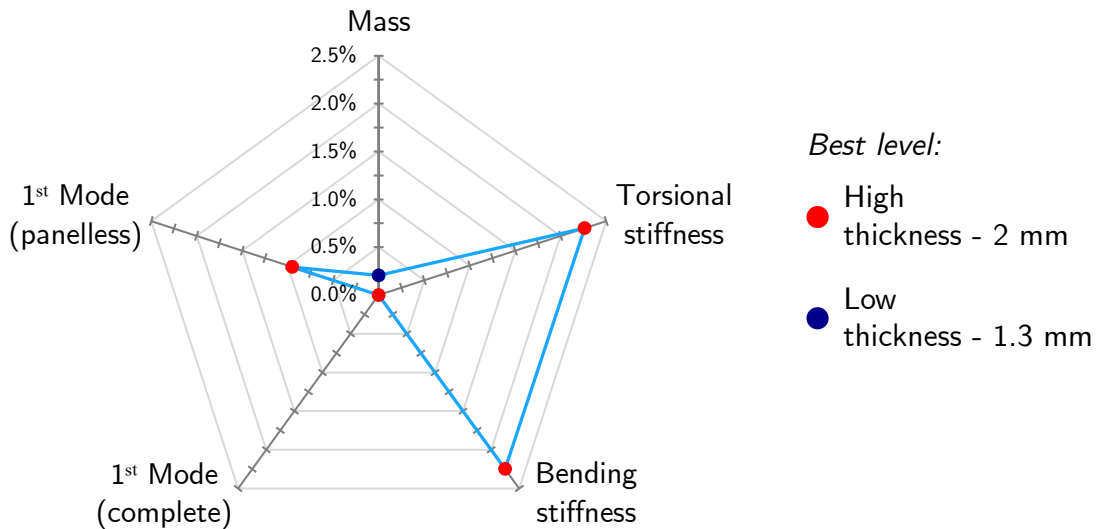


Figure 6.46: Front floor cross-member thickness influence and preferred configuration for the analyzed responses

solution was the one with high thickness steel, improving both torsional and bending stiffness, as well as the panelless 1st mode. These improvements were accompanied by

a low weight increase, which was thus justified.

It is important to emphasize that this component needs to be optimized for better occupant ergonomics in the pedal-box area. This reshaping, together with further optimization of the component cross-section could lead to a higher impact on the stiffness, thus allowing a lower steel gauge to be used.

In general, as the previously analyzed one, this parameter was just slightly influential in the conducted analysis.

Battery Pack Material

The battery pack material was the most influential factor on the system mass. Its influence on the mass and the other responses are compared in figure 6.47.

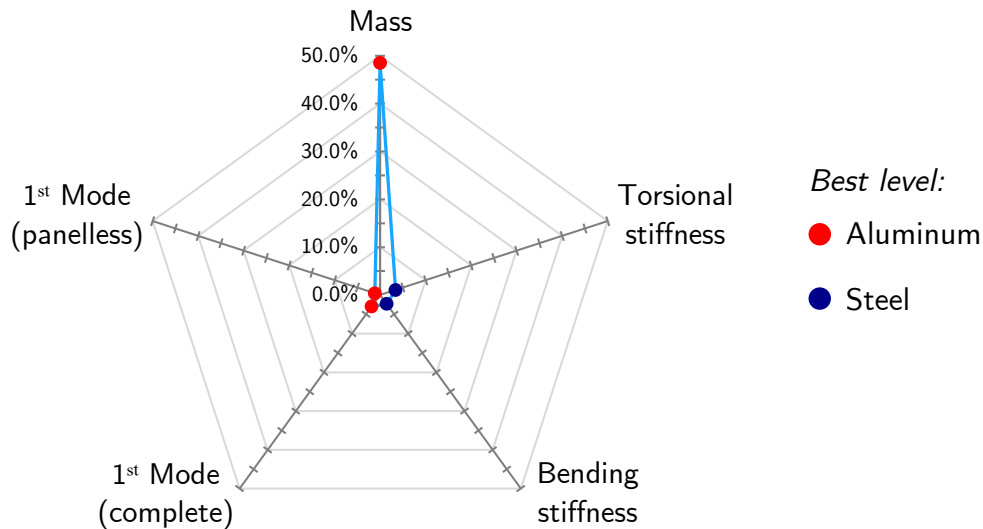


Figure 6.47: Battery pack material influence and preferred configuration for the analyzed responses

The lightweighting allowed by the aluminum battery pack was considerable, causing minimal decrements in the torsional and bending stiffness, which were slightly influenced by this factor. The battery pack structure had shown to be an intrinsically very stiff design, which could be effectively lightened by applying aluminum alloys, with minimal decrements in the static stiffness. Furthermore, the aluminum solutions showed slightly better results in the dynamic stiffness tests. The aluminum battery pack was thus the preferable choice, allowing lightweighting and adequate performances, as well as offering the possibility of integrating an effective side impact crash absorption structure.

This solution may be more complex to realize and manufacture, but offer a high potential for lightweighting, which is crucial for BEVs.

Panels Embossing

From the conducted analysis it was confirmed the necessity of implementing some sort of panel stiffening to avoid low-frequency resonances. Panels embossing was revealed to be an effective solution for the vehicle floor. Additional stiffening is still needed for the battery pack panels which are effectively wider in case of simple internal battery pack structure. Moreover, these panels are loaded by the battery cells, further increasing the chances of low-frequency resonances.

Additional stiffening is necessary for these panels, but a more weight-efficient solution needs to be developed, to avoid using a high number of internal cross-members, which causes a considerable increase in the mass.

6.5.3 Excluded Components

To conclude, it is important to note that several elements were excluded from the design space. For these elements few variations were encountered during the benchmarking analysis and could thus be chosen as the average solution already available on the market, following the indications in chapters 3 and 4. In addition, the used model was a simplified representation of the structure under study. This leaves room for additional optimization of the components initially excluded or kept fixed since considered of lower relevance for the scope of the analysis.

Despite the simplifying assumptions, the conducted analysis was able to deliver preliminary design indications for the future developments of the new BEV platforms, allowing to focus the attention on further design optimization, or the optimization of other components.

7 | Conclusions and Future Work

In this final chapter, the conclusions of the study are presented, together with some hints at future works on the subject of the analysis.

7.1 Summary and Conclusions

Under the increased environmental concerns and the more stringent government emissions regulations, the OEMs are investing in BEVs, which can effectively reduce the road transport carbon footprint.

This new powertrain demands dedicated solutions in order to exploit the advantages of the electric traction and cope with its limitations.

The scope of the study was to investigate the structural design of these two components of the BEVs platform, to determine preliminary guidelines for a weight-efficient design of these systems.

To better understand the current state-of-the-art, a benchmarking analysis was conducted, and a validated classification scheme was developed.

This allowed to concentrate the attention on the characteristics that are distinctive of the BEV underbody and battery pack, without focusing on components and design choices that are already well established from the conventional ICEV platforms.

The scheme demonstrated to be adequately flexible and delivering a coherent classification when applied to vehicles not included in the original sample.

The clustered design of the scheme allows more flexibility in using each cluster singularly or collectively as well as future expandability to other aspects of the BEVs design.

The derived scheme proved to be a useful benchmarking tool to highlight the principal features of the BEVs platform design and emphasize the main differences between the studied vehicles. Moreover, it was effectively used as a concept selection tool for the following phase of the analysis.

This tool will help the designers in the preliminary development phases to focus on the most critical parameters and choose which solution to implement according to the

technological state-of-the-art.

Starting from the results of the first part of the project, a parametric FEA model and a DOE were developed to investigate the most influential factors for the static and dynamic stiffness performance of the underbody and battery pack system.

The conducted DOE highlighted as highest impacting factors the torque boxes material and shape, the rocker rails internal structure and the material of the battery pack. Furthermore, the influence of the different interactions was found to be marginal when compared to the contribution of the principal factors, allowing a simpler component-focused optimization.

These results are important to confirm the qualitative observations of the benchmarking analysis, highlighting the areas on which to concentrate more detailed studies.

The analysis of the batteryless model allowed to assess the high influence of the battery pack on the structure rigidity, being able to increase the stiffness by more than 50% for the torsion load case and 45% in the bending loading. This shows the capability of this component to house and protect the battery cells as well as enhancing the platform structural performance. It was thus possible to evidence how the integration of a structural battery pack will be critical for the future developments of weight-efficient and high-performance platforms.

From the conducted analyses, a linear regression model was derived and used to perform a response optimization. The two optimized configurations revealed both good performances and lightweighting, with the first leading to the best compromise between static and dynamic stiffness and system mass. The optimized configurations represent a good starting point for future designs, allowing to focus the attention on improving the single components.

Another relevant outcome of the analyses was the low-frequency resonance of the underbody and battery pack flat panels. This behaviour could negatively affect the NVH performance of the vehicles as well as cause vibration-induced safety-critical conditions for the battery pack cells.

To reduce these phenomena, panels embossing was applied on the improved optimized solutions showing relatively good improvements. More detailed studies are needed, with particular attention to the battery pack panels. In fact, with the current trends towards reducing the number of internal structure members, there will be the need for adequate and weight-efficient panel stiffening solutions.

The work was concluded by collecting the gathered results into design guidelines. Every analyzed factor was thus presented illustrating the suggested design choices that emerged from the study.

The obtained validated design guidelines represent a valuable starting point for the

development of new dedicated BEVs platforms. The study provides suggestions on the more convenient design choices, giving preliminary indications to direct the next engineering efforts on specific areas of the development in order to make optimal use of the available resources.

7.2 Future Work

The project was developed to focus the attention on the structural design of the BEVs underbody and battery pack, evaluating mass, torsional stiffness, bending stiffness and resonance modes. To conduct the analysis and deliver significant results, some aspects were excluded from the study and the model needed to be largely simplified. In the future developments of this study, it is thus worth focusing the attention on the following aspects:

- *Crashworthiness analysis.* Together with the structure stiffness, crash absorption is one of the most influential factors in the platform design. In fact, some design choices are necessarily driven by the need of having efficient crash absorption structures as well as have adequate strength of the occupant cage. BEVs add an additional aspect to the crash safety, with the battery pack which must be protected from external impact to avoid possible fires or explosions. This needs a different approach to the problem, using a non-linear FEA to study the consequences of the structural deformations under crash. Due to these critical aspects, future works need to focus on the crash analysis of these structures to complement the derived guidelines with the need for crash protection.
- *Higher Resolution DOE and enhanced optimization.* The used fractional factorial experiment allows to highly reduce the number of experiments but causes confounding between interactions that may be relevant. Possibly, after conducting the crash analysis and stress analysis and having gathered a more complete view of the principal influential factors, a full factorial experiment should be conducted, limiting the design space to the five most relevant factors. In fact, the fractional factorial experiment highlighted that some interactions may be present but was unable to distinguish the root cause due to confounding. This more detailed analysis will allow a better understanding of the interactions of the factors. Furthermore, it may allow to further focus on fewer parameters and thus implement a Central Composite Design (CCD) DOE with a lower number of factors, to derive then a response surface for more effective optimization.
- *Cross-section optimization.* The cross-sections were not optimized or varied to

restrict the design space. Further studies are needed on the components cross-section optimization which would allow for further lightweighting and performance improvements. This can be conducted through topology and topography optimization methods, which highlights regions in which more or less material is needed, morphing the shape according to the established targets. These types of optimization analysis may lead to complex shape solutions which will then need to be adequately adapted and simplified for manufacturing.

- *Cross-section optimization for aluminum design.* The material choice analysis was conducted directly substituting aluminum on a structure that was dimensioned according to steel-intensive reference BIWs. An optimized design for aluminum structures will allow further lightweighting and higher stiffness performances.
- *Excluded elements.* Several elements were excluded since not directly part of the main underbody but are crucial for the structural design of the vehicle platform. Future studies shall include a design of other relevant structures, such as the suspension domes, the firewall, and front and rear wheel arches.
- *Simplified structure modelling.* The structure was modelled with simple extruded surfaces, thus not adequately reproducing the actual components made of overlapping welded, bonded, or fastened panels. The connections between the different elements were obtained by building a continuous mesh. More detailed components connections are thus needed for a more realistic FEM model.
- *Improvements of the classification scheme.* Expanding the developed classification scheme by investigating other crucial components of the BEVs platform, such as the vehicle chassis, the e-motors or the battery management system will allow obtaining a more complete tool that would be even more useful for future benchmarking studies or concepts selection.
- *Stress analysis.* In addition to the conducted linear static deformation analysis, a more in-depth study is needed to assess the maximum stresses the structure has to support under limit loading conditions. This may also include puncture tests especially critical for the battery pack mounted in the vehicle underfloor.
- *Battery pack integration.* The effect of different pack-to-underbody connection schemes should be analyzed to reach the best compromise between assembly efficiency and structural performance. This must be considered together with the structural layout of the pack, which, with the current trend of a simpler internal structure would prevent connections in the central part of the vehicle floor.

- *More detailed battery model.* A higher detail level is needed to better describe the real structure of the battery pack, including its internal components, from the battery cells to the thermal management system. A detailed assessment should be carried out to evaluate the effect of the internal members on the pack static and dynamic structural performance as well as investigate the effects of the structure deformation on the battery cells. Additional studies should focus on the implementation of weight-efficient flat panel stiffening solutions to improve the battery pack NVH performance.
- *Structural battery packs.* Given the current trends towards structural battery packs, specific studies of these solutions are needed by developing structural cells and structural adhesive models to investigate the possibilities of this upcoming design trend.
- *Lightweight materials.* The investigation may also be expanded to other lightweight materials, such as composites, which may allow a weight saving as well as guaranteeing good crash absorption performance. In general, a critical role in the implementation of advanced materials structures is the combination and joining of different materials which may lead to manufacturing criticalities. Extensive studies are thus needed for the efficient and effective application of lightweight material, considering a trade-off between weight saving and manufacturing complexity.

These additional studies will allow to have a more complete view on this new dedicated BEV architecture, laying the path for the next optimization of the cost-effectiveness of the solutions, following a design to cost approach, which will allow the OEMs to bring closer the costs of BEV and ICEV, while still keeping good profit margins [62].

Bibliography

- [1] Hannah Ritchie. *Cars, planes, trains: where do CO2 emissions from transport come from?* Oct. 2020. URL: <https://ourworldindata.org/co2-emissions-from-transport> (Accessed on Feb. 20, 2021).
- [2] Amir Khajepour, M. Saber Fallah, and Avesta Goodarzi. “Body and Chassis Technologies”. In: *Electric and hybrid vehicles: technologies, modeling and control-a mechatronic approach*. John Wiley & Sons, 2014.
- [3] IEA (2021). *Global EV Outlook 2021*. Paris: IEA, 2021. URL: <https://www.iea.org/reports/global-ev-outlook-2021> (Accessed on June 19, 2021).
- [4] Daniel Harrison. *Automotive Powertrain Forecast 2020-2030*. Tech. rep. Ultima Media Ltd - Süddeutscher Verlag, 2019.
- [5] Roland Irl. *Global plug-in vehicle sales reached Over 3,2 million in 2020*. URL: <http://www.ev-volumes.com/news/86364/> (Accessed on Feb. 20, 2021).
- [6] Rebecca Matulka. *The History of the Electric Car*. Sept. 2014. URL: <https://www.energy.gov/articles/history-electric-car> (Accessed on Feb. 13, 2021).
- [7] Zachary Shahan. *Electric Car Evolution*. Mar. 2016. URL: <https://cleantech.nica.com/2015/04/26/electric-car-history/> (Accessed on Feb. 18, 2021).
- [8] Sam Abuelsamid. *Meet The Father Of The Auto 'Skateboard' Chassis Used By Tesla: Chris Borroni-Bird*. May 2016. URL: <https://www.forbes.com/sites/samabuelsamid/2016/05/23/the-father-of-the-skateboard-chassis-dr-chris-borroni-bird/?sh=331a05a47b30> (Accessed on Feb. 10, 2021).
- [9] Auto Concept Reviews. *General Motors Autonomy Concept car 2002*. URL: http://www.autoconcept-reviews.com/cars_reviews/gm/gm-autonomy-concept-2002/cars_reviews-gm-autonomy-concept-2002.html (Accessed on Jan. 15, 2021).
- [10] A2mac1 Automotive Benchmarking. URL: <https://www.a2mac1.com> (Accessed on Nov. 6, 2020).

-
- [11] Peter Dore Rawlinson and Alan Paul Clarke. *Augmented vehicle seat mount*. US Patent 8,336,658. 2012.
- [12] Tesla Motors. *Model S Owner’s Manual*. URL: <https://www.tesla.com/> (Accessed on Jan. 15, 2021).
- [13] Frost & Sullivan. *Electric Vehicle Platform Strategy of Global Passenger Vehicle OEMs, Forecast to 2025*. 2017.
- [14] O. Edenhofer et al. *Climate Change 2014: Mitigation of Climate Change. Contribution of Working Group III to the Fifth Assessment Report of the Intergovernmental Panel on Climate Change*. Tech. rep. Cambridge University Press, Cambridge, United Kingdom and New York, NY, USA.: IPCC, 2014.
- [15] P Mock. “CO₂ emission standards for passenger cars and light-commercial vehicles in the European Union”. In: *International Council on Clean Transportation, Washington, DC, USA* (2019).
- [16] Directorate-General for Climate Action - European Commission. *Reducing CO₂ emissions from passenger cars*. 2019. URL: https://ec.europa.eu/clima/policies/transport/vehicles/cars_en (Accessed on Oct. 15, 2020).
- [17] Steve Carden - PA Consulting. *CO₂ Emissions Are Increasing*. 2019. URL: <https://www.paconsulting.com/insights/2019/co2-emissions-are-increasing/> (Accessed on Jan. 20, 2021).
- [18] Xiongwen Zhang et al. “Towards a smart energy network: The roles of fuel / electrolysis cells and technological perspectives”. In: *International Journal of Hydrogen Energy* 40 (Mar. 2015). DOI: 10.1016/j.ijhydene.2015.03.133.
- [19] Auke Hoekstra. “The Underestimated Potential of Battery Electric Vehicles to Reduce Emissions”. In: *Joule* 3.6 (2019), pp. 1412–1414. ISSN: 2542-4351.
- [20] Lai Yang et al. “Life cycle environmental assessment of electric and internal combustion engine vehicles in China”. In: *Journal of Cleaner Production* 285 (2021), p. 124899.
- [21] IEA (2021). *Executive summary – The Role of Critical Minerals in Clean Energy Transitions – Analysis*. Paris: IEA, 2021. URL: <https://www.iea.org/reports/the-role-of-critical-minerals-in-clean-energy-transitions> (Accessed on June 18, 2021).
- [22] Yuan-Li Ding et al. “Automotive Li-Ion Batteries: Current Status and Future Perspectives”. In: *Electrochemical Energy Reviews* 2 (Mar. 2019), pp. 1–28.

-
- [23] Hauke Engel, Patrick Hertzke, and Giulia Siccardo. “Second-life EV batteries: The newest value pool in energy storage”. In: *McKinsey & Company* (May 2019). URL: <https://www.mckinsey.com/industries/automotive-and-assembly/our-insights/second-life-ev-batteries-the-newest-value-pool-in-energy-storage> (Accessed on June 20, 2021).
- [24] Cédric Weiss and Arnaud Goy. *Batteries of the Future*. A2mac1.com, 2021.
- [25] Bruno G. Pollet, Iain Staffell, and Jin Lei Shang. “Current status of hybrid, battery and fuel cell electric vehicles: From electrochemistry to market prospects”. In: *Electrochimica Acta* 84 (2012), pp. 235–249.
- [26] P. Gaffron. “Noise pollution and cars”. In: *Encyclopedia of transportation: Social science and policy*. Ed. by Mark Garrett. Vol. 1. SAGE Publications, 2014.
- [27] Xiao Yu et al. “Suitability of energy sources for automotive application—A review”. In: *Applied Energy* 271 (2020), pp. 115–169.
- [28] Victor RJH Timmers and Peter AJ Achten. “Non-exhaust PM emissions from electric vehicles”. In: *Atmospheric Environment* 134 (2016), pp. 10–17.
- [29] Prajyot Sathe. *Global Electric Vehicle Market Outlook, 2019*. Tech. rep. Frost & Sullivan, 2019.
- [30] *The Lucid Air Is the Fastest Charging EV Ever*. URL: <https://www.lucidmotors.com/stories/lucid-air-fastest-charging-ev/> (Accessed on Feb. 15, 2021).
- [31] Alessio Viola. “Porsche Taycan - Prova su Strada”. In: *Quattroruote* 778 (June 2020), pp. 164–165.
- [32] Daniel Küpper et al. *The Future of Battery Production for Electric Vehicles*. Tech. rep. Boston Consulting Group, 2018.
- [33] S Biswas. “Thermal Management System and Performance Characteristics of Electric Vehicle”. In: *SAE Technical Paper*. SAE International, Aug. 2020.
- [34] *BENTELEER Electric Drive System 2.0*. Sept. 2020. URL: <https://www.benteleer-automotive.com/en/products-competencies/electro-mobility/benteleer-electric-drive-system-20/> (Accessed on Feb. 12, 2021).
- [35] *Jeep® Compass 4xe | Il SUV ibrido plug-in | Jeep®*. URL: <https://www.jeep-official.it/4xe-ibrido/compass-4xe> (Accessed on Jan. 15, 2021).
- [36] Lorenzo Morello et al. “Body Work”. In: *The Automotive Body: Volume I: Components Design*. Springer Netherlands, 2011, pp. 91–205.

-
- [37] Lorenzo Morello et al. *The Automotive Body: Volume I: Components Design*. Springer Science & Business Media, 2011.
- [38] Marco Traverso. *Audi reveals details on the new A8 space frame*. Apr. 2017. URL: <https://www.carbodydesign.com/2017/04/audi-reveals-details-on-the-new-a8-space-frame/> (Accessed on Feb. 5, 2021).
- [39] Lorenzo Morello et al. “Structural Integrity”. In: *The Automotive Body: Volume II: System Design*. Springer Netherlands, 2011.
- [40] Jibing Zhang et al. “Multidisciplinary Design Optimization of BEV Body Structure”. In: *SAE Technical Paper*. SAE International, Jan. 2015. URL: <https://doi.org/10.4271/2015-26-0229>.
- [41] Lorenzo Morello et al. “Noise, Vibration, Harshness”. In: *The Automotive Body: Volume II: System Design*. Springer Netherlands, 2011.
- [42] Lorenzo Morello et al. “Passive Safety”. In: *The Automotive Body: Volume II: System Design*. Springer Netherlands, 2011.
- [43] Daimler AG. *Mercedes-Benz C-Class, safety structure front crash*. 2014. URL: <https://media.daimler.com/marsMediaSite/en/instance/ko/Body-Rigid-body--lightly-done.xhtml?oid=9904514> (Accessed on Feb. 20, 2021).
- [44] A2Mac1. *AutoReverse*. 2021. URL: www.a2mac1.com (Accessed on Apr. 12, 2021).
- [45] Pedro Lima. *Volkswagen e-Golf is now cheaper - PushEVs*. Aug. 2019. URL: <https://pushevs.com/2019/08/31/volkswagen-e-golf-is-now-cheaper/> (Accessed on Jan. 13, 2021).
- [46] Jordi Gil. *Los coches eléctricos de Volkswagen en EXPOelèctric*. Oct. 2014. URL: <https://www.hibridosyelectricos.com/articulo/actualidad/coches-electricos-volkswagen-expoelectric/20141027151318008169.html> (Accessed on Jan. 18, 2021).
- [47] Bengt Halvorson. *Here’s the battery pack behind VW’s global electric-vehicle push*. Sept. 2018. URL: https://www.greencarreports.com/news/1118974_heres-the-battery-pack-behind-vws-global-electric-vehicle-push (Accessed on Jan. 18, 2021).
- [48] Battery University. *Bu-205: Types of lithium-ion*. Mar. 2020. URL: <https://batteryuniversity.com/article/bu-205-types-of-lithium-ion> (Accessed on June 18, 2021).

-
- [49] Outokumpu.com. *Safe electric vehicle battery housings using high-performance stainless steels*. URL: <https://www.outokumpu.com/de-de/expertise/2021/safe-ev-battery-housings-using-high-performance-stainless-steels> (Accessed on June 18, 2021).
- [50] Hayata Uwai, Atsushi Isoda, and Nobuhiko Takahashi. *Development of Crash Safety of the Newly Developed Electric Vehicle*. Tech. rep. SAE Technical Paper, 2011.
- [51] Shashank Arora, Weixiang Shen, and Ajay Kapoor. “Review of mechanical design and strategic placement technique of a robust battery pack for electric vehicles”. In: *Renewable and Sustainable Energy Reviews* 60 (2016), pp. 1319–1331.
- [52] Li Shui et al. “Design optimization of battery pack enclosure for electric vehicle”. In: *Structural and Multidisciplinary Optimization* (2018), pp. 331–347.
- [53] Lothar Wech et al. “Crash safety aspects of HV batteries for vehicles”. In: *Proceedings of the international technical conference on the enhanced safety of vehicles ESV-22. Washington, USA*. 2011.
- [54] Fred Lambert. *First look at Tesla’s new structural battery pack that will power its future electric cars*. Jan. 2021. URL: <https://electrek.co/2021/01/19/tesla-structural-battery-pack-first-picture/> (Accessed on June 21, 2021).
- [55] Harilaos Vasiliadis. *Advanced Lightweight Electric Vehicle Architectures*. Bax & Willems Consulting Venturing. Nov. 2013.
- [56] Micha Lesemann. *Advanced Electric Vehicle Architectures*. Deliverable D6.6 - Final Report 265898. 2014.
- [57] Arturo Dávila et al. *ELVA-Innovative Architectures for Next Generation Electric Vehicles*. Tech. rep. SAE Technical Paper, 2013.
- [58] Tom Phillips. *Top Five: Global EV Platforms*. June 2020. URL: <https://www.automotive-iq.com/chassis-systems/articles/top-five-global-ev-platforms> (Accessed on Feb. 15, 2021).
- [59] Harry Singh. *Body Structure Evolution From Internal Combustion Engine to Electric Vehicles*. Application Engineering – Automotive Center United States Steel Corporation. Feb. 2019.

-
- [60] Peter Els. *Automotive IQ Guides: Electric Vehicle platforms*. July 2019. URL: <https://www.automotive-iq.com/electrics-electronics/articles/automotive-iq-guides-electric-vehicle-platforms> (Accessed on Feb. 15, 2021).
- [61] Mauro Erriquez et al. *Trends in Electric Vehicle Design*. Tech. rep. McKinsey Center for Future Mobility, 2017.
- [62] Mauro Erriquez et al. *Trends in Electric Vehicle Design Issue no. 2*. Tech. rep. McKinsey Center for Future Mobility®, 2017.
- [63] Jibing Zhang et al. “Multidisciplinary Design Optimization of BEV Body Structure”. In: *SAE Technical Paper*. SAE International, Jan. 2015. DOI: 10.4271/2015-26-0229.
- [64] Dohyun Park et al. “Material arrangement optimization for weight minimization of an automotive body in white using a bi-level design strategy”. In: *Proceedings of the Institution of Mechanical Engineers, Part D: Journal of Automobile Engineering* 230.3 (2016), pp. 395–405. DOI: 10.1177/0954407015586677.
- [65] Fei Lei et al. *Research on Three Main Lightweight Approaches for Automotive Body Engineering Considering Materials, Structural Performances and Costs*. Tech. rep. SAE Technical Paper, 2015.
- [66] EAA. “Design with Aluminium”. In: *Aluminium Automotive Manual*. Avenue de Tervueren 168 B-1150 Brussels, Belgium: European Aluminium Association, 2011.
- [67] Peter Dore Rawlinson. *Integration system for a vehicle battery pack*. US Patent 8,833,499. 2014.
- [68] Peter Dore Rawlinson, Hitendra Laxmidas Gadhiya, and Alexi Charbonneau. *Rear vehicle torque box*. US Patent 8,585,131. 2013.
- [69] Alexi Charbonneau et al. *System for absorbing and distributing side impact energy utilizing an integrated battery pack and side sill assembly*. US Patent 8,702,161. 2014.
- [70] Leo F Schwab, Tao Wang, and Phillip D Hamelin. *Structurally integrated propulsion battery*. US Patent 9,533,600. 2017.
- [71] SeungMin Jeong. *Under body for electric vehicle*. US patent 9,908,396. 2020.
- [72] Carsten Wesche et al. *Battery Housing and Motor Vehicle Comprising a Battery Housing of this Kind*. DE patent 10 2018 210 126 A1. 2019.
- [73] Ovgard; Fredrik. *Reinforcement structure*. US patent 10,589,614. 2020.

-
- [74] Hofer; Bernhard. *Vehicle with supporting structure*. US patent 10,661,647. 2020.
- [75] Brett T. Evans. *Hyundai E-GMP EV Platform Revealed With Up To 310 Miles Of Range*. Dec. 2020. URL: <https://www.motor1.com/news/457798/2022-hyundai-egmp-modular-ev-platform/> (Accessed on Jan. 15, 2021).
- [76] Vlad Radu. *A Complete Overview of the Ford Mustang Mach-E's Diverse Powertrain Options*. Jan. 2021. URL: https://www.autoevolution.com/news/a-complete-overview-of-the-ford-mustang-mach-es-diverse-powertrain-options-154178.html#agal_9 (Accessed on Jan. 18, 2021).
- [77] A2mac1 Automotive Benchmarking. *Intelligence - Static Benchmarking*. URL: <https://www.a2mac1.com/Documentation/Documentation.asp> (Accessed on Apr. 20, 2021).
- [78] *Porsche Tycan - Prova su Strada*. URL: <https://www.quattroruote.it/prove/prove-strada/> (Accessed on Feb. 15, 2021).
- [79] A2Mac1. *BIW analysis*. 2021. URL: www.a2mac1.com (Accessed on May 25, 2021).
- [80] A2Mac1. *xEV Powertrain*. 2021. URL: www.a2mac1.com (Accessed on May 25, 2021).
- [81] Jake Lingeman. *2019 Audi e-tron first drive: Just like a regular car, man*. Sept. 2020. URL: <https://www.autoweek.com/drives/a1713091/2019-audi-e-tron-first-drive-way-future/> (Accessed on Jan. 15, 2021).
- [82] Dell K. Allen. "Classification Systems". In: *Mechanical Engineers' Handbook*. John Wiley & Sons, Ltd, 2005. Chap. 3, pp. 68–109. ISBN: 9780471777465. DOI: <https://doi.org/10.1002/0471777463.ch3>.
- [83] José Pontes. *Record Electric Vehicle Sales in China*. Dec. 2020. URL: <https://cleantechnica.com/2020/12/27/record-electric-vehicle-sales-in-china/> (Accessed on Feb. 15, 2021).
- [84] Giancarlo Genta et al. "Economic Figures - Market Segmentation". In: *The Motor Car: Past, Present and Future*. Springer Science & Business Media, 2014.
- [85] Felipe Munoz. *My segmentation*. Apr. 2021. URL: <https://fiatgroupworld.com/my-segmentation/> (Accessed on May 15, 2021).
- [86] H. Dirk and JA. Lukaszewicz. "Automotive composite structures for crashworthiness". In: *Advanced composite materials for automotive applications: structural integrity and crashworthiness* (2013), pp. 99–127.

-
- [87] David Roper. *Here's How To Calculate Conflicting EV Range Test Cycles: EPA, WLTP, NEDC*. Mar. 2019. URL: <https://insideevs.com/features/343231/heres-how-to-calculate-conflicting-ev-range-test-cycles-epa-wltp-nedc/> (Accessed on Feb. 15, 2021).
- [88] *ID.3 Sets the Tone for a Safe and Clean Future*. Oct. 2020. URL: <https://euroncap.newsmarket.com/LATEST-RELEASE/id.3-sets-the-tone-for-a-safe-and-clean-future/s/ae66920f-5cd5-4c3e-b6cb-27dca72279f8> (Accessed on June 18, 2021).
- [89] A2Mac1. *Vehicle Occupant Packaging*. 2021. URL: www.a2mac1.com (Accessed on May 25, 2021).
- [90] *MSC Nastran 2012 Linear Static Analysis User's Guide*. MSC Software Corporation. 2012. URL: <http://simcompanion.mscsoftware.com/infocenter/index?page=content&id=D0C10003> (Accessed on June 15, 2021).
- [91] Jeff Gardiner. *Finite element analysis convergence and mesh independence*. 2017. URL: <https://www.xceed-eng.com/finite-element-analysis-convergence-and-mesh-independence/> (Accessed on June 15, 2021).
- [92] EnDuraSim. *The concise guide to Nastran Rigid Elements*. EnDuraSim Pty Ltd. 2008. URL: <http://www.endurasim.com.au/wp-content/uploads/2015/02/EnDuraSim-Rigid-Elements.pdf> (Accessed on June 15, 2021).
- [93] WD Callister and DG Rethwisch. "Mechanical Properties of Metals". In: *Materials Science and Engineering – An Introduction*. John Wiley & Sons, Inc., Dec. 2009. Chap. 6.
- [94] Karan Khanse and Shekhar Pathak. "Test Set-Up of BIW (Body in White) Stiffness Measurements". In: Apr. 2013. DOI: 10.4271/2013-01-1439.
- [95] Altair University. *Modal Analysis with Altair OptiStruct / HyperMesh*. 2017. URL: https://altairuniversity.com/wp-content/uploads/2017/09/modal_analysis_MG.pdf (Accessed on June 15, 2021).
- [96] Paul D Berger, Robert E Maurer, and Giovana B Celli. *Experimental Design with Applications in Management, Engineering, and the Sciences*. eng. Springer International Publishing AG, 2017.
- [97] Mario Vianello. "Reliability Tools". In: vol. PRODUCT RELIABILITY DESIGN. Polytecnic Press. Chap. 4.

- [98] Minitab LLC. *What is the design resolution in a factorial design?* 2018. URL: <https://support.minitab.com/en-us/minitab/18/help-and-how-to/modeling-statistics/doe/supporting-topics/factorial-and-screening-designs/what-is-design-resolution/> (Accessed on June 15, 2021).
- [99] Minitab LLC. *What is ANOVA?* 2018. URL: <https://support.minitab.com/en-us/minitab/18/help-and-how-to/modeling-statistics/anova/supporting-topics/basics/what-is-anova/> (Accessed on June 15, 2021).
- [100] Minitab LLC. *Model Reduction*. 2018. URL: <https://support.minitab.com/en-us/minitab/18/help-and-how-to/modeling-statistics/regression/supporting-topics/regression-models/model-reduction/> (Accessed on June 15, 2021).
- [101] Minitab LLC. *Methods and formulas for the analysis of variance in Analyze Factorial Design*. 2018. URL: <https://support.minitab.com/en-us/minitab/18/help-and-how-to/modeling-statistics/doe/how-to/factorial/analyze-factorial-design/methods-and-formulas/analysis-of-variance/> (Accessed on June 15, 2021).
- [102] Minitab LLC. *What is response optimization?* 2018. URL: <https://support.minitab.com/en-us/minitab/18/help-and-how-to/modeling-statistics/using-fitted-models/supporting-topics/response-optimization/what-is-response-optimization/> (Accessed on June 15, 2021).
- [103] Giovanni Belingardi and Giorgio Chiandussi. “Vehicle Crashworthiness Design - General Principles and Potentialities of Composite Material Structures”. In: *Impact Engineering of Composite Structures*. Ed. by Serge Abrate. Vienna: Springer Vienna, 2011, pp. 193–264.

Appendix A | Fractional Factorial Plan

The following tables A.1 and A.2 report the used fractional factorial DOE plan.

Table A.1: Designed Fractional Factorial plan - factors 1 to 6

Side memb.	F-c-memb.	# batt-long. memb.	Lower enclosure	T-box shape	F-floor c-memb.
S	1.3	0	frame	ortho	1.3
A	1.3	0	frame	ortho	2
S	2	0	frame	ortho	2
A	2	0	frame	ortho	1.3
S	1.3	1	frame	ortho	2
A	1.3	1	frame	ortho	1.3
S	2	1	frame	ortho	1.3
A	2	1	frame	ortho	2
S	1.3	0	tray	ortho	1.3
A	1.3	0	tray	ortho	2
S	2	0	tray	ortho	2
A	2	0	tray	ortho	1.3
S	1.3	1	tray	ortho	2
A	1.3	1	tray	ortho	1.3
S	2	1	tray	ortho	1.3
A	2	1	tray	ortho	2
S	1.3	0	frame	angled	1.3
A	1.3	0	frame	angled	2
S	2	0	frame	angled	2
A	2	0	frame	angled	1.3
S	1.3	1	frame	angled	2
A	1.3	1	frame	angled	1.3
S	2	1	frame	angled	1.3
A	2	1	frame	angled	2
S	1.3	0	tray	angled	1.3
A	1.3	0	tray	angled	2
S	2	0	tray	angled	2
A	2	0	tray	angled	1.3
S	1.3	1	tray	angled	2
A	1.3	1	tray	angled	1.3
S	2	1	tray	angled	1.3
A	2	1	tray	angled	2

Table A.2: Designed Fractional Factorial plan - factors 7 to 11

No. batt. c-members	Rocker int. structure	T-box material	R-c-member material	Battery pack material
0	stamped	S	S	S
0	stamped	A	A	S
5	stamped	S	S	A
5	stamped	A	A	A
5	extruded	A	S	S
5	extruded	S	A	S
0	extruded	A	S	A
0	extruded	S	A	A
5	extruded	A	A	A
5	extruded	S	S	A
0	extruded	A	A	S
0	extruded	S	S	S
0	stamped	S	A	A
0	stamped	A	S	A
5	stamped	S	A	S
5	stamped	A	S	S
0	extruded	S	A	A
0	extruded	A	S	A
5	extruded	S	A	S
5	extruded	A	S	S
5	stamped	A	A	A
5	stamped	S	S	A
0	stamped	A	A	S
0	stamped	S	S	S
5	stamped	A	S	S
5	stamped	S	A	S
0	stamped	A	S	A
0	stamped	S	A	A
0	extruded	S	S	S
0	extruded	A	A	S
5	extruded	S	S	A
5	extruded	A	A	A

Appendix B | ANOVA detailed results

In this appendix the detailed results from the conducted ANOVA are listed for the conducted complete and panelless models analysis. The following abbreviations will be used: DF=degrees of freedom; Adj SS=adjusted sum of squares.

At first the aliasing structure is presented:

Table B.1: DOE factors and aliasing structure

Factor	Factor Name	Aliased interactions
A	Side members mat.	AB + CF + GJ + KL
B	Front cross-member thick.	AC + BF + DJ + HK
C	No. battery pack long. members	AD + CJ + EK + FG
D	Lower battery enclosure shape	AE + DK + HJ
E	Torque boxes shape	AF + BC + DG + HL
F	Front-floor cross-member thick.	AG + BJ + DF
G	No. battery pack cross-members	AH + CK + EJ + FL
H	Rocker internal structure	AJ + BG + CD + EH
J	Torque boxes mat.	AK + BL + CH + DE
K	Rear cross-member mat.	AL + BK + FH
L	Battery pack mat.	BD + CG + EL + FJ BE + DL + GH BH + CL + EG + FK CE + DH + GL + JK EF + GK + JL

B.1 Complete Model Analysis

Mass ANOVA

Table B.2: ANOVA results for the mass response

Source	DF	Adj SS	P-Value
Factor	11	22186.6	0.00000
Side members mat.	1	306.9	0.00000
Front cross-member thick.	1	6.8	0.00000
No. battery pack long. members	1	187.7	0.00000
Lower battery enclosure shape	1	22.6	0.00000
Torque boxes shape	1	0.0	0.00742
Front-floor cross-member thick.	1	46.3	0.00000
No. battery pack cross-members	1	3190	0.00000
Rocker internal structure	1	6461	0.00000
Torque boxes mat.	1	997.9	0.00000
Rear cross-member mat.	1	26.5	0.00000
Battery pack mat.	1	10940.9	0.00000
2-Way Interactions	15	371.9	0.00000
Side members mat.*Front cross-member thick.	1	0.0	0.56231
Side members mat.*No. battery pack long. members	1	0.0	0.56231
Side members mat.*Lower battery enclosure shape	1	0.0	0.12189
Side members mat.*T-box shape	1	0.0	0.56231
Side members mat.*Front-floor cross-member thick.	1	0.6	0.00000
Side members mat.*No. battery pack cross-members	1	0.0	0.56231
Side members mat.*Rocker internal structure	1	27.9	0.00000
Side members mat.*Torque boxes mat.	1	0.0	0.12189
Side members mat.*Rear cross-member mat.	1	0.4	0.00000
Side members mat.*Battery pack mat.	1	0.0	0.56231
Front cross-member thick.*Lower battery enclosure shape	1	3.1	0.00000
Front cross-member thick.*T-box shape	1	10.2	0.00000
Front cross-member thick.*Rocker internal structure	1	18.8	0.00000
No. battery pack long. members*T-box shape	1	308.1	0.00000
Torque boxes shape*Front-floor cross-member thick.	1	2.8	0.00000
Error	5	0.0	
Total	31	22558.5	

Table B.3: ANOVA results for the mass response - after pooling process

Source	DF	Adj SS	P-Value
Factors	11	22186.6	0.000
Side members mat.	1	306.9	0.000
Front cross-member thick.	1	6.8	0.000
No. battery pack long. members	1	187.7	0.000
Lower battery enclosure shape	1	22.6	0.000
Torque boxes shape	1	0	0.000
Front-floor cross-member thick.	1	46.3	0.000
No. battery pack cross-members	1	3190	0.000
Rocker internal structure	1	6461	0.000
Torque boxes mat.	1	997.9	0.000
Rear cross-member mat.	1	26.5	0.000
Battery pack mat.	1	10940.9	0.000
2-Way Interactions	10	371.9	0.000
Side members mat.*Lower battery enclosure shape	1	0	0.049
Side members mat.*Front-floor cross-member thick.	1	0.6	0.000
Side members mat.*Rocker internal structure	1	27.9	0.000
Side members mat.*Torque boxes mat.	1	0	0.049
Side members mat.*Rear cross-member mat.	1	0.4	0.000
Front cross-member thick.*Lower battery enclosure shape	1	3.1	0.000
Front cross-member thick.*T-box shape	1	10.2	0.000
Front cross-member thick.*Rocker internal structure	1	18.8	0.000
No. battery pack long. members*T-box shape	1	308.1	0.000
Torque boxes shape*Front-floor cross-member thick.	1	2.8	0.000
Error	10	0	
Total	31	22558.5	

Torsional Stiffness ANOVA

Table B.4: ANOVA results for the torsional stiffness response

Source	DF	Adj SS	P-Value
Factors	11	39035.9	0.000
Side members mat.	1	86.2	0.000
Front cross-member thick.	1	683.7	0.000
No. battery pack long. members	1	0.3	0.561
Lower battery enclosure shape	1	13.4	0.006
Torque boxes shape	1	19311.6	0.000
Front-floor cross-member thick.	1	925.4	0.000
No. battery pack cross-members	1	4.9	0.040
Rocker internal structure	1	42.2	0.000
Torque boxes mat.	1	15554.3	0.000
Rear cross-member mat.	1	1030.9	0.000
Battery pack mat.	1	1383.1	0.000
2-Way Interactions	15	1855.6	0.000
Side members mat.*Front cross-member thick.	1	0.3	0.504
Side members mat.*No. battery pack long. members	1	2.1	0.132
Side members mat.*Lower battery enclosure shape	1	17.8	0.003
Side members mat.*T-box shape	1	0.0	0.808
Side members mat.*Front-floor cross-member thick.	1	3.4	0.070
Side members mat.*No. battery pack cross-members	1	1.4	0.200
Side members mat.*Rocker internal structure	1	1124.9	0.000
Side members mat.*Torque boxes mat.	1	141.1	0.000
Side members mat.*Rear cross-member mat.	1	378.3	0.000
Side members mat.*Battery pack mat.	1	0.7	0.350
Front cross-member thick.*Lower battery enclosure shape	1	18.8	0.003
Front cross-member thick.*T-box shape	1	162.0	0.000
Front cross-member thick.*Rocker internal structure	1	0.6	0.400
No. battery pack long. members*T-box shape	1	2.3	0.122
Torque boxes shape*Front-floor cross-member thick.	1	1.9	0.147
Error	5	3.3	
Total	31	40894.7	

Table B.5: ANOVA results for the torsional stiffness response - after pooling process

Source	DF	Adj SS	P-Value
Factors	11	39035.9	0.000
Side members mat.	1	86.2	0.000
Front cross-member thick.	1	683.7	0.000
No. battery pack long. members	1	0.3	0.646
Lower battery enclosure shape	1	13.4	0.004
Torque boxes shape	1	19311.6	0.000
Front-floor cross-member thick.	1	925.4	0.000
No. battery pack cross-members	1	4.9	0.057
Rocker internal structure	1	42.2	0.000
Torque boxes mat.	1	15554.3	0.000
Rear cross-member mat.	1	1030.9	0.000
Battery pack mat.	1	1383.1	0.000
2-Way Interactions	6	1842.8	0.000
Side members mat.*Lower battery enclosure shape	1	17.8	0.001
Side members mat.*Rocker internal structure	1	1124.9	0.000
Side members mat.*Torque boxes mat.	1	141.1	0.000
Side members mat.*Rear cross-member mat.	1	378.3	0.000
Front cross-member thick.*Lower battery enclosure shape	1	18.8	0.001
Front cross-member thick.*T-box shape	1	162.0	0.000
Error	14	16.0	
Total	31	40894.7	

Bending Stiffness ANOVA

Table B.6: ANOVA results for the bending stiffness response

Source	DF	Adj SS	P-Value
Factors	11	46.79	0.000
Side members mat.	1	0.43	0.009
Front cross-member thick.	1	0.02	0.374
No. battery pack long. members	1	0.37	0.011
Lower battery enclosure shape	1	0.00	0.804
Torque boxes shape	1	0.06	0.194
Front-floor cross-member thick.	1	1.13	0.001
No. battery pack cross-members	1	0.73	0.003
Rocker internal structure	1	5.05	0.000
Torque boxes mat.	1	37.81	0.000
Rear cross-member mat.	1	0.02	0.390
Battery pack mat.	1	1.16	0.001
2-Way Interactions	15	3.38	0.011
Side members mat.*Front cross-member thick.	1	0.01	0.523
Side members mat.*No. battery pack long. members	1	0.02	0.470
Side members mat.*Lower battery enclosure shape	1	0.03	0.319
Side members mat.*T-box shape	1	0.18	0.044
Side members mat.*Front-floor cross-member thick.	1	0.50	0.006
Side members mat.*No. battery pack cross-members	1	0.03	0.332
Side members mat.*Rocker internal structure	1	1.09	0.001
Side members mat.*Torque boxes mat.	1	0.09	0.110
Side members mat.*Rear cross-member mat.	1	0.03	0.305
Side members mat.*Battery pack mat.	1	0.01	0.561
Front cross-member thick.*Lower battery enclosure shape	1	0.06	0.184
Front cross-member thick.*T-box shape	1	0.44	0.008
Front cross-member thick.*Rocker internal structure	1	0.06	0.168
No. battery pack long. members*T-box shape	1	0.00	0.716
Torque boxes shape*Front-floor cross-member thick.	1	0.83	0.002
Error	5	0.12	
Total	31	50.29	

Table B.7: ANOVA results for the bending stiffness response - after pooling process

Source	DF	Adj SS	P-Value
Factors	11	46.79	0.000
Side members mat.	1	0.43	0.002
Front cross-member thick.	1	0.02	0.401
No. battery pack long. members	1	0.37	0.004
Lower battery enclosure shape	1	0.00	0.820
Torque boxes shape	1	0.06	0.203
Front-floor cross-member thick.	1	1.13	0.000
No. battery pack cross-members	1	0.73	0.000
Rocker internal structure	1	5.05	0.000
Torque boxes mat.	1	37.81	0.000
Rear cross-member mat.	1	0.02	0.417
Battery pack mat.	1	1.16	0.000
2-Way Interactions	5	3.04	0.000
Side members mat.*T-box shape	1	0.18	0.031
Side members mat.*Front-floor cross-member thick.	1	0.50	0.001
Side members mat.*Rocker internal structure	1	1.09	0.000
Front cross-member thick.*T-box shape	1	0.44	0.002
Torque boxes shape*Front-floor cross-member thick.	1	0.83	0.000
Error	15	0.47	
Total	31	50.29	

1st Modal Frequency ANOVA**Table B.8:** ANOVA results for the 1st modal frequency response

Source	DF	Adj SS	P-Value
Factors	11	1087.48	0.001
Side members mat.	1	0.00	0.987
Front cross-member thick.	1	2.06	0.435
No. battery pack long. members	1	108.85	0.002
Lower battery enclosure shape	1	0.40	0.723
Torque boxes shape	1	18.92	0.050
Front-floor cross-member thick.	1	0.00	0.970
No. battery pack cross-members	1	899.35	0.000
Rocker internal structure	1	18.87	0.050
Torque boxes mat.	1	0.00	0.995
Rear cross-member mat.	1	0.00	0.997
Battery pack mat.	1	39.02	0.014
2-Way Interactions	15	204.43	0.047
Side members mat.*Front cross-member thick.	1	0.00	0.995
Side members mat.*No. battery pack long. members	1	0.00	0.993
Side members mat.*Lower battery enclosure shape	1	0.00	0.970
Side members mat.*T-box shape	1	0.00	0.996
Side members mat.*Front-floor cross-member thick.	1	0.37	0.734
Side members mat.*No. battery pack cross-members	1	0.00	0.990
Side members mat.*Rocker internal structure	1	0.00	0.996
Side members mat.*Torque boxes mat.	1	2.08	0.433
Side members mat.*Rear cross-member mat.	1	14.40	0.075
Side members mat.*Battery pack mat.	1	0.00	0.993
Front cross-member thick.*Lower battery enclosure shape	1	108.70	0.002
Front cross-member thick.*T-box shape	1	19.24	0.049
Front cross-member thick.*Rocker internal structure	1	21.14	0.042
No. battery pack long. members*T-box shape	1	38.50	0.015
Torque boxes shape*Front-floor cross-member thick.	1	0.00	0.997
Error	5	14.35	
Total	31	1306.26	

Table B.9: ANOVA results for the 1st modal frequency response - after pooling process

Source	DF	Adj SS	P-Value
Factors	11	1087.48	0.000
Side members mat.	1	0.00	0.979
Front cross-member thick.	1	2.06	0.195
No. battery pack long. members	1	108.85	0.000
Lower battery enclosure shape	1	0.40	0.557
Torque boxes shape	1	18.92	0.001
Front-floor cross-member thick.	1	0.00	0.950
No. battery pack cross-members	1	899.35	0.000
Rocker internal structure	1	18.87	0.001
Torque boxes mat.	1	0.00	0.991
Rear cross-member mat.	1	0.00	0.995
Battery pack mat.	1	39.02	0.000
2-Way Interactions	5	201.97	0.000
Side members mat.*Rear cross-member mat.	1	14.40	0.003
Front cross-member thick.*Lower battery enclosure shape	1	108.70	0.000
Front cross-member thick.*T-box shape	1	19.24	0.001
Front cross-member thick.*Rocker internal structure	1	21.14	0.001
No. battery pack long. members*T-box shape	1	38.50	0.000
Error	15	16.80	
Total	31	1306.26	

B.2 Panelless Model

1st Modal Frequency ANOVA

Table B.10: ANOVA results for the 1st modal frequency response - panelless model

Source	DF	Adj SS	P-Value
Factors	11	255.68	0.000
Side members mat.	1	184.85	0.000
Front cross-member thick.	1	0.29	0.010
No. battery pack long. members	1	1.07	0.001
Lower battery enclosure shape	1	1.36	0.000
Torque boxes shape	1	7.90	0.000
Front-floor cross-member thick.	1	2.51	0.000
No. battery pack cross-members	1	4.28	0.000
Rocker internal structure	1	42.53	0.000
Torque boxes mat.	1	0.49	0.003
Rear cross-member mat.	1	7.35	0.000
Battery pack mat.	1	3.04	0.000
2-Way Interactions	15	9.14	0.001
Side members mat.*Front cross-member thick.	1	0.05	0.170
Side members mat.*No. battery pack long. members	1	0.14	0.039
Side members mat.*Lower battery enclosure shape	1	0.09	0.074
Side members mat.*T-box shape	1	0.69	0.002
Side members mat.*Front-floor cross-member thick.	1	0.13	0.040
Side members mat.*No. battery pack cross-members	1	0.05	0.142
Side members mat.*Rocker internal structure	1	5.58	0.000
Side members mat.*Torque boxes mat.	1	0.39	0.005
Side members mat.*Rear cross-member mat.	1	0.02	0.302
Side members mat.*Battery pack mat.	1	0.44	0.004
Front cross-member thick.*Lower battery enclosure shape	1	0.09	0.074
Front cross-member thick.*T-box shape	1	0.26	0.012
Front cross-member thick.*Rocker internal structure	1	0.35	0.007
No. battery pack long. members*T-box shape	1	0.86	0.001
Torque boxes shape*Front-floor cross-member thick.	1	0.01	0.503
Error	5	0.09	
Total	31	264.91	

Table B.11: ANOVA results for the 1st modal frequency response - panelless model after pooling

Source	DF	Adj SS	P-Value
Factors	11	255.68	0.000
Side members mat.	1	184.85	0.000
Front cross-member thick.	1	0.29	0.033
No. battery pack long. members	1	1.07	0.001
Lower battery enclosure shape	1	1.36	0.000
Torque boxes shape	1	7.90	0.000
Front-floor cross-member thick.	1	2.51	0.000
No. battery pack cross-members	1	4.28	0.000
Rocker internal structure	1	42.53	0.000
Torque boxes mat.	1	0.49	0.009
Rear cross-member mat.	1	7.35	0.000
Battery pack mat.	1	3.04	0.000
2-Way Interactions	7	8.56	0.000
Side members mat.*T-box shape	1	0.69	0.003
Side members mat.*Rocker internal structure	1	5.58	0.000
Side members mat.*Torque boxes mat.	1	0.39	0.017
Side members mat.*Battery pack mat.	1	0.44	0.012
Front cross-member thick.*T-box shape	1	0.26	0.044
Front cross-member thick.*Rocker internal structure	1	0.35	0.022
No. battery pack long. members*T-box shape	1	0.86	0.001
Error	13	0.67	
Total	31	264.91	

Vita Auctoris

NAME: Gabriele Rosso
PLACE OF BIRTH: Chivasso, Turin, Italy
YEAR OF BIRTH: 1997
EDUCATION: Liceo Scientifico “Isaac Newton”, Chivasso, TO, Italy, 2011-2016
Politecnico di Torino, B.Sc., Turin, Italy, 2016-2019
Politecnico di Torino, M.Sc., Turin, Italy, 2019-2021
University of Windsor, M.A.Sc., Windsor, ON, Canada, 2020-2021